

Modelling, Simulation, Testing, and Optimization of Advanced Hybrid  
Vehicle Powertrains

By

Jeffrey Daniel Wishart

B. App. Sc., University of British Columbia, 1998

M. Sc., University of Saskatchewan, 2001

A Thesis Submitted in Partial Fulfillment of the Requirements for the Degree of  
Doctor of Philosophy  
in the  
Department of Mechanical Engineering

©Jeffrey Wishart, 2008

University of Victoria

All rights reserved. This thesis may not be reproduced in whole or in part, by photocopy or other means, without the permission of the author.

Modelling, Simulation, Testing and Optimization of Advanced Hybrid  
Vehicle Powertrains

By

Jeffrey Daniel Wishart

B. App. Sc., University of British Columbia, 1998

M. Sc., University of Saskatchewan, 2001

**Supervisory Committee:**

Dr. Zuomin Dong, Supervisor, Department of Mechanical Engineering

Dr. Andrew Rowe, Departmental Member, Department of Mechanical Engineering

Dr. Peter Wild, Departmental Member, Department of Mechanical Engineering

Dr. Subhasis Nandi, Outside Member, Department of Electrical Engineering

Dr. Jie Chen, External Examiner, Indiana University Purdue University at Indianapolis

Supervisory Committee:

Dr. Zuomin Dong, Supervisor, Department of Mechanical Engineering

Dr. Andrew Rowe, Departmental Member, Department of Mechanical Engineering

Dr. Peter Wild, Departmental Member, Department of Mechanical Engineering

Dr. Subhasis Nandi, Outside Member, Department of Electrical Engineering

Dr. Jie Chen, External Examiner, Indiana University Purdue University at Indianapolis

## **Abstract**

The internal combustion engine (ICE) vehicle has dominated the transportation market for nearly 100 years. Numerous concerns with continued use of fossil fuels arise, however, and these concerns have created an impetus to develop more efficient vehicles that release fewer emissions. There are several powertrain technologies that could supplant conventional ICEs as the dominant technology, most notably electric and hybrid powertrains. In order to achieve the levels of performance and cost of conventional powertrains, electric and hybrid powertrain designers must use design techniques and tools such as computer modelling, simulation and optimization. These tools facilitate development of a virtual prototype that allows the designer to rapidly see the effects of design modifications and precludes the need to manufacture multiple expensive physical prototypes.

A comprehensive survey of the state of the art of commercialized hybrid vehicle powertrains is conducted, and the term *multi-regime* in ICE hybrid vehicle (ICEHV) modelling is introduced to describe designs that allow for multiple configurations and operating regimes. A dynamic mathematical model of a power-split architecture with two modes (or configurations) introduced by General Motors Corporation is developed and a steady-state version is programmed into the ADvanced VehIcle SimulatOR (ADVISOR) simulation software package. This ADVISOR model is applied to a commercial delivery vehicle, and the fuel consumption of

the vehicle undergoing a variety of drive cycles is determined. The two-mode model is compared to the ADVISOR models for the Toyota Hybrid System (THS), parallel hybrid, and conventional powertrains in the same vehicle. The results show that for this vehicle type, the two-mode design achieves lower fuel consumption than the THS and conventional powertrains, and only slightly greater fuel consumption than the parallel hybrid design. There is also considerable potential for improvement in performance of the two-mode model through the development of an optimal power management strategy.

In the medium- to long-term, the necessity for zero-emission vehicles may position fuel cell systems (FCSs) to be commercialized as on-board energy conversion devices. FCSs are currently inordinately expensive with power density and durability issues, among other design problems. Fuel cell hybrid vehicle (FCHV) designers must use the available design techniques intelligently to overcome the limitations and take advantage of the higher efficiency capabilities of the fuel cell. As the first step in creating a virtual prototype of a FCS, a semi-empirical model of the system is developed and further enhancements such as transient response modelling are proposed. An optimization of the operating parameters to maximize average net power and average exergetic efficiency is conducted, and the technique is applied to the FCS model for the prototype fuel cell hybrid scooter (FCHS). The optimizations demonstrate that significant improvements in performance can be achieved, and that optimizations with more design variables are warranted.

Models of a conventional battery scooter (BS) and of the FCHS are developed in ADVISOR. Simulations are conducted which compare the performance of the two models. Subsequently, performance tests of the BS and FCHS are conducted using a chassis dynamometer. Despite problems with the prototype FCHS, the tests confirm the theoretical results: the FCHS model achieves higher performance in terms of acceleration and power, while the BS model operates more efficiently and requires less energy.

This study provides better understanding on the emerging FCHV and ICEHV technologies; introduced new and improved models for FCHV and multi-regime hybrid powertrains;

developed FCHV and ICEHV performance simulation and design optimization methods using the new computer models; explored the methods for validating the computer models using prototype BS and FCMS on a research dynamometer; identified areas of improvements of the new experiment methods; and formed the foundation for future research in related areas.

## Table of Contents

<b>Supervisory Committee:</b> .....	<b>ii</b>
<b>Abstract</b> .....	<b>iii</b>
<b>Table of Contents</b> .....	<b>vi</b>
<b>List of Figures</b> .....	<b>x</b>
<b>List of Tables</b> .....	<b>xiv</b>
<b>List of Abbreviations</b> .....	<b>xvi</b>
<b>Acknowledgements</b> .....	<b>xxi</b>
<b>Frontispiece</b> .....	<b>xxii</b>
<b>Chapter 1     Background and Motivation</b> .....	<b>1</b>
1.1     Environmental Concerns .....	1
1.2     Resource Supply and Energy Efficiency .....	4
1.3     Contemporary Vehicle Powertrain Technologies .....	5
1.4     Internal Combustion Engine Vehicles .....	6
1.5     Electric Vehicles .....	12
1.5.1     Fuel cell vehicles.....	15
1.6     Hybrid Vehicles .....	19
1.6.1     Hybrid vehicle history.....	22
1.6.2     Fuel cell hybrid vehicles .....	25
1.6.3     Commercialization barriers to fuel cell hybrid vehicles .....	26
1.6.4     Fuel cell hybrid vehicle industry status .....	28
1.6.5     Fuel cell low-speed vehicles .....	30
1.7     Research Focus.....	33
1.8     Research Tools .....	36
<b>Chapter 2     State of the Art of Commercialized Hybrid Vehicles</b> .....	<b>38</b>
2.1     Categories of Internal Combustion Engine Hybrid Vehicles .....	38
2.1.1     Series architecture.....	41
2.1.2     Parallel architecture .....	43
2.1.3     Power-split architecture .....	45
2.1.4     One-mode, two-mode and multi-regime powertrain architectures.....	49
2.2     General Motors Designs.....	51
2.3     Renault Design .....	61
2.4     Timken Design .....	62
2.5     Silvatech Design.....	64
2.6     University of Michigan-Dearborn Design.....	66

<b>Chapter 3</b>	<b>Multi-Regime Powertrain Architecture Modelling.....</b>	<b>69</b>
3.1	Previous Multi-regime Powertrain Architecture Modelling.....	69
3.2	Study Multi-Regime Powertrain Architecture Model .....	71
3.2.1	Mechanical path .....	74
3.2.2	Node points .....	85
3.2.3	Electrical path .....	86
3.2.4	Power management strategy .....	88
3.2.5	Vehicle models .....	94
3.2.6	Simulations .....	96
3.2.7	Study results and discussion .....	98
<b>Chapter 4</b>	<b>PEM Fuel Cell and Stack Modelling.....</b>	<b>104</b>
4.1	Previous Fuel Cell Modelling .....	104
4.2	PEM Fuel Cell and Stack Model.....	110
4.2.1	PEM fuel cell fundamentals.....	111
4.2.2	Theoretical PEM fuel cell potential .....	113
4.2.3	Nernst voltage .....	114
4.2.4	PEM fuel cell terminal voltage .....	117
4.2.5	Activation overvoltage.....	119
4.2.6	Ohmic overvoltage.....	120
4.2.7	Concentration overvoltage.....	122
4.3	Proposed Modifications to the Generalized Electrochemical Steady-State Degradation Model.....	123
4.3.1	Fuel crossover and internal currents .....	124
4.3.2	Contact resistance .....	125
4.3.3	Electrochemical dynamic effects .....	126
4.3.4	Membrane hydration model.....	129
4.3.5	Anode flow module.....	132
4.3.6	Cathode flow module.....	134
<b>Chapter 5</b>	<b>Fuel Cell System Modelling.....</b>	<b>140</b>
5.1	Previous Fuel Cell System Modelling.....	140
5.2	Fuel Cell System Model.....	141
5.3	Oxidant Flow Module .....	143
5.3.1	Compressor module .....	143
5.3.2	Supply manifold module.....	147
5.3.3	Return manifold .....	149
5.3.4	Oxidant humidifier module.....	150
5.4	Hydrogen Flow Module .....	156
5.5	Thermal Management Module .....	162
5.5.1	Passive heat loss.....	163

5.5.2	Active heat loss .....	165
5.6	Fuel Cell System Net Output .....	167
5.6.1	Efficiency analysis .....	168
<b>Chapter 6</b>	<b>Low-Speed Vehicle Modelling.....</b>	<b>171</b>
6.1	Previous Fuel Cell Hybrid Scooter Modelling.....	172
6.2	Low-Speed Vehicle Models.....	173
6.2.1	Vehicle body.....	173
6.2.2	Electric machine.....	176
6.2.3	Fuel cell hybrid scooter powertrain model .....	179
6.2.4	Battery models .....	181
6.2.5	Control strategy models .....	183
6.3	LSV Simulations .....	183
6.3.1	Acceleration simulation .....	184
6.3.2	Gradeability simulation.....	186
6.3.3	New York City Cycle simulation .....	187
6.3.4	Step input drive cycle simulation.....	189
6.3.5	Range simulation .....	190
<b>Chapter 7</b>	<b>Low-Speed Vehicle Testing.....</b>	<b>192</b>
7.1	Dynamometer Relationships .....	196
7.2	Dynamometer Calibration .....	199
7.3	Experimental Results.....	203
7.3.1	Dynamometer gradeability test.....	203
7.3.2	Dynamometer step-input test .....	206
7.3.3	Dynamometer range test .....	211
<b>Chapter 8</b>	<b>Fuel Cell System Optimization .....</b>	<b>213</b>
8.1	Previous Fuel Cell-Related Optimization .....	213
8.1.1	Fuel cell optimization .....	214
8.1.2	Fuel cell stack optimization .....	214
8.1.3	Fuel cell system optimization .....	215
8.2	Study optimization of a fuel cell system .....	216
8.2.1	Multi-objective optimization .....	218
8.2.2	Single-objective optimization problem.....	225
8.3	Study Optimization of a Fuel Cell Hybrid Scooter Powertrain .....	232
<b>Chapter 9</b>	<b>Conclusions and Outlook .....</b>	<b>238</b>
9.1	Internal combustion engine hybrid vehicle powertrains .....	238
9.2	Fuel cell system model.....	241
9.3	LSV models.....	243
9.4	Dynamometer testing .....	245

9.5	Fuel cell hybrid scooter design.....	246
9.6	Design tools.....	248
9.6.1	Simulation software .....	248
9.6.2	Computer-aided design model .....	249
9.6.3	Mathematical optimization .....	250
9.7	Hybrid vehicle outlook.....	251
<b>References.....</b>		<b>254</b>
<b>Appendix A: Vehicle Classifications.....</b>		<b>270</b>
<b>Appendix B: Stack Degradation .....</b>		<b>272</b>
<b>Appendix C: Optimization Algorithms.....</b>		<b>278</b>

## List of Figures

Figure 1-1. Current vehicle powertrain technology categories.....	6
Figure 1-2. Changes in internal combustion engine vehicles 1975-2007.....	11
Figure 1-3. Fuel cell stack (a) and system (b) cost break-down.....	17
Figure 1-4. The Lohner-Porsche Mixte.....	23
Figure 2-1. Types of internal combustion engine hybrid vehicles.....	40
Figure 2-2. Configuration of a generic series hybrid vehicle.....	42
Figure 2-3. Configuration of a generic parallel hybrid vehicle.....	44
Figure 2-4. Configuration of a parallel hybrid four wheel drive.....	45
Figure 2-5. Illustration of a planetary gear.....	52
Figure 2-6. GM-1 architecture.....	53
Figure 2-7. GM-2 architecture.....	56
Figure 2-8. Two-Mode EVT architecture.....	57
Figure 2-9. Two-Mode Hybrid architecture.....	60
Figure 2-10. Renault IVT architecture.....	61
Figure 2-11. Timken eCVT architecture.....	63
Figure 2-12. Silvatech EMCVT architecture.....	65
Figure 2-13. University of Michigan-Dearborn architecture.....	67
Figure 3-1. Architecture of the study multi-regime powertrain.....	72
Figure 3-2. Free-body diagram of the first planet gear.....	77
Figure 3-3. Free-body diagram of the first sun gear.....	79
Figure 3-4. Free-body diagram of the first ring gear.....	80
Figure 3-5. Free-body diagram of rigid body of carrier gears, intermediate and drive shafts.....	82
Figure 3-6. Schematic representation of backward-looking structure model.....	89
Figure 3-7. Schematic representation of forward-looking structure model.....	89
Figure 3-8. Schematic of the study multi-regime architecture control strategy.....	93
Figure 3-9. Sample N/V plot for the study multi-regime architecture.....	94

Figure 3-10. ICEHV Simulation drive cycles.....	98
Figure 3-11. ICEHV simulation results: fuel consumption for the unloaded case .....	99
Figure 3-12. ICEHV simulation results: fuel consumption for the loaded case .....	100
Figure 3-13. ICEHV simulation results: engine power of the multi-regime powertrain during the City-Suburban Heavy Vehicle Route cycle .....	101
Figure 3-14. ICEHV simulation results: MG1 power of the multi-regime powertrain during the City-Suburban Heavy Vehicle Route cycle .....	101
Figure 3-15. ICEHV simulation results: MG2 power of the multi-regime powertrain during the City-Suburban Heavy Vehicle Route cycle .....	102
Figure 3-16. ICEHV simulation results: ESS SOC history of the multi-regime powertrain during the City-Suburban Heavy Vehicle Route cycle .....	102
Figure 4-1. Reactions of a PEMFC.....	112
Figure 4-2. Polarization curve of a PEMFC .....	118
Figure 4-3. Fuel cell equivalent RC circuit.....	127
Figure 5-1. Fuel cell system schematic.....	142
Figure 5-2. Oxidant humidifier schematic .....	151
Figure 5-3. Fuel cell system schematic with hydrogen re-circulation .....	161
Figure 6-1. Scooter tire and rim dimensions.....	175
Figure 6-2. Three-dimensional motor efficiency map estimate .....	178
Figure 6-3. Contour plot of the motor efficiency map estimate .....	179
Figure 6-4. Schematic of the prototype fuel cell hybrid scooter powertrain .....	180
Figure 6-5. Internal resistor battery model .....	181
Figure 6-6. New York City Cycle drive cycle.....	188
Figure 7-1. Dynamometer components.....	194
Figure 7-2. Prototype low-speed vehicles and the fuel cell system of the fuel cell hybrid scooter .....	194
Figure 7-3. Test screen of the dynamometer computer software .....	195

Figure 7-4. Measured dynamometer friction torque versus roller speed .....	199
Figure 7-5. Scooter wheel friction torques versus roller speed .....	201
Figure 7-6. Required current and calculated torque versus vehicle velocity .....	203
Figure 7-7. Torque-speed curve from dynamometer gradeability results .....	205
Figure 7-8. Peak roller speeds achieved by the LSVs during the step-input dynamometer tests .....	207
Figure 7-9. LSV motor torque values at peak speed for the step-input tests .....	208
Figure 7-10. LSV motor power values at peak speed for the step-input tests .....	209
Figure 7-11. LSV motor torque values at peak acceleration for the step-input tests .....	210
Figure 7-12. LSV motor power values at peak acceleration for the step-input tests .....	211
Figure 8-1. Flow diagram of optimization methodology .....	218
Figure 8-2. Net Power curve for the non-weighted, multi-objective problem: average net power .....	221
Figure 8-3. Gross power curve for the non-weighted, multi-objective problem: average net power .....	222
Figure 8-4. Air compressor power curve for the non-weighted, multi-objective problem: average net power .....	223
Figure 8-5. System exergetic efficiency curve for the non-weighted, multi-objective problem: average net power .....	224
Figure 8-6. System exergetic efficiency curve for the non-weighted, multi-objective problem: average system exergetic efficiency .....	225
Figure 8-7. Net power curve for the single-objective problem: peak net power (SQP-1 algorithm) .....	228
Figure 8-8. Gross power curve for the single-objective problem: peak net power (SQP-1 algorithm) .....	228
Figure 8-9. Net power curve for the single-objective problem: peak net power (global optimization and SQP-2 algorithms) .....	229

Figure 8-10. Gross power curve for the single-objective problem: peak net power (global optimization and SQP-2 algorithms) .....	230
Figure 8-11. Air compressor power curve for the single-objective problem: peak net power (global optimization and SQP-2 algorithms).....	230
Figure 8-12. System exergetic efficiency curve for the single-objective problem: peak system exergetic efficiency .....	232
Figure 8-13. New York City Cycle fuel cell system power request distribution .....	234
Figure B-1. Catalytic activity term versus age.....	274
Figure B-2. Internal resistance and semi-empirical membrane parameter versus age .....	275
Figure B-3. Voltage degradation model versus experimental results.....	277
Figure C-1. Flowchart for the GA process.....	281
Figure C-2. Illustration of the crossover process .....	283

## List of Tables

Table 1-1. Sample internal combustion engine vehicle emission improvements .....	10
Table 1-2. Battery and ultracapacitor technology comparison .....	14
Table 1-3. Fuel cell industry reported results and U.S. Department of Energy targets .....	18
Table 1-4. Commercial battery scooters .....	31
Table 1-5. Fuel cell hybrid scooters .....	32
Table 2-1. Classification system of the California Air Resources Board for hybrid vehicles .....	39
Table 2-2. Power-split architecture operation .....	48
Table 2-3. Operating regimes of the GM-1 architecture .....	54
Table 2-4. Operating regimes of the GM-2 architecture .....	56
Table 2-5. Operating regimes of the Two-Mode EVT architecture .....	58
Table 2-6. Operating regimes of the Two-Mode Hybrid architecture .....	60
Table 2-7. Operating regimes of the Renault architecture .....	62
Table 2-8. Operating regimes of the Timken architecture .....	64
Table 2-9. Operating regimes of the Silvatech architecture .....	66
Table 2-10. Operating regimes of University of Michigan-Dearborn architecture .....	68
Table 3-1. ICEHV study model operating regimes .....	74
Table 3-2. Characteristics of the ICEHV study vehicle .....	95
Table 3-3. Powertrain components of the ICEHV simulation architectures .....	96
Table 4-1. Activation overvoltage coefficients .....	120
Table 5-1. Compressor regression coefficients .....	147
Table 6-1. Acceleration simulation results for the battery scooter model .....	185
Table 6-2. Acceleration simulation results for the fuel cell hybrid scooter model .....	186
Table 6-3. Gradeability simulation results for the LSV models .....	187
Table 6-4. New York City Cycle simulation results for the LSV models .....	188
Table 6-5. Step input simulation results for the LSV models .....	189
Table 6-6. Range simulation results for the LSV models .....	190

Table 7-1. Results of the dynamometer and simulation gradeability tests .....	204
Table 7-2. Motor torque values for the dynamometer gradeability test.....	205
Table 7-3. Comparison of the power at the wheels and output by the motor .....	206
Table 7-4. Battery scooter range test pulse-width modulation changes.....	212
Table 8-1. Solution to the non-weighted multi-objective problem: average net power.....	220
Table 8-2. Solution of the non-weighted multi-objective problem: average exergetic efficiency.....	224
Table 8-3. Solution to the single-objective problem: peak net power .....	226
Table 8-4. Solution to the single-objective problem: peak system exergetic efficiency.....	231
Table 8-5. Power request categories .....	234
Table 8-6. Optimization solutions for weighted, multi-objective problems, 39 cells.....	235
Table 8-7. Solutions of the weighted, multi-objective problem: average exergetic efficiency...	236
Table A-1. Classification and acronym summary .....	270

## List of Abbreviations

ADVISOR:	ADvanced VehIcle SimulatOR
AEE:	advanced engineering environment
AER:	all-electric regime
AFC:	alkaline fuel cell
AGCC:	anthropogenic global climate change
ANN:	artificial neural network
ANL:	Argonne National Laboratory
ARSM:	Adaptive Response Surface Method
BV:	battery vehicle
BLDC:	brushless direct current
BOP:	balance of plant
CAC:	criteria air contaminant
CAD/CAM/CAE	computer aided drafting/manufacturing/engineering
CAFE:	Corporate Automobile Fuel Economy
CARB:	California Air Resources Board
cc:	cubic centimetre
CCD:	Central Composite Design
CFCD:	computational fuel cell dynamics
CFD:	computational fluid dynamics
CHP:	combined heat and power
CO:	carbon monoxide
CO <sub>2</sub> :	carbon dioxide
CO <sub>2</sub> e:	carbon dioxide equivalent
DALY:	Disability Adjusted Life Year
DC:	direct current
DIRECT:	DIviding RECTangles

DoE:	Department of Energy
DOH:	degree of hybridization
DPF:	diesel particulate filter
DPM:	diesel particulate matter
ECU:	electronic control unit
EM:	electric machine
EMF:	electromotive force
ESS:	energy storage system
EV:	electric vehicle
EVT:	electronically variable transmission
FCB:	fuel cell bus
FCHV:	fuel cell-hybrid vehicle
FCHS:	fuel cell-hybrid scooter
FCS:	fuel cell system
FCV:	fuel cell vehicle
FEA:	finite element analysis
GA:	Genetic Algorithms
GCM:	Global Circulation Model
GCTool:	Generalized Computational Toolkit
GDL:	Gas Diffusion Layer
GESSDM:	Generalized Electrochemical Steady-State Degradation Model
GHG:	greenhouse gas
GM:	General Motors
GO:	global optimization
HC:	hydrocarbon
HV:	hybrid electric vehicle
HHV:	higher heating value

HY-ZEM:	Hybrid-Zero Emission Mobility
ICE:	internal combustion engine
ICEHV:	internal combustion engine-hybrid vehicle
ICES:	internal combustion engine scooter
IEC:	International Electrotechnical Commission
IESVic:	Integrated Energy Systems at the University of Victoria
IGEC:	International Green Energy Conference
ISG:	integrated starter-generator
ITRI:	Industrial Technology Research Institute of Taiwan
L-A:	lead-acid
LCA:	life-cycle analysis
LHV:	lower heating value
LION:	Lithium-Ion
LSVTF:	Low-Speed Vehicle Testing Facility
LSV:	low-speed vehicle
MEA:	membrane-electrode assembly
MH:	metal hydride
MOI:	moment of inertia
MPSM:	Mode-Pursuing Sampling Method
NASA:	National Aeronautics and Space Administration
NEDC:	New European Drive Cycle
NiMH:	nickel metal hydride
NO <sub>x</sub> :	Nitrogen oxides (various)
NREL:	National Renewable Energy Laboratory
NYCC:	New York City Cycle
OCV:	open-circuit voltage
OEM:	original equipment manufacturer

PEMFC:	proton exchange membrane fuel cell
PHV:	plug-in hybrid electric vehicle
PM:	permanent magnet
PR:	power request
PROX:	preferential oxidation
PSAT:	Powertrain Systems Analysis Tool
PTL:	Porous Transport Layer
PWM:	pulse-width modulation
RMC:	Royal Military College
SA:	Simulated Annealing
SI:	spark ignition
SOC:	state of charge
SMR:	steam methane reformer
SQP:	Sequential Quadratic Programming
SSSF:	steady-state, steady-flow
STP:	Standard Temperature and Pressure (298.15K, 101.325 Pa)
TERS:	Tri-stream, External manifolding, and Radiator Stack
TMDC:	Taipei Motorcycle Drive Cycle
UCV:	ultracapacitor vehicle
USD	United States Dollar
VM:	virtual manufacturing
VOC:	volatile organic compound
VP:	virtual prototyping
WGS:	water gas shift
WHO:	World Health Organization
WOT:	wide-open throttle
WTM:	water and thermal management

ZEV: zero-emission vehicle

## Acknowledgements

There are many people I would like to thank for their help and encouragement throughout my time here at the University of Victoria. I will confine myself to people who had direct involvement with my degree and not list the many other people in my life that are important to me and make life so enjoyable: you know who you are.

Dr. Zuomin Dong, my supervisor, is given special acknowledgement for the mentoring and many enlightening discussions we had about fuel cells, hybrid vehicles, and anything else we thought would be interesting.

The work done by fellow (and former) graduate students Leon Zhou, Matthew Guenther, Sezer Tezcan, Richard Stackhouse, and Michael Pastula contributed immensely to my work.

Dr. Andrew Rowe was always there to help me with my myriad of questions on any number of topics from hydrogen storage technologies to the amount of weight that is reasonable to lift at the gym.

Dr. Peter Wild was able to give very useful advice, no matter what the topic, and his course on renewable energy was certainly an eye-opener for me.

Dr. Lawrence Pitt is one of the most knowledgeable people I have ever met, and I learned so much from him during our discussions.

Dr. Nedjib Djilali helped with my professional development in the area of fuel cells.

Dr. Henning Struchtrup was supportive in my efforts to understand exergy.

Susan Walton, Peggy White and Erin Robinson were tireless in their administrative efforts.

My crack editing team, consisting of Dr. Thomas (Pops) Wishart, Jacquie and Wynn Downing, Victoria Wishart, Marc Secanell, Richard (DB) Humphries and Amber McGown, graciously and courageously helped me complete this tome.

Fellow students, in (approximate) order that I met you: Christina Ianniciello, David Brodrecht, Jeffrey Coleman, Aimy Bazylak, Matthew Schuett, Juan Mejia, Ramadan Abdiwe, Michael Carl, Michael Optis, James Biggar and the members of Common Energy. You have all helped confirm that life in graduate studies is not only about the degree.

## Frontispiece

### The Hydrogen Prayer

Oh Hydrogen, which art ubiquitous,  
Hallowed be thy promise.  
Thy time will come, our will be done,  
In the marketplace as it is in our imagination.  
Provide us forever our diurnal energy needs,  
And forgive us our setbacks,  
As we strive to overcome the naysayers set against you.  
And lead us not into further environmental despoiling,  
But deliver us from reliance on fossil fuels,  
Now, and to avoid the hour of our ecosystem's death,

Amen

©Jeffrey Wishart, 2005

## **Chapter 1    Background and Motivation**

In the more than 100 years since its inception, the internal combustion engine vehicle (ICEV) has transformed modern civilization. Many benefits have been derived from the freedom and convenience these vehicles have provided. The technology has not been without its negative effects, however. For instance, the highway and road infrastructure to accommodate the increasing number of vehicles has placed a severe financial burden on governments for initial construction and subsequent maintenance. In the United States, for example, \$80 billion dollars are spent each year on maintenance and upgrading of the interstate system [1]. Despite these drawbacks, vehicles are certain to become even more ubiquitous in the future, especially in developing nations. It is forecast that the number of cars per hundred people in China and India will increase from two in 2006 to 29 and 21, respectively, by 2040, adding some 720 million new cars to the current population [2].

### **1.1 Environmental Concerns**

Considerable public and media attention has recently been devoted to the issue of fossil fuel-powered ICEVs and the inherent problems with their continued use. Examples of some of the key controversies surrounding the continued use of petroleum for vehicular applications include [3]:

- current high (and rising) prices for gasoline, petroleum, and natural gas
- lack of petroleum refining capacity
- declining conventional petroleum supplies
- geopolitical concerns with a significant number of the remaining petroleum resource locations
- environmental disasters that arise from oil tanker spills and oil extraction
- infringement of landowners' rights for pipeline installation
- the effects of both smog-inducing criteria air contaminant (CAC) pollution and

- potentially catastrophic anthropogenic global climate change (AGCC)

Each of the points listed arguably provides sufficient incentive by itself to usher in an era of non-fossil fuel-powered vehicles. The last point is particularly critical. One study found that worldwide, 600 million people are exposed to dangerous levels of CACs [4]. The World Health Organization (WHO) estimates that annually some 800,000 deaths and 7.9 million Disability Adjusted Life Years (DALYs)—a measure of premature deaths, disability and days of infirmity due to a certain cause—can be directly or indirectly attributed to the effects of CACs [5]. While a significant portion of CAC pollution in Canada comes from industry and power production facilities, 16% of the volatile organic compounds (VOCs), 32% of the nitrogen oxides (NO<sub>x</sub>), and 32% of the carbon monoxide (CO) are emitted by the exhaust of the ICEV [6].

Smog and pollution are particularly devastating in developing countries such as China and India, where a significant portion of ICEVs are two-wheeled vehicles that use outdated two-stroke technology. A typical two-stroke, 50 cubic centimetre (cc) motorcycle, although much less powerful, emits six times as many VOCs and nearly twice as much CO (although fewer NO<sub>x</sub>s) as does a 125 cc four-stroke motorcycle [7]. One study found that as much as 75% of the population of China must endure air quality levels below the levels deemed acceptable by the Chinese government [8]. CAC effects are also a pressing issue in developed nations: in 2005, Toronto, Canada experienced a record 48 “smog days”, during which the population is advised to avoid inhalation of the outside air [9]. The rapid, worldwide urbanization of nations is certain to continue the severe deterioration of air quality and dramatically increase the number of fatalities.

Concurrently, the link between greenhouse gases (GHGs) and global climate change strengthens continuously with a growing body of evidence and the endorsement of a large majority of scientists in a multitude of diverse fields. Most climate experts believe there is a high probability that the increased GHGs in the atmosphere are largely responsible for the 0.74 °C increase in global average temperature from 1906 to 2005 [10]. Globally, ten of the eleven hottest years on record since 1850 have occurred since 1995 (the only year in the last eleven not

on the list is 1996, replaced by 1990) [11]. The predicted range of temperature increases by 2100 resulting from 'business-as-usual' fossil fuel use predicted by the Global Circulation Models (GCMs) from climate scientists such as those at the Hadley Centre in England, the Lawrence Livermore National Laboratory in the U.S., the Canadian Centre for Climate Modelling and Analysis, and the Max Plank Institute for Meteorology in Germany is from 1.9 °C up to an incredible 11.2 °C by 2100 [12].

The economic costs of AGCC are impossible to predict with any precision but the conclusions of the largest attempt at quantification, by Sir Nicholas Stern of the U.K., are that failure to act to prevent the effects of AGCC will result in a perennial loss of 5% of global GDP and perhaps up to 20% or more [13]. With decreased farm production, acute water shortages, and more frequent and more devastating extreme weather events (likely by-products of a warmer planet), there is little doubt that the costs in human lives may be immense. Even more difficult is the quantification of the loss of flora and fauna species that are unable to adapt to the rapidly rising temperatures and ecosystem changes. As a result, the public at large is beginning to take notice and accept the basic tenets of the consensus amongst climate scientists that AGCC is a real and imminent threat [14]. These changes in public opinion are reflected in the push by governments to achieve zero emissions in order to reduce the risk of AGCC and to reduce the effects of CACs. With the ratification of the Kyoto protocol requiring a yearly reduction of 260 Mt of CO<sub>2</sub> equivalent (CO<sub>2</sub>e) emissions from the current Canadian output, vehicles have become a prime candidate for targeted GHG reduction [15]. From 1990 to 1999, vehicular applications accounted for nearly 22% of GHG emissions in Canada [15]. While the intensity of GHG emissions per vehicle has been declining slowly because of increasing fuel efficiency, it is possible that the overall output will increase due to more vehicles and an escalation in usage. The result will be an exacerbation of the deleterious effects of anthropogenic global climate change (AGCC).

## 1.2 Resource Supply and Energy Efficiency

The supply of petroleum is also of grave concern. Many analysts believe that the era of inexpensive gasoline has come to an end, and that the 100 USD per barrel price that was recently surpassed is only the first warning sign of imminent and drastic increases in price [16]. It has been suggested that the production of petroleum from conventional sources, i.e. not from tar sands or derived from coal, has already peaked. With the slowdown in new field discoveries, and dwindling reserves from today's production wells, the world-wide supply of oil could decrease, even if production from unconventional sources is increased dramatically. At the same time, the staggering economic growth in developing countries, and especially China and India, is rapidly increasing demand. It is becoming increasingly possible that the high demand will cause supply problems. This would bring disruptions in the world economy like those seen during the OPEC oil embargo of 1973 [3]. Supply concerns arise also because of the location of the vast majority of conventional oil reserves in the unstable Middle East.

These supply concerns provide yet another inducement for non-fossil fuel-powered vehicles as well as for ICE-powered vehicles that are more efficient and consume less fuel. Energy efficiency has been espoused by many in the energy industry for decades, most notably Amory Lovins [17]. Regulations of fuel consumption for automobiles did not occur until 1975 when the Corporate Automobile Fuel Economy (CAFE) standard of the United States was established. The objective was to halve the fuel consumption levels of new automobiles to a level of  $8.6 \text{ L}\cdot(100 \text{ km})^{-1}$  by 1985 [18]. This standard was followed by the Company Average Fuel Consumption (CAFC) standards in Canada, although the latter are strictly voluntary. The average fuel consumption of the U.S. car and truck fleet is currently  $9.3 \text{ L}\cdot(100 \text{ km})^{-1}$ ; this is slightly higher than the  $9.1 \text{ L}\cdot(100 \text{ km})^{-1}$  fleet average minimum achieved in 1987. The reasons for the increase include heavier vehicles, higher performance, and a higher proportion of trucks and SUVs. No changes to either standard were made after 1985 until the recent Energy Independence and Security Act of 2007 signed into law in the United States dictating that the fuel economy of automobiles, SUVs and trucks will be  $6.75 \text{ L}\cdot(100 \text{ km})^{-1}$  by 2020 [19]. The

Harper Conservative government has recently announced that it will implement a fuel economy standard to come into effect for the 2011 model year. This standard will reportedly be at least as stringent as those dictated in the Energy Independence and Security Act of 2007, which as already noted, will not be enforced until 2020 [20].

The Union of Concerned Scientists (UCS) has published a report claiming that a fuel consumption level of  $5.9 \text{ L}\cdot(100 \text{ km})^{-1}$  is achievable for a minivan with contemporary technologies [21]. In fact, there are several vehicle models already available that achieve laudably low levels of fuel consumption. Automotive companies such as Honda and Toyota have gained a reputation for production of efficient vehicles. This has no doubt been part of the reason for Toyota overtaking General Motors (GM) in world-wide sales in 2007 [22]. It is clear that vehicles which are more efficient are both necessary and desirable, and the public is more aware of this need than at any time in the history of the automobile.

### **1.3 Contemporary Vehicle Powertrain Technologies**

There are three main categories of powertrain technologies: (1) ICEVs, (2) Electric vehicles (EVs), and (3) Hybrid vehicles (HVs). The vehicles in these categories (with appropriate names and acronyms included) are presented in Figure 1 below. It should be noted that experimental technologies, such as compressed air propulsion systems, which are being pursued sporadically in research and development have not been included in this survey.

Several of the entries in Figure 1-1 are often written to include the term 'ESS'. ESS refers to an energy storage system, which can be a battery, an ultracapacitor, a flywheel or a combination of the three. The flywheel technology is rarely used in vehicular applications because of the danger associated with a large, heavy mass spinning with considerable angular momentum being unleashed in the event of an accident. As such, they are not included in this dissertation.

Due to the increasing problems of continued unfettered fossil fuel usage in vehicular applications, an interest in the development of partial- and zero-emission vehicles, known as

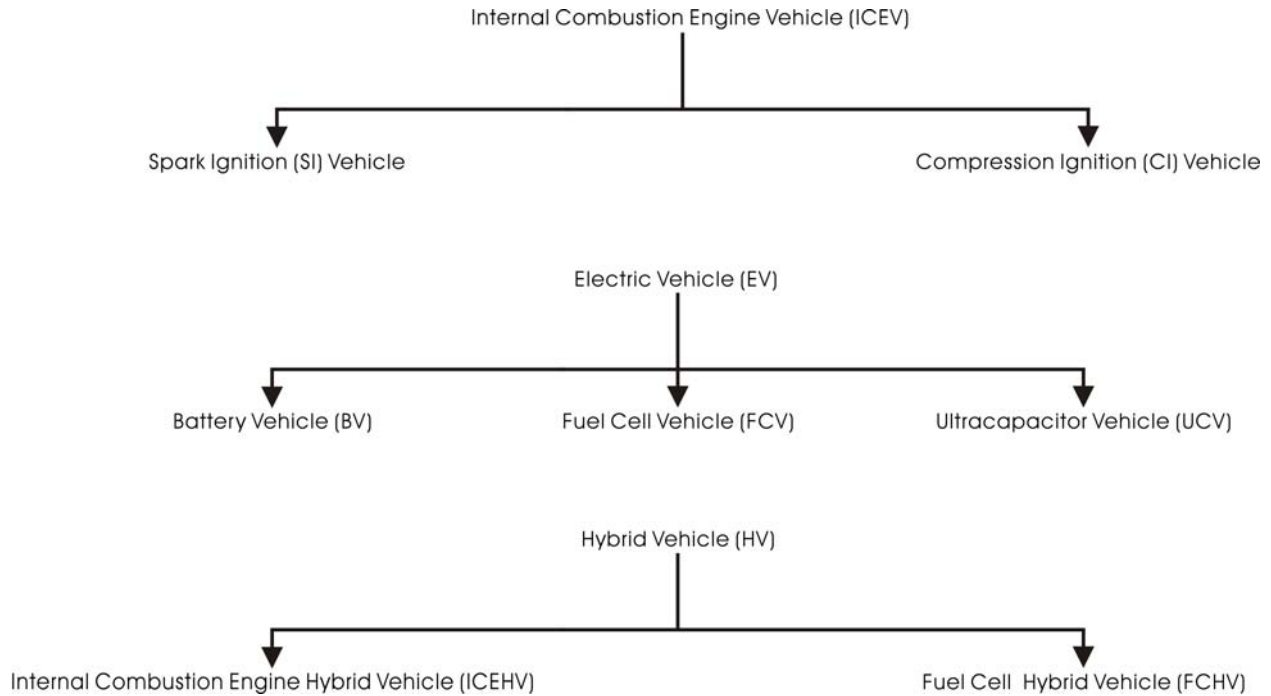


**Figure 1-1. Current vehicle powertrain technology categories**

PZEVs and ZEVs, respectively, has arisen. A PZEV is defined as a vehicle that is 90% “cleaner” than the average new model year vehicle, while the ZEV is 98% cleaner than the average new model year vehicle [23]. However, there exists considerable confusion in the literature nomenclature for classifying the types of powertrain technologies of PZEVs and ZEVs. The following three sections outline the development of the three main categories in Figure 1-1. A more complete summary of the vehicle types, acronyms and classifications can be found in Appendix A.

#### 1.4 Internal Combustion Engine Vehicles

In the late 19<sup>th</sup> century, many independent researchers were attempting to design what is now considered to be the modern automobile. While the person who first succeeded is still debated, Karl Benz is widely considered to have achieved the honour in 1885 when he built an Otto-cycle ICEV known as the Benz Patent Motorwagen [24]. However, the ICEV did not dominate immediately. ICEVs were considered noisy and dirty in comparison to EVs. In

1897, Hiram Maxim invented the muffler, almost eliminating the former concern. The ICEV improved quickly, and the longer range possible with the higher specific energy of gasoline, which today reaches approximately  $12,000 \text{ Wh}\cdot\text{kg}^{-1}$ , put the performance of the ICEV out of reach of the EVs of the era. The ICEV has been the dominant technology from that point to the present day.

The ICEV is never a ZEV, although a PZEV classification is possible. The two types of ICEVs are spark-ignition (SI) and compression-ignition (CI). The main difference between the two is that the former uses spark plugs to ignite the fuel while the latter uses a higher compression ratio to force the fuel to ignite. The fuel used most commonly in SI-ICEs is known as petrol or gasoline, while the most common fuel for CI-ICEs is known as diesel. SI-ICEs are less efficient than CI-ICEs, but have superior cold weather and high-speed torque output performance. SI-ICEs dominate the North American market, while CI-ICEs are very popular in Europe. The dichotomy is due, in part, to the emissions regulations in North America favouring lower CAC emission technologies, while the opposite is true for the regulations of Europe.

Recently, there has been considerable attention on alternative fuels such as ethanol and biodiesel. Ethanol is usually produced from an agricultural feedstock, mostly corn in the United States and sugarcane in Brazil. Cellulosic ethanol can also be produced from a variety of more abundant biomass feedstocks such as woodchips and switchgrass, but the energy required in the refining process is greater. Biodiesel can be manufactured from an agricultural feedstock, but can also be produced using waste resources such as used cooking oil. The production from biomass and waste streams is attractive because the energy is extracted from renewable sources that would otherwise be discarded; the volumes of these feedstocks are, however, fairly small relative to the amount required for fleet-wide usage of these alternative fuels. For this reason, alternative fuels produced in this manner will likely only be produced in niche conditions.

Increasing production of alternative fuels to fleet-wide usage levels would necessitate the

conversion of large swaths of land to farmland devoted exclusively to fuel feedstock production. For example, if E10 (a mixture of 90% gasoline and 10% ethanol) were used by every car in the United States, this would require approximately 430,000 barrels·day<sup>-1</sup> of ethanol would be consumed, and the land needed to grow sufficient quantities of corn would have to be increased by 50% over the current allocation, an unrealistic scenario [25]. Using farmland to grow corn for fuel instead of food is blamed for the worst tortilla price crisis in the history of Mexico in 2007 where tortillas form a large portion of the diet, especially of the poor [26]. When farmers must decide between food for the world's poor and fuel for the world's vehicles, the latter will win out because of the higher buying power of fuel suppliers. It is unclear whether a sufficient quantity of either ethanol or biodiesel can be produced without negatively impacting world food markets.

From a life-cycle analysis (LCA) perspective, combustion of alternative fuels will release fewer GHG emissions than fossil fuels because of the CO<sub>2</sub> absorbed during photosynthesis. However, the CAC emission benefits are debatable and in some cases, combustion of alternative fuels will worsen local pollution [27]. It is possible that ethanol and biodiesel produced from properly chosen feedstocks could have environmental benefits. The performance of ICEVs using these fuels is lower, however, than with conventional fossil fuels. The reason is that there is less embedded energy in the alternative fuels, resulting in a loss of range and power. For example, reference [28] mentions two studies on direct-injection SI-ICEs using ethanol which found that the decrease in efficiency was between 13-28% from a gasoline benchmark. It is unclear whether ethanol or biodiesel will ever represent a large portion of the liquid fuel market.

When hydrogen is combusted in a conventional ICE, usually a SI-ICE, the emissions are significantly less than that of other fuels combusted in a comparable ICE. Although harmful NO<sub>x</sub> compounds are still released, the vehicle using hydrogen as fuel could be placed in the PZEV category. The GHG emissions are essentially zero. Recent research has shown that adding a catalytic conversion exhaust treatment known as exhaust gas re-circulation (EGR) can lower emissions to ZEV levels [29]. The performance of an ICE burning hydrogen is also

currently lower than a comparable engine burning conventional liquid fuels. Problems such as knock, where the air/fuel mixture ignites without the spark plug causing pressure to build up in the cylinder, sometimes catastrophically, are seen as being difficult challenges to overcome, although BMW, in particular, has designed a production-ready, H<sub>2</sub>-combustion version of its 7 Series sedan. It remains to be seen if hydrogen-fuelled ICEVs can be made to attain ZEV status and indeed whether combustion of hydrogen in an ICE is the best method of hydrogen energy conversion.

Except in the solitary case of hydrogen, the probability that ICEVs will reach ZEV status is almost, by definition, zero, unless a revolutionary method of on-board carbon dioxide sequestration is coupled to a drastically improved CAC filtration system. There are methods that the ICEV industry have attempted in order to improve the emissions. For example, the introduction of catalytic converters on a wide-spread basis in North America in 1975 reduced the amount of NO<sub>x</sub>, CO, and hydrocarbon emissions significantly. CI-ICEs release significantly less CO and, because of the increased fuel efficiency, less CO<sub>2</sub>. However, this type of combustion also results in higher emissions of unburned carbon compounds known as diesel particulate matter (DPM) that have proven problematic, especially in light of the aforementioned urban pollution problems. Even with the diesel particulate filter (DPF) installed on newer CI-ICEV models, the total emissions fail to approach the levels of PZEVs and are considerably higher than the desired ZEV level. Daimler AG has recently introduced a technology for diesel-fuelled vehicles known as “BLUETEC”. This innovation reportedly allows reduced emissions from diesel vehicles. Most importantly, sufficient reductions are made to meet the U.S. Bin 8 standard [30] by reducing the NO<sub>x</sub> emissions by 20% and PM emissions by 90% from 2000 models [31].

Therefore, in discussing the deficiencies of the ICEV, it is important not to overlook its considerable progress. Emissions from ICEVs have improved significantly, as shown below in Table 1-1. The table presents the emission data for a U.K. Ford model that has undergone five “generations”. A 1976 1.0 L SI M1 Ford Fiesta is compared with its 2007 1.25 L SI MK6

counterpart. Two of the aforementioned CAC emissions, NO<sub>x</sub> and CO, are listed, along with hydrocarbons (HCs). The CAC emissions have been improved immensely, while the GHG emission improvements have been marginal. It is unclear whether further improvements in CAC emissions in ICEVs can be made economically by the automotive OEMs [32]. However, despite the progress, the emissions of both ICE types pose significant, and growing, problems in terms of both local pollution and AGCC.

**Table 1-1. Sample internal combustion engine vehicle emission improvements**

Source: [32], page 7.

<b>Pollutant (g·km<sup>-1</sup>)</b>	<b>1976 Ford Fiesta MK1 (1.0 L SI)</b>	<b>2007 Ford Fiesta MK6 (1.25 L SI)</b>	<b>% Improvement</b>
NO <sub>x</sub>	1.72	0.0225	98.7
CO	18.311	0.2567	98.6
HC	2.513	0.049	98.1
CO <sub>2</sub>	149.7	142	5.1

Other characteristics of ICEVs have been evolving as well. The changes in technology from 1975 to 2007 for U.S. cars are summarized below in Figure 1-2, adapted from a 2007 report released by the U.S. Environmental Protection Agency [33].

As shown in the figure, the following changes occurred in the average fleet characteristics in the years 1975 to 2007:

- Weight increased by 16% for trucks and decreased by 12% in cars
- Engine power increased by 74% for trucks and by 48% for cars
- Acceleration times from 0 to 96 km/hr decreased by 29% for trucks and by 33% for cars
- Top speed increased by 23% for trucks and by 24% for cars
- Fuel consumption decreased by 35% for trucks and by 42% for cars

Overall, it is apparent that the technology improved in both performance and in fuel efficiency. This broad view overlooks, however, the trends from 1975 to 1987 and from 1987 to 2007. While the weight of cars did, in fact, decrease from 1975 to 2007, during the shorter period between 1987 and 2007, the weight actually increased by 18%. Likewise, while the fuel

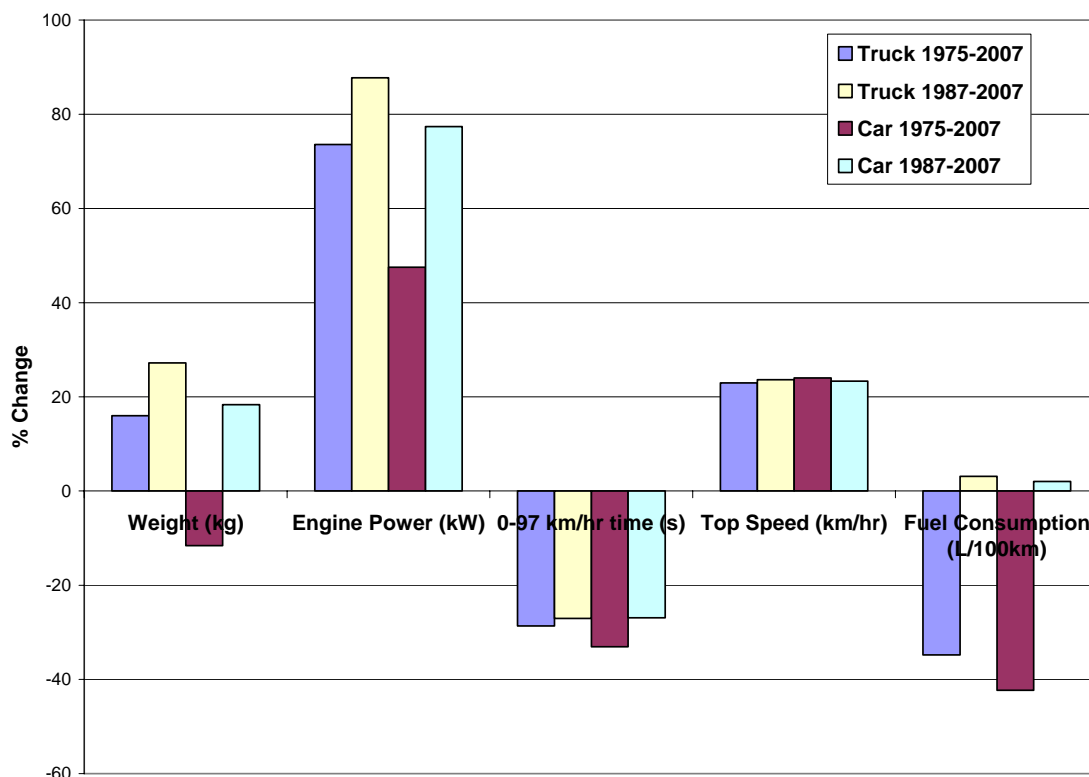


**Figure 1-2. Changes in internal combustion engine vehicles 1975-2007**

consumption of both trucks and cars decreased from 1975 to 2007, it increased by 3% and 2%, respectively, from 1987 to 2007. The improved performance has thus come at a cost of lowered fuel efficiency which the artificially low costs of fossil fuels have enabled. It must be said that in Europe, vehicles have decreased in both size and fuel consumption while increasing propulsion performance. Among other factors, the higher costs of gasoline and diesel fuel in European countries encourage the development of more fuel-efficient vehicles.

It is clear that the ICEV presents a “moving target”. Surpassing its level of performance and low cost with another powertrain technology is a difficult challenge. Without price signals such as GHG-emission taxes or tax incentives for purchasing more fuel efficient vehicles, the market will likely be dominated by ICEVs for at least the short- to medium-term future. When the concerns about fossil fuel-powered vehicles listed in the opening section are considered, however, the prospects of the ICEV must be looked at from a different perspective.

## 1.5 Electric Vehicles

The most well-known ZEV technology is the EV, which has a history as long as that of the ICEV. In fact, in 1900, 38% of all vehicles sold were EVs while only 22% were powered by ICEs (40% were steam-powered) [34]. EV technology was relegated to minority status and nearly forgotten because ICE technology evolved rapidly, enabling cheaper and significantly more powerful vehicles. The concept of a battery vehicle (BV) was revived during the aforementioned OPEC oil embargo of 1973. Several car manufacturers developed BVs that eventually became commercialized realities, most notably the General Motors' (GM) EV1. By 2001, there were some 2,500 BVs in operation in California alone [35]. These efforts were put on hiatus however, and, as depicted in the 2006 film "Who Killed the Electric Car?", the reasons for discontinuing development are controversial [36]. It is certain, however, that the BVs which were made available used mostly lead-acid (L-A) batteries and displayed performances that did not compare favourably with ICEVs. The desired specifications of the average consumer were not met.

The BV is currently enjoying another renaissance of sorts. The reason for the resurgence is the improved batteries that have been developed and made available recently, most notably the nickel metal hydride (NiMH) and Lithium-Ion (Li-Ion) batteries. The former currently dominates the automotive market while the latter has been ubiquitous in the portable electronics industry. Recently, however, the battery industry has begun to favour Li-Ion batteries over NiMH as the battery of choice in vehicles. The energy density of Li-Ion batteries is approximately twice that of NiMH batteries, and, as economies of scale improve, Li-Ion batteries will become cheaper as well. It is expected that Li-Ion will become the dominant battery technology [37].

The most high-profile example of a next-generation BV is the Tesla Roadster from the upstart company, Tesla Motors. The Roadster, powered by Li-Ion batteries, boasts an acceleration of 0 to 96 km·hr<sup>-1</sup> in four seconds and a range of up to 320 km, and has sold out the first production run months before the scheduled release date [38]. The BV, as shown by the

Roadster, is capable of impressive acceleration and is mechanically simple since the high torque at low speeds of an electric machine (EM) precludes the need for low transmission gears and torque converters. The BV is also much quieter than a comparable ICEV and enjoys the ZEV designation.

Another potential energy storage technology for EVs is the ultracapacitor in an ultracapacitor vehicle (UCV). The ultracapacitor was introduced in 1957 with a patent by General Electric [39], although the physical phenomenon used – the double-layer capacitor model – was first described by Helmholtz in the late 19<sup>th</sup> century [40]. Conventional capacitors are solid-state devices that physically store charge in metal foil plates separated by a dielectric film. Ultracapacitors differ from their conventional counterparts in that instead of a dielectric film, the plates are separated by activated carbon foil electrodes which are infused with a conductive electrolyte. A separator impermeable to ions lies between the positive and negative electrodes. An ultracapacitor is non-Faradic in that there is no ionic or electronic transfer and only charge separation. The voltage across the ultracapacitor causes the negative ions in the polarized electrolyte to be attracted to the positive electrode and the positive ions to be attracted to the negative electrode. The increased capacitance over conventional capacitors is due to the much higher surface area of the porous electrodes and the small separation distance of the charges on the order of 10 Å. The solid-state nature of the ultracapacitor means that there are no transport delays or time dynamics of an electrochemical reaction that take place throughout a bulk electrode in a battery [40]. The lack of transport delays results in ultracapacitors having the advantage of much lower charge/discharge response times, and associated higher power capacities, as compared to batteries, since only stored charge is added or removed from the electrode-electrolyte interfaces. The solid-state nature also provides durability: ultracapacitors have cycle lives on the order of 10<sup>5</sup> cycles versus 100-1000 for batteries [34]. The current energy density and specific energy of UCs are, however, at least an order of magnitude lower than those displayed by contemporary batteries. UCVs are still largely a theoretical possibility, although the author's supervisor did witness in Shanghai, China, a bus powered by UCs in which

the UCs are quickly recharged at each stop and at the two terminus stops along its route [41].

A summary of state-of-the-art characteristics of batteries and UCs is provided below in Table 1-2, with approximate numbers shown for comparison purposes. The battery characteristics are from reference [42], released in 2003, and the UC characteristics are taken from reference [43], a class lecture given in 2005. These values should not be seen as a definitive account of the state of the energy storage industry, but rather used as a guide to differentiate between the competing technologies. Also included in the table are the targets of the United States Advanced Battery Consortium (USABC) for long-term commercialization of EVs; the first value given represents the minimum target for commercialization and the second value represents the long-term goal. The targets vary for the desired application: EV, PHV, high-energy battery, and high-power battery. The cost target for the EV batteries is 150-100 \$·kWhr<sup>-1</sup> [44].

**Table 1-2. Battery and ultracapacitor technology comparison**

Source: [42], page 52; [43], page 6; and [44], page 1.

Type	Specific Energy (Wh·kg <sup>-1</sup> )	Energy Density (Wh·l <sup>-1</sup> )	Specific Power (W·kg <sup>-1</sup> )	Power Density (W·l <sup>-1</sup> )
L-A	30	75	250	625
NiMH	65	150	200	462
Li-Ion	90	150	300	500
UC (carbon-carbon)	4.5	6.6	3500	4200
USABC long-term target	150-200	230-300	300-400	460-600

It can be seen from Table 1-2 that none of the ESS technologies currently satisfy the specific energy and energy density requirements of the USABC for EV commercialization, although the Li-Ion technology comes nearest. The UC technology achievement is lowest for these metrics, and it is apparent that EVs using solely UC are currently infeasible. The ESS technologies perform significantly better when measured against the specific power and power density metric. Again, the Li-Ion technology is superior among the battery technologies, but the UC exceeds the target by an order of magnitude. It is clear that it is energy capacity, and not power capacity, where continued progress must be made for ESS technology.

Thus, even with state-of-the-art batteries, the range of EVs using either batteries or UCs limits their usage largely to urban transportation, impacting negatively on the convenience factor that is so important to citizens of large countries such as Canada, where journeys of 600 km or more are common. This curtailing of convenience is exacerbated by the multiple-hour period required to re-charge batteries. Furthermore, constant, near-complete depletion of the battery pack will shorten its lifespan dramatically and result in decreased performance and costly replacements, as the performance of a BV decreases as the state-of-charge (SOC) approaches depletion. UCVs fare even worse in terms of range because of the lower energy storage capacity, although the damage and performance degradation from rapid power transients and high-discharge cycles are not factors. The result is that BVs and UCVs will remain niche vehicles for the foreseeable future, until such time as a revolutionary battery or UC technology emerges that significantly increases the energy density, specific energy, power density, specific power, and cycle lifetime, and significantly decreases the charging time.

### 1.5.1 Fuel cell vehicles

The fuel cell was invented by Sir William Grove in 1839, but was not used in a practical application until proton-exchange membrane fuel cells (PEMFCs), made by General Electric, were employed in the National Aeronautics and Space Administration (NASA) Gemini missions in the early 1960s. The advantages of this fuel cell type, namely the low operating temperature and associated quick operation start-up, and the ability to make use of a thin electrolyte, initially made the PEMFC the frontrunner of the various fuel cell types. However, severe water management issues arose and were seen as insurmountable at the time. Furthermore, early PEMFCs required a substantial amount of expensive platinum coating of the electrodes to catalyze the electrochemical reaction, and the available current and power density levels were unsatisfactory. As a result, the Alkaline Fuel Cell (AFC) was used for a time by NASA, and the use of PEMFCs became almost non-existent [45].

In the 1990s, the PEMFC regained its status as the dominant fuel cell type, and fuel cells in general have received considerable attention as an alternative to fossil fuel combustion. Much

of the credit for the revitalization of the PEMFC must be given to Ballard Power Systems and to the Los Alamos National Laboratory [46]. The PEMFC is now seen by many researchers and companies as the only fuel cell type suitable for vehicular applications, due to a relatively high power density, low operating temperature and solid electrolyte [47]. In addition, the broad range of applications for PEMFCs extends from low-wattage electronic applications to megawatt combined heat and power (CHP) or cogeneration systems [46]. Indeed, this new technology is generally surmised to be the next logical step in the continuing de-carbonization of the energy portfolio. In order to overcome the present limitations and drawbacks of the PEMFC technology, scientists and engineers the world over are conducting extensive research with an aim of solving the various problems erecting roadblocks in the path of fuel cell commercialization.

A significant amount of fuel cell research focuses on fundamental issues of performance and cost. For example, at the time of the Gemini 7 mission in 1965, the fuel cells powering the internal electronics of the spacecraft used up to  $28 \text{ mg}\cdot\text{cm}^{-2}$  of platinum, and were capable of providing only small current densities in the  $\text{mA}\cdot\text{cm}^{-2}$  range. Contemporary research has resulted in the newest PEMFCs using only  $0.2 \text{ mg}\cdot\text{cm}^{-2}$  or less of platinum, and allowing for  $1 \text{ A}\cdot\text{cm}^{-2}$  or more of current density [46]. In fact, the latest platinum loading achievement in a stack is  $0.05 \text{ mg}\cdot\text{cm}^{-2}$  [48]. Thus, the notorious platinum catalyst costs have been reduced to approximately 10 USD in a 1 kW fuel cell, and now account for a small portion of the present overall cost of the stack. However, the current cost of manufacturing a 1 kW ICE is on the order of 10 USD, the same cost for only the catalyst in a PEMFC [46]. The ICE industry thus represents a formidable challenge.

Ballard Power Systems, arguably the world leader in fuel cell technology, has a “road map” which lays out its progress in stack costs and performance. Ballard demonstrated in February 2005 that a Ballard fuel cell stack could be manufactured (at high volumes) for  $73 \text{ USD}\cdot\text{kW}^{-1}$  [49], a marked improvement. The prototype stacks achieved a power density of  $1.47 \text{ kW}\cdot\text{l}^{-1}$  and operated for 2100 hours without significant degradation. The prototypes also reached 50%

power in 8 seconds at -15 °C, in 16 seconds at -20 °C and in 90 seconds at -25 °C [49].

A 2007 study performed by researchers from Argonne National Laboratory and private company TIAX LLC, using a novel nano-structured thin-film catalyst structure, resulted in a stack cost estimate of 31 USD·kW<sup>-1</sup> for high-volume production. In the same study, the fuel cell system (FCS) cost estimate for high-volume production was 68 USD·kW<sup>-1</sup> [50]. The study also provides a useful cost break-down of the stack and system components, shown below in (a) and (b) of Figure 1-3, respectively. It is easily observable that the largest potential for stack cost reduction is associated with the electrodes, while the compressor (denoted by “Air Management”) is the component with the most potential for cost reduction in the system (apart from the stack itself).

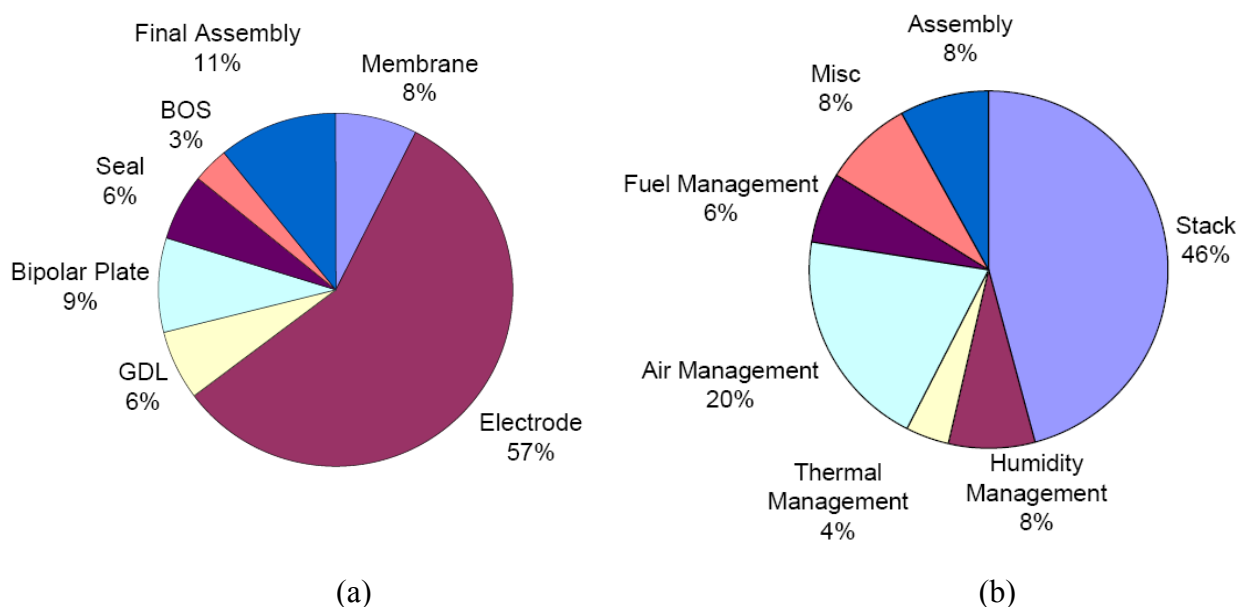


**Figure 1-3. Fuel cell stack (a) and system (b) cost break-down**

Source: [50], pages 13-14.

Progress has unquestioningly been made in fuel cell performance and cost. This progress inspires confidence that the criteria required in order for the fuel cell to become commercially viable will be met. The Department of Energy (DoE) in the United States has set ambitious

objectives to be achieved by 2010 for fuel cell stacks and systems. These objectives are contrasted with the results from reference [50] below in Table 1-3. Two of the most important targets are the stack and system costs. It can be seen from the table that the stack target has essentially been met three years ahead of schedule, while the system costs require considerable reductions. The table does not show, however, the significant progress in reducing system costs that has been made.

**Table 1-3. Fuel cell industry reported results and U.S. Department of Energy targets**

Source: [50], page 15.

Criterion	Unit	Reference [50] reported results	2010 U.S. DoE Target
System Cost	USD·kW <sup>-1</sup>	68	45
System Efficiency @ 25% Rated Power	%	60	60
System Efficiency @ Rated Power	%	50	50
System Specific Power	kW·kg <sup>-1</sup>	0.79	0.65
System Power Density	kW·l <sup>-1</sup>	0.64	0.65
System Durability	hr	-	5000
Stack Cost	USD·kW <sup>-1</sup>	30	30
Stack Efficiency @ 25% Rated Power	%	62	54
Stack Efficiency @ Rated Power	%	55	54
Stack Specific Power	kW·kg <sup>-1</sup>	1.9	2.0
Stack Power Density	W·l <sup>-1</sup>	2.07	2.0
MEA Cost	USD·kW <sup>-1</sup>	21	15
MEA Performance @ Rated Power	mW·cm <sup>-2</sup>	740	1280
MEA Degradation Over Lifetime	%	-	10
PGM* Cost	USD·kW <sup>-1</sup>	16	8
PGM Content (peak)	g·kW <sup>-1</sup>	0.4	0.5
PGM Loading (both electrodes)	mg·cm <sup>-2</sup>	0.3	0.3
Membrane Cost	USD·kW <sup>-1</sup>	16	40
Bipolar Plate Cost	USD·kW <sup>-1</sup>	3	6
CEM** System Cost	USD	1080	400

\* platinum group metal

\*\* compressor-expander module

Fuel cell technology is thus continuously improving and the ambitious DoE targets appear attainable. The other components of the electric drivetrain are improving concurrently as well,

do in no small part to the aforementioned resurgence of the BV and emergence of the HV. These improvements made it possible to build workable prototypes, but there are no FCVs being built by automotive OEMs today. The FCV combines the efficiency and environmental advantages of electric drivetrains with the range advantage of an external fuel tank. However, there are also performance-related concerns, specifically the ability of the FCS to deliver the high transients demanded of contemporary vehicles while at the same time demonstrating durability and reliability levels comparable to ICEVs. Furthermore, powering the fuel cell system compressor during start-up, especially during cold-starts required of North American vehicles, is very difficult without an external energy storage technology. Finally, the inherent inability of a FCV to capture any regenerative braking seems nonsensical when the energy from braking is so easily available in electric form. These drawbacks have essentially precluded the possibility of the FCV [51].

## **1.6 Hybrid Vehicles**

The HV is the main area of focus of the research in this dissertation. As the technology is still somewhat immature, the nomenclature used by the industry is sometimes unclear and confusing. The International Electrotechnical Commission (IEC) proposed the following definition for HVs [52]:

“A hybrid road vehicle is one in which propulsion energy, during specified operational missions, is available from two or more kinds or types of energy stores, sources, or converters. At least one store or converter must be on-board.”

More specifically, a sub-category of hybrid electric vehicle (HEV) was defined as:

“A hybrid electric vehicle is a hybrid vehicle in which at least one of the energy stores, sources, or converter can deliver electric energy.”

The latter HEV term is commonly used to describe any hybrid vehicle. It should be noted that the first definition for HV may be used instead of the now-customary HEV moniker, since the “electric” term is largely redundant. Unless a flywheel is used (ignored in this research for

reasons presented earlier), or the hybrid consists of two fuels being combusted separately in the same vehicle (an extremely unlikely scenario), there will inevitably be one or more EMs in the powertrain. Speculative technology such as hydraulic accumulators as an ESS technology remain unproven on a commercial scale, and are unlikely to ever gain significant HV market share. The ESS of choice for the foreseeable future will be some sort of electrochemical storage device, either battery or ultracapacitor technology (or both). In light of these realities, there will always be an electric component to the powertrain; thus, there is no need to mention this electricity explicitly in the name. For this reason, the word “electric” is omitted from all HV nomenclature in this dissertation.

The IEC definition is actually too specific, because its stipulation that propulsion energy must be available from both sources means that one form of the internal combustion engine hybrid vehicle (ICEHV) would not be included: the micro-parallel configuration of Section 2.1.2. The definition of the term ‘hybrid’ is thus used to describe powertrains that contain two or more power sources that are both directly connected to the wheels. This definition differs slightly from that of the IEC since it is not necessary that propulsion power is supplied: power can be transferred from the wheels to one of the power sources and not in the opposite direction, and the vehicle will still qualify as a hybrid vehicle. To clarify the nomenclature, the term “hybridization” can be introduced. Hybridization refers to a continuum of designs in which the power production responsibilities are partitioned among the power sources. This partitioning can be expressed by an industry measure known as the degree of hybridization (DOH). When an ICE is one of the power sources, the DOH can be defined as [42]:

$$\text{DOH}_{ICE, power} = \frac{P_{elec}}{P_{elec} + P_{eng}} \quad (1.1)$$

where  $P_{elec}$  is the power capacity of the EM(s) and  $P_{eng}$  is the power capacity of the engine. A vehicle of this type will be known throughout the document as an ICEHV. The DOH is then a measure of the relative amount of total vehicle powertrain power that is delivered by the EM(s). Thus, at a DOH of zero, the vehicle is a conventional ICEV, while at a DOH of one the vehicle is

an EV. An ICEHV will lie between the two extremes, with larger values signifying the usage of a smaller ICE and larger EM(s) role.

The DOH for an ICEHV will also determine the capacity and the capabilities of the electric portion of the powertrain. These characteristics can vary from marginal to substantial. For example, some ICEHVs have an integrated starter-generator (ISG) that enables instantaneous engine start, allowing for the engine to be turned off when the vehicle is idle, in addition to a moderate degree of regenerative braking capability. In this case, no propulsion power is derived from EM, and the DOH is quite small. As the DOH is increased, more capabilities are possible, including electric propulsion and a higher degree of regenerative braking.

The extent to which a vehicle is hybridized could also be measured in terms of the relative energy contents of the power sources. For the case of an ICE and battery combination, the degree of hybridization could be given by

$$\text{DOH}_{ICE, \text{energy}} = \frac{E_{ESS}}{E_{tank} + E_{ESS}} \quad (1.2)$$

where  $E_{ESS}$  is the energy content of the ESS and  $E_{tank}$  is the energy content of the fuel to be combusted. The DOH can thus be used to characterize both the power capability and the energy capacity of the hybrid components.

HVs can be PZEV, ZEV, or neither, depending on the technology used. For example, if an ICE engine is coupled to a very small ESS, the reduction in emissions may be so marginal that a classification of PZEV is not possible. The classification of a HV as a PZEV or ZEV will depend on the fuel used, the power sources, the DOH (in some cases), and also the power management strategy that manages these power sources.

It should be noted that each type of HV could be converted to a plug-in hybrid vehicle (PHV). The ESS of a PHV, if it is comprised of a battery bank, ultracapacitors, or some combination of the two (but not a flywheel), must be charged using an external electrical source, most commonly electricity from the grid. The ESS would have a much higher capacity in a PHV than in a HV and the vehicle would be capable of extended range in the all-electric regime

(AER) that HVs cannot provide. PHVs have recently received considerable attention in the media because of enthusiasts' conversions of a Toyota Prius to PHVs, and the much-touted possibility of all-electric driving in urban commutes while also promising considerable inter-city range with the ICE [53]. The AFS Trinity Corporation has taken the concept a step further: since the current Prius conversions cannot overcome the proprietary control system algorithm that demands the starting of the ICE engine above speeds of  $67.6 \text{ km}\cdot\text{hr}^{-1}$ , this company has introduced the Extreme Hybrid™ powertrain that purportedly allows for 40 km of all-electric travel at speeds up to  $110 \text{ km}\cdot\text{hr}^{-1}$  [54]. PHVs are the focus of many research groups, as evidenced by the large number of papers on this subject at the 2007 23<sup>rd</sup> Electric Vehicle Symposium (EVS-23), and could very well exemplify the future of the automobile [55].

#### 1.6.1 Hybrid vehicle history

The ICEHV was originally introduced in 1899 by Dr. Ferdinand Porsche. The first HV was called the Lohner-Porsche Mixte. The Mixte used an ICE rotating at a constant speed to drive a dynamo, which in turn charged a bank of accumulators. These accumulators delivered current to EMs contained within the hubs of the front wheels. Due to its remarkable simplicity, the transmission operated with an efficiency of 83%, which was high for that era, due to minimal mechanical friction losses. Over 300 Mixtes were produced, and the technology seemed promising indeed. A Mixte that is housed in a museum in Norway is depicted below in Figure 1-4.

Advances in ICE technology, however, condemned HV technology to the background, only being revived periodically (albeit infrequently) throughout the 20th century. For example, the Volkswagen Taxi was introduced to take advantage of the panic ensuing from the 1973 Arab oil embargo. This parallel hybrid vehicle, despite logging over 13,000 km in test drives and being shown in many automotive industry shows, never reached the production stage [56].

The concerns about AGCC and energy efficiency have created a confluence of circumstances that have provided an opportunity for the revival of the HV (and also EV). The ICEHV has been popularized with the introduction of the Honda Insight in 1999 and especially



**Figure 1-4. The Lohner-Porsche Mixte**

Source: [56].

the Toyota Prius in 2000. Both vehicles offer gas mileages more than twice those mandated by the current CAFE standard of the United States of  $8.6 \text{ L} \cdot (100 \text{ km})^{-1}$  [18]. Both vehicles have also been designated as PZEVs. The market for HVs continues to grow. An estimated 345,000 hybrid vehicles were sold in the United States in 2007, an increase of 35% over the 2006 figure [57]. Toyota Motor Corporation and Honda Motor Company have each projected that HVs will comprise some 10 to 15% of the U. S. automobile market by 2009. Toyota has pledged to produce 1 million HVs a year by 2012 [58]. GM claims that the company plans to introduce a new hybrid vehicle every three months from 2008 until 2012 [59]. The aforementioned U.S. Energy Independence and Security Act of 2007 bill to increase the fuel economy of automobiles, SUVs and trucks to 35 mpg by 2020 will create an even greater incentive for hybrid vehicles [19].

To date, most ICEHV applications have been restricted to spark-ignition (SI) engine applications. However, in Europe considerable attention is directed towards achieving the capabilities of the micro-hybrid in a CI engine due to the widespread usage of CI vehicles [60]. The challenge for introduction of CI ICEHVs is to overcome the market barriers for CI vehicles that have historically kept this technology rare in North American vehicles because of previous

problems of noise, emissions, low torque at high speeds, and cold-weather difficulties. However, the market for CI-ICEVs in North America appears to be growing. In addition to solving the historical performance deficiencies of CI vehicles, the emissions problems are being overcome as well. The latter development is illustrated, for example, by the BLUETEC filtration system mentioned previously. Also, the ultra-low sulphur diesel (ULSD) requirements enacted in 2006 have significantly reduced the amount of SO<sub>x</sub> emissions from diesel vehicles. These advances make the introduction of CI-ICEHVs a distinct possibility in the future.

ICEHV technology has been seen by many as a “bridge” technology that will improve the performance and cost structure of electric powertrains while also providing better gas mileage than the incumbent ICEV. The future looks bright for this technology, and a portion of the research conducted during the course of this Ph.D program was spent studying the current state of ICEHV technology. However, the emissions, while significantly reduced, will still contain a significant amount of harmful GHGs, smog-producing gases and other particulates, and the ICEHV is considered to be a stop-gap measure until true ZEVs can take over the marketplace. Even an ICEHV that uses hydrogen combustion in the ICE will likely only ever achieve a PZEV designation. In the short- to medium-term, however, the ICEHV is likely to dominate the hybrid vehicle market where there exists considerable potential for improvements in performance and cost.

The enthusiasm in the industry for ICEHVs has made research in this area very pertinent. The decision was made in the course of the work for this dissertation to broaden the scope to include ICEVs. This was due, in part, to a collaboration begun with Azure Dynamics, a company that designs, installs, and manufactures hybrid powertrains for commercial vehicles. The intent of this collaboration is to assist the company in developing hybrid powertrain designs that reflect the current state of the art of ICEHVs. A portion of this dissertation thus presents the research on the topic of ICEHVs. The design techniques of computer modelling and simulation are utilized as tools to assist in the development of improved powertrain designs.

## 1.6.2 Fuel cell hybrid vehicles

Despite the considerable progress that has been made to develop ICE-based vehicles that are more efficient and release fewer emissions, the objective of the ZEV remains elusive. It is almost inconceivable that any ICE-based vehicle will achieve this status. The fuel cell hybrid vehicle (FCHV) may be the desired “end-game” technology: the powertrain of this vehicle type could achieve all performance criteria while also eliminating harmful emissions. The reasons for anticipating that the FCHV will become the ZEV that ultimately dominates the vehicular market include:

- it has the potential to achieve performance comparable to ICEVs and ICEHVs since the ESS can ensure that the transient deficiency and start-up problems of the FCV are eliminated
- durability concerns can be mitigated by lower demand placed on both the FCS and ESS, decreasing the rate of degradation
- the desired vehicle range is achievable because of the external fuel storage
- costs are decreased because the presence of the ESS translates into a smaller FCS, the most expensive component in the FCV

A FCHV will use a FCS and ESS as its power sources in a hybrid configuration, both powering EMs that will provide the propulsion power. In this case, the DOH of Equation (1.1) is modified:

$$\text{DOH}_{FC, power} = \frac{P_{ESS}}{P_{ESS} + P_{FC}} \quad (1.3)$$

where  $P_{ESS}$  and  $P_{FC}$  denote the power provided by the ESS and fuel cell, respectively. In terms of energy, the DOH of Equation (1.2) becomes

$$\text{DOH}_{FC, energy} = \frac{E_{ESS}}{E_{ESS} + E_{H_2, onboard}} \quad (1.4)$$

A DOH of zero is, in this case, a FCV while a DOH of one will again be an electric vehicle powered entirely by an ESS. A DOH between 0 and 1 will signify a fuel cell-ESS hybrid. In

fact, a vehicle with a fuel cell will likely never be manufactured as a FCV but rather as a FCHV. It simply would not make sense to forego the benefits of regenerative braking (impossible without an ESS) and transient buffering that an ESS provides. The FCHV category is thus the only vehicle type that can balance performance and emission aspirations at present.

### 1.6.3 Commercialization barriers to fuel cell hybrid vehicles

The commercialization of FCHVs, which appeared imminent at the beginning of the previous decade, has progressed much more slowly than expected. Reasons for this sluggish commercial development are both varied and contentious, with few agreements on the exact causes. Certainly at least part of the current backlash has been caused by the fanciful optimism often espoused by the so-called “hydrogen economy” enthusiasts [61, 62]. The lack of hydrogen supply infrastructure and continuing higher costs and lower performance of fuel cell technology, in addition to the uncertainty surrounding the selection of the most advantageous hydrogen storage technology have also prevented the public at large from embracing the technology to date.

Until the life-cycle costs, as well as the performance of FCHVs, are competitive with those of the other powertrain technologies, it will be difficult for this technology to penetrate the vehicular market. There are many aspects of FCHVs that must be improved in order to compete commercially with the incumbent ICEV and other emerging technologies. Two main issues are maintenance and operating costs, which are dominated by hydrogen supply and battery and stack replacement costs. A third is production costs, although fuel cell system production costs will inevitably fall as manufacturing techniques improve and economies of scale allow for large volumes of product to reduce costs per unit item. However, in the near-term it is imperative that intelligent design decisions which will minimize the total cost of FCHV ownership are made. Cost reductions are possible for other powertrain technologies as well, but the possible cost reductions for FCHVs are much larger. Since the fuel cell stack is the most expensive component of the FCHV powertrain, one of the simplest methods of cost minimization is to reduce the power output of the fuel cell stack, thereby reducing the size (and cost) of the

fuel cell component, and compensating for this power loss through various techniques. For example, the voltage of a fuel cell is directly related to its active area, and increasing the active area of the fuel cell allows for lower current density draw, resulting in a higher output voltage, i.e. higher efficiency. One design option is to use larger sized fuel cells in stacks containing fewer individual cells; however, the fuel cell physical size cannot be made arbitrarily large due to volume constraints inherent in vehicular applications.

The hybridization of the powertrain also presents opportunities for design decision to have a large impact on costs and performance. Intelligent usage of the ESS in the hybrid configuration allows for smaller FCSs, where the ESS can make up for the lost power of the decreased stack size. Besides improving the cost structure, the benefits of a hybrid electric vehicle include large impacts on system performance and measures such as powertrain power density, powertrain volumetric density, and vehicle range. A major advantage of designing a FCHV rather than a pure FCV is that regenerative braking capabilities can dramatically improve the operating efficiency. As mentioned previously, it is only in rare, exceptional cases wherein a fuel cell-based vehicle will not be a hybrid. The performance, cost and propulsion system size and weight will depend strongly on the DOH and power management strategy chosen for the FCHV. While improving performance and cost structure, the hybridization increases the complexity of the design, and introduces another crucial design consideration in the type of ESS used. The choices range from mature, cheap lead-acid technology to novel, high-performance ultracapacitor technology. The optimal DOH and ESS design choices will vary for every FCHV application, and tactics to automate the selection based on given criteria must be developed.

The performance in terms of the durability of fuel cells is also a crucial issue to be resolved before commercialization can be realized. Although strides have been made in increasing the number of hours of operation of a stack before the voltage degradation becomes acute, FCSs continue to lag behind ICEs in system lifetime. The combination of a FCS and ESS in a hybrid configuration allows for the development of an operating strategy that optimizes the distribution

of power demand between the FCS and ESS. Since the operating strategy has a large effect on the lifetime of a FCS, and a well-conceived control algorithm that maintains the fuel cell stack operation in the region of highest efficiency will reduce the voltage demand on the stack, it is possible to greatly increase the interval before voltage degradation renders the fuel cell inoperative. For example, it has been shown that maintaining the current density demand of the FCS within a certain region that precludes both membrane flooding and dehydration extends the stack lifespan significantly [63]. Furthermore, fuel cells exhibit low efficiencies at high and very low power demands and peak efficiencies in the region of 25% of the stack rated power; thus, a power management strategy that maximizes the amount of operating time in this optimal region would be highly effective [64].

#### 1.6.4 Fuel cell hybrid vehicle industry status

Despite the slow pace of progress, there is cause for optimism for the future of the FCHV. The current climate surrounding the perception and opinion of the public towards continued fossil fuel usage has altered the market-based realities and feasibility of FCHV technology. The FCHV is attractive for its ZEV status, and thus its inherent ability to reduce AGCC and CAC pollution effects. Initiatives have been implemented in a plethora of locales to increase the number of these vehicles. For example, in 1990, the California Air Resources Board (CARB) adopted a policy requiring 2% of vehicles sold in California to meet the ZEV criteria by year 1998, rising to 5% in 2001 and 10% in 2003. Although the organization backed down from this mandate due to legal pressure from the Bush administration and automakers, this example of policy-making (copied by seven other states between 1990 and 2004) in the interest of the environment illustrates the wide-spread cognizance of the problem [36]. The confluence of public opinion, maturing FCHV technology and environmental concerns is making the conditions for commercial introduction of FCHVs much more favourable in the near- and long-term.

Almost every major automotive company has spent considerable research time and money on the development of FCHV technology. BMW Group of Germany (whose efforts are

directed solely at hydrogen combustion technology) is the single notable exception. Several models are nearing commercialization, including the Toyota FCHV, Mercedes-Benz F 600 Hygenius and Ford Focus FCV. The Toyota FCHV was recently successfully trialed on a 3732 km journey from Fairbanks, AL to Vancouver, BC to measure both fuel consumption and low-temperature performance. The same vehicle was then driven from Las Vegas, NV to San Diego, CA and set the single-tank range record for this vehicle at 702 km. The only vehicle that has thus far been commercialized is the Honda FCX, although the leasing was done in a pseudo manner as the price to the two customers, one in 2005 and one in 2007, was artificially low. It is reportedly the first fuel cell vehicle that has been fully certified to meet the U.S. government ZEV emissions standard as well as the crash-safety requirements. The 2008 FCX Clarity, which debuted at the 2007 Los Angeles Auto Show, is set to be marketed to a “limited number” of fleet and retail customers in southern California and in Japan beginning in the summer of 2008 [65]. The Chevrolet Equinox Fuel Cell SUV was purportedly released in a similar trial lease format to 100 customers for Project Driveway in the fall of 2007 [66], although no details of the trial progress could be found. Although there were many predictions that fuel cell-based personal vehicles would be commercially available on a wide basis by 2010, most observers have pushed this optimistic schedule back to 2012-2015. It seems, however, that the future continues to be promising for this burgeoning field, with growing public interest and knowledge and renewed industry effort.

The application of FCSs to vehicles is even more promising in buses. Public transit buses applications have the inherent advantage of a central refuelling station. This advantage means that the need for a vast *a priori* infrastructure to supply the hydrogen to FCHVs is eliminated, and the infamous so-called “chicken-or-egg” conundrum of hydrogen supply plaguing the hydrogen economy can be avoided. Furthermore, municipalities and governments can afford the current costs of fuel cells, and there is, in some cases, a public mandate to reduce local pollution and GHG emissions. The largest trial of fuel cell buses (FCBs) is the Clean Urban Transport for Europe (CUTE) project that deployed 27 buses in nine European cities. The

CUTE demonstration project began in 2006 and is ongoing. Significant progress has reportedly been made in terms of durability and low-temperature operation. BC Transit has recently committed to introducing the largest FCB fleet in the world, with 20 buses to be deployed in Whistler, B.C. in time for the 2010 Winter Olympic Games. This \$89M project could help develop the economy-of-scale needed to bring the costs of fuel cells down. The extensive real-world operation and resultant performance data of these buses should also be of enormous benefit to FCB researchers. FCBs appear to be on the verge of wide-spread adoption; more fleet purchases are likely to occur in countries such as Germany, Japan, and Australia.

#### 1.6.5 Fuel cell low-speed vehicles

A less well-known concept is the development of electric drivetrains with fuel cell power plants in applications other than for conventional automobiles, namely LSVs. LSVs are defined as vehicles with a velocity range of 32 to 45km·hr<sup>-1</sup>; the powerplant is limited to 6kW or less [7]. An example of this application is a work vehicle such as a forklift, where the vehicle is often used in enclosed areas that do not permit ICEs due to health concerns associated with engine exhaust. Using a battery-powered forklift is expensive since there must be three batteries for each forklift: one powering the vehicle, one in reserve, and another on the charging unit. It is also time-consuming since the batteries must constantly be replaced as they become depleted, and this has a deleterious effect on productivity. A fuel cell-powered forklift would allow for much longer intervals between “re-charging” of the vehicle, while also requiring only the single power plant and providing a much faster recharge. Materials handling is seen as one of the possible “wedge” applications that will help commercialize fuel cells, and large corporations such as Wal-Mart are currently testing fuel cell-powered forklifts in warehouses to measure the feasibility of moving away from battery-powered forklifts.

The largest segment of LSVs is in the scooter area. In an increasingly urban worldwide population, these vehicles are dramatically increasing in worldwide popularity due to the readily apparent convenience factors for commuters suffering from increasingly stifling traffic and from the dearth of urban parking spaces. A large proportion of currently manufactured scooters are

ICEVs that use highly polluting two-stroke engines, especially those produced in developing countries. Approximately 65 million ICE scooters are sold each year, of which two-thirds are 50 cubic centimetre (cc) versions. China and India lead the world in annual sales, with 33 and 28 million sales, respectively [67]. The annual worldwide sales number for battery scooters (BSs) was 1,621,000 in 2003 and 2,160,000 in 2004. This is an increase of over 33% in a single year. Cumulatively, the worldwide sales reached 6,000,000 by the end of 2005, with the trend expected to continue [67]. When the sales estimate for the years prior to 2000 is considered (approximately 200,000 units sold cumulatively), it is readily apparent that the market for BSs is currently experiencing substantial growth.

Most of the efforts that have been made towards the development of BSs are intended to compete with the current state-of-the-art 50 cc ICE scooters. Some high-performance attempts have also been made. A representative sample of these commercialized products are included in Table 1-4 below, along with some specifications for a Honda Metropolitan, the latter being used as a representation of the state-of-the-art ICE scooter [68].

**Table 1-4. Commercial battery scooters**

<b>Manufacturer/Model</b>	<b>Maximum Speed</b>	<b>Range</b>	<b>Power Source</b>	<b>Approximate Retail Cost</b>
Electric Vehicle Technologies EVT-4000E [69]	60 km/hr	40 km	Sealed Lead-Acid Battery	2,195 USD
eGO Vehicles Inc. eGO Cycle2 [70]	37 km/hr	40 km	Sealed Lead-Acid Battery	1,199 USD
Vectrix Maxi-Scooter [71]	100 km/hr	64-97 km (maximum of 109 km)	Nickel-Metal Hydride Battery	11,000USD
Typical ICE scooter [68]	70 km/hr	240 km	49 cc ICE	1,849 USD

The performance of these vehicles has been disappointing to the average consumer, especially in the area of vehicle range, and none have made a significant impact in the vehicle

market. Testing of several electric scooters previously powered by lead-acid batteries switched to cutting-edge zinc-air batteries has shown considerable improvement in range. It remains to be seen, however, if this technology, or, for that matter, any advanced battery technology (e.g. lithium-sulphur) can be made as reliable and affordable as current battery technology [42, 72].

Due to the perceived limitations of BSs, scooters and bicycles were thought to be promising applications of fuel cells. The reasons that the fuel cell hybrid scooter (FCHS) seemed compelling include the fact that the engineering challenges are made less complicated because of the smaller power plants and fewer auxiliary devices compared to the full-size FCHV [73]. Furthermore, refuelling of FCHSs can be accomplished by small, interchangeable tanks so that, as in the case of bus applications, the need for a wide-spread hydrogen infrastructure is simplified immensely. It was believed by some parts of the industry that there existed an opportunity for the FCHS to gain significant market share. Several companies began working on fuel cell-powered scooters and several efforts seemed on the verge of commercialization. Some of these are listed in Table 1-5 with several pertinent performance characteristics. The details on the Honda Motor Co., Inc, website were scarce with regards to the expected performance characteristics of the Honda FCMC scooter, but it is targeted towards the market for 125 cc scooters [74].

**Table 1-5. Fuel cell hybrid scooters**

<b>Manufacturer/Model</b>	<b>Maximum Speed</b>	<b>Acceleration</b>	<b>Range</b>
Vectrix VX-FCe [75]	100 km/hr	0-80 km/hr in 6.8 s	250 km @ 40 km/hr
Asia Pacific Fuel Cell Technologies ZES IV.5 [76]	52 km/hr	Unknown	60 km @ 35 km/hr
Honda FCMC <sup>TM</sup> [74]	Unknown	Unknown	Unknown
Intelligent Energy ENV [77]	80 km/hr	0-80 km/hr in 12.1 s	> 160 km

Due to this optimism, two battery scooters (BSs) were purchased, and an industry partner, Palcan Fuel Cells Ltd., was contracted to convert one BS to a FCHS. The intent was to have two LSVs, identical in every way except for the powertrain, so that the challenges and opportunities for the design of FCHSs could be elucidated.

It is clear from the survey of private companies with FCHS programs that there are, in fact, very few developmental attempts to commercialize this technology. None of the FCHSs in Table 1-5 has reached the point of commercialization, despite repeated claims that such commercialization is imminent. It has thus become apparent that the costs of the hybrid powertrain, with either an ICE or FCS as the main power source, likely preclude implementation in this vehicle type. The cost and performance of contemporary battery technologies can easily satisfy the range demand for a vehicle that is designed for urban use only. A portion of the research for this dissertation focuses on this application for a FCHV because a scooter platform is much simpler than that of a full-scale automotive application. It thus presents an opportunity to learn more about the issues associated with FCHVs. The intent is to assess the design and to conclude where improvements can be made in performance and cost. The design tools of modelling, simulation and optimization are used to achieve improved performance from the powertrain design.

## **1.7 Research Focus**

From the survey discussed above, it is clear that a significant amount of design and development is necessary in order to achieve a substantial advancement in emissions reduction and efficiency increase in the vehicle system. Hybrid vehicles, especially, present a multi-faceted design problem because of the additional degrees of freedom of added components and the more complex control of the powertrain. In any design process, the optimal design involves a compromise between the competing objectives of performance and life cycle costs. For example, designing for a higher acceleration performance will in all likelihood increase the overall weight of the vehicle; meanwhile, using advanced technology components can mitigate

this increase, albeit at a higher expense. It is crucial that comprehensive models of all components are included and that the criteria, such as vehicle range, upon which design decisions will be made, be quantified. Furthermore, this quantization must be done in an organized and logical fashion. It is especially beneficial to the design process if the criteria are defined at the earliest possible juncture, as this will have the potential to significantly reduce the cost and time cycle of the design process. Historically, a general automotive engineering rule of thumb has been that costs and manufacturing time are proportional to vehicle weight and size. Approximations are no longer acceptable, however, and it is crucial in the competitive market of today that these criteria are modelled in sufficient depth to reveal the characteristics and subtle differences between a multiplicity of designs [78].

The work performed for this Ph.D. research began with a thorough survey of the current trends in HV development, with a documentation of the state of the art of hybrid vehicle research. With a clear view of the path chosen by industry to development of this powertrain technology, the research focused on the development of virtual prototypes of hybrid vehicle powertrains through the use of design tools. Dynamic modelling of the selected designs is used to accurately describe the powertrain mechanisms' functions. Simulations are conducted to predict the performance of the developed models. An optimization of one of the powertrain components is performed to demonstrate the potential of optimization to improve designs. Finally, experimental validation of the results of the modelling and simulation is conducted to confirm or refute theoretical predictions. These steps are crucial aspects of the development of the virtual prototype. A virtual prototype is indispensable in the competitive industry of automotive development because it allows for design change effects to be measured quickly and easily and without the need to manufacture expensive physical prototypes with each change.

The dissertation research can be separated into five parts, with some overlap among the components: (1) ICE-based hybrid vehicle modelling, (2) fuel cell stack and system modelling, (3) LSV modelling, (4) LSV dynamometer testing, and (5) optimization of the operating

parameters of a FCS. Firstly, an overview of the state of the art of ICEHVs is presented in Chapter 2, outlining the current trends and classifications of contemporary ICE-based hybrid vehicles. The advantages of the latest designs over previous architectures are documented. Next, dynamic modelling and simulation results of a chosen ICEHV design are provided in Chapter 3. The *multi-regime* architecture nomenclature is introduced into the literature and the first attempt to contrast the performance of a multi-regime architecture versus established powertrain architectures is described. The dynamic model developed for a particular design is more accurate and more in-depth than previous work.

The focus of the document then shifts to a discussion of fuel cells, which are widely considered to be the next generation of powertrain technology. In Chapter 4, a comprehensive review of the fuel cell modelling literature is presented and the choice of fuel cell stack model is justified and presented. Modifications that are proposed for the stack model such as the inclusion of transient effects are described. In Chapter 5, the system model to which the stack model is coupled is presented. The modules included in the system model are reactant supply, humidification, and cooling systems. Modifications that capture transient effects to achieve a dynamic model of the full fuel cell system are also proposed.

In Chapter 6, the modelling of the LSVs is presented in detail. The two models undergo identical simulations in order to gauge the relative performance achieved by the two powertrains. Subsequently, in Chapter 7, the method used in the physical testing and validation of the simulation results is described. The two prototype LSVs are tested in the IESVic Low-Speed Vehicle Testing Facility (LSVTF) to determine their performance relative to each other. The experimental results are contrasted with those of the simulations, and a discussion of the possible reasons for the dissimilarities is presented.

In Chapter 8, the steady-state version of the fuel cell system model is used and optimization techniques are employed to gauge the potential improvement in performance of a fuel cell system by optimizing the operational parameters of the system. The optimization is applied to two generic applications, where the power demand is expected to vary, as in a vehicle, or when

the power demand is constant, as in a stationary power plant. The former application technique is then used to optimize the operating parameters of the FCS of the FCHS for a vehicle undergoing a simulation.

The document concludes with the section on Conclusions and Outlook in Chapter 9. In this section, a discussion of the important findings of the research is provided, and suggestions for avenues of future, related research are discussed.

## **1.8 Research Tools**

The computer modelling tools used for the research are two software packages. The MATLAB software from The MathWorks is used for computational modelling. This software is widely used by a multitude of industries and research areas for this purpose. The software has an optional “Optimization Toolbox” that was purchased for mathematical optimization. In addition to the local optimization algorithms provided by the toolbox, algorithms coded by the author’s research group in MATLAB were also employed in the research.

The second software is one developed by the National Renewable Energy Laboratory (NREL) in 1994 (and continuously improved through an open-source process) for vehicle modelling and simulation known as the ADvanced VehIcle SimulatOR (ADVISOR). ADVISOR was based on the MATLAB/Simulink platform, making its use flexible for coupling optimization routines that had been previously developed by the author’s research group. The ADVISOR software was open-source, where a large number of research groups contributed to the model libraries, allowing the tool to become the industry standard. ADVISOR allows for easy use and replicable results; however, the component models are empirically based instead of phenomenologically based physical models. While the work included in the dissertation was performed using ADVISOR, subsequent on-going work is using a different simulation software package, and this transition is discussed in Section 9.6.1.

The third design tool is the LSVTF in which experimental validation of modelling and simulation results can be performed. The facility allows for repeatable and accurate results in a

controlled environment. The prototype LSVs can also be thought of as design tools. Testing of these vehicles provides an appreciation of the vehicle model accuracy.

This dissertation is adapted, in part, from several articles written by the author, listed here in reverse order of date of publication:

**Wishart, J.**, Zhou, Y., Firmani, F., Dong, Z. (2008). “Dynamic modelling and simulation of a multi-regime hybrid vehicle powertrain architecture,” *International Journal of Electric and Hybrid Vehicles*, **1**(2), awaiting publication.

**Wishart, J.**, Zhou, Y., Dong, Z. (2008). “Review of multi-regime hybrid vehicle powertrain architecture,” *International Journal of Electric and Hybrid Vehicles*, **1**(3), awaiting publication.

**Wishart, J.**, Zhou, Y., Dong, Z. (2007). “Review, modelling, and simulation of two-mode hybrid vehicle architecture,” *Proceedings of the ASME 2007 International Design Engineering Technical Conferences & Computers and Information in Engineering Conference*, 22 pages.

**Wishart, J.**, Dong, Z., Secanell, M. (2006). “Optimization of a PEM fuel cell system based on Empirical data and a generalized electrochemical semi-empirical model,” *Journal of Power Sources*, **161**(2), pp. 1041-1055.

**Wishart, J.**, Dong, Z., Secanell, M. (2006). “Optimization of a PEM fuel cell system for low-speed hybrid electric vehicles,” *Proceedings of the ASME 2006 International Design Engineering Technical Conferences & Computers and Information in Engineering Conference*, 16 pages.

**Wishart, J.**, Dong, Z., Secanell, M., (2005). “Optimization of a fuel cell system based on empirical data of a PEM fuel cell stack and the generalized electrochemical model,” *Proceedings of the 1<sup>st</sup> International Green Energy Conference*, Waterloo, Canada, 11 pages.

## **Chapter 2 State of the Art of Commercialized Hybrid Vehicles**

The ICEHV is the only type of hybrid vehicle to be commercialized at present, and it thus presents the near-term solution to increased vehicle efficiency and reduced emissions. This chapter discusses the current state of the hybrid vehicle industry, beginning with a categorization of the main types of ICEHVs. Once the differentiation between architectures has been established, a summary of each is presented. Finally, the multi-regime architecture that represents the state of the art for ICEHVs, and the type that is modelled in Chapter 3, is introduced. The designs that can be found in the literature are presented and the details of the designs are discussed. The examined architectures have been created by GM, Renault, The Timken Company, Silvatech, and researchers at the University of Michigan-Dearborn. There are no performance data or details accompanying the description in the literature, so a comparative analysis between these multi-regime designs and other powertrain designs is not possible at this time.

### **2.1 Categories of Internal Combustion Engine Hybrid Vehicles**

It is useful to distinguish the different types of hybrid vehicles currently in various stages of development. Historically, these hybrids have been placed in one of three categories: (1) series hybrids, (2) parallel hybrids, and (3) power-split hybrids. ICEHVs can be further classified in three categories: micro, mild and full. At this point, authors use differing classifying criteria to place vehicles into categories. A ‘micro-hybrid’ is a vehicle in which one electric machine is used for functions such as ICE stop/start and regenerative braking but is not used to supply additional torque when the engine is running and the vehicle is not powered by electric motive power alone [79]. Some authors further define micro-hybrids as HVs that improve upon the fuel economy by 5 to 10% of a conventional vehicle with the same body characteristics and that have EMs that are 5 kW or less [58]. By definition, micro-hybrids are parallel architectures since none of the engine power passes through the electric machine, a

requirement in the other two types.

A ‘mild-hybrid’ is defined as a vehicle with the same capabilities of a micro-hybrid with the additional requirement that the electric machine(s) are also able to provide up to approximately 10 per cent of the maximum engine power [79] or between 7 and 12 kW [58]. A mild-hybrid can be either a parallel or power-split architecture, although the latter design would be rare and would require unusual gearing in its transmission.

A ‘full-hybrid’ is defined as a vehicle with the same capabilities of a micro-hybrid but with the additional requirement that the electric machine(s) are able to provide torques that are up to 40% of the maximum engine torque [79]. A full-hybrid will have an all-electric motive power mode, also known as an all-electric regime (AER), in which all of the mechanical power at the wheels will originate in the ESS.

CARB uses a different method and classifies ICEHVs according to the criteria outlined in Table 2-1. CARB distinguishes between low- and high-voltage HVs along with the amount of EM power. Additionally, the different levels of hybridization can be used by the vehicle owner in applying for a tax credit under the auspices of the ZEV program of California.

**Table 2-1. Classification system of the California Air Resources Board for hybrid vehicles**

Source: [42], page 13.

	<b>Level 1: low-voltage, Low-power HV</b>	<b>Level 2: high-voltage, medium-power HV</b>	<b>Level 3: high-voltage, high-power HV</b>
<b>Motor voltage</b>	$< 60 \text{ V}$	$\geq 60 \text{ V}$	$\geq 60 \text{ V}$
<b>Motor peak power</b>	$4 \text{ kW} \leq P_{elec} < 10 \text{ kW}$	$10 \text{ kW} \leq P_{elec} < 50 \text{ kW}$	$P_{elec} \geq 50 \text{ kW}$
<b>ZEV program credit</b>	0.2	0.4	0.5

As the previous classification examples illustrate, there is a distinct lack of uniformity and agreement on nomenclature in the industry. With the renaissance of the HV in its early stages, this is to be expected. As the technology matures and become more ubiquitous, standardization of the industry terminology is bound to follow. The hybrid vehicle categories and sub-types are shown in Figure 2-1.

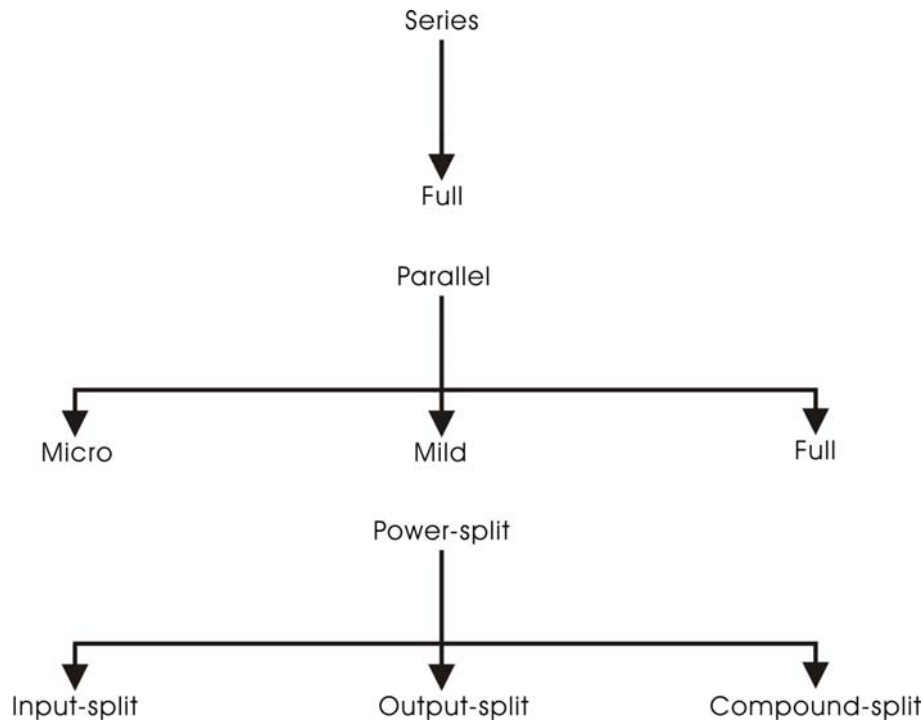


**Figure 2-1. Types of internal combustion engine hybrid vehicles**

The figure shows that a series hybrid is always “full”; this is because the EM provides all of the direct mechanical power to the wheels. Parallel hybrids can be micro, mild or full. Power-split hybrids will invariably be full. Using the DOH concept of Equation (1.1), it is apparent that the DOH of parallel hybrids will always be smaller than the DOH of series hybrids, precisely because the EM in the latter must be large enough to handle the power of the ICE and the ESS.

The classifications found in Figure 2-1 are useful, but several contemporary designs cannot be classified easily using these categories. Therefore, the concept of the “multi-regime” architecture must be introduced at this point. Multi-regime designs can have any combination of series, parallel, and power-split configurations. Some hybrid vehicles have an AER; however, this regime can be thought of as a series regime with the engine off, and so it will not be considered to be a separate regime from series. The multiple configurations of multi-regime

designs allow the electronic control unit (ECU) to select transmission configurations with widely ranging characteristics and advantages according to the vehicle load and powertrain components. Depending on the design goals, this means that the power management strategy can ensure that the vehicle achieves optimal performance in metrics such as acceleration, towing capacity, or fuel consumption. It is this flexibility that is the rationale for the more complex power management strategy and additional components. Furthermore, a multi-regime architecture that incorporates multiple categories is more adaptable to a wide range of vehicle types and applications.

The architectures that are examined in detail in Chapter 3 of this document are multi-regime designs. The designs have been referred to as “multi-mode” in some references, for example [80]. Some confusion arises in the literature since the patents and academic papers by GM sometimes refers an operating regime such as series as a mode, and sometimes reserves the term mode strictly for power-split configurations. To avoid overlapping definitions, designs that allow for singular and multiple operating regimes are heretofore known as “single-regime” and “multi-regime”, respectively, and the term “mode” shall be reserved for power-split designs only. Unless specified as multi-regime, a single-regime architecture will be assumed. The multi-regime architecture is the focus of the first component of the dissertation, and so to provide context into its development, an overview of the various operating regimes of which the multi-regime design consists is provided.

### 2.1.1 Series architecture

In the series architecture all of the mechanical power derived from the engine is converted to electricity by a generator and directed along an electrical path to the battery, the traction motor, or both. Note that in this case, the traction motor provides all of the power to the wheels, and this why the architecture must be classified as “full”. Figure 2-2 below depicts a schematic of a generic series hybrid powertrain. Note that in this and all subsequent figures a solid line denotes a mechanical connection while a dashed line denotes an electrical connection. The “FD” label in-between the wheels on the schematic (and in all subsequent schematics) denotes the final

drive gearing and differential.

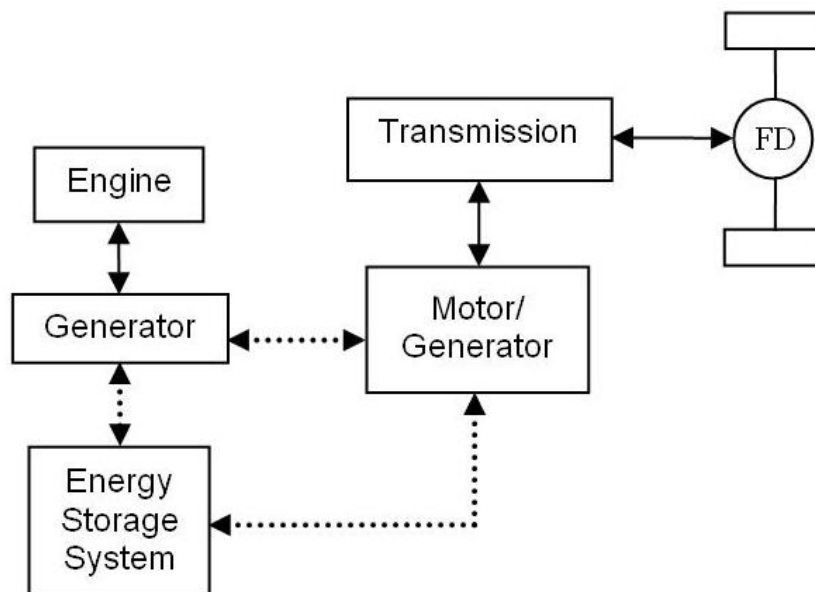


**Figure 2-2. Configuration of a generic series hybrid vehicle**

Early on in the latest renaissance of the hybrid vehicle, several automotive OEMs examined the possibility of development programs for series hybrid vehicles. Some of the most notable single-regime series designs are the Mitsubishi ESR, the Volvo ECC, and the BMW 3 Series [81].

Despite the early research and prototypes, the possibility that single-regime series hybrids will be commonly used in vehicular applications is remote. The series hybrid design has been relegated mostly to niche applications like the diesel-powered hybrid railway engine, although series hybrid transit vehicles from, for example, the ISE Corporation, continue to be manufactured [82]. The configuration can be highly efficient for certain applications and having the engine run at its optimal speed as a trickle-charger of the batteries results in an extremely large vehicular range. Indeed, for low average power applications, the series configuration is likely optimal [83]. The engine is never connected to the mechanical transmission, and therefore its speed is independent of the vehicle speed, a desirable characteristic that allows for more flexibility in engine selection. However, all of the mechanical traction originates in the EM, thereby tying vehicle performance to EM size. This

increases the weight of the vehicle, but more importantly the cost, since a large EM is required to achieve performance targets. Furthermore, the efficiency of the series architecture for high average-power applications, for example for frequent grades or highway speeds, is lower than for other architectures [83].

### 2.1.2 Parallel architecture

The parallel architecture is the most common design for current commercialized hybrid vehicles. In this architecture, both the engine and the motor provide traction power to the wheels. As a result, for a low DOH, the motors can be smaller and thus cheaper. This makes the parallel architecture more viable for automotive original equipment manufacturers (OEMs) concerned with a large increase in vehicle price due to hybridization. Some of the early developments of parallel hybrid vehicles include the BMW 518, the Citroën Xzara Dyn-active and Saxo Dynavolt, the Daimler-Chrysler ESX 3, the Fiat Multipla, and the Ford Multipla and P2000 Prodigy [81]. The most well-known examples for light-duty vehicles (LDVs) are vehicles in the Honda hybrid vehicle collection, such as the Honda Insight (now discontinued), and Accord Hybrid. Parallel designs are also found in commercial hybrid vehicles from manufacturers such as Azure Dynamics and Nissan [84]. Many manufacturers design single-regime, parallel hybrid powertrains because of their relative simplicity and low cost, and also because of the capacity to retro-fit conventional vehicles with a parallel hybrid transmission cost-effectively. A generic parallel architecture is depicted in Figure 2-3 below.

It should be noted that the motor/generator can be pre-transmission (where it can be used as a starter-alternator), post-transmission, or between the differential and wheels in hub motor technology. If the pre-transmission configuration is chosen, the motor torque is summed with the motor torque at the transmission input shaft; contemporary parallel hybrid vehicles employ this strategy almost exclusively. When the configuration is post-transmission, the electric torque is summed to the engine torque at the output shaft of the transmission. The motor/generator is thus at a fixed gear ratio with respect to the wheels, and a disconnect device such as a clutch is required to avoid situations in which the motor/generator either over-revs or

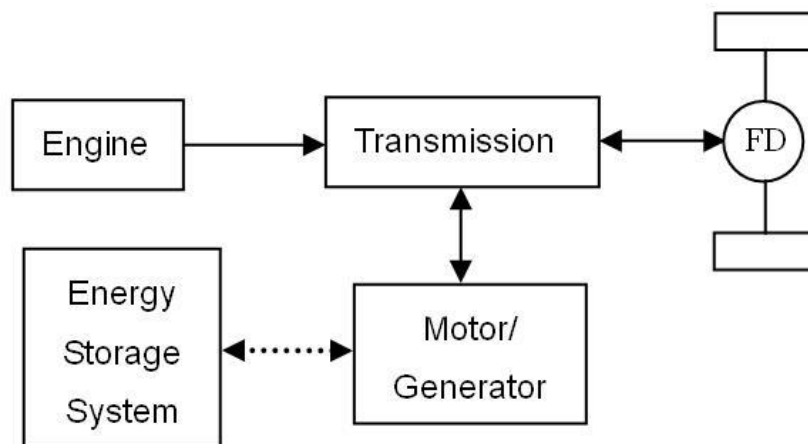


**Figure 2-3. Configuration of a generic parallel hybrid vehicle**

incurs spin losses when not in use [40]. Post-transmission electric hybrids are rare; however, post-transmission hybrids employing hydraulic technology have been pursued largely as launch-assist devices in heavy-duty trucks and commercial vehicles.

There are many ways in which to design a parallel hybrid, as well as a myriad of strategies to increase performance. For example, the vehicle may run on purely electric power while in the city and on engine power on the highway. Most contemporary parallel vehicles use the EM and ICE in combination, using complex control systems and algorithms to optimize both performance and range. The ESS is often used as a load-leveling technology that allows the ICE to work at high efficiency range; the engine can be shut off during idling to reduce emissions and increase the fuel economy. This flexibility in design, in addition to the elimination of the need for a large motor, has caused interest in parallel hybrids to be much higher than for series hybrid development. An intriguing design is shown in Figure 2-4, where a four-wheel drive parallel hybrid vehicle is depicted. In this design, the road itself is the medium that connects the engine and EM. It should be noted that the ECU must ensure that the front and rear wheels rotate at the same speeds.

The design is most beneficial if the ICE powers the rear wheels and the motor the front wheels. The reason is that during braking, more weight is borne by the front wheels, resulting

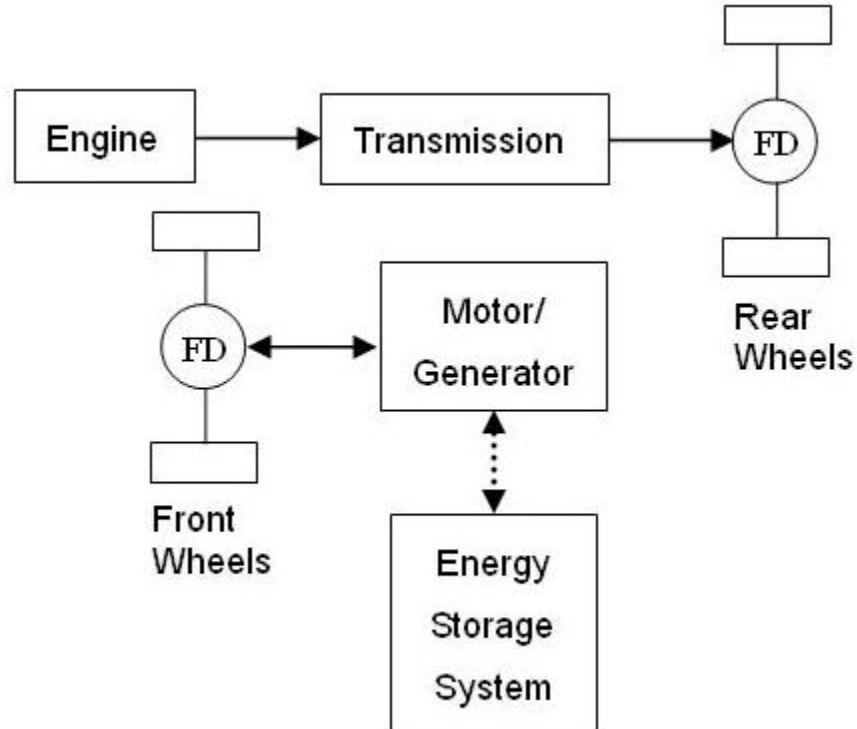


**Figure 2-4. Configuration of a parallel hybrid four wheel drive**

in more regenerative power being captured. The design is very effective on slippery surfaces and provides vehicle longitudinal stability control that is not possible with other types of hybrid designs. The power to each axle is manipulated by a single controller, although this requires a fast communication bus. It is unclear whether any automotive OEM is currently looking seriously at this type of design.

### 2.1.3 Power-split architecture

The final category from Figure 2-1 is the power-split design. Early versions of power-split design can be found in some lawn tractors [85]. Manufacturers are making significant progress with the power-split design and, consequently, it has come to dominate the LDV market. The “split” nomenclature refers to the fact that the design uses a power-split device (PSD), usually a planetary gear, to allow the engine power input to be split between mechanical and electrical paths (also known as the electric variator, where the electrical power is transferred between the

EMs and the ESS). One of the advantages of the power-split design is that a transition from forward to reverse vehicular motion can occur without need for a clutch actuation [85]. The power-split architecture can be considered a compromise between the advantages of the series and parallel architectures, while also providing an ingeniously devised continuously variable transmission (CVT).

In fact, power-split architectures can be considered a special case of CVTs: the infinitely variable transmission (IVT) (also known as electronic CVT, or e-CVT). Conventional CVTs can provide continuously variable speed ratios over the velocity range of the vehicle but require launch-clutches or engine-disconnect devices for vehicle start-up because the input-to-output speed ratio must be finite (i.e. the output cannot be zero for non-zero input). Furthermore, most CVT designs are friction-based belt and traction types that are unsuitable for high-torque and high-power applications [86]. Conversely, an IVT can provide an infinite number of output-to-input speed ratios, including a geared neutral. This allows the output velocity of the vehicle to vary from reverse, through zero (stationary), to forward. There is no need for a launch device such as a torque converter in an automatic transmission or a clutch in a manual transmission is necessary, and the engine can remain directly connected to the transmission for all speeds [86].

One of the important characteristics of the power-split architectures is that at certain operating points the power through the electrical variator is zero; at these points, the system passes through what is known as a node point. The mechanical path is more efficient than the electrical path, and it is possible for a given configuration to have multiple node points. Therefore, the overall transmission efficiency can be increased by the addition of more node points. This will increase the system cost and complexity, however, because additional nodes are usually obtained by introducing additional PSDs and/or additional clutches. PSDs are relatively large, heavy, and expensive components and clutches are prone to failure. Furthermore, clutches are sources of power loss and possibly driveline shudder, and driveline oscillations if the shifts are not done synchronously [40].

In normal power feed-forward operation, the power through both the electric variator and mechanical path flows from input to output of the transmission; the input to the transmission is the engine and the output is the differential. However, there are some situations where the power-split design has inherent inefficiency, known as power-loop operation, which are of two types: *negative recirculation* and *positive recirculation*. When negative recirculation occurs, the power in the electric variator flows from output to input, causing the power in the mechanical path to be greater than the input power. When positive recirculation occurs, the power in the mechanical path flows from output to input, causing the power in the electric variator to be greater than the input power. Both operations decrease the efficiency of the transmission, and as a result, decrease the output power. This situation is therefore usually undesirable, but, in some cases, this situation can be purposefully caused in order to slow down the engine and increase fuel economy, a phenomenon known as engine lagging or negative split. In some power-split designs, mechanical power loops can also occur which decreases the powertrain efficiency because the moment of inertia (MOI) of additional rotating elements will consume input power. For these reason, the ECU should be programmed to ensure that power loops are avoided unless engine lagging is desired.

The method for determining whether negative recirculation, power feed-forward or positive recirculation occurs is to calculate the ratio of the power input to the electric variator to the input power from the engine [87]:

$$P_{ratio} = \frac{P_{var, in}}{P_{input}} \quad (2.1)$$

where  $P_{var, in}$  is positive when the power through the variator is from input to outlet. The value of  $P_{ratio}$  dictates the type of operation, as shown in Table 2-2.

Power-split designs include input-split, output-split and compound-split architectures. In input-split and output-split architectures, the mechanical power of the engine is split once between mechanical power that directly powers the wheels and electrical power that is sent to the EMs and battery. Conversely, compound-split architectures split the mechanical power of the

**Table 2-2. Power-split architecture operation**

Source: [87], page 3.

$P_{ratio}$	Description	Power-split operation
$P_{ratio} \leq -1$	Power through variator is larger than or equal to input power; power flow through variator from outlet to inlet	Negative recirculation
$-1 < P_{ratio} < 0$	Power through variator is less than input power; power flow through variator from outlet to inlet	Negative recirculation
$P_{ratio} = 0$	No power through variator	Power-split, node point
$0 < P_{ratio} < 0.5$	Power through variator is less than through mechanical path	Power-split
$0.5 \leq P_{ratio} < 1$	Power through variator is greater than or equal to that through mechanical path	Power-split
$P_{ratio} \geq 1$	Power through variator is larger than or equal to input power; power flow through mechanical path from inlet to outlet	Positive recirculation

engine between two or more mechanical paths and the electrical path; the split mechanical power is re-combined at the output of the transmission.

The input power of an input-split transmission is split at the input to the PSD, and the output of the PSD is the combination of mechanical and electrical power paths. The node points for input-split design are at low output-to-input speeds ratios, and so this type of transmission can provide a high level of efficiency when the output-to-input speed ratio is low. As the output-to-input speed ratio increases, the power through the variator increases, decreasing the transmission efficiency, until the point at which power-loop operation occurs.

The split of the engine input power of an output-split transmission occurs after the PSD in an output-split architecture. The node points for this architecture occur at high output-to-input speed ratios, so this type of transmission is useful for high ratios. At lower speed ratios, power-loop operation occurs since the power through the variator increases with deviation from the node point speed ratios. As the speed ratios increase, the power feed-forward operation begins and becomes more and more efficient with increasing ratio before the node point is reached.

Finally, compound-split transmissions have at least two PSDs. Compound-split transmissions that provide two node points operate most efficiently between these points. As the output-to-input speed ratio decreases below the first node point and above the second node point, the efficiency decreases. Therefore, additional regimes of input-split and output-split or parallel for low and high output-to-input speed ratios, respectively, are often used to increase the transmission efficiency for a wide range of speeds. Adding more PSDs will result in more mechanical paths from engine to wheels and will provide more nodes at the expense of higher component and complexity costs.

#### 2.1.4 One-mode, two-mode and multi-regime powertrain architectures

The power-split design that is currently dominating the market is the single-regime, power-split architecture, popularized by the Toyota hybrid System (THS) installed in the Toyota Prius and known as “one-mode” architecture. A considerable amount of work has been done to model and simulate the performance of the market-leading Prius THS system, from an environmental perspective [88], to performance evaluation [89] and component development [90], and even a method to use the electrical system of the THS to provide electricity in the event of a power outage [91]. A high degree of confidence has been achieved in the understanding of the THS system, even though a full dynamic analysis has, to the authors’ knowledge, only been attempted by Liu *et al.* [89]. The same research group also optimized the power management strategy of the Prius using an instantaneous optimization algorithm called the Equivalent Consumption Minimization Strategy (ECMS) and compared the results to those achieved using a dynamic programming (DP) technique [92].

The advantage of the input-split THS design is its relative simplicity and its increased performance over competing hybrid designs; however, the performance at high speeds and on steep grades is not outstanding due to the undersized engine running an Atkinson cycle rather than the customary Otto cycle. Furthermore, the achieved fuel economy by customers has been in general lower than the value declared by the Environmental Protection Agency (EPA) in the United States and Energuide in Canada [93]. This is common to many vehicle types, because

actual driving conditions are different than the idealized conditions in the laboratory testing, such as faster accelerations and higher top speeds. When the THS is employed in heavier vehicles, for example a vehicle that is used for towing applications or one that is used for delivering heavy payloads, this hybrid design is likely not the optimal one because of the inflexibility of this type of power-split architecture. The input-split nature of the design allows for only one node or mechanical point, and as the vehicle loading increases, the power flow through the powertrain may move away from the peak efficiency point; if the engine speed changes, so will the node points. In normal light-duty vehicle operation, the node point occurs at a high enough velocity that the efficiency is not drastically diminished; however, for a commercial vehicle with a full payload, the node point occurs at a lower velocity, resulting in low efficiencies at moderate and high speeds.

The introduction of the multi-mode architecture is an attempt to improve upon the THS design. For example, a two-mode power-split design allows for two input-split, output-split, or compound-split pairs, or any combination of two modes. The key difference between uni- and multi-mode designs is the addition of clutches and/or brakes to create different transmission configurations. This increases the number of possible power flow paths through the transmission and adds nodes to the transmission. The clutches are engaged and disengaged by the ECU that oversees the entire transmission. The ECU uses system information such as component efficiency maps, ESS SOC, road load and driver demand to determine which mode is optimal for the given conditions. The additional modes should, in theory, provide more efficient performance over a wider range of vehicle loads than that achieved by the single-regime designs. The multi-regime architecture will retain the ability to operate as an eCVT: the additional nodes result in more output-to-input speed ratios at which the power is transmitted only via the mechanical path. However, the additional mechanical components will certainly increase both capital and maintenance costs.

A two-mode design can be considered to be a multi-regime architecture; however, multi-regime architectures can take the design concept of the two-mode further and incorporate

other types of hybrid configurations in order to achieve optimal efficiency for as many types of driving conditions and driver demands as possible. Multi-regime designs can have any combination of series, parallel, and power-split configurations. The multiple configurations allow the ECU to select transmission configurations with widely ranging characteristics and advantages in response to the vehicle load. Depending on the design goals, this means that the power management strategy can ensure that the vehicle achieves optimal performance in metrics such as acceleration, towing capacity, or fuel economy. It is this flexibility that is the rationale for the more complex power management strategy and additional components.

## 2.2 General Motors Designs

GM has registered 33 U.S. patents with different designs for multi-regime powertrains, and a description in this document of every patent is infeasible. The initial design that began the two-mode development will first be discussed. A four-mode design will then be examined to illustrate the differences in mode number on design. Subsequently, the two designs that have been commercialized will be examined.

The U.S. patent awarded in 1996 to M. Schmidt and assigned to GM includes eight separate configurations [94], one of which is described below and labelled GM-1. The design in GM-1 is also examined in reference [95]. This patent is particularly important because it represents the introduction of power-split two-mode architecture in the literature.

Before the various designs are considered, a planetary gear will be defined. A planetary gear consists of an internal sun gear (with external teeth), about which one or more planet gears (with external teeth) revolve, surrounded by an external ring gear (with internal teeth). A carrier is fixed to the planet gears at their axes of rotation. A planetary gear with four planets is shown below in Figure 2-5.

The following schematic conventions are applied to all figures in this section. The components of the PSD is denoted by “S”, “C”, and “R” for sun gear, carrier, and ring gear, respectively. The first motor/generator (MG) in the schematic is labelled “MG1” and the second

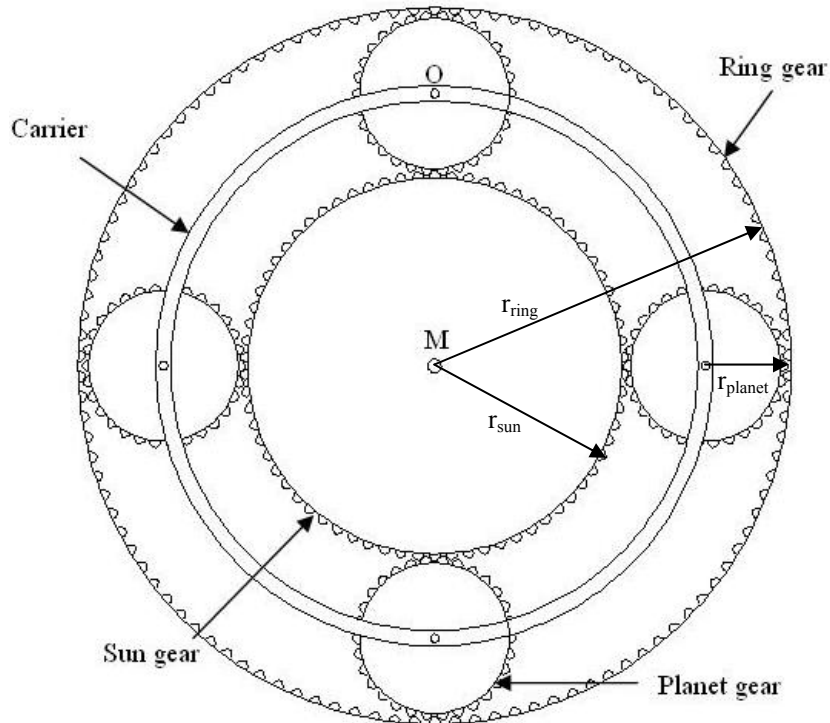


**Figure 2-5. Illustration of a planetary gear**

by “MG2”. The differential and final drive gears are denoted by “FD”; the designs are for vehicles with one set of driven wheels but could easily be modified to accommodate all-wheel drive designs. The power electronics devices such as inverters and mechanical gears are not included for the sake of simplicity.

The first design from the original two-mode power-split patent of 1996 is the primary configuration of the patent, and is of the compound-split type, with two PSDs. The design is labelled GM-1 and shown below in Figure 2-6. The GM-1 architecture contains two planetary gear and three clutches.

The engine is connected via a clutch (CL3) to the first ring gear, and the first ring gear is connected via a clutch (CL1) to the second ring gear and driveshaft; MG1 is mechanically connected to the carrier; MG2 is mechanically connected to the two sun gears which are in turn connected. The operating regimes are shown below in Table 2-3. Some of the subsequent operating regime tables will include descriptions of reverse, parking, and engine starting regimes, in accordance with the available information from the appropriate reference. The description in

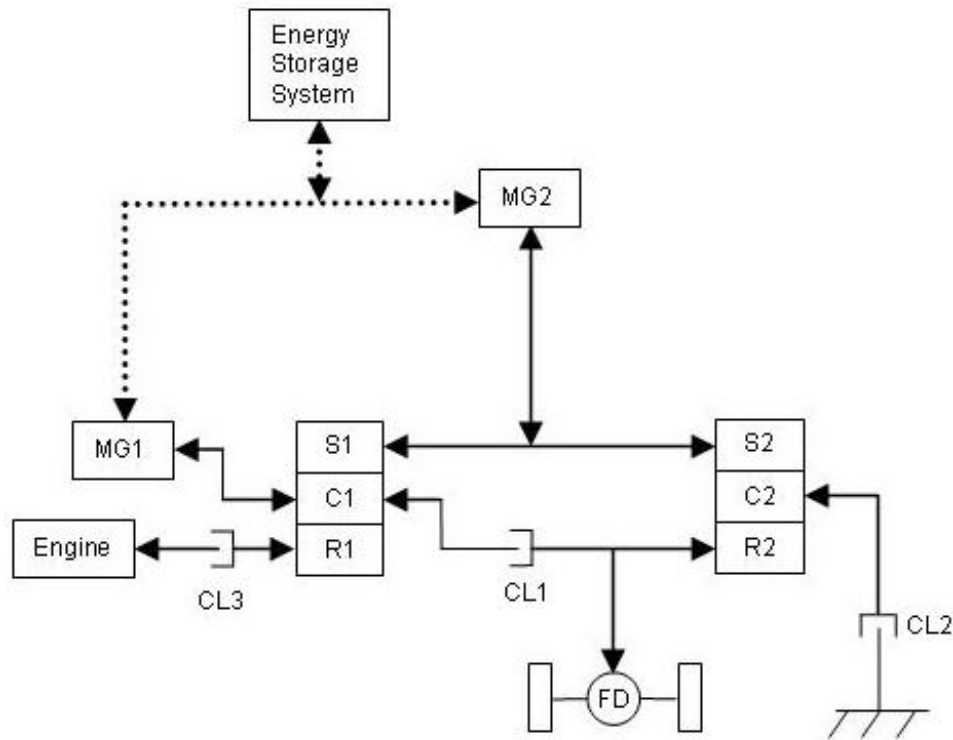


**Figure 2-6. GM-1 architecture**

Source: Adapted from [94], page 3.

the parentheses in the “Regime” column indicates the speed range of the vehicle and in some cases provides the mode of power-split. For all of the configurations, when CL2 is on (and CL1 is off), Mode 1 of the power-split is selected, and when CL1 is on (and CL2 is off), Mode 2 is selected. When both CL1 and CL2 are on, the transmission is transitioning from one mode to the next.

There are two main operating regimes considered in Table 2-3: Forward and Braking. For the forward regime, there are four different sub-operating regimes, each with multiple modes: AER, eCVT, Hybrid, and ESS Charge. The AER regime has two regions that depend on the vehicle velocity, and the engine is always off. The first region is for low speeds, the second region for faster speeds. The eCVT regime has engine power and no power flow to or from the ESS, and occurs when the vehicle load is relatively low. When the vehicle is moving slowly in this regime Mode 1 is chosen; when the vehicle is moving at medium or fast speeds, Mode 2 is selected. The Hybrid regime occurs when significant transmission power is required: the

**Table 2-3. Operating regimes of the GM-1 architecture**

<b>Regime</b>	<b>Electric Machines</b>	<b>CL1</b>	<b>CL2</b>	<b>CL3</b>
<b>Forward:</b>				
AER (slow)	MG1: off; MG2: motor	On	On	Off
AER (fast)	MG1, MG2: motor	On	Off	Off
eCVT (slow)	MG1: generator; MG2: motor	Off	On	On
eCVT (medium)	MG1: motor; MG2: generator	On	Off	On
eCVT (fast)	MG1: generator; MG2: motor	On	Off	On
Hybrid (very slow)	MG1: generator; MG2: motor	Off	On	On
Hybrid (slow)	MG1: motor; MG2: generator	On	Off	On
Hybrid (medium)	MG1, MG2: motor	On	Off	On
Hybrid (fast)	MG1: generator; MG2: motor	On	Off	On
ESS Charge (slow, Mode 1)	MG1: generator; MG2: motor	Off	On	On
ESS Charge (medium, Mode 1)	MG1, MG2: generator	Off	On	On
ESS Charge (slow, Mode 2)	MG1: motor; MG2: generator	On	Off	On
ESS Charge (medium, Mode 2)	MG1, MG2: generator	On	Off	On
ESS Charge (fast, Mode 2)	MG1: generator; MG2: motor	On	Off	On
<b>Braking:</b>				
Regen (slow)	MG1, MG2: generator	On	On	Off
Regen (fast)	MG1: generator; MG2: off	On	Off	Off
Engine lagging (slow)	MG1: motor; MG2: generator	Off	On	On
Engine lagging (medium)	MG1: generator; MG2: off	On	Off	On
Engine lagging (fast)	MG1: motor; MG2: generator	On	Off	On
Regen+Engine lagging (very slow)	MG1: motor; MG2: generator	Off	On	On
Regen+Engine lagging (slow)	MG1: generator; MG2: off	On	Off	On
Regen+Engine lagging (medium)	MG1, MG2: generator	On	Off	On
Regen+Engine lagging (fast)	MG1: motor; MG2: generator	On	Off	On

engine is on and there is power flow from the ESS. At very low speeds, Mode 1 is selected and then Mode 2 is selected as the transition to low speeds is made. Once a medium speed is reached, the configuration returns to Mode 1, until fast speeds are attained, at which point Mode

2 is selected. Finally, the ESS Charge regime occurs when the ESS SOC is low and the engine power is higher than the vehicle load in order to charge the ESS. At very low to medium speeds, Mode 1 is selected. From medium to fast speeds, Mode 2 is chosen.

There are three sub-regimes for the braking regime in Table 2-3. The first sub-regime is regenerative braking (Regen), wherein charging of the ESS occurs. For slow speeds, a combination of Mode 1 and Mode 2 is chosen, while for faster speeds, Mode 2 is selected. The second sub-regime is Engine Lagging, in which the ESS is off, and the braking that is not done by the mechanical brakes is absorbed by the engine. Engine lagging allows the engine to operate at lower speeds, thereby increasing fuel economy. At low speeds in the Engine Lagging sub-regime, Mode 1 is chosen while for medium to fast speeds, Mode 2 is selected. Finally, the Regen+Engine lagging regime is one in which the ESS and engine slow down the vehicle simultaneously. For very slow speeds, Mode 1 is selected, and for slow through medium to fast speeds, Mode 2 is chosen.

The second GM architecture that will be examined is labelled GM-2 and is shown below in Figure 2-7. The design comes from U.S. patent number 5,571,058 [83]. This design is a multi-regime architecture with four power-split modes. There are four PSDs and five clutches, although the fourth PSD is not strictly necessary. GM has named this design an input-split architecture [83]; in this author's view, this characterization is incorrect since the design is compound-split, and the design should be labelled as such.

The engine is connected via CL1 to the first carrier, MG1 is connected to both the second carrier and the third sun gear, and MG1 is connected to the second sun gear and via CL2 to the intermediate shaft. The intermediate shaft is the point where the mechanical power from the first ring gear (when CL4 is engaged), third sun gear (when CL5 is engaged), the third carrier, and the sum of the second sun gear and MG2 is combined. The intermediate shaft delivers power to the fourth ring gear, and this power is split between the wheels and a steer unit that is included since this design was specifically designed for track-driven vehicles; the steer unit regulates the speed of each track and allows the vehicle to pivot and turn [83]. For a wheeled

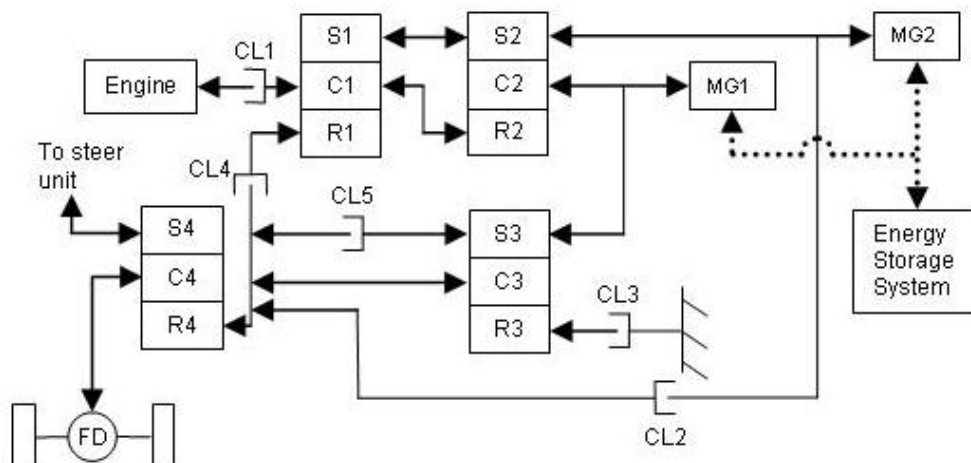


**Figure 2-7. GM-2 architecture**

Source: Adapted from [83], page 1.

vehicle, the intermediate shaft becomes the driveshaft leading to the output gearing and differential. The operating regime table is shown below in Table 2-4 [83].

**Table 2-4. Operating regimes of the GM-2 architecture**

Regime	Electric Machines	CL1	CL2	CL3	CL4	CL5
Forward:						
Mode 1	MG1: generator; MG2: motor	Off/ On	On	Off	Off	Off
Mode 2, slow	MG1: motor; MG2: generator	On	Off	On	Off	Off
Mode 2, medium	MG1, MG2: motors	On	Off	On	Off	Off
Mode 2, fast	MG1: generator; MG2: motor	On	Off	On	Off	Off
Mode 3, slow	MG1: motor; MG2: generator	On	Off	Off	On	Off
Mode 3, medium	MG1, MG2: motors	On	Off	Off	On	Off
Mode 3, fast	MG1: generator; MG2: motor	On	Off	Off	On	Off
Mode 4, slow	MG1: motor; MG2: generator	On	Off	Off	Off	On
Mode 4, medium	MG1, MG2: motors	On	Off	Off	Off	On
Mode 4, fast	MG1: generator; MG2: motor	On	Off	Off	Off	On

As can be seen from Table 2-4, for Modes 2, 3 and 4, there are multiple output speed ranges for each mode. Mode 1 has only one speed range, and is used for starting the vehicle since it provides the highest tractive effort [96].

The design that is employed in the Two-Mode EVT (which stands for electronically variable

transmission), installed in transit buses is shown in Figure 2-8 [97]. The design is also known as the EP40/50. The design comes from patent number 5,931,757 granted to M. Schmidt and assigned to General Motors in 1999 and is a two-mode design. In this design, the first PSD causes the first power split, providing the input-split regime, while the second PSD adds a second power split, resulting in the architecture forming a compound-split configuration. The third PSD acts as a torque multiplier to the driveshaft [97]. The engine is connected to the first ring gear, and can be connected via a clutch (not shown) if desired. The first and second carriers are connected to the main transmission shaft. The second ring gear is connected to MG1 and the first sun gear. MG2 is connected to both the second and third sun gears, which are in turn connected. The main transmission shaft is connected via clutch CL2 to the third carrier and to the wheels. The third ring gear is connected via clutch CL1 to a fixed member.

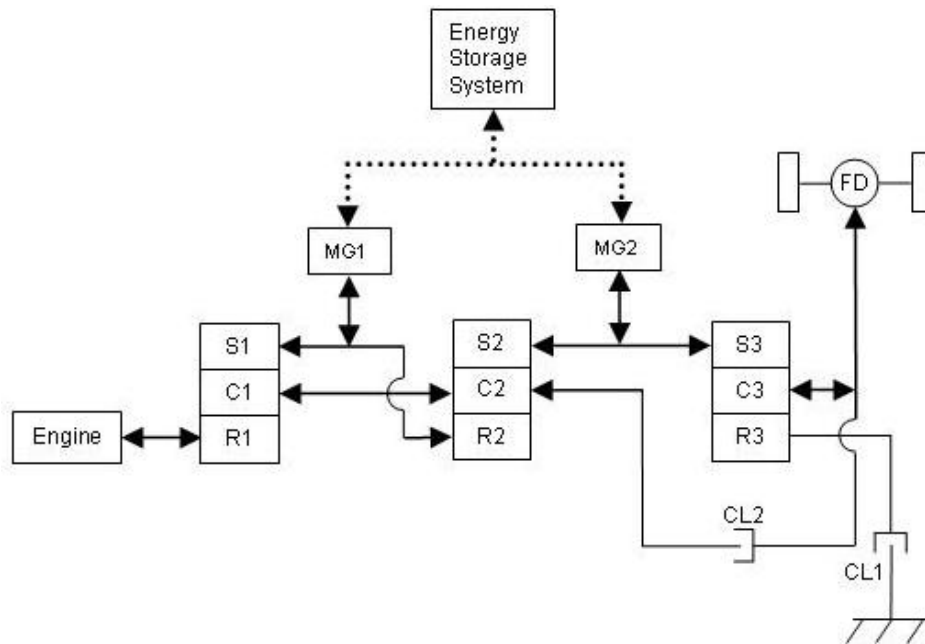


**Figure 2-8. Two-Mode EVT architecture**

Source: Adapted from [97], page 1.

The modes of operation are controlled by the control system and the clutches. In the first mode, CL1 is engaged, locking the third ring gear, and CL2 is disengaged, meaning that the main transmission shaft is disconnected from the wheels. MG2 operates as a motor throughout the

first mode and increases its speed of rotation, while MG1 operates as a generator while decreasing its speed of rotation. At the node point, the speed of MG1 is zero, and it switches its operation to motor mode. Also at the node point, CL1 is disengaged, allowing the third ring gear to rotate freely, while CL2 is engaged, connecting the main transmission shaft to the wheels. MG1 initially switches to generator operation at the beginning of the second mode, before reverting to motor operation early on as the vehicle velocity increases, and continues to operate as a motor throughout the rest of the second mode. MG2 continues to act as a motor at the beginning of the second mode, while switching to generator operation after the switch by MG1, and continuing to operate as generator throughout the rest of the second mode. The operation regimes are summarized below in Table 2-5. It is unclear whether an AER is included: similar to the THS design, the transmission may operate in the AER up to a certain speed above which the ring gear must spin. At this speed, the engine will begin to turn and the AER will end.

**Table 2-5. Operating regimes of the Two-Mode EVT architecture**

<b>Regime</b>	<b>Electric Machines</b>	<b>CL1</b>	<b>CL2</b>
<b>Forward:</b>			
AER <sup>†</sup>	MG1: off/motor MG2: motor	On	Off
Mode 1, slow	MG1: generator MG2: motor	On	Off
Mode 1, fast	MG1, MG2: motors	On	Off
Mode 2, slow	MG1: generator MG2: motor	Off	On
Mode 2, medium	MG1, MG2: motors	Off	On
Mode 2, fast	MG1: motor MG2: generator	Off	On

<sup>†</sup> may not be present in the power management strategy

In order to transfer the design to LDVs, the design was modified to include four fixed-gear ratios. Without these ratios, the design have suffered from either an enlarged transmission or a reduced capacity for towing; indeed, a typical SUV is often used to tow a load that is greater in

weight than the vehicle itself [98]. The resultant patent associated with the LDV designs, such as the 2008 Chevrolet Tahoe hybrid, is U.S. patent number 6,953,409 B2 awarded to M. Schmidt [98]. This design is known as the Two-Mode Hybrid, and is shown below in Figure 2-9. In this author's opinion, this is a misnomer because it fails to describe the parallel operating regime capabilities. The architecture is also known as the Allison Hybrid System-2 (AHS2). This hybrid powertrain may also be installed in hybrid versions of the GMC Yukon from GM, and Dodge Durango and Chrysler Aspen SUVs from Chrysler. The ICE for the Two-mode Hybrid of the Tahoe is a Vortec 6.0 L V8, the ESS is a 300 V NiMH battery pack and the two MGs are PM 60 kW [99]. The hybrid transmission is designed to fit within the same volume as a conventional powertrain. A slight difference between the design shown in the figure and the schematic of the patent is the connection of clutch CL4: in the patent, CL4 is connected to the second carrier, while in the figure the clutch is connected to the second ring gear. In either case, activation of CL4 will lock the first two planetary gears, and all components will have the same angular speed about the PSD center (and the planet gears will not rotate.)

The Two-Mode Hybrid design allows for four fixed gear ratios in addition to the two possible power-split modes. This combination means that the design is a multi-regime design and is not limited to the two power-split modes as the name suggests. As can be seen from comparing Figure 2-8 and Figure 2-9, the only difference between the Two-mode EVT and the Two-Mode Hybrid architectures are the two additional clutches in the latter, CL3 and CL4. These two clutches provide the four fixed gear ratios that allow the transmission to operate in parallel mode.

The power-split modes of the Two-Mode Hybrid are identical to that of the Two-mode EVT with regards to CL1 and CL2. The operating regimes are shown below in Table 2-6 [96]. It should be noted that the 1<sup>st</sup> and 2<sup>nd</sup> fixed gear ratio regimes can occur at any point within the first power-split mode and the 3<sup>rd</sup> and 4<sup>th</sup> gear ratios can likewise occur at any point within the second power-split mode. The activation of the fixed gear ratios will depend on the power demanded by the driver. For example, if the vehicle is stationary, and maximum acceleration is demanded,

the 1st fixed gear ratio can be chosen for maximum efficiency. The architecture allows for three nodes (one in Mode 1, two in Mode 2) along with the fixed gear ratios for a wide-ranging level of high efficiency.

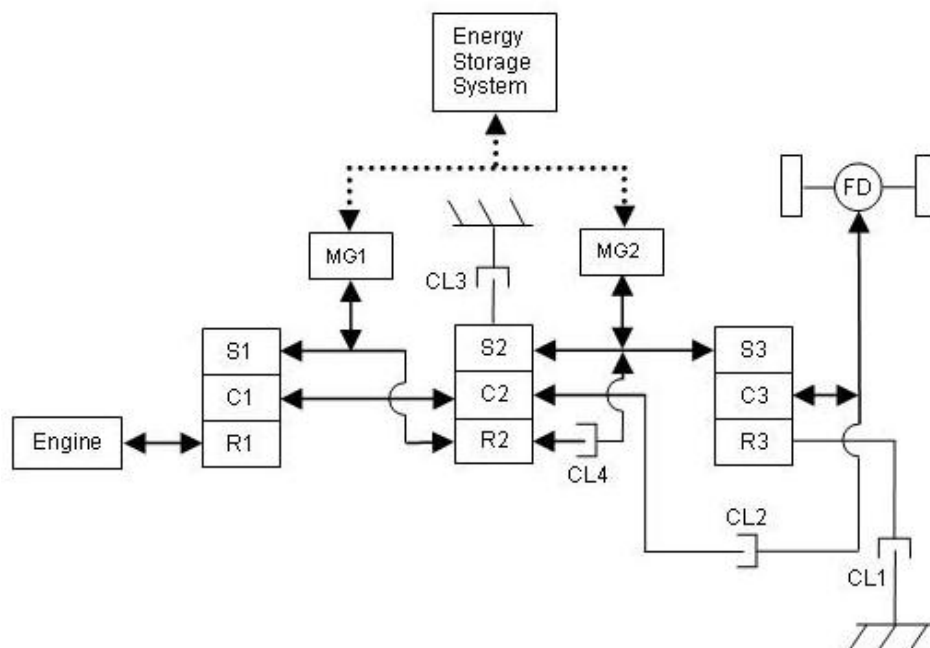


**Figure 2-9. Two-Mode Hybrid architecture**

Source: Adapted from [96], page 5.

**Table 2-6. Operating regimes of the Two-Mode Hybrid architecture**

Regime	Electric Machines	CL1	CL2	CL3	CL4
<b>Forward:</b>					
AER <sup>†</sup>	MG1: off; MG2: motor	On	Off	Off	Off
Power-split 1, slow	MG1: generator; MG2: motor	On	Off	Off	Off
Fixed 1	MG1, MG2: off/motors	On	Off	Off	On
Power-split 1, medium	MG1, MG2: motors	On	Off	Off	Off
Fixed 2	MG1, MG2: off/motors	On	On	Off	Off
Power-split 2, slow	MG1, MG2: motors	Off	On	Off	Off
Fixed 3	MG1, MG2: off/motors	Off	On	Off	On
Power-split 2, medium	MG1: generator; MG2: motor	Off	On	Off	Off
Fixed 4	MG1, MG2: off/motors	Off	On	On	Off

<sup>†</sup> may not be present in the power management strategy

## 2.3 Renault Design

The Renault IVT design differs from the GM designs in that dog clutches are used to achieve the two power-split modes. The schematic for the IVT is shown below in Figure 2-10. At present, no plans to manufacture any vehicle with the IVT powertrain by Renault have been uncovered.

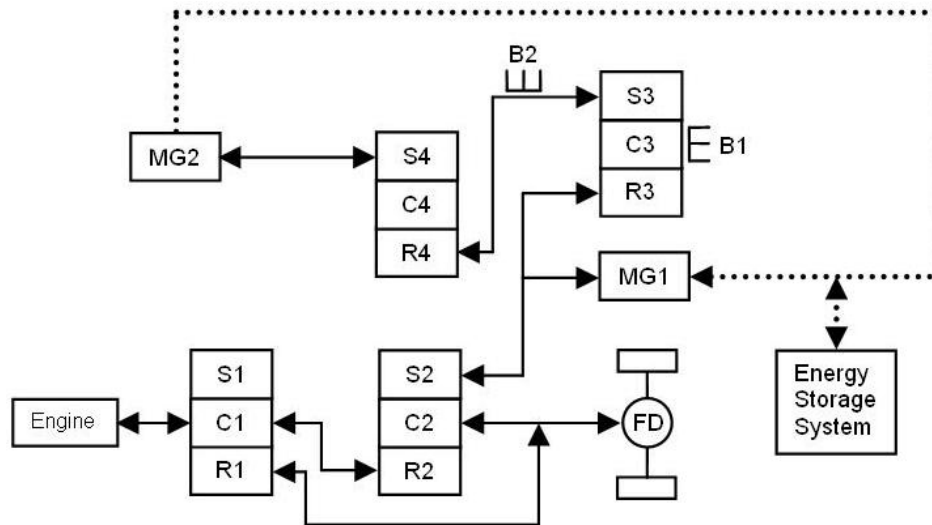


**Figure 2-10. Renault IVT architecture**

Source: Adapted from [87], page 5.

The IVT has four planetary gears and two dog clutches (a type of brake); the first and second pair of planetary gears is compounded. The engine is connected to the first carrier; MG1 is connected to the second sun gear and third ring gear; MG2 is connected to the fourth sun gear. The driveshaft is connected to the first ring gear and second carrier. The first brake can selectively lock the third carrier while the second brake can selectively lock the third sun gear and fourth ring gear. The operating regimes are shown below in Table 2-7.

In the low mode, MG1 initially operates as a motor and MG2 as a generator. The operations then switch as the vehicular velocity increases such that MG1 operates as a generator and MG2 as motor for the rest of the mode. Brake B2 rotates freely in this regime, while brake B1 is on.

**Table 2-7. Operating regimes of the Renault architecture**

<b>Mode</b>	<b>Electric Machines</b>	<b>B1</b>	<b>B2</b>
<b>Forward:</b>			
AER, low power <sup>†</sup>	MG1: motor; MG2: off	Off	On
AER, high power <sup>†</sup>	MG1, MG2: motors	Off	Off
Power-split 1, slow	MG1: motor; MG2: generator	On	Off
Power-split 1, fast	MG1: generator; MG2: motor	On	Off
Conventional <sup>†</sup>	MG1, MG2: off	On	On
Power-split 2	MG1: motor; MG2: generator	On	Off

<sup>†</sup>may not be present in the power management strategy

The transition to the high mode occurs when the speed of both electric machines is zero, therefore at zero electric variator power. At the transition point, B2 is activated and B1 is de-activated and allowed to spin freely. MG1 operates as a motor and MG2 as a generator for the duration of the mode. The architecture allows for two node points, one in each mode.

The architecture also has the capability of operating in AER and conventional regimes. Neither possibility is mentioned in reference [87], but could be implemented in the power management strategy. These additions could help improve the transmission efficiency over a wider range of vehicular velocities.

## 2.4 Timken Design

The Timken eCVT differs from the other multi-regime designs by including two types of mechanical torque transfer devices: clutches and brakes. The schematic for the eCVT is shown below in Figure 2-11. No production plans for the Timken eCVT have been found anywhere in the literature or the automotive industry news publications. The Timken Company conference paper designates the low-mode operation of this architecture as output-split [86], but an examination of the design reveals that it is in fact no different from the THS one-mode power-split architecture, or from the low-mode of GM-1, and so it should be designated as input-split as well.

The eCVT contains two planetary gears, two clutches, and two brakes. The brakes again

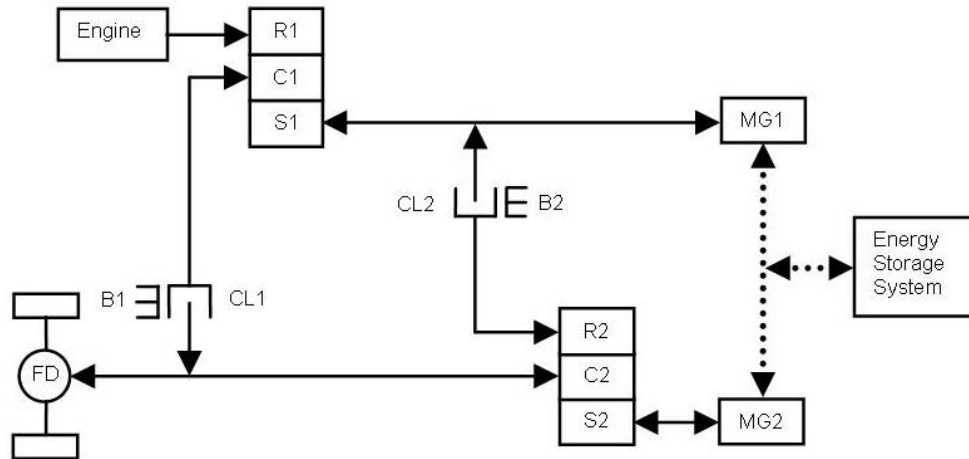


**Figure 2-11. Timken eCVT architecture**

Source: Adapted from [86], page 30.

selectively connect a shaft to a fixed member. The engine is connected to the first ring gear; MG1 is connected to the first sun gear and via a clutch (CL2) to the second ring gear; MG2 is connected to the second sun gear. The first carrier is connected via a clutch (CL1) to the driveshaft; the second carrier is directly connected to the driveshaft. The operating regimes are summarized below in Table 2-8.

For the forward sub-regime, there are five different operations. There is AER (low power), AER (high power), three power-split modes and a series regime. The high power AER regime can only occur if the speed is not too large, since at high speeds of the first sun gear and carrier, the ring gear (and engine) will begin to rotate. The power-split regimes allow for two node points, one in the low mode and one in high mode. A series regime is possible, but reference [100] does not mention this capability.

**Table 2-8. Operating regimes of the Timken architecture**

Source: Adapted from [86], page 33.

<b>Regime</b>	<b>Electric Machines</b>	<b>CL1</b>	<b>B1</b>	<b>CL2</b>	<b>B2</b>
<b>Forward:</b>					
AER, low power	MG1:off; MG2: motor	Off	Off	Off	On
AER, high power	MG1, MG2: motors	Off	Off	On	Off
Power-split 1	MG1: generator; MG2: motor	On	Off	Off	On
Power-split 2, slow	MG1: motor; MG2: generator	Off	On	Off	Off
Power-split 2, fast	MG1: generator; MG2: motor	Off	On	Off	Off
Series <sup>†</sup>	MG1, MG2: motors	Off	On	Off	On
<b>Reverse:</b>					
Reverse (series)	MG1: generator; MG2: motor	Off	On	Off	On
Reverse (power-split)	MG1: generator; MG2: motor	On	Off	Off	On
<b>Stationary:</b>					
Parking (engine off)	MG1, MG2: off	On	On	On	On
Parking (engine on)	MG1: generator; MG2: off/generator	On	On	Off	On/Off
Neutral	MG1, MG2: off	Off	Off	Off	Off
<b>Starting:</b>					
Vehicle stationary	MG1: off; MG2: motor	On	Off	On	On
Vehicle in motion	MG1: motor; MG2: off	Off	On	Off	Off

<sup>†</sup> may not be present in the power management strategy

## 2.5 Silvatech Design

The Silvatech multi-regime design schematic is depicted below in Figure 2-12. At present, no plans to manufacture any vehicle with the powertrain designed by Silvatech, known as the Electro-Mechanical Continuously Variable Transmission (EMCVT), have been uncovered.

The engine is directly connected to the carrier and also via CL1 to the sun gear, via CL2 to a fixed member, and CL3 to MG1. MG1 is connected via CL4 to MG2, and MG2 is directly connected to the driveshaft. The ring gear is connected via CL5 to the driveshaft. The operating regimes are listed below in Table 2-9.

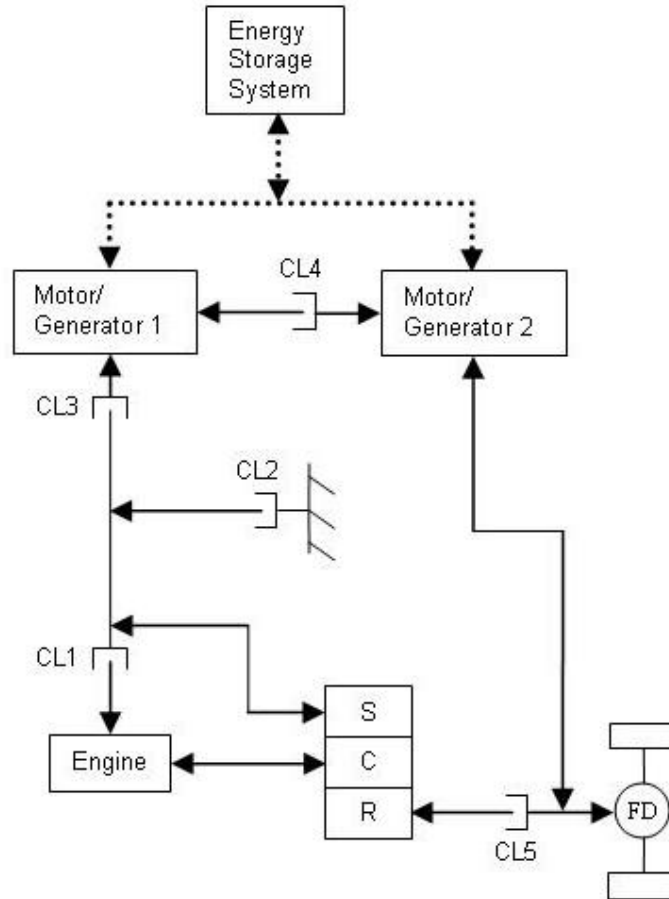


**Figure 2-12. Silvatech EMCVT architecture**

Source: Adapted from [100], page 2.

There are six regimes in the Forward regime: AER (economy), AER (full), Series, Parallel, eCVT, and Conventional. The Series operation is not mentioned in reference [100] as a capability of the architecture. There are three types of Reverse: Reverse AER (economy), Reverse AER (full), and Series. A Parallel regime is also mentioned for reverse operation, but the architecture does not support the regime in the method described: the engine direction is not transformed into the opposite direction by any gearing, and so it cannot cause reverse motion. For the Braking operation, Light Regen., Max. Regen., Parallel, and Engine lagging are available. Reference [80] has CL3 engaged for Max. Regen, but this is not necessary. The Parallel reverse regime has both ESS charging and engine braking. Finally, the Engine starting operation has two regimes: Vehicle stationary and Vehicle in motion whose use should be obvious.

**Table 2-9. Operating regimes of the Silvatech architecture**

Source: Adapted from [100], page 9.

<b>Regime</b>	<b>Electric Machines</b>	<b>CL1</b>	<b>CL2</b>	<b>CL3</b>	<b>CL4</b>	<b>CL5</b>
<b>Forward:</b>						
Economy Electrical	MG1: off; MG2: motor	Off	Off	Off	Off	Off
Full Electrical	MG1, MG2: motor	Off	Off	Off	On	Off
Series <sup>†</sup>	MG1: generator; MG2: motor	On	Off	On	Off	Off
Parallel	MG1, MG2: motors	On	Off	Off	On	On
EMCVT	MG1: generator; MG2: motor	Off	Off	On	Off	On
Conventional	MG1, MG2: off	Off	On	On	Off	On
<b>Reverse:</b>						
AER (economy)	MG1: off; MG2: motor (in reverse)	Off	Off	Off	Off	Off
AER (full)	MG1, MG2: motors (in reverse)	Off	Off	Off	On	Off
Series <sup>†</sup>	MG1: generator; MG2: motor (in reverse)	On	Off	On	Off	Off
<b>Braking:</b>						
Light regen. (light braking)	MG1: off; MG2: generator	Off	Off	Off	Off	Off
Max. regen. (heavy braking)	MG1, MG2: generators	Off	Off	Off	On	Off
Parallel	MG1: off; MG2: generator	Off	Off	Off	Off	On
Engine lagging	MG1: motor; MG2: generator	Off	Off	On	Off	On
<b>Engine starting:</b>						
Vehicle stationary	MG1: motor, MG2: off	On	Off	On	Off	Off
Vehicle in motion	MG1: motor; MG2: generator	On	Off	On	Off	Off

<sup>†</sup> may not be present in the power management strategy

## 2.6 University of Michigan-Dearborn Design

Researchers at the University of Michigan-Dearborn (UMD) recently introduced a novel multi-regime design. The architecture allows for parallel and power-split regimes. A schematic of the design is depicted below in Figure 2-13.

The engine is directly connected to the carrier and the solitary MG is alternatively connected to either the sun gear or the output shaft via CL4. The schematic is modified from that of reference [80] in that the ring gear is connected to the driveshaft via a clutch (CL3) instead of

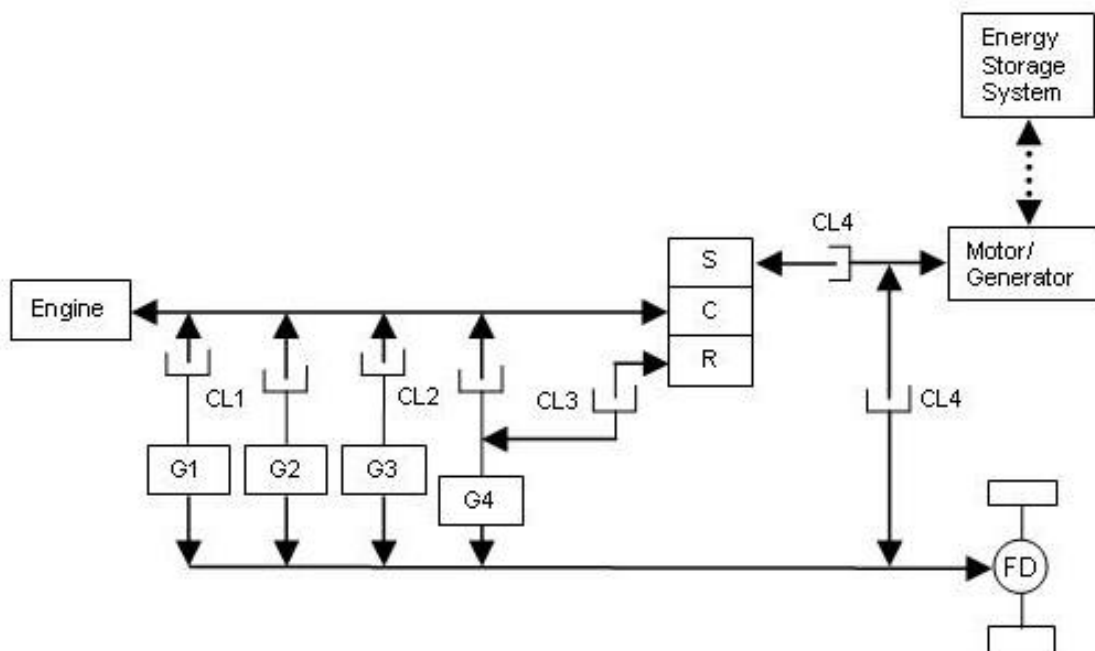


**Figure 2-13. University of Michigan-Dearborn architecture**

Source: Adapted from [80], page 80.

directly connected. It is this author's belief that the design intent was that when the fourth gear (G4) is chosen that all of the engine power passes through the gear and none through the PSD. In the diagram of the reference, the power from the engine is split between the direct gear path and the PSD and then recombined at the gear input; this mini-power loop involves the PSD unnecessarily, and will decrease efficiency because of the inertias of the extraneous mechanical components. Note also that for clarity two separate clutches are drawn and labelled CL1, CL2 and CL4. These clutches are shifters that can engage one or the other of the gear pair or one or the other of the PSD and driveshaft, respectively. The gears G1 through G4 are also shown in the schematic to illustrate the differences between the fixed gear paths. The summary of operating regimes is presented below in Table 2-10.

There are three regimes of which the architecture is capable. In the Forward regime, AER, four Parallel, four Conventional, four Charging, and an eCVT operation are possible. In the AER, CL4 engages and the MG is directly connected to the driveshaft. For Parallel operation, CL4 connects the MG to the driveshaft, and the engine power is directed to the driveshaft

Table 2-10. Operating regimes of University of Michigan-Dearborn architecture

Regime	Electric Machines	CL1	CL2	CL3	CL4
<b>Forward:</b>					
AER	MG: motor	Off	Off	Off	On: drive-shaft
Parallel 1	MG: motor	On:G1	Off	Off	On: drive-shaft
Parallel 2	MG: motor	On:G2	Off	Off	On: drive-shaft
Parallel 3	MG: motor	Off	On:G3	Off	On: drive-shaft
Parallel 4	MG: motor	Off	On:G4	Off	On: drive-shaft
Conventional 1	MG: off	On:G1	Off	Off	Off
Conventional 2	MG: off	On:G2	Off	Off	Off
Conventional 3	MG: off	Off	On:G3	Off	Off
Conventional 4	MG: off	Off	On:G4	Off	Off
Charge 1	MG: generator	On:G1	Off	Off	On: sun
Charge 2	MG: generator	On:G2	Off	Off	On: sun
Charge 3	MG: generator	Off	On:G3	Off	On: sun
Charge 4	MG: generator	Off	On:G4	Off	On: sun
eCVT	MG: generator	Off	Off	On	On: sun
<b>Braking:</b>					
Regen	MG: generator	Off	Off	Off	On: drive-shaft

through any of the four gears. For Conventional operation, CL4 is disengaged, while in Charge operation, CL4 connected the MG to the sun gear and the MG operates as a generator to charge the ESS. Finally, the eCVT operation involves CL4 again connected the MG to the sun gear so that some of the engine power can charge the ESS; the rest of the engine power is directed to the driveshaft. This configuration allows for the engine speed to be decoupled from the driveshaft speed as long as the ESS can continue to accept power.

## **Chapter 3 Multi-Regime Powertrain Architecture Modelling**

A multi-regime architecture that incorporates multiple capabilities such as parallel and power-split operation is more adaptable to a wide range of vehicle types and applications. It is this flexibility that has convinced many automotive industry analysts that the multi-regime architecture will surpass Toyota's THS design as the dominant hybrid powertrain. That GM has licensed the transmission design patents to Daimler AG, Chrysler, and BMW and the automotive companies are now collaborating using these patents as a base indicates that the management of these companies also believes that multi-regime powertrain architectures are promising. The dynamic model that has been chosen as a representative example of the multi-regime architecture is presented here and the modelling results from the research study are discussed.

### **3.1 Previous Multi-regime Powertrain Architecture Modelling**

Multi-regime architectures have only recently been discussed in the literature. The patents and academic articles reviewed during the research for this portion of the dissertation are discussed below. A series of papers and presentations [58, 85, 101] and a section of a book [40] by Miller serve as valuable reviews of the current state of the two-mode designs by GM, The Timken Company and Renault.

It should be noted that an inaccurate statement is made in the PSD modelling of the papers by Miller, wherein it is stated that the torque ratios amongst the PSD components are fixed and not dependent upon the rotation of the gears. This is a common misconception, and can be found in several papers that model powertrain architectures with PSDs; for example, references [80, 102-104] present three equations that show simple relationships between the gear torques that depend only on the gear ratios. As will be discussed in Section 3.2.1, this relationship is only valid in an artificial case and assumptions must be made that do not reflect the actual gear mechanism. In order to derive the true equations for the relationship between the input and output torques of the PSD, a dynamic analysis must be undertaken. Examples of this approach

found in the literature were done by [89] for the THS and by [95] and [105] for GM two-mode and one- and three-mode designs, respectively.

Information on the designs of GM, The Timken Company, and Silvatech can be obtained from the relevant U.S. patent documents. The team led by Schmidt has been granted 12 patents on multi-regime architecture alone (all assigned to GM), beginning in 1996 with four patents [83, 94, 106, 107] and most recently adding three more in 2007 [108-110]. The designs of The Timken Company design are introduced in U.S. patent number 6,595,884 [111] and developed further in U.S. patent number 6,964,627 B2 [112], and that of Silvatech in U.S. patent number 7,008,342 [100]. GM [95, 105], Renault [87], and The Timken Company [86] have each published academic articles discussing their designs, although in the GM case, only a small selection from a large number of designs is examined. The researchers from the University of Michigan-Dearborn also published a recent article describing their multi-regime design [80].

In the GM articles, dynamic analyses using Kane's method were performed on two-mode and one- and three-mode architectures, respectively. These articles did not explicitly compare the performances of the designs to any baseline conventional vehicle or any other hybrid design. In reference [95], a model for evaluating the two-mode design found in patent number 5,558,588 [94], designated here as GM-1, was introduced. However, only normalized results of the engine, battery and EMs were published. Furthermore, the analysis was confined to simulations of the transmission output power capacity at the optimal brake-specific fuel consumption (BSFC) curve of the engine and the maximum power output of the EMs; performance of a fully modelled vehicle undergoing a drive cycle was not executed. The same limitations apply to reference [105], in which the one- and three-mode transmission architectures of patents 5,558,595 [113] and 5,730,676 [114], respectively, were presented. There was neither quantitative nor even qualitative analysis of the improved performance of the three-mode design over the one-mode.

The Timken Company academic paper [86] provides a summary of CVTs, both mechanical and electronic, and of power-split types. The paper also presents the results of simulations

conducted in the EASY5 environment developed by The Boeing Company and augmented by powertrain components developed by Ricardo Inc. While the paper includes a description of the design, a detailed presentation of the model used in the simulation is not added.

The Renault academic paper [87] describes the differences in transmission operation of a one-mode power-split versus a two-mode design and also describes the power management strategy algorithm of the latter model. Forward motion regimes are explicitly examined, but little mention is made of any other operating regime such as reverse or neutral gearing.

The paper by the researchers at the University of Michigan-Dearborn [80] provides an overview of the physical design and a more detailed explanation of the power management strategy. Simulation of the model takes place in ADVISOR. The model is compared against the first-generation THS model that is included with the ADVISOR software. It should be noted that both models have the same error mentioned previously about fixed torque ratio at the PSD.

Furthermore, to the author's knowledge, the models in the aforementioned papers, and indeed most others in the genre, do not account for the effects on fuel economy of transients in engine operation. Large engine transients have a compromising effect on fuel economy, and a model that incorporates a penalty in fuel economy for large transients is left for future work.

### **3.2 Study Multi-Regime Powertrain Architecture Model**

The powertrain design chosen for the study is shown below in Figure 3-1. The design is from patent number 6,478,705 that was granted in 2002 to A. Holmes *et al.* and assigned to General Motors [115]. The study powertrain design was chosen because it appeared in the scientific literature in addition to the patent. The selection was also made before the commercialized design details of the Two-mode Hybrid architecture installed in hybrid versions of the 2008 Chevrolet Tahoe and GMC Yukon (and potentially Dodge Durango and Chrysler Aspen) models had been released; subsequent studies will use this architecture.

The architecture contains two PSDs, three clutches and two electric machines. The

PSDs are denoted as before by the “S”, “C”, and “R” labels for the sun gear, carrier, and ring gear, respectively. In the design, the engine is connected via a clutch (CL3) to the first ring gear (R1); the first motor/generator (MG1) is directly connected to the first sun gear (S1) and also via a counter shaft and a clutch (CL2) to the second ring gear (R2); the first (C1) and second (C2) carriers are directly connected to the driveshaft; R2 is connected to a fixed member via a clutch (CL1); the second motor/generator (MG2) is connected to the second sun gear (S2).

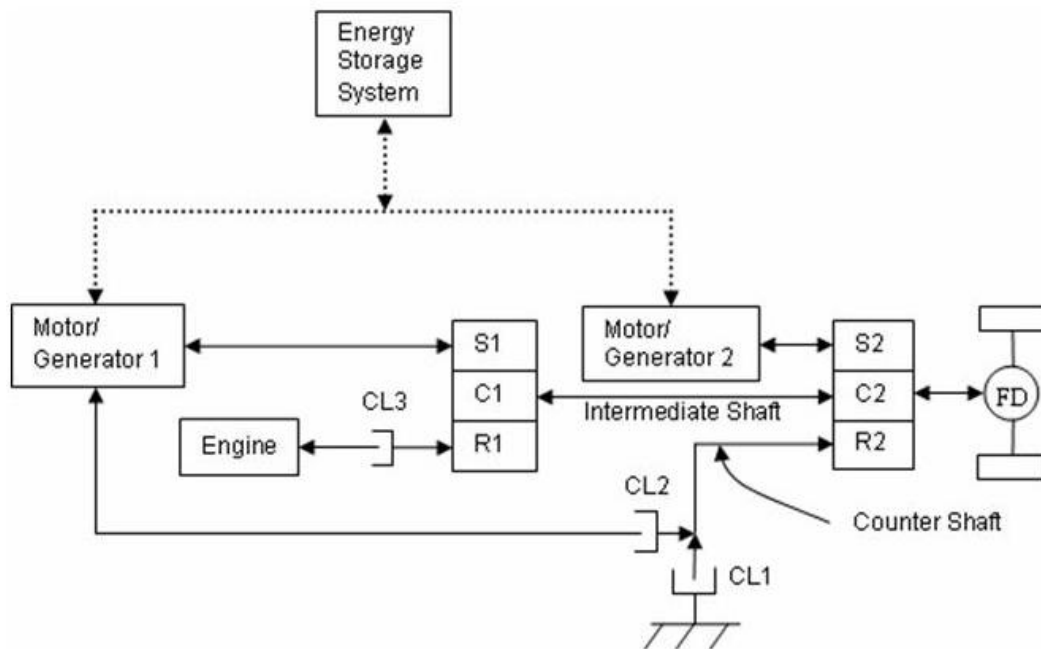


**Figure 3-1. Architecture of the study multi-regime powertrain**

Source: Adapted from [115], page 1.

The three-regime study powertrain architecture is capable of operating as an EV or in one of two power-split modes. The AER made possible by the EV configuration is confined by the ECU to low speeds and powers so that the ESS is not drained deleteriously. AER is almost exclusively used for vehicle launch. EV operation is enabled by disengaging CL3 and having the ESS send power to MG2, which in turn powers the wheels. Both the engine and MG1 are off.

For power-split operation, CL3 is engaged along with one of the other two clutches. The engine is also started and begins to provide power. The two power-split modes cover two

conditions: low and high speed. The low-speed mode is enabled by engaging CL1 and disengaging CL2. This action disconnects MG1 from the second PSD, locks R2 to a fixed member, and results in an input-split configuration. This mode is used between the low-speed requirements that can be satisfied by the AER and the high-speed requirements satisfied by the high-speed mode. The road load and driver demand will dictate the power level of the powertrain and thus the speeds at which the regimes change will vary. It should be noted that in low mode the schematic is nearly identical to the Toyota Prius THS design. The two differences between the designs are the connection of the engine to the ring gear in the former and the type of output gearing present: the GM design uses a PSD with the ring gear fixed and the THS uses a conventional geartrain. The low-speed mode has one node, which occurs at the point of transition to the high-speed mode.

The high-speed mode is enabled at the first node, at a velocity denoted by  $V_{\text{shift}}$ , by disengaging CL1 and engaging CL2. This action, known as a mechanical point, connects MG1 to R2 and results in a compound-split configuration. This mode has two nodes, the first being the one shared with the low-speed mode and a second mode, denoted by  $V_{S3}$ , at a higher output-to-input speed ratio. The additional node provides more efficient operation at higher speeds. The various operating regimes are summarized below in Table 3-1. It should be noted that only regimes in which there is forward vehicle motion are shown, although reverse regimes are also possible. An ESS-charging regime in which there is no forward movement is achievable by applying the mechanical brakes to prevent any forward motion. Two other important velocities in the second mode are denoted by  $V_{S2}$  and  $V_{S4}$ .  $V_{S2}$  is the velocity above the first node at which MG2 begins to operate as a generator.  $V_{S4}$  is the velocity above the second node past which both EMs operate as motors. The locations of these two velocities will depend on the battery SOC; if the battery SOC remains sufficiently high, both EMs can operate as motors throughout the second mode for additional power.

The model equations are presented in detail in the following sections. The mechanical path to the wheels will be considered first, followed by the electric variator path. Finally, the power

Table 3-1. ICEHV study model operating regimes

Regime	Electric Machines	CL1	CL2	CL3
<b>Forward:</b>				
<b>AER</b>	<b>MG1: off/motor, MG2: motor</b>	<b>On</b>	<b>Off</b>	<b>Off</b>
<b>Low-speed mode, <math>V &lt; V_{\text{shift}}</math></b>	<b>MG1: generator, MG2: motor</b>	<b>On</b>	<b>Off</b>	<b>On</b>
<b>High-speed mode, <math>V_{\text{shift}} &lt; V &lt; V_{S2}</math></b>	<b>MG1: motor, MG2: motor</b>	<b>Off</b>	<b>On</b>	<b>On</b>
<b>High-speed mode, <math>V_{S2} &lt; V &lt; V_{S3}</math></b>	<b>MG1: motor, MG2: generator</b>	<b>Off</b>	<b>On</b>	<b>On</b>
<b>High-speed mode, <math>V_{S3} &lt; V &lt; V_{S4}</math></b>	<b>MG1: generator, MG2: motor</b>	<b>Off</b>	<b>On</b>	<b>On</b>
<b>High-speed mode, <math>V_{S4} &lt; V</math></b>	<b>MG1: motor, MG2: motor</b>	<b>Off</b>	<b>On</b>	<b>On</b>
<b>Braking:</b>				
<b>Regenerative</b>	<b>MG1: off MG2: generator</b>	<b>On/Off</b>	<b>On/Off</b>	<b>On/Off</b>
<b>Engine lagging</b>	<b>MG1: motor, MG2: generator</b>	<b>On/Off</b>	<b>On/Off</b>	<b>On/Off</b>
<b>Regen+Engine lagging</b>	<b>MG1: motor, MG2: generator</b>	<b>On/Off</b>	<b>On/Off</b>	<b>On/Off</b>

management strategy of the ECU is discussed.

### 3.2.1 Mechanical path

The mechanical path from engine to wheels will first be considered. The first step in understanding the power-split architecture model is to determine the mechanics of the PSDs. As will be shown, a dynamic analysis is necessary to properly describe the mechanical system. The generalized PSD will be analyzed first.

The angular speed relationship between the sun, ring and carriers of any PSD can be obtained from a simple consideration of the gear ratios between the gears, and is given by

$$\omega_{\text{sun}} + k\omega_{\text{ring}} = (k+1)\omega_{\text{carrier}} \quad (3.1)$$

where  $k$  is the planetary gear ratio that is governed by the following relationship between the

radii of the ring and sun gears:

$$k = \frac{r_{ring}}{r_{sun}} \quad (3.2)$$

For the first PSD in the study model, Equation (3.1) becomes

$$\omega_{S1} + k_1 \omega_{R1} = (k_1 + 1) \omega_{C1} \quad (3.3)$$

where the value for  $k_1$  was assumed to be 2.6; this is the value for the second-generation Toyota Prius THS system; and  $\omega_{S1}$ ,  $\omega_{R1}$ , and  $\omega_{C1}$  are the angular speeds of the first sun gear, ring gear and carrier.

The relationship for the torques on the various PSD gears is not as simple. Several papers in the literature have used a static analysis to conclude that the torque relations are constant for all speeds. The results of the static analysis are three equations that show simple relationships between the gear torques that depend only on the gear ratio:

$$T_{sun} = -\frac{1}{k+1} T_{carrier} \quad (3.4)$$

$$T_{ring} = -\frac{k}{k+1} T_{carrier} \quad (3.5)$$

$$T_{sun} = \frac{1}{k} T_{ring} \quad (3.6)$$

Dynamic analysis of a PSD shows that these torque relations are valid only for artificial, kinetostatic conditions, i.e. one of the shafts is fixed, or if the sun gear, ring gear, and carrier rotate at equal angular velocities and the planets do not rotate about the gear center at all. In this situation, no torque is transferred between the gears, and so all torques are zero. These fixed torque relations apply also if the resistance torque in the gears is neglected and there is either no angular acceleration of the gear components or the moments of inertia are negligible. The simplifications of neglected rotational resistance, angular acceleration, and moments of inertia distort the physical phenomena of the system. It is therefore necessary to derive the true dynamic equations for the relationship between the input and output torques of the PSD, as was done in the previously mentioned studies in references [95, 105].

The derivation of the dynamics of the PSD can be determined through either Kane's

equations or free-body analysis and the equation of rotational motion, derived from Newton's 2<sup>nd</sup> Law. The latter method is chosen so that the forces and torques at each rotating component can be seen explicitly.

The engine can only rotate in the positive direction. When moving forward, the driveshaft and axle also rotate in the positive direction. In the following analysis, all gears are assumed to be perfect cylinders with no slip between meshing gears. The forces between meshing gears are assumed to be tangential, as the normal components cancel out throughout all contact points of the meshing gears. Also, no Coriolis effects or clearance among gears are considered. Friction torques in the bearings of rotating members can be modelled to include both damping and frictional effects. The quadratic function for the friction torque of component  $i$  can be modelled as [89]:

$$T_{i-friction} = A\omega_i^2 + B\omega_i + C \quad (3.7)$$

However, in order to use Equation (3.7), experimental values for the coefficients  $A$ ,  $B$ , and  $C$  must be used. In the absence of this data, all friction torques for the current study will assume a negligible value but will be included in the formulaic derivation for completeness. This will bias the simulation results to a slightly more optimistic value for fuel consumption.

Since the equation of rotational motion will be used, the angular accelerations of the various components will be determined. The ECU will receive signals of the current angular velocity of the engine, driveshaft, and two MGs. The angular acceleration of component  $i$  is related to the initial speed  $\omega_{i,init}$  and final angular speed  $\omega_{i,final}$  and the time  $t$  during which the torque is applied by the equation

$$\alpha_i = \frac{\omega_{i,final} - \omega_{i,init}}{t} \quad (3.8)$$

where the amount of time each torque is applied is also determined by the ECU.

The free body of a planet on the first PSD, designated as P1, will be analyzed first. For simplicity, the forces and torques acting on all planets are aggregated to one planet; the distribution of the forces on the planets can be determined by dividing the determined forces and

torques by the number of planets. The planet gear will have two distinct motions: rotation about its axis of symmetry (designated as point O) and revolution about the center of the PSD assembly (designated as point C). The revolution component can be thought of as a pinion gear moving horizontally and meshing with (and constrained by) two horizontal racks, where the ring and sun gears are said racks. A free-body diagram of the planet gear is shown below in Figure 3-2.

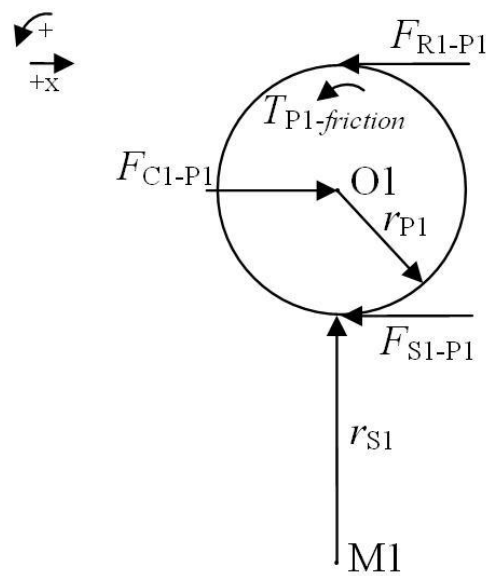


**Figure 3-2. Free-body diagram of the first planet gear**

The revolving movement of the planet gear will now be considered through free-body analysis. The carrier C1 applies a force on the planet at the point of connection between the two. The planet is dragged around the shaft and its teeth make contact with the teeth of the ring R1 and sun S1 gears. Consequently, R1 and S1 exert a reaction force opposite to the force caused by C1. The direction of these reaction forces may change depending on the rotation of the planets about their own axes resulting in various operating conditions. Using the equation of rotational motion, the sum of the torques about point M1 cause a resultant angular acceleration of P1:

$$\begin{aligned} \sum T_{about\ M1} &= J_{P1} \alpha_{P1, about\ M1} \\ F_{R1-P1} (2r_{P1} + r_{S1}) - F_{C1-P1} (r_{P1} + r_{S1}) + F_{S1-P1} r_{S1} &= J_{P1, C} \alpha_{P1, about\ M1} \end{aligned} \quad (3.9)$$

where  $\alpha_{P1, about\ M1}$  is the angular acceleration of the planet about point M1 and  $J_{P1, M1}$  is the moment of inertial (MOI) of the planet about point M1, which will include a Parallel-Axis Theorem component, and  $r_{P1}$  and  $r_{S1}$  are the radii of P1 and S1, respectively. The angular acceleration is also equal to the angular acceleration of C1. The effect of gravity will be cancelled out due to the symmetric distribution of the planets around the sun gear. The gravitational forces on the other gears will not be included in subsequent free-body diagrams since the gravitational forces all act at the axis of rotation, thus no moments are created.

At any given instant, P1 will have rectilinear acceleration as well. Assuming P1 at its highest possible vertical location, Newton's Second Law becomes:

$$F_{R1-P1} - F_{C1-P1} + F_{S1-P1} = m_{P1} a_{P1, x} \quad (3.10)$$

where  $a_{P1, x}$  is the rectilinear acceleration in the x-direction. Notice that the resistance in the bearings of P1 does not affect this acceleration since the torque acting in all directions and the positive x-direction components cancel out the negative ones. The rectilinear acceleration is related to the revolutionary angular acceleration by the equation

$$a_{P1, x} = \alpha_{P1, about\ M1} (r_{S1} + r_{P1}) \quad (3.11)$$

where

$$\alpha_{P1, about\ M1} = \alpha_{C1} \quad (3.12)$$

Similar equations can easily be derived for the planets at the other revolving positions; in each case, the tangential acceleration is directly proportional to the rotation of C1.

For the rotational motion of P1, the equation of rotational motion is about O1, the center of the planet gear is

$$F_{R1-P1} r_{P1} \pm T_{P1-friction} - F_{S1-P1} r_{P1} = J_{P1} \alpha_{P1, about\ O1} \quad (3.13)$$

where  $J_{P1}$  is the MOI of the planet about its axis of symmetry and  $\alpha_{P1, about\ O1}$  is the rotational angular acceleration of P1.  $T_{P1-friction}$  denotes the friction in the planet bearings, and its direction

depends on whether the planet has positive or negative angular velocity: if the planet rotation is positive, then the friction torque will be negative and vice versa.

Equation (3.13) is a significant departure from the dynamic analysis done by reference [89]. In the latter derivation, the forces of the ring and sun gear acting on the planet gears are assumed to be equal because resistance in the planets' bearings is considered negligible, as is the planet gears' MOI. However, it can be easily seen that for  $k=2.6$  (the planetary gear ratio of the study model),

$$r_{P1} = \frac{r_{R1} - r_{S1}}{2} = r_{R1} \frac{k-1}{2k} \approx 0.3r_{R1} \quad (3.14)$$

The MOI of a circular disk is equal to the product of mass and the square of the disk radius, and the aggregate MOI of the planet gears should not be easily dismissed. It is also not clear that the planet gear resistance will be negligible either; further study is required to elucidate the effects of resistance in the planet gear bearings.

The analysis of S1 will now be performed. There is a resultant force due to P1, a resistance torque due to the shaft and rotor of MG1, a resistance torque due to the bearings of S1, and the torque due to MG1. The free-body diagram of S1 is shown below in Figure 3-3.

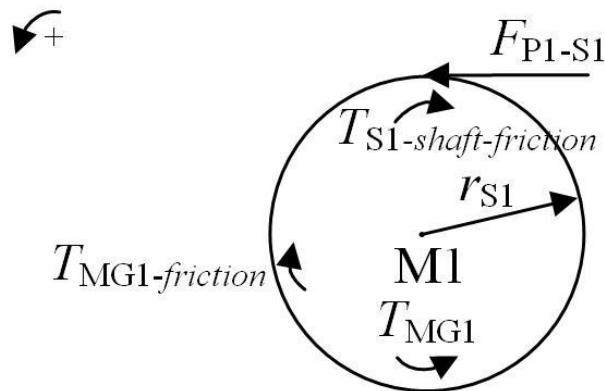


**Figure 3-3. Free-body diagram of the first sun gear**

The equation of rotational motion for S1 is then

$$-F_{P1-S1}r_{S1} + T_{MG1} \pm T_{MG1-friction} \pm T_{S1-shaft-friction} = J_{S1+MG1+S1-shaft}\alpha_{S1} \quad (3.15)$$

where the force term is the reaction force equal in magnitude and opposite direction to the force  $F_{S1-P1}$  in Equations (3.9), (3.10) and (3.13), and the term  $J_{S1+MG1+S1-shaft}$  includes the MOIs of the sun gear, MG1, and of the shaft connecting the two. It should be noted that the torque of MG1 is in the same direction as its shaft rotation when the MG is operating as a motor and in the opposite direction to its shaft rotation when it is operating as a generator. The two friction terms oppose the rotational motion.

The free-body analysis of R1 shows that the engine is forcing R1 to rotate positively, and there is the reaction force due to the planet gears, as well as friction torques from the rotating engine components and the ring gear bearing. The latter torques will either be zero (for AER) or in the opposite direction to the engine rotation. The free-body diagram of the first ring gear is shown below in Figure 3-4.

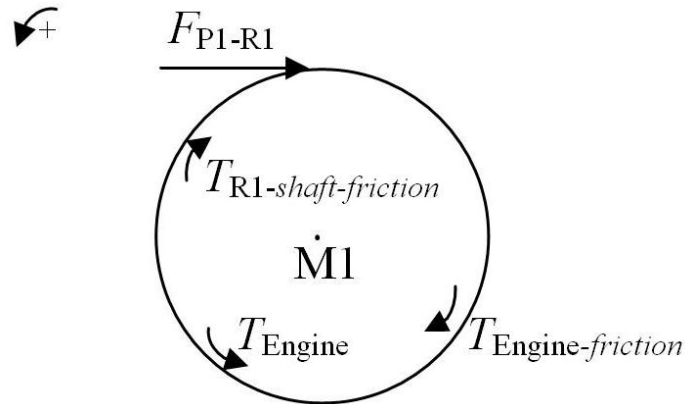


**Figure 3-4. Free-body diagram of the first ring gear**

The equation of rotational motion for R1 is then

$$T_{\text{engine}} - F_{P1-R1}r_{R1} - T_{R1-shaft-friction} - T_{\text{engine-friction}} = J_{R1+engine+R1-shaft}\alpha_{R1} \quad (3.16)$$

The second PSD can be analyzed in a similar manner. The speed relationship for the second PSD is

$$\omega_{S2} + k_2\omega_{R2} = (k_2 + 1)\omega_{C2} \quad (3.17)$$

where  $k_2$  is assigned a value of 2.6. In the AER and in the low-speed mode, Equation (3.17) becomes

$$\omega_{MG2} = (k_2 + 1)\omega_{drive} \quad (3.18)$$

while for the high-speed mode, the speed relationship is

$$\omega_{MG2} + k_2\omega_{MG1} = (k_2 + 1)\omega_{drive} \quad (3.19)$$

The equation of revolving motion for the planet gear of the second PSD about the center M2 is

$$\begin{aligned} \sum T_{about\ M2} &= J_{P2}\alpha_{P2, about\ M2} \\ F_{R2-P2}(2r_{P2} + r_{S2}) - F_{C2-P2}(r_{P2} + r_{S2}) + F_{S2-P2}r_{S2} &= J_{P2, M2}\alpha_{P2, about\ M2} \end{aligned} \quad (3.20)$$

Assuming P2 at its highest possible vertical location, Newton's Second Law becomes:

$$F_{R2-P2} - F_{C2-P2} + F_{S2-P2} = m_{P2}a_{P2, x} \quad (3.21)$$

The rectilinear acceleration is related to the revolutionary angular acceleration by the equation

$$a_{P2, x} = \alpha_{P2, about\ M2}(r_{S2} + r_{P2}) \quad (3.22)$$

where

$$\alpha_{P2, about\ M2} = \alpha_{C2} \quad (3.23)$$

As before, similar equations can be derived for the planets at the other revolving positions; in each case, the tangential acceleration is directly proportional to the rotation of C2.

For the rotational motion of P2, the equation of rotational motion is

$$F_{R2-P2}r_{P2} \pm T_{P2-friction} - F_{S2-P2}r_{P2} = J_{P2}\alpha_{P2, about\ O2} \quad (3.24)$$

The analysis of S2 is identical to that of S1, except that MG2 is substituted for MG1 and S2 for S1 in Equation (3.15):

$$T_{MG2} - F_{P2-S2}r_{S2} \pm T_{MG2-friction} \pm T_{S2-shaft-friction} = J_{S2+MG2+shaft}\alpha_{S2} \quad (3.25)$$

The equation of rotational motion is applied to R2 only in the high-speed regime, since R2 is fixed in the AER and in the low-speed mode. In the high-speed regime, the equation of rotational motion is

$$T_{MG1} - F_{P2-R2}r_{R2} \pm T_{R2-friction} \pm T_{MG1-friction} = J_{R2+MG1+shaft}\alpha_{R2} \quad (3.26)$$

Finally, the rigid body consisting of C1, C2, the intermediate shaft and the drive shaft will be analyzed. P1 and P2 will impose a force and the intermediate shaft and driveshaft will together impose a negative reaction torque. The MOI term will include both carriers, the intermediate shaft and the driveshaft. The friction term will include the friction in the bearings of C1 and C2. The FBD of this rigid body is depicted using the first carrier in Figure 3-5.

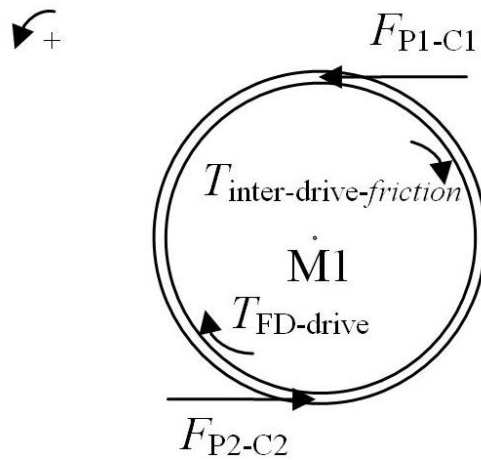


**Figure 3-5. Free-body diagram of rigid body of carrier gears, intermediate and drive shafts**

The equation of rotation motion for this rigid body is then given by

$$F_{P1-C1}(r_{P1} + r_{S1}) + F_{P2-C2}(r_{P2} + r_{S2}) - T_{FD-drive} - T_{inter-drive-friction} = J_{inter+C1+C2+drive}\alpha_{drive} \quad (3.27)$$

where  $T_{FD-drive}$  is the reaction torque applied by the axle through the final drive on the driveshaft.

The transfer of mechanical power through the final drive will be modelled as a simple gear, such that the equation of rotational motion for the final drive is

$$T_{drive-FD} - T_{axle-FD} - T_{FD-friction} = J_{FD}\alpha_{FD} \quad (3.28)$$

where  $T_{FD-friction}$  is the rotation friction,  $J_{FD}$  is the MOI, and  $\alpha_{FC}$  is the angular acceleration of the final drive. The axle and the wheel form a rigid body. All of the dynamics are depicted as occurring at a single wheel; this artificial situation does not affect the end result and is used

simply as a matter of convenience. The ground is assumed to be rigid, i.e. there is no deformation. Thus, the normal force exerted on the wheel is perpendicular to the ground. The torques included are the driving torque  $T_{FD}$ , a torque due to the mechanical brakes (assumed to act at some radius of the wheel), the axle resistance, and the frictional torque acting on the axle:

$$T_{FD-axle} - T_{axle-friction} - T_{brake} - F_{rolling-friction} r_{wheel} = J_{axles+wheels} \alpha_{wheel} \quad (3.29)$$

where the MOI term includes the MOIs of all four wheels and front and back axles. The rolling friction term will be different for front and back wheels, although the aggregate sum can be used as long as wheel slip is accounted for. The present formulation will ignore the effects of “squat” and “dive” that changes the distribution of mass during acceleration and deceleration, respectively, and assume a front-wheel driven design. The maximum friction possible on the drive wheel, beyond which the wheel will slip is known as the limiting tractive effort, given by [40]:

$$F_{tractive, limit} = \mu(s) F_{normal} \quad (3.30)$$

where the coefficient of friction  $\mu(s)$  is a function of the wheel slip and can be approximated by empirical data using the relation [40]:

$$\mu(s) = \mu_{static, peak} \left[ a(1 - e^{-bs}) - cs \right] \quad (3.31)$$

where  $\mu_{static, peak}$  is the peak static friction,  $s$  is the wheel slip and  $a$ ,  $b$ , and  $c$  are empirical constants. The wheel slip is defined as [40]:

$$s = \left( 1 - \frac{V_{vehicle}}{\omega_{wheel} r_{wheel}} \right) \quad (3.32)$$

The normal force of Equation (3.30) is given by [40]:

$$F_{normal} = \left[ \frac{B}{L} m_{sprung} + \frac{m_{unsprung}}{2} \right] \quad (3.33)$$

where  $B$  is the distance from the rear axle to the centroid of the vehicle and  $L$  is the distance between the axles. The *sprung* and *unsprung* mass terms refer to the vehicle mass fraction that is supported by the suspension and the mass fraction that is supported directly by the tires,

respectively. In order to determine the amount of slip, the driving torques are converted to forces and equated to the tractive limit:

$$\frac{1}{r_{\text{wheel}}} (T_{\text{FD-axle}} - T_{\text{axle-friction}} - T_{\text{brake}}) = F_{\text{tractive, limit}} \quad (3.34)$$

The analysis can now be moved to the overall vehicle, which will have an identical rectilinear acceleration to the wheel. In terms of rectilinear acceleration of the entire vehicle, an incline term and air drag must be considered. Firstly, the total acceleration of the vehicle will be the vector difference of the acceleration from the wheels, the acceleration from air drag on the vehicle and the inclination:

$$\vec{a}_{\text{vehicle}} = \vec{a}_{\text{wheel}} - \vec{a}_{\text{air drag}} - g \sin \theta \quad (3.35)$$

The latter acceleration is expressed as

$$\vec{a}_{\text{air drag}} = \frac{\frac{1}{2} \rho_{\text{air}} C_D A_F \vec{v}_{\text{aero}}^2}{m_{\text{vehicle}}} \quad (3.36)$$

where  $\rho_{\text{air}}$  is the density of air;  $C_d$  is the drag coefficient;  $A_F$  is the frontal cross-sectional area; and  $\vec{v}_{\text{aero}}$  is the vector sum of the vehicle velocity and wind parallel to the vehicular motion:

$$\vec{v}_{\text{aero}} = \vec{v}_{\text{vehicle}} - \vec{v}_{\text{wind}} \quad (3.37)$$

The wind vector is assumed to be positive if it is in the opposite direction to the vehicle motion. It should be noted that in extreme circumstances at low speeds the wind may be a tailwind, meaning that  $A_F$  and  $C_d$  will be associated with the rear geometry of the vehicle. The total acceleration of the vehicle is then

$$\begin{aligned} a_{\text{vehicle}} = & \frac{r_{\text{wheel}}}{J_{\text{axles+wheels}}} (1-s) \cdot \\ & (T_{\text{FD-axle}} - T_{\text{axle-resistance}} - T_{\text{brake}} - C_{rr} m_{\text{vehicle}} g \cos \varphi r_{\text{wheel}}) \\ & - g \sin \theta - \frac{\frac{1}{2} \rho_{\text{air}} C_D A_F \vec{v}_{\text{aero}}^2}{m_{\text{vehicle}}} \end{aligned} \quad (3.38)$$

where the wheels are assumed to be perfectly cylindrical but are subject to wheel slip  $s$ , and  $C_{rr}$

is the coefficient of rolling resistance. This latter coefficient is given by

$$C_{rr} = f_1 + f_2 v_{vehicle}^2 \quad (39)$$

where  $f_1$  and  $f_2$  are constants, and  $f_2$  is usually negligible.

The expression for  $T_{FD-axle}$  is then

$$T_{FD-axle} = \frac{J_{axles+wheels}}{r_{wheel}(1-s)} \left( a_{vehicle} + g \sin \theta + \frac{\frac{1}{2} \rho_{air} C_D A_F \bar{v}_{aero}^2}{m_{vehicle}} \right) + T_{axle-friction} + T_{brake} + R_{rolling} m_{vehicle} g \cos \theta r_{wheel} \quad (3.40)$$

### 3.2.2 Node points

The next step is to calculate the node points of the system. As mentioned previously, node points are the locations in which the power through the electric variator is zero, and the node points occur when one of the EMs has zero speed. The node points can be found by finding the locations where the MGs have zero speed. The first node occurs when MG1 is at zero speed at the transition point between low- and high-speed mode. Using Equation (3.3), and defining  $R_{o-i}$  as the output-to-input speed ratio where  $\omega_{engine}$  is the input and  $\omega_{inter}$  is the output given by

$$R_{o-i} = \frac{k_1}{k_1 + 1} \quad (3.41)$$

for a value of 0.72. When the output-to-input speed ratio equals this value, all of the power from the engine will travel via the mechanical path. When the output-to-input speed ratio is near the value of Equation (3.41), the transmission system efficiency is high. Choosing the gear ratio of the PSD is therefore a crucial element in the design strategy. The second node occurs when MG2 is at zero speed. Using Equation (3.19), the node occurs at the point:

$$R_{o-i} = \frac{k_1 k_2}{k_1 k_2 - 1} \quad (3.42)$$

This gives a value of 1.17, and this second node will occur in the high-speed mode.

### 3.2.3 Electrical path

The power through the electrical path will now be considered. Firstly, the electrical power flow from MG1 is given by

$$P_{MG1,elec} = -\eta_{MG1} T_{MG1} \omega_{S1} \quad (3.43)$$

where the electrical power flowing from MG1 is zero for two cases: (1) if the torque of MG1 is zero, as the ECU dictates in, for example, the case of low-power AER operation, and (2) if the speed of S1 is zero, as is the case at the first node point. The efficiency term represents the efficiency of the electric machine in converting mechanical power to electrical power, and will correspond to an efficiency map for the particular electric machine chosen; in the study model, MG1 is an 8-pole permanent-magnet (PM) AC-synchronous machine with a rated power of 83 kW and a maximum rotation speed of 10,000 rpm. The negative sign in Equation (3.43) reflects the negative mechanical power associated with the electric machine operating as a generator. Therefore, if the value of  $P_{MG1,elec}$  is positive, electrical power flows from MG1 to the ESS and/or MG2, and if the value is negative, MG1 operates as a motor and receives power from one or both of MG2 and the ESS.

The electrical power to MG2 is given by

$$P_{MG2,elec} = -\eta_{MG2} T_{MG2} \omega_{S2} \quad (3.44)$$

MG2 and MG1 are identical machines. The power through MG2 will also be zero for two cases: (1) if the torque of MG2 is zero, as dictated by the ECU, and (2) at the second node point. Similar the MG1, when  $P_{MG2,elec}$  is negative, MG2 is operating as a motor and when it is positive, MG2 is operating as a generator.

The ESS of the study model is a nickel metal hydride (NiMH) battery pack with 200 modules. The ESS consists of 200 modules of 6 cells·module<sup>-1</sup> and 1.2 V·cell<sup>-1</sup> connected in series. The power flow of the ESS can be approximated by an internal resistance model:

$$P_{ESS} = V_{OC} \cdot I_{ESS} - I_{ESS}^2 \cdot R_{ESS} \quad (3.45)$$

where  $V_{OC}$  is the open-circuit voltage,  $I_{ESS}$  is the current and  $R_{ESS}$  is the internal resistance. The

sign convention of the ESS power flow is that it is positive when it is flowing *into* the ESS. The open-circuit voltage and internal resistance are both functions of the ESS SOC, the latter of which is defined by the differential equation

$$\frac{d(\text{SOC})}{dt} = -\frac{I_{\text{ESS}}}{C_{\text{ESS}}} \quad (3.46)$$

where  $C_{\text{ESS}}$  is the ESS capacity in  $\text{A}\cdot\text{hr}^{-1}$ . When  $P_{\text{ESS}}$  and  $I_{\text{ESS}}$  are both positive, the ESS is being charged, while when both are negative, the ESS is being discharged. When  $P_{\text{ESS}}$  and  $I_{\text{ESS}}$  equal zero, the SOC is constant. The governing equation of the ESS state is then given by

$$\frac{d(\text{SOC})}{dt} = -\frac{V_{oc} \pm \sqrt{V_{oc}^2 - 4P_{\text{ESS}}R_{\text{ESS}}}}{2R_{\text{ESS}}C_{\text{ESS}}} \quad (3.47)$$

where  $\text{SOC}_{\text{init}}$ , the initial SOC, is known and  $\text{SOC}_{\text{final}}$ , the final SOC at the end of the time step is to be determined.

In the low-power AER, the power flow of the ESS is directed towards MG2, and is defined as

$$P_{\text{ESS}} = \frac{P_{\text{MG2}, \text{elec}}}{\eta_{\text{ESS-MG2}}} \quad (3.48)$$

The efficiency term represents the efficiency of the power electronics in delivering the ESS power to MG2, and will include the inverter efficiency, since the power control unit has an inverter (in addition to the boost converter for the ESS) in order to operate at the proper AC voltage required of the electric machine. The efficiency of this and other electrical connections through the power electronics is assumed to be constant regardless of the electrical power transferred. The equation applies also to propulsion in reverse, although the speed of the driveshaft and the applied torque by MG2 will be in the opposite direction. When regenerative braking occurs, and power is flowing from MG2 to the ESS, the power of MG2 becomes positive, and Equation (3.48) changes sign on the RHS to reflect power flowing into the battery. In high-power AER, and also in order to implement engine lagging operation, the power flow from the ESS is directed towards both MGs:

$$P_{\text{ESS}} = \frac{P_{\text{MG2}, \text{elec}}}{\eta_{\text{ESS-MG2}}} + \frac{P_{\text{MG1}, \text{elec}}}{\eta_{\text{ESS-MG1}}} \quad (3.49)$$

When MG1 is operating as a generator, the power flow is

$$P_{\text{MG1}, \text{elec}} = -\frac{P_{\text{MG2}, \text{elec}}}{\eta_{\text{MG1-MG2}}} + \frac{P_{\text{ESS}}}{\eta_{\text{MG1-ESS}}} \quad (3.50)$$

where the ESS power term on the RHS can be zero if no power is flowing to or from the ESS, greater than zero if the ESS is charging, or less than zero if the ESS is also directing power to MG2. In some instances of ESS charging, especially when idling, all of the power from MG1 will be directed into the ESS, and the power into MG2 will be zero.

When MG2 is operating as a generator, the power flow is

$$P_{\text{MG2}, \text{elec}} = -\frac{P_{\text{MG2}, \text{elec}}}{\eta_{\text{MG2-MG1}}} + \frac{P_{\text{ESS}}}{\eta_{\text{MG2-ESS}}} \quad (3.51)$$

### 3.2.4 Power management strategy

The flow diagram of a model simulation implemented in the *backward-looking* framework of ADVISOR is shown in Figure 3-6. The diagram illustrates how the flow is from “wheels” to “driver”; this is opposite to *forward-looking* simulation software packages such as Program for new generation vehicles Systems Analysis Toolkit (PSAT) [116] and Modelica-based Dymola, where the flow is from “driver” to “wheels”, shown in Figure 3-7.

Discussion of the relative merits of the two types of models is included in Section 9.6.1. It is sufficient at this point to note that in a backward-looking model, the desired velocity is input to the vehicle model and the output is the required mechanical response of the propulsion system to meet the demanded velocity. The calculations must sometimes be performed iteratively for cases where a component in the model is not capable of meeting the requirement demanded of it by the velocity request, and the vehicle response in turn does not meet the demand. When this occurs in one or more components, the power demand is modified, and the response of the components of the vehicle model, some or all of which depend on the response of “guilty” component(s), must be re-calculated, and this complicates the method programming and extends

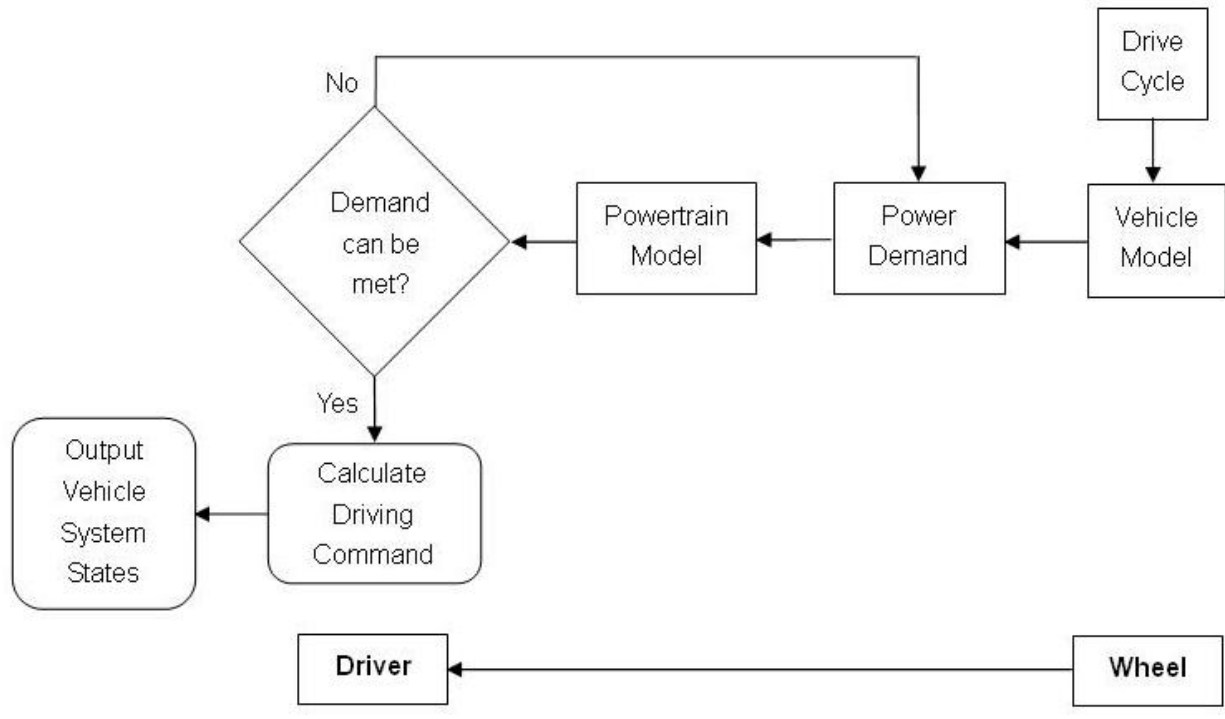


Figure 3-6. Schematic representation of backward-looking structure model

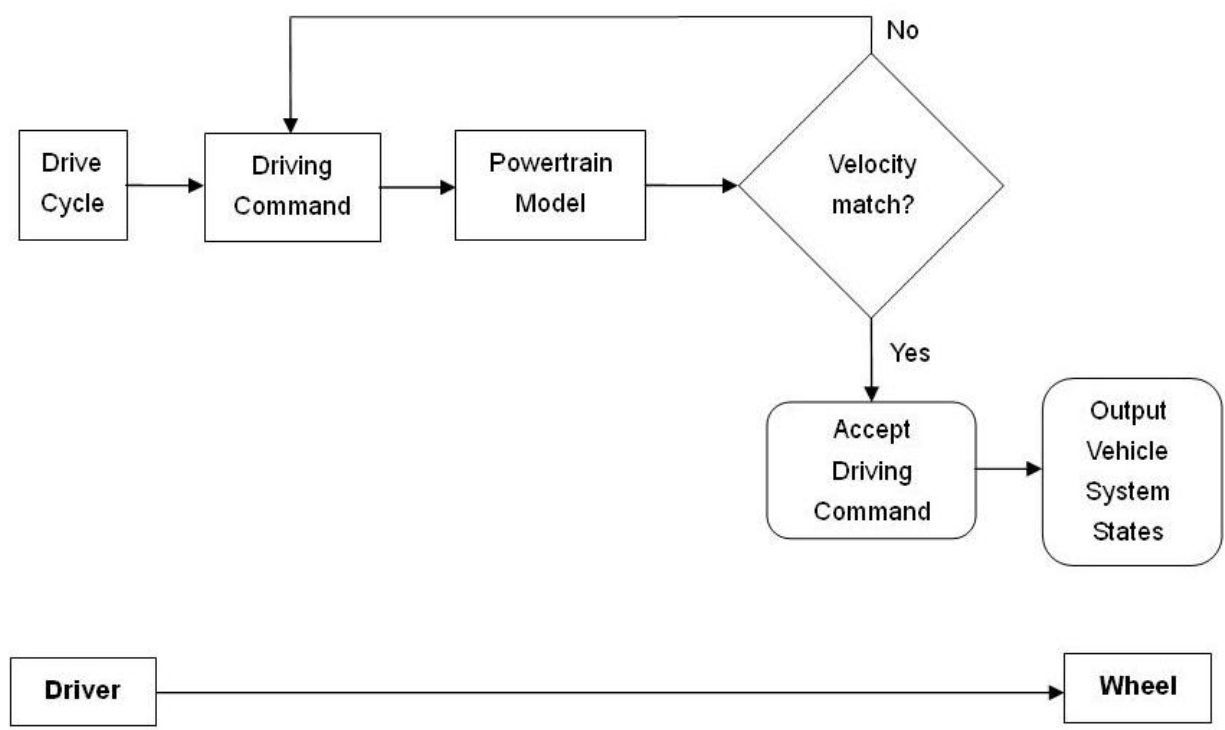


Figure 3-7. Schematic representation of forward-looking structure model

computer run-times.

At pre-determined intervals, the control system accepts signals from the driver (or drive cycle) in the form of a desired velocity. It uses the current and desired vehicle velocities to determine the power demanded of the engine, MGs and ESS. The powertrain module is then used to determine the operating regime, the status of the clutches, the torque-speed values of the engine and MGs, and the power flow of the ESS. The engine and MG power flows are based on component performance maps, while the ESS power flow is based on a performance map that depends on the ESS SOC. The power management strategy of the engine also dictates that it will not be shut off for fewer than 3 seconds. If the SOC is projected to be too low once the strategy is implemented, the engine power must be increased; conversely, if the SOC is projected to be too high, the engine power must be decreased. If the engine coolant temperature is too low, the engine must stay on until the coolant reaches a minimum temperature of 75 °C. Once the demand power is satisfied, the power output strategy is implemented; the power achieved by the powertrain might not meet exactly the power demanded, and ADVISOR keeps track of the points along the drive cycle where the power demand could not be met. The steps of the power management strategy are provided below:

- 1) Determine current vehicle output states at time  $t$ .
- 2) Accept the velocity value input from driver or drive cycle for time  $t=t+i$ .
- 3) Determine the operating regime and engage/disengage clutches as necessary.
- 4) Accept the 8-second engine power average and engine power values from previous 3 seconds.
- 5) Calculate the required speeds and torques of the engine, MG1, and MG2 and power flow of the ESS.
- 6) Calculate ESS SOC if determined action will occur.
- 7) If ESS SOC is too low, increase the engine power, return to step 5).
- 8) If ESS SOC is too high, decrease the engine power, return to step 5).

- 9) If engine coolant temperature is too low AND if the engine is off, the engine is turned on, return to step 5).
- 10) Set the ESS power flow to discharge electrical energy to either MG1 or MG2 or to accept it from either or both sources.
- 11) Set the torque of the engine. The engine power demand is used to determine the optimal engine operating point and corresponding engine speed (the amount of fuel required according to the brake-specific fuel consumption (BSFC) map is sent accordingly to the engine.)
- 12) Set the torque of MG1 to apply to its shaft that will either increase or decrease its shaft speed, depending on whether MG1 is operating as a motor or generator, respectively.
- 13) Set the torque of MG2 to apply to the driveshaft that will either increase or decrease the driveshaft, and hence wheel, angular speed, depending on whether MG2 is operating as a motor or generator, respectively. When operating as a generator, MG2 will discharge the electrical energy into the ESS until it is full; after this point, the vehicle enters the “Negative-Split” regime, and the electrical energy will be shunted to MG1, which will in turn convert it to mechanical power and slow down the engine speed to conserve fuel and slow down the vehicle in a manner analogous to compression braking on a conventional vehicle.
- 14) If the required braking power exceeds the capacity of MG2 to convert the kinetic energy to electrical power, apply the mechanical brakes.
- 15) Apply torques and/or brakes until time  $t=t+i$ .
- 16) Return to step 1).

The time step  $i$  can be any length, but the accuracy of the vehicle matching the driver input will obviously improve with smaller intervals, although computation time will increase. A schematic flow diagram of the previous list of steps is shown below in Figure 3-8.

One advantage of the power-split architectures over parallel hybrid designs, in particular designs that are capable of multiple modes, is the flexibility to control the engine speed

throughout the vehicle speed range. A higher-efficiency engine speed on a multi-regime vehicle can be achieved by controlling the speed of the electric motors. By maintaining a more constant engine speed and eliminating the fluctuations normally present in both hybrid and conventional powertrain vehicles, an overall improvement in efficiency is achievable. This is due to avoidance of the sharp efficiency decreases occurring during engine transients. From the literature, it appears as though the fuel consumption penalty associated with high engine transients is not considered in most modelling efforts.

The overall power management strategy used in the model is the one provided in ADVISOR for the THS. The only modification was to the engine power management strategy. Instead of using an instant power demand, the model uses the previous eight seconds to calculate the average power demand over this period and assigns this average power to the current power demand. The ESS accounts for any shortfall in the power available that occurs as a result of the engine power levelling, SOC-permitting. This strategy considerably reduced the power demand transients at the expense of higher ESS depletion; this may have resulted in a higher overall fuel consumption. However, this action is judged to have provided more realistic results than models that allow for large transients to occur without fuel consumption penalty. To further improve the engine efficiency, a longer power period than 8 seconds could be employed. However, larger and higher power energy storage systems could be required as result of an increased power levelling load.

It should also be noted that the ECU used for the THS in ADVISOR assumes the fixed torque relations of Equations (3.4)-(3.6), and that this power management strategy was also employed for the multi-regime model. The power management strategy was not altered for this first modelling attempt, although it is likely that a strategy that uses the dynamic modelling into account will allow for superior performance and will be investigated in subsequent studies.

To illustrate the various operating regimes of the study model, an example of what is known as an N/V (rotational speed versus velocity) plot for a constantly accelerating drive cycle is illustrated in Figure 3-9 below. The N/V plot shows the speeds of MG1, MG2, the engine, and

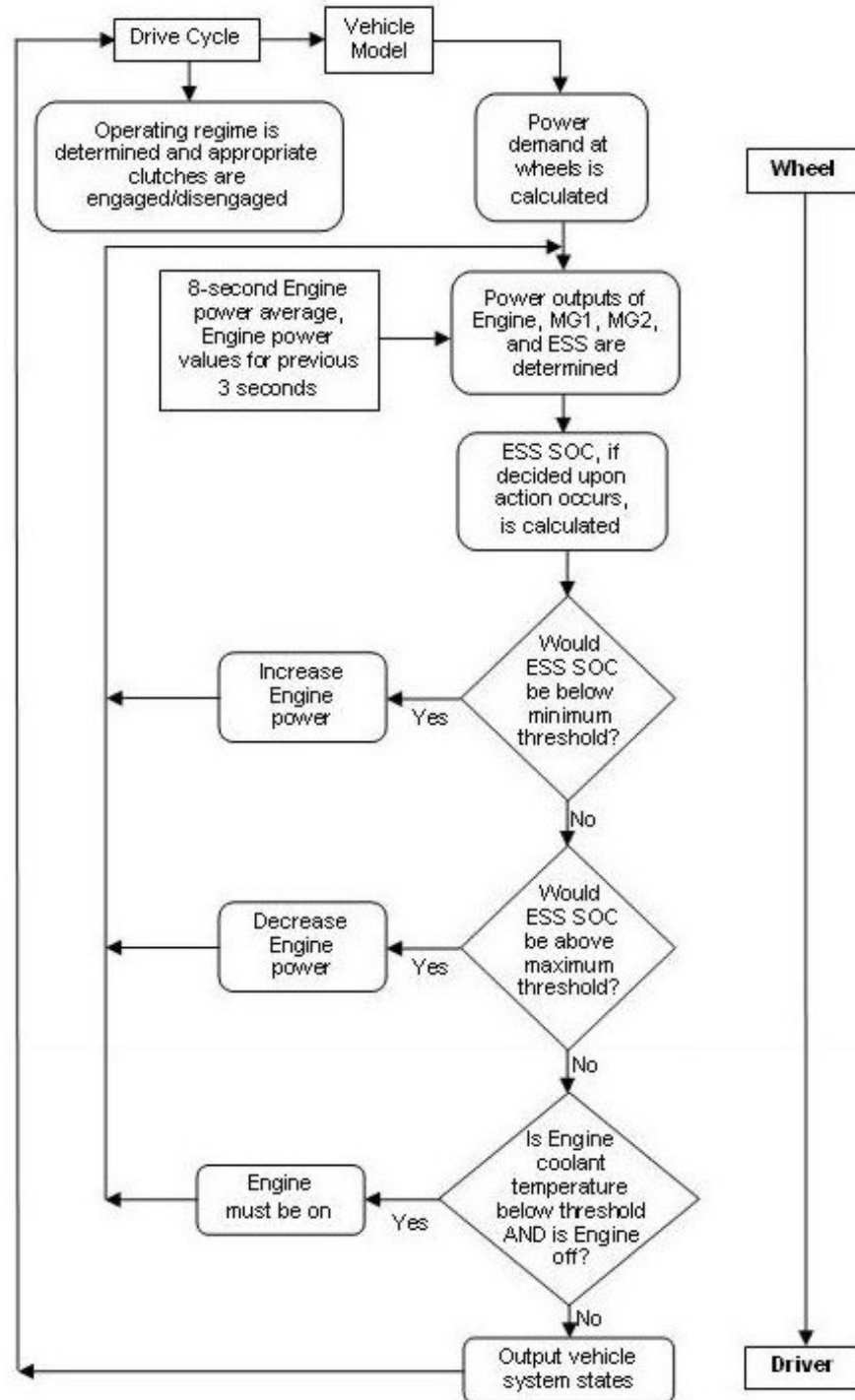


**Figure 3-8. Schematic of the study multi-regime architecture control strategy**

the driveshaft versus the vehicle velocity. The transmission operates in AER until approximately  $25 \text{ km} \cdot \text{hr}^{-1}$ , after which the engine is started by MG1. The engine quickly

arrives at a constant speed that it maintains throughout the remainder of the vehicle velocity increase. The velocities  $V_{\text{shift}}$ ,  $V_{S2}$ ,  $V_{S3}$ , and  $V_{S4}$  are also shown. As noted previously,  $V_{\text{shift}}$  and  $V_{S3}$  are determined by the speed of MG1 and MG2, respectively.  $V_{S2}$  and  $V_{S4}$  may occur at any point between  $V_{\text{shift}}$  and  $V_{S3}$  and beyond  $V_{S3}$ , respectively, or not at all; the ESS SOC will determine whether one of the MGs must operate as a generator or not.

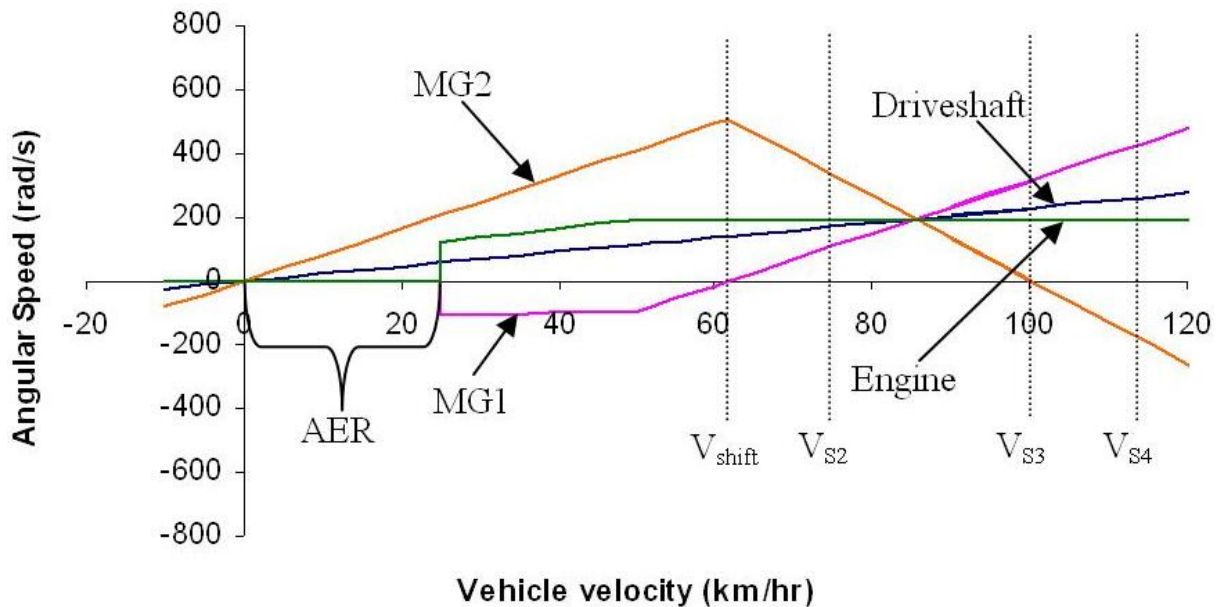


**Figure 3-9. Sample N/V plot for the study multi-regime architecture**

At present, the basic power management strategy employed in the study is likely not the optimal overall strategy. Future work using DP techniques will determine how the control system can best utilize the flexibility of power distribution to optimize the efficiency of the drivetrain and to achieve optimal performance.

### 3.2.5 Vehicle models

In order to compare and analyze the performance of the multi-regime architecture, a simulation investigation was conducted in which the multi-regime model was compared and contrasted with models of the THS, full-parallel hybrid and conventional powertrain

architectures. The vehicle configurations were modelled using the MATLAB/Simulink programming language and integrated with the ADVISOR vehicle simulation. The version used is the open-source 2002 version, not the most recent 2004 version commercialized by AVL Powertrain Engineering, Inc. It is important to note that ADVISOR is a steady-state simulation, and is not capable of simulating transient effects. Therefore, the full dynamic equations are not used and the component behaviour between the steady-states cannot be analyzed.

ADVISOR contains a large library of generic vehicle types from which to choose. Base models for the THS, full-parallel, and conventional powertrains were available, and were subsequently altered to exhibit the desired characteristics of the study vehicle. The multi-regime model was developed by significantly modifying the THS model. The body of the vehicle chosen to be simulated was based on a Kenworth T400 truck, a typical commercial vehicle. Characteristics of the vehicle including all components except for the powertrain components are summarized in Table 3-2. Two different base vehicle weights are considered for the cases in which the vehicle has a payload (“loaded”) or no payload (“unloaded”).

The major powertrain components of the different architectures are shown below in Table 3-3. All four configurations use a compression ignition (CI) engine, with a smaller engine size for the three hybrid models. As can be seen in the table, the Multi-regime and THS models have much the same powertrain components, and the Parallel configuration has the same engine and motor models included. Because the four architectures will have different weights, an

**Table 3-2. Characteristics of the ICEHV study vehicle**

Component	Description/Size
Wheelbase	9.75 m
Wheel radius	0.5 m
Vehicle weight (unloaded)	5933 kg
Vehicle weight (loaded)	11333 kg
Rolling resistance coefficient	0.00938
Aerodynamics coefficient	0.7
Frontal area	8.55 m <sup>2</sup>

attempt was made to account for the differences. In a study by the Electric Power Research Institute, the weight of the powertrain of a conventional vehicle was 20% less than that of the parallel-full hybrid vehicle powertrain [117]. This difference has been retained for this study. Further, it was assumed that the THS and Multi-regime vehicle powertrains were heavier than that of the Conventional vehicle by 25% and 27%, respectively. The latter two weight assumptions were made somewhat arbitrarily; however, the assumptions reflect estimates of the weights of the additional MG, power electronics and PSD(s). The additional weights are included in Table 3-3. Note also that the motor power capabilities provided are the rated, continuous value, not the peak value. Finally, the ESS models of the multi-regime and THS designs have the configuration outlined in section 3.2.3, while the ESS model of the Parallel design has 100 modules of 6 cells·module<sup>-1</sup> and 1.2 V·cell<sup>-1</sup> connected in series.

**Table 3-3. Powertrain components of the ICEHV simulation architectures**

<b>Component</b>	<b>Multi-regime</b>	<b>THS</b>	<b>Parallel</b>	<b>Conventional</b>
<b>Engine</b>	171 kW CI	171 kW CI	171 kW CI	246 kW CI
<b>MG1</b>	83 kW PM	83 kW PM	83 kW PM	-
<b>MG2</b>	83 kW PM	83 kW PM	-	-
<b>ESS</b>	200 modules NiMH	200 modules NiMH	100 modules NiMH	-
<b>Transmission</b>	Dual PSD (ratio of 2.6), Final drive ratio of 4	Single PSD (ratio of 2.6), Final drive ratio of 4	10 speed	10 speed
<b>Powertrain mass</b>	1736 kg	1709 kg	1640 kg	1367 kg

### 3.2.6 Simulations

A variety of drive cycles that represent the typical working conditions of heavy commercial vehicles were chosen for the comparison simulations. The fuel consumption was measured over the course of the drive cycles, which are depicted below in Figure 3-10, and are described by [118]. These drive cycles include:

- 1) Urban Dynamometer Driving Schedule for Heavy Duty Vehicles (UDDSHDV), representative of an idealized urban drive schedule for heavy vehicles. The cycle includes middle- or high-speed travel with periodic full stops. The cycle peak velocity is  $93.3 \text{ km}\cdot\text{hr}^{-1}$ , and the average speed is  $30.3 \text{ km}\cdot\text{hr}^{-1}$  over a 1061 s time interval. The peak acceleration is  $2.0 \text{ m}\cdot\text{s}^{-2}$ .
- 2) New York City Truck (NYCT), representative of a heavy vehicle drive in New York City. The cycle has a very low average speed of only  $12.1 \text{ km}\cdot\text{hr}^{-1}$ , and a top speed of  $54.7 \text{ km}\cdot\text{hr}^{-1}$ . The peak acceleration is  $2.0 \text{ m}\cdot\text{s}^{-2}$ , and the cycle duration is 1017 s.
- 3) City-Suburban Heavy Vehicle Route (CSHVR), a composite of various short trips typical for a heavy delivery vehicle. The speeds range from slow, suburban velocities to higher-speed urban velocities. The cycle peak velocity is  $70.5 \text{ km}\cdot\text{hr}^{-1}$  and the average velocity is  $21.8 \text{ km}\cdot\text{hr}^{-1}$ . The peak acceleration is  $1.2 \text{ m}\cdot\text{s}^{-1}$ , and the cycle duration is 1781 s.
- 4) Highway Fuel Economy Test (HWFET), used by the U.S. EPA for CAFE certification. The cycle is the highest-average speed of the four cycles, with an average value of  $77.2 \text{ km}\cdot\text{hr}^{-1}$ . The peak velocity is  $96.3 \text{ km}\cdot\text{hr}^{-1}$ , the peak acceleration is  $1.4 \text{ m}\cdot\text{s}^{-1}$ , and the cycle duration is 766 s.

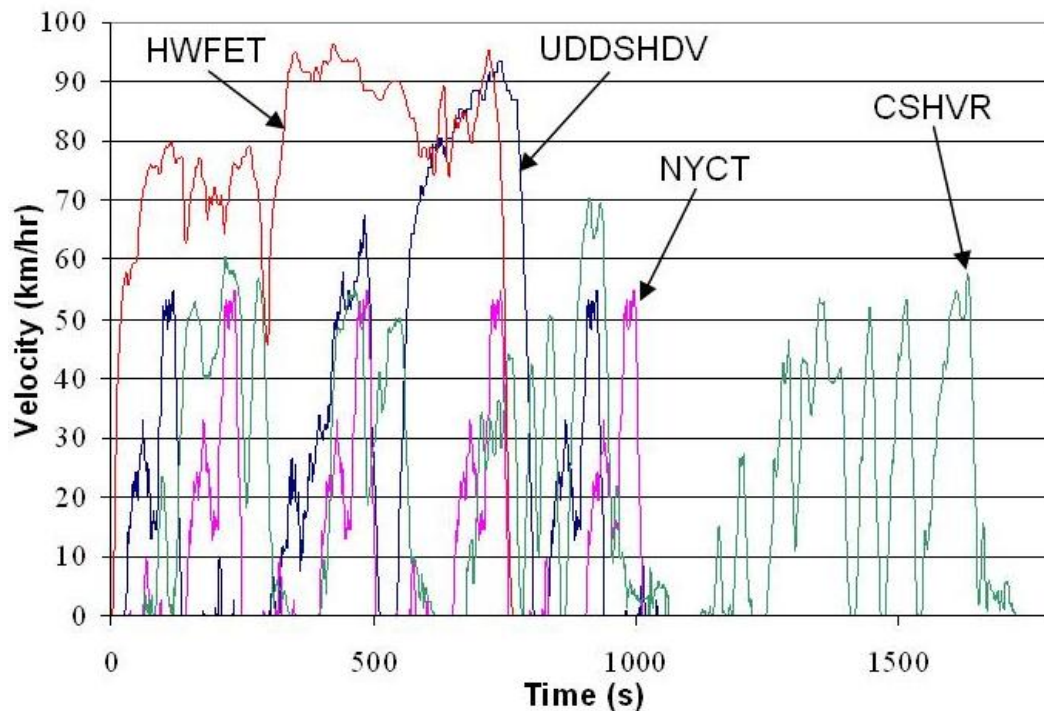


**Figure 3-10. ICEHV Simulation drive cycles**

### 3.2.7 Study results and discussion

The results of the study demonstrate that Multi-regime architectures are promising for use in heavy vehicles with varying payloads. The fuel consumption simulation results are shown in Figure 3-11, for the “unloaded” case, and Figure 3-12, for the “loaded” case. As can be seen from the figures, the Multi-regime vehicle model outperformed the THS and Conventional powertrain vehicles for all drive cycles and loading conditions. The average percent difference between the fuel consumption achieved by the Multi-regime and the Conventional designs is 22.4%, with the greatest difference occurring for the CSHVR (loaded) at 57.8%. The average percent difference between the fuel consumption achieved by the Multi-regime and the THS designs is 65.1%, with the greatest difference occurring for the CSHVR (unloaded) at 88.1%. The Multi-regime does not achieve a fuel consumption as low as the Parallel design on average. The average percent difference between the Multi-regime and the Parallel designs is 3.3%, with the greatest difference occurring for the NYCT (loaded) with 20.1%. However, the

Multi-regime design outperforms the Parallel design in four cases: UDDSHDV (unloaded), -1.2%; CSHVR (unloaded), -11.6%; HWFET (unloaded), -9.6%; and HWFET (loaded), -4.7%. The Multi-regime is thus the best design for a highway drive cycle.

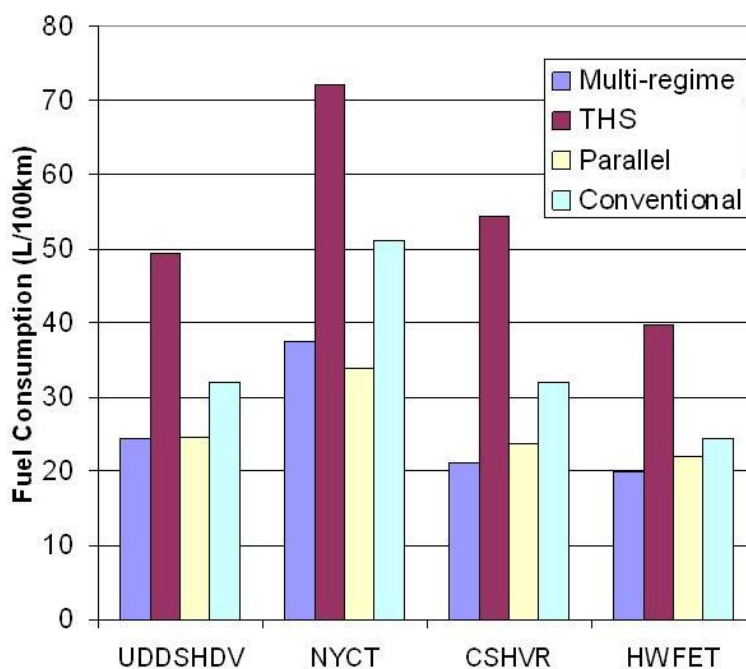


**Figure 3-11. ICEHV simulation results: fuel consumption for the unloaded case**

The Parallel hybrid, as the most common hybrid design for commercial vehicles (some manufacturers use a series design [119-121]), demonstrates the best over-all performance, and an average percent difference in fuel consumption of 25.6% over the conventional design.

The THS architecture was significantly inadequate for the chosen drive cycles and the heavy vehicle with varying payloads. Far from providing an improvement in fuel consumption, the one-mode vehicle had an average fuel consumption increase of 44.5% over the Conventional design and fared even worse against the Parallel architecture, with an average difference of 68.0% in fuel consumption.

The Multi-regime architecture simulations can also be analyzed in detail. The CSHVR drive cycle, with both loaded and unloaded payload conditions was chosen for illustrative purposes. Figure 3-13 below depicts the engine power throughout the drive cycle. As expected, the engine power requirements are significantly higher during the full-load situation,

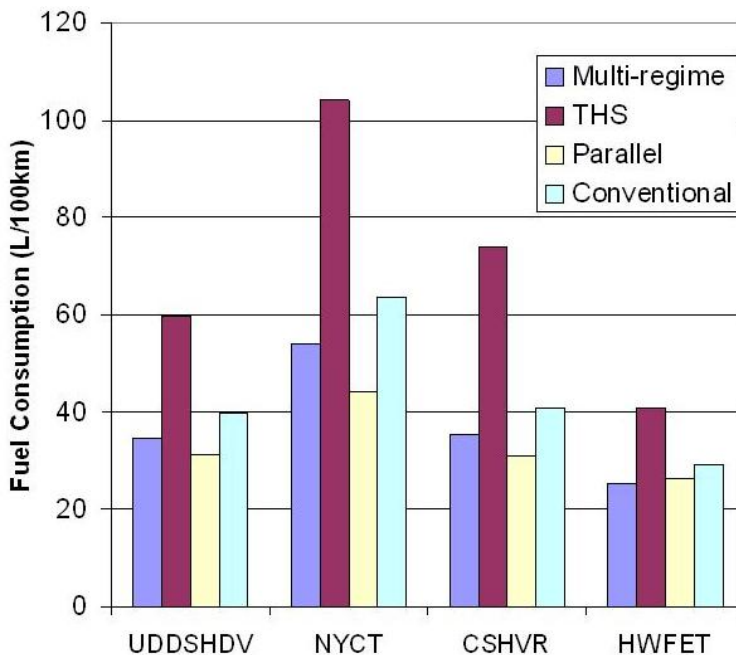


**Figure 3-12. ICEHV simulation results: fuel consumption for the loaded case**

on average 18.9 kW higher.

Figure 3-14 below depicts the power of MG1 throughout the drive cycle. As with the engine power, the loaded case demands more power from the MG, on average 7.4 kW higher.

Figure 3-15 below depicts the power of MG2 throughout the drive cycle. As expected, the loaded case demands more power from the MG, on average 6.8 kW higher.

Figure 3-16 depicts the ESS SOC throughout the drive cycle. In this case, the average SOC for the unloaded case is unexpectedly lower than that of the loaded case. The average difference between the two cases is 1.6%. It is unknown whether this surprising result is an undesirable artifact of the power management strategy or if the engine power for the unloaded case is less efficient at a lower power, thereby requiring more power from the ESS.

The results of the simulations show that the Multi-regime and Parallel architectures show marked improvement in fuel consumption performance with respect to the baseline conventional vehicle. The one-mode architecture performed poorly in contrast to the other three. The Parallel architecture achieves the lowest fuel consumption overall; however, the level achieved by the Multi-regime architecture is not significantly different.

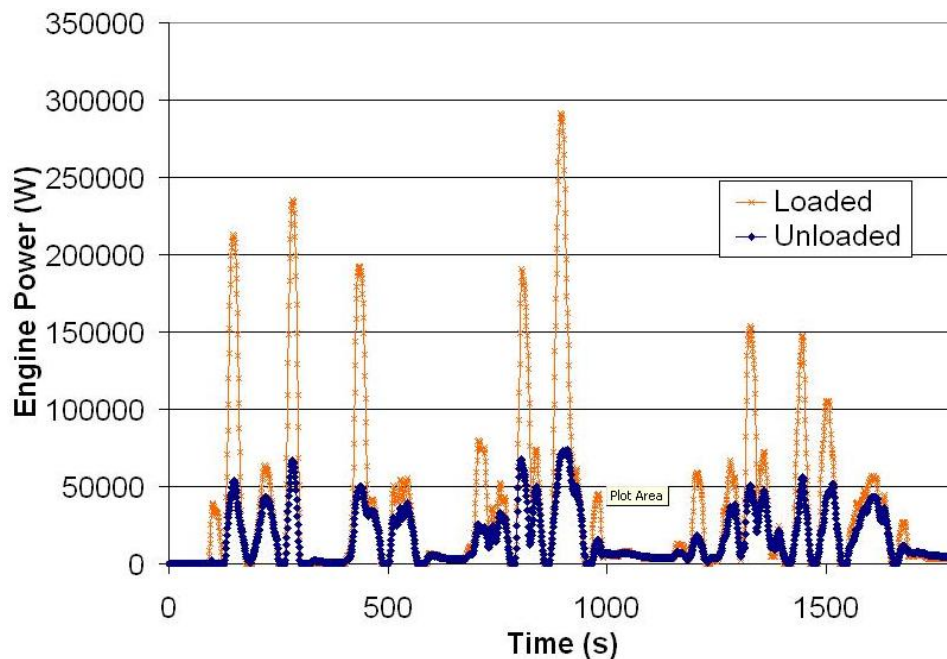


Figure 3-13. ICEHV simulation results: engine power of the multi-regime powertrain during the City-Suburban Heavy Vehicle Route cycle

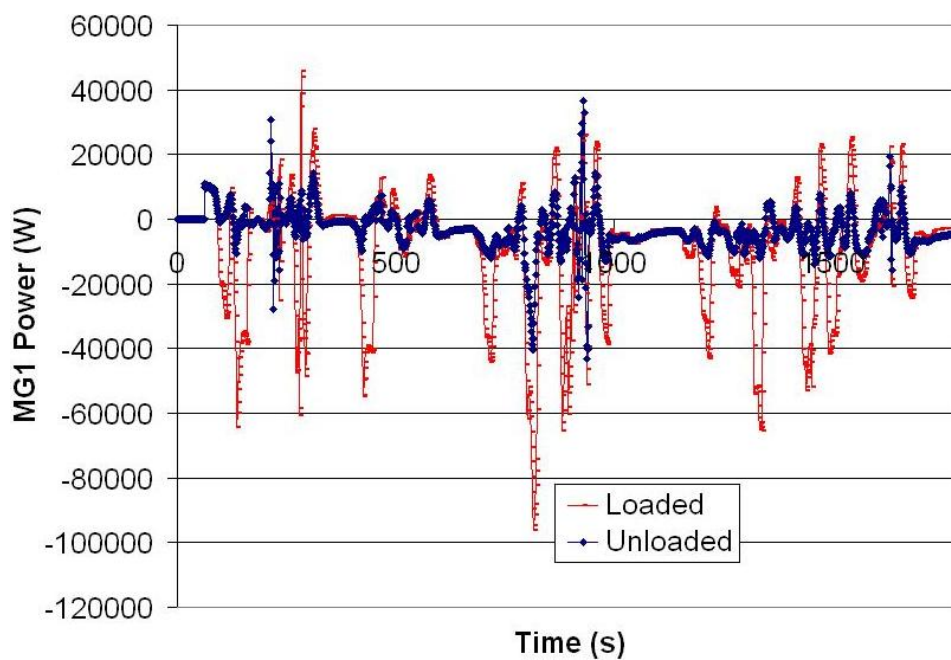
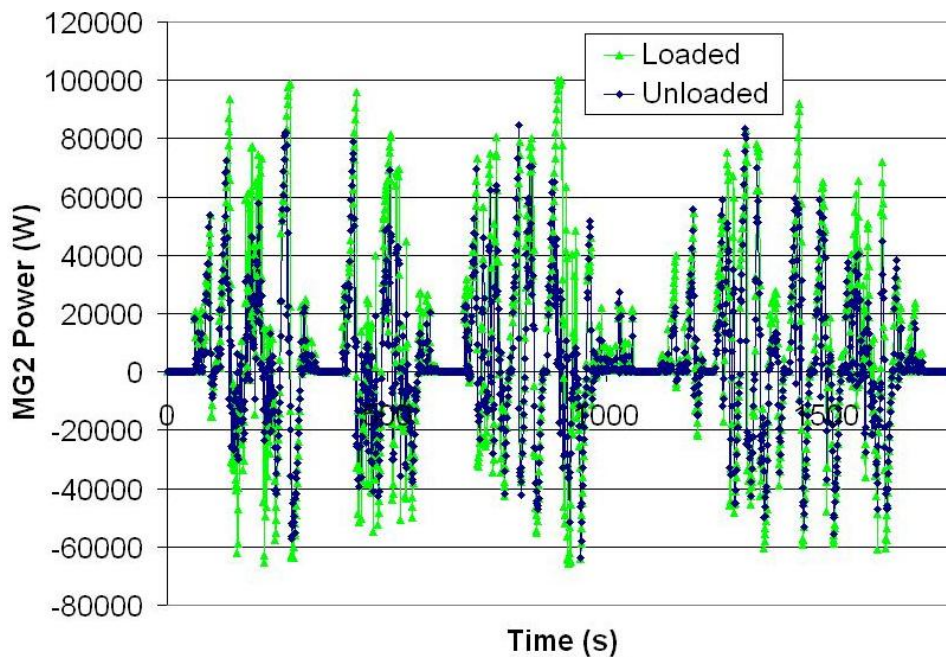
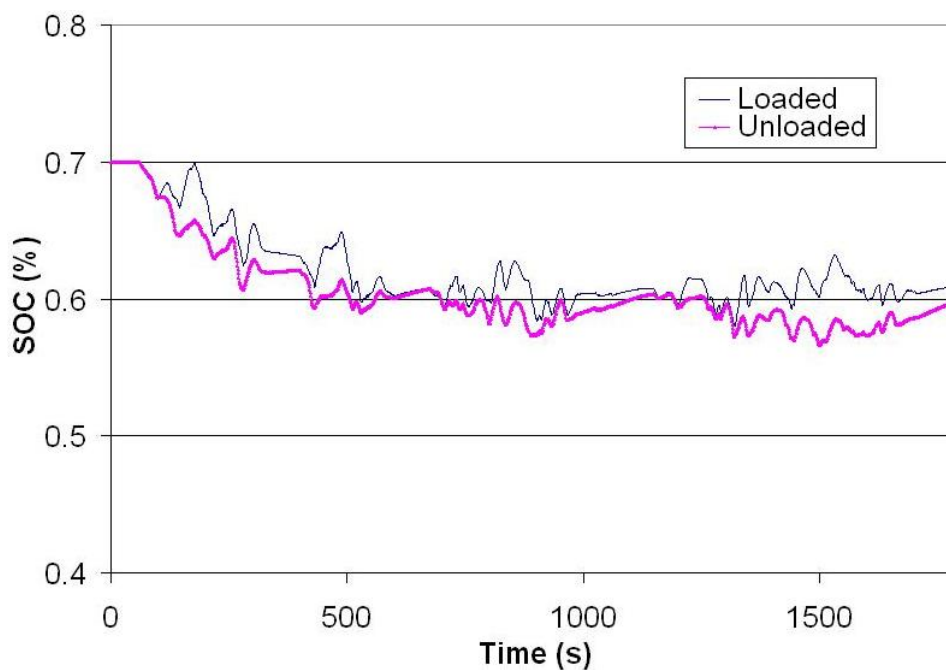


Figure 3-14. ICEHV simulation results: MG1 power of the multi-regime powertrain during the City-Suburban Heavy Vehicle Route cycle



**Figure 3-15. ICEHV simulation results: MG2 power of the multi-regime powertrain during the City-Suburban Heavy Vehicle Route cycle**



**Figure 3-16. ICEHV simulation results: ESS SOC history of the multi-regime powertrain during the City-Suburban Heavy Vehicle Route cycle**

Analysis of the simulation results leads to several conclusions. Firstly, the Multi-regime architecture was shown to be a very promising design for improving fuel consumption, especially in vehicles with widely varying loading conditions. Indeed, the first modelling attempt was able to approach the performance of the (commercial) industry-leading parallel hybrid technology. The study has demonstrated the potential benefits of the advanced multi-regime design concept over current single-regime designs. Secondly, the power management strategy of hybrid vehicles is a crucial area of potential improvement. Since parallel hybrid technology is much more wide-spread and mature, the control strategies have experienced considerable improvement.

In regards to the performance of the one-mode architecture, the author suspects that the existing power management strategy implemented in ADVISOR for this vehicle cannot be applied to scaled-up components and a larger commercial vehicle. The result does not necessarily force a conclusion that this architecture is unsuitable in principle for heavier vehicles; with a properly designed power management strategy, the architecture could surpass the performance of even the parallel design, although it would likely never improve upon the fuel consumption achieved by the multi-regime system. It is clear that future modelling work must focus on the development of the power management strategy of the multi-regime architecture, especially since it provides more degrees of freedom to achieve performance improvement than single-regime architectures.

The next step in the development of the model is then to improve the power management strategy for the multi-regime architecture. The goal will be to develop a real-time, adaptive energy management system. With this system in place, design optimization will be employed to size the powertrain components and optimize the power management strategy. Subsequent studies will focus on the industry-leading GM designs that have been commercialized in transit and passenger vehicles.

## Chapter 4 PEM Fuel Cell and Stack Modelling

Fuel cell modelling is in its relative infancy, but already a significant amount of effort has been put forth to understand the parameters and issues affecting the performance of the fuel cell. Indeed, there are many research groups endeavouring to develop accurate and useful models. Fuel cell modelling requires a broad skill base, as electrochemical, thermodynamic and fluid dynamic relationships must be combined with heat transfer and mass and energy balance equations in order to construct an appropriate model [122]. A balance must be found between simplifying assumptions that compromise the accuracy of the model and increasing complexity that makes the model unworkable.

Fuel cell models can be distinguished by their placement in several categories. The first such category is the basic model focus. The model may be used to describe the fundamental physical phenomena at the electrochemical level, to describe the operation of an assembled fuel cell stack, or to describe the operation of an entire FCS including the Balance of Plant (BOP) components such as pumps and compressors. Once the focus of the model has been determined, the model approach can then be considered. The following sections describe the various approaches found in the literature for cell and stack modelling. The choice of model used in the dissertation research is then discussed and justified.

### 4.1 Previous Fuel Cell Modelling

There are several types of cell model approaches, and the line separating the approaches is often blurry. Essentially, however, the approaches may be classified as one of: a) theoretical (sometimes known as ‘mechanistic’), b) semi-empirical, and c) empirical. The level of model complexity decreases from the highest for theoretical models to the lowest for empirical models.

For each type of approach, a further classification indicates whether the model accounts for static or transient phenomena, or both. Static models, also known as steady-state models, describe the performance of fuel cells at a single operating point, i.e. at a single cell temperature

and reactant pressure. These models are valuable for assessing the aptitude of the chosen components of a system, such as the size of a pump or the amount of catalyst on an electrode. A static model is the model type primarily used to make predictions that are validated in laboratory testing of fuel cell stacks, although transient modelling and subsequent transient testing is a crucial aspect of fuel cell development and is becoming increasingly common. For situations where the operating parameters of the fuel cell change, such as in the case of vehicular applications, a dynamic model is required to achieve accuracy. Dynamic models, also known as transient models, are particularly useful in analysis of start-up and shutdown portions of the operation cycle of a fuel cell and also in optimization of the fuel cell response time to changes in load [122].

Theoretical cell models are constructed with involved partial differential equations that are solved either numerically or analytically – depending on the dimensionality and complexity of the equations – to determine the fuel cell polarization curve, i.e. a curve which represents the relationship between the output voltage and the operating current. These models make use of equations such as the Nernst-Planck equation for species transport in an electrolyte; the Butler-Volmer equation describing electrochemical cell voltages; and the Stefan-Maxwell equation governing gas phase transport [122]. The advantages of this approach include phenomenologically based equations with a sound physical justification for their derivation. However, it is often difficult to achieve experimental validation of these theoretical models, because the focus of the model is often at a fundamental level for which experiments are exceedingly difficult. Additionally, in cases where the model is constructed with a large enough focus, the author often has to make simplifying assumptions that compromise the accuracy. When the focus of an individual theoretical model is insufficiently broad, and the model is focused on a small portion of the overall function of a fuel cell, several models must be combined to provide a comprehensive model, a time-consuming and extremely difficult task; the computational demands are also exacting. The spatial dimension and the level of complexity to which the model delves are thus key factors that must be addressed when constructing a

theoretical model.

The complexity of the model is a function of the number of different phenomena for which no simplifying assumptions are made and phenomenologically based equations are implemented [123]. The spatial dimension scope of the model will also affect the model complexity. The FCS models, discussed in the following section, are generally modelled at the zero-dimensional level, while a theoretical fuel cell model can be up to three-dimensional, although this increases the complexity of the model significantly [124]. Various research groups have attempted the full spectrum of spatial dimensions for their theoretical models. For example, Boettner *et al.* [124] developed a zero-dimensional model; one-dimensional models were developed by Maggio *et al.* and Eaton *et al.* [125, 126]; two-dimensional models were developed by Dannenberg *et al.*, You & Liu, and Secanell *et al.* [127-129]; and three-dimensional models were developed by Kulikovskiy *et al.* and Berning *et al.* [130, 131]. All of the developed models have limitations, and none have been widely accepted by the fuel cell modelling community.

A subset of the mechanistic category are computational fuel cell dynamics (CFCD) simulation stack models that solve the set of partial differential equations governing the fluid flows within the fuel cell, in order to model and understand the flows of the reactants and products to arrive at a description of the fuel cell performance. This approach excels as a tool for improving the design of flow channels in the fuel cell. However, as in all mechanistic fuel cell models, the scope of the CFCD simulation models is often very limited, and it is difficult to arrive at an assessment of the performance of the fuel cell as a whole, let alone an entire fuel cell stack. These models often also require powerful computers as the set of coupled partial differential equations that must be solved is large and complex. The equations need to be solved in a refined grid that can contain a large number of nodes.

Nguyen developed a three-dimensional model that accounts for a variety of physical phenomena, including the ability to calculate local voltage overpotentials, for a fuel cell with serpentine gas channels [132]. The aforementioned three-dimensional model by Berning *et al.* is another attempt at a CFCD model, which offers a description of the temperature gradients

within the membrane-electrode assembly (MEA) [131]. Several commercial software packages exist that can be used to develop CFCD models. The most notable entry in this latter category is the finite element analysis-based (FEA) FEMLab (now Comsol Multiphysics). Using this software, a two-dimensional model that accounts for both steady-state and transient phenomena as well as heat and mass transfer effects has been developed [133]. The model is thus comprehensive in scope and is widely used throughout the fuel cell industry. For example, Noponen *et al.* [134] developed a two-phase, non-isothermal model and Ziegler *et al.* [135] proposed a two-phase model dynamic model; both models were implemented in Comsol Multiphysics and compared with earlier experimental values. Also, researchers at the Institute for Integrated Energy Systems at the University of Victoria (IESVic) and elsewhere have made significant use of this software in a variety of different applications. For example, the Microfluidics Lab has used Comsol Multiphysics extensively to model microscale fluid flows and study the electrokinetic effects encountered in applications from micro-mixing to micro-fuel cells.

Other numerical software packages exist that and have also been utilized to develop CFCD PEMFC models. The computational fluid dynamics (CFD) software Fluent has been used to develop a three-dimensional PEMFC model that includes multiple phenomena [136]. A single-phase, three-dimensional, non-isothermal CFCD model was developed by Sivertsen and Djilali in Fluent as well [137]. The model takes the distributed overpotential in the catalyst layer of the cathode in account and keeps the heat sources and sinks separate for each electrode. It also features parallel computing that allows for a large number of computational nodes and greater mesh resolution. The potential for usage of the latter Fluent model could be included in future work.

Purely empirical models of PEMFCs exist, and because they are based entirely on experimental data, their predictive outputs match the experimental values almost exactly while requiring little in the way of computational power. The accuracy of the results is essentially limited only by the experimental procedure and instrumentation employed. A model that

employs an Artificial Neural Network (ANN) is an example of an empirical model. The network can be trained such that the polarization curves output by the model display very little divergence from the experimental data. However, these models are only valid for the specific cell or stack for which the experimental data was obtained. Furthermore, the model is valid only in the range of operating conditions at which the experiment was performed. Therefore, the usefulness of these models is extremely limited. It is impossible to guarantee accuracy when scaling or extrapolating results to accommodate other stack sizes and operating conditions. Thus, research in the area of pure empirical fuel cell modelling is less active than in the other areas, and the use of such a model was eliminated from contention for the current research.

Fuel cell models can also be semi-empirical, meaning that the modelling approach lies somewhere in the middle between the two extremes of mechanistic and empirical models. The equations are phenomenologically based, but in this case the equations contain parameters that are empirically determined. The parameters are found by experimentation on specific fuel cells for various operating conditions. Because the model is inherently validated by experiment, there is significant agreement between model predictions and reality. Early semi-empirical models were similar to the purely empirical models in that the semi-empirical models were valid only for the test system on which experimentation took place. In fact, the only difference between the two approaches was that the equations for the semi-empirical models were slightly more mechanistically based, and thus they represented a more realistic picture of the actual physical phenomenon about which they were modelling and were inherently more accurate. The early semi-empirical models typically used an input of the cell temperature alone to calculate the polarization curve. Contemporary semi-empirical models, however, have become much more complex and now take into consideration many more fuel cell-specific and operating parameters to give the model a more theoretically based and sound foundation. Current semi-empirical models can provide performance predictions for a myriad of operating conditions. This is in stark contrast to the empirical models in which only the operating conditions that are experimentally determined can be obtained from the model with a high degree of accuracy of the

numbers, and also to the early semi-empirical models that could extrapolate from the data only in a very limited manner.

There have been several attempts at development of a semi-empirical model for fuel cells. The first attempts included Lee *et al.* [138], Kim *et al.* [139] and Squadrito *et al.* [140] which all used the common methodology of employing the Tafel equations to obtain a polarization curve in what is basically a curve-fitting exercise using experimental stack data. Pisani *et al.* [141] employed a significantly more mechanistic approach in developing a model with a flexibility that was nevertheless somewhat compromised because of the inclusion of an empirical ohmic overvoltage term. This group of researchers have also abandoned the semi-empirical approach and have since directed their efforts towards theoretical models. All of the aforementioned models were steady-state. The most concerted effort at development of a semi-empirical model has been at the Royal Military College (RMC) in Kingston, Ontario. A steady output of papers depicting an incrementally improved model [142-145] have resulted in a robust, flexible model known as the Generalized Electrochemical Steady-State Degradation Model (GESSDM). The RMC model has been used by members of industry, where Ballard Power Systems is the most notable example [146], and by other research groups that have incorporated early versions of the model and used experimentation to validate its veracity [147]. The model has achieved an accuracy and adaptability that has allowed it to be deemed functional for the current research. The RMC model was selected as the cell model on which the project fuel cell system research is based, and is discussed further in Section 4.2.

A glaring omission in the literature is the inclusion of comprehensive fuel cell stack models. In order to model a FC stack, the air and hydrogen streams inside each cell must be modelled and the effect of the design of the bipolar plate included. The stack model must take into consideration the variation in the delivery of reactants to the individual cells, the variation in reaction along the flow channel as the concentration of oxygen diminishes in the cathode, as well as phenomena such as bipolar plate current resistance and non-uniform current density distribution across bipolar plate surfaces [148]. The level of compression of the fuel cells by

the compression rods might also have a detectable effect on the stack performance. The current stack models can be considered to be quasi-stack models: the output voltage of the fuel cell models is multiplied by the number of cells in the stack to arrive at an overall output. This absence of a fully-developed stack model should be addressed in order to obtain accurate modelling results that can be empirically validated.

The aforementioned deficiencies in current stack models have not been addressed in this work. This is left to future work, as discussed in the concluding chapter of the dissertation. The GESSDM model is improved, however, with the addition of several modules. The following sections contain a description of the stack model developed during the Ph.D. research. It begins by documenting the version of the GESSDM published by the RMC researchers in Section 4.2. In Section 4.3, the modifications to the GESSDM are discussed.

## **4.2 PEM Fuel Cell and Stack Model**

The model advanced by researchers at RMC known as the Generalized Electrochemical Steady-State Degradation Model (GESSDM) [145] was chosen as the backbone to the FCS model. The use of a semi-empirical model is seen as viable for the research because of the flexibility of use and the simplicity without significant compromise in accuracy. The model has been used in previous research projects at IESVic and this experience has generated considerable confidence in the model. For example, the GSSEDM model without degradation, known as the Generalized Steady-State Electrochemical Model (GSSEM), has been tested against the beginning-of-life performance of the Ballard Mark IV and Mark V fuel cells, with considerable success [144].

The complete model has been developed in MATLAB, and thus a thorough understanding of its intricacies exists. The input to the fuel cell voltage module is the current demand from the application, and this module outputs the amount of voltage that the stack can provide from a determination of the stack polarization curve for the specific operating parameters assigned. The model is steady-state, zero-dimensional, and semi-empirical, which means that it is largely

mechanistically based with additional experimentally derived parameters that are used to predict the output voltage of the fuel cell stack. The semi-empirical parameters include the catalytic activity and membrane conductivity parameters, and a factor in the concentration overvoltage, discussed in detail in the activation, ohmic, and concentration overvoltage section, respectively. Different MEA structures are allowed, with varying active areas and membrane thicknesses accounted for in the calculations. The simplifying assumptions of the GSSEDM are [145]:

- the stack is isothermal
- flooding is controllable through removal of excess water by the air stream
- the excess water content in the membrane will not cause long-term degradation, only short-term decrease in performance
- there are no contaminants or poisons, such as CO present
- there is no degradation from cycling effects

The formulaic description of the GESSDM follows in the following sections. Some of the formulae are unchanged from the original GESSDM formulation in references [142, 144, 145], while others have been modified or substituted completely. Subsequently, the additional modules proposed to model additional stack phenomena are discussed in Section 4.3. The degradation aspects are included in Appendix B since no degradation is considered in the current model. The equations in the model have been included in the MATLAB program.

#### 4.2.1 PEM fuel cell fundamentals

The GSSEDM was designed to model the operation of PEMFCs, where the electrodes are made from carbon cloth coated in a platinum catalyst and the electrolyte is a solid polymeric sheet. The fuel cell is fed hydrogen ( $H_2$ ) and air gases as the reactants and the reactions that occur at the anode and cathode are depicted in Figure 4-1. The oxygen in the reaction is derived from the air stream.

As can be seen by the above figure, the products of the reaction are a flow of electrons (DC electricity) and water. Additionally, some thermal energy is produced, since the exergy of the products is less than that of the reactants and an exergy balance dictates that some heat will be

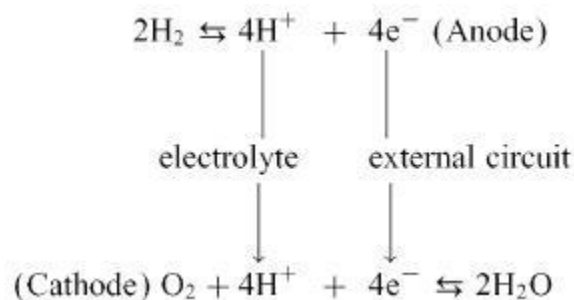


**Figure 4-1. Reactions of a PEMFC**

Source: [149], page 1204.

produced. Fuel cells display a varying efficiency with current density, and as the efficiency decreases, more heat will be produced at the expense of output voltage. Air is used instead of pure oxygen because it is freely available. The stoichiometry of the cathode side is generally greater than that of the anode because the increased air flow can remove the generated water vapour from the cell and also to assist with cell cooling.

The cathode voltage is more positive than that of the anode by 1.229V at 25 °C and 1 atm, standard temperature and pressure (STP) [46]. The actual practical voltage depends on the stack temperature and pressure, as will be seen below. This difference in voltage pulls the unfettered electrons through the external circuit, the motion of charge creating the current that is used to power whatever load is coupled to the fuel cell. The arrival of the electrons at the cathode means that there is an accumulative negative charge that attracts the protons through the electrolyte of the MEA. It should be noted that the external circuit must be made from a material that is a good electron conductor while also being a good proton insulator; the opposite is required of the electrolyte. The  $\text{H}^+$  ions migrate through the electrolyte to the cathode, attracted by the electrostatic forces of the electrons that have passed through the external circuit to arrive at the cathode. The separate electrons and protons are met at the cathode by  $\text{O}_2$  molecules. These oxygen molecules undergo analogous molecular splitting and ionization that the hydrogen atoms experienced at the anode. The resulting electrons and ions have a strong affinity for recombination, and the result is the forming of  $\text{H}_2\text{O}$  molecules.

#### 4.2.2 Theoretical PEM fuel cell potential

In order to quantify the amount of energy that is released in this reaction, the concept of the Gibbs free energy of formation is introduced. The Gibbs free energy of a system is related to the enthalpy and entropy by [46]:

$$G = H - TS \quad (4.1)$$

where  $G$  is the Gibbs free energy,  $H$  is the enthalpy,  $T$  is the temperature and  $S$  is the entropy. In terms of molar quantities of formation, this equation can be modified to become [46]:

$$\bar{g}_f = \bar{h}_f - T\bar{s}_f \quad (4.2)$$

where  $\bar{g}_f$  is the Gibbs free energy of formation in  $\text{J}\cdot\text{mol}^{-1}$ ,  $\bar{h}_f$  is the enthalpy of formation in  $\text{J}\cdot\text{mol}^{-1}$ , and  $\bar{s}_f$  is the entropy of formation in  $\text{J}\cdot\text{mol}^{-1}\cdot\text{K}^{-1}$ . It is the change in energy between two states that provides the energy production of a fuel cell, so Equation (4.2) in terms of energy change is [46]:

$$\Delta\bar{g}_f = \Delta\bar{h}_f - T\Delta\bar{s}_f \quad (4.3)$$

The change in the enthalpy of formation is equal to the difference between the enthalpy of formation of the products minus that of the reactants of the electrochemical reaction, and the change in entropy of formation is similarly described. Thus in light of the reactions of Figure 1, Equation (4.3) becomes [46]:

$$\Delta\bar{g}_f = (\bar{h}_f)_{H_2O} - (\bar{h}_f)_{H_2} - \frac{1}{2}(\bar{h}_f)_{O_2} - T \cdot \left[ (\bar{s}_f)_{H_2O} - (\bar{s}_f)_{H_2} - \frac{1}{2}(\bar{s}_f)_{O_2} \right] \quad (4.4)$$

The enthalpy and entropy terms are functions of temperature, and are given by [46]:

$$\bar{h}_f \Big|_{\text{at } T} = \bar{h}_f \Big|_{\text{at } 298.15\text{K}} + \int_{298.15}^T \bar{c}_p dT \quad (4.5)$$

where the integrand is the molar heat capacity at constant pressure, and

$$\bar{s} \Big|_{\text{at } T} = \bar{s} \Big|_{\text{at } 298.15\text{K}} + \int_{298.15}^T \frac{1}{T} \bar{c}_p dT \quad (4.6)$$

The values of molar enthalpy and entropy can easily be found in thermodynamic tables such as

those found in reference [150].

If the reaction in a fuel cell is ideal, meaning that there are no losses, then the system is said to be reversible. Because there are two electrons released for each molecule of water that is produced, for every mole of water produced (or moles of hydrogen gas used, or half-moles of oxygen used), two electrons are released and thus the charge produced and sent as current through the external circuit is equal to  $-2F$ , where  $F$  is Faraday's constant (which has a value of  $96485.34 \text{ C}\cdot(\text{mole}\cdot\text{electron})^{-1}$ ). The voltage of the fuel cell ( $E$ , also known as the electromotive force, EMF) is the mechanism that imposes work on the electrons, causing motion in the direction from anode to cathode. For the no-loss case, the total electrical work done, the product of the charge flowing through the electric circuit and the voltage, is exactly equal to the Gibbs free energy of formation released, therefore [46]:

$$\Delta\bar{g}_f = -2F \cdot E \quad (4.7)$$

and

$$E = \frac{-\Delta\bar{g}_f}{2F} \quad (4.8)$$

Equations (4.4), (4.5), and (4.6) are then used to calculate the ideal, or reversible, no-loss voltage of the fuel cell, Equation (4.8). The maximum difference in potential between anode and cathode voltage of Equation (4.8) was listed previously as 1.229 V, occurring at STP, and for the case where the product of the electrochemical reaction is liquid water.

### 4.2.3 Nernst voltage

The changes in the Gibbs free energy, as well as enthalpy and entropy changes, are all dependent upon temperature, but also on pressure and concentration of the gas reactants in the cell as well. Specifically, it is the activity,  $a$ , of the reactants that has a strong effect on the output voltage of the fuel cell. Activity is a measure of a species' affinity for reaction in a given environment, with both the amount (thermodynamics) and speed (kinetics) of the reaction providing the rate. The no-loss voltage is therefore reduced by an amount that is determined by

the reactant activities. For an ideal gas, activity is defined as [46]:

$$a_{gas} = \frac{\bar{p}_{gas}}{P^0} \quad (4.9)$$

where  $\bar{p}_{gas}$  is the partial pressure of the gas and  $P^0$  is standard pressure, 101.325 kPa. Activity can be shown to be of the following form for water vapour [46]:

$$a_{vapour} = \frac{\bar{p}_{vapour}}{P_{vapour}^{sat}} \quad (4.10)$$

where  $\bar{p}_{vapour}$  is the partial pressure of the water vapour while  $P_{vapour}^{sat}$  is the saturation pressure of the water vapour at a given temperature, i.e. the pressure at which the air is saturated with water. The Nernst voltage, or irreversible open-circuit voltage (OCV), can be determined by using one form of the Nernst equations that have been developed in the field of electrochemistry [46]:

$$E_{Nernst} = E^0 + \frac{RT}{2F} \ln \left( \frac{a_{anode, H_2} \cdot a_{cathode, O_2}^{1/2}}{a_{cathode, vapour, gen}} \right) \quad (4.11)$$

where  $E^0$  is the reversible OCV,  $R$  is the ideal gas constant,  $a_{anode, H_2}$  and  $a_{cathode, O_2}$  are the hydrogen and oxygen activities at the surface of the catalyst at the anode and cathode, respectively, and  $a_{cathode, vapour, gen}$  is the activity of the vapour at the cathode catalyst generated from the electrochemical reaction. The generated water is assumed to be completely in vapour form. The activity of the vapour generated in the cathode is determined in the cathode flow module of Section 4.3.6.

The maximum reversible OCV,  $E_{max}^0$ , has a value of 1.229 V. The reversible OCV will vary with temperature according to [46]:

$$E^0 = E_{max}^0 - (T - T_0) \left( \frac{\Delta s^0}{nF} \right) \quad (4.12)$$

where  $\Delta s^0$  is the change in standard-state entropy, which for the reaction of Figure 4-1 can be

calculated by [151]:

$$\Delta s^0_{reaction} = \Delta s^0_{H_2O} - \frac{1}{2} \Delta s^0_{O_2} - \Delta s^0_{H_2} \quad (4.13)$$

and has a value taken to be constant of  $-163.303 \text{ J}\cdot\text{mol}^{-1}\cdot\text{K}^{-1}$  (it will actually change with temperature, but only marginally.) The equation for the reversible OCV is thus [152]:

$$E^0 = 1.229V - 0.8463 \times 10^{-3} \frac{V}{K} (T - 298.15K) \quad (4.14)$$

and the Nernst equation then becomes:

$$E_{Nernst} = 1.229 - 0.8463 \cdot 10^{-3} (T - 298.15) + 4.3087 \cdot 10^{-5} \cdot T \left( \ln(a_{anode, H_2}) + 0.5 \ln(a_{cathode, O_2}) - \ln(a_{cathode, vapour, gen}) \right) \quad (4.15)$$

where  $T$  is the stack temperature (in K). The inclusion of the water activity in the cathode is a modification of the GESSDM, and indeed of all the Nernst voltage equations reported in the literature reviewed for the current research.

The partial pressures at the catalyst surface are assumed to be the same across the entire anode and cathode, respectively, and are given by [152]:

$$\bar{p}_{anode, H_2} = (0.5 P_{H_2O}^{sat}) \left[ \frac{1}{e^{\frac{1.653i}{T^{1.334}}} \cdot x_{anode, H_2O}} - 1 \right] \quad (4.16)$$

and

$$\bar{p}_{cathode, O_2} = P_{cathode} \left[ 1 - x_{cathode, H_2O}^{sat} - x_{cathode, other\ gases} \cdot e^{\frac{0.291i}{T^{0.832}}} \right] \quad (4.17)$$

where  $x_{anode, H_2O}$  and  $x_{cathode, H_2O}$  are the molar fractions of water in the anode and cathode, respectively, and  $x_{cathode, H_2O}^{sat}$  is the molar fraction of water in the air stream at saturation for a given temperature,  $x_{cathode, other\ gases}$  is the molar fraction of other gases (apart from oxygen) in the air stream,  $P_{cathode}$  is the cathode pressure, and  $i$  is the current density (in  $\text{A}\cdot\text{cm}^{-2}$ ). The derivation of Equations (4.16) and (4.17) is based on the Stefan-Maxwell equation and correlations made by Slattery and Bird, and the interested reader is referred to reference [142] for

a more detailed explanation.

The molar fraction of water at saturation in a gas stream for a given temperature and pressure  $P$  is given by

$$x_{H_2O}^{sat} = \frac{P_{H_2O}^{sat}}{P} \quad (4.18)$$

The  $P_{H_2O}^{sat}$  term is determined in a fuel cell by the following empirical equation [152]:

$$\ln(P_{H_2O}^{sat}) = 70.434643 - \frac{7362.6981}{T} + 0.006952085 \cdot T - 9.0000 \cdot \ln T \quad (4.19)$$

Thus, the expression for saturation pressure is a function of stack temperature only.

The molar fraction of other gases (mostly nitrogen gas) in the air stream is given by a log mean average between the molar fraction of other gases in a humidified stream of air at the inlet and the molar fraction at the outlet [152]:

$$x_{cathode, other\ gases} = \frac{x_{cathode, other\ gases, in} - x_{cathode, other\ gases, out}}{\ln\left(\frac{x_{cathode, other\ gases, in}}{x_{cathode, other\ gases, out}}\right)} \quad (4.20)$$

where

$$x_{cathode, other\ gases, in} = (1 - x_{H_2O}^{sat}) \cdot 0.794 \quad (4.21)$$

and

$$x_{cathode, other\ gases, out} = \frac{1 - x_{H_2O}^{sat}}{1 + \left(\frac{\lambda_{air} - 1}{\lambda_{air}}\right)\left(\frac{0.206}{0.794}\right)} \quad (4.22)$$

In Equations (4.21) and (4.22), the 0.794 term refers to the dry molar fraction of other gases in air, while in Equation (4.22), the 0.206 term refers to the dry molar fraction of oxygen in air. The  $\lambda_{air}$  term denotes the stoichiometry of the air stream.

#### 4.2.4 PEM fuel cell terminal voltage

The Nernst voltage described in Equation (4.15) in the previous section is for the reversible case, and in practice is never achieved by a PEMFC during operation. Figure 4-2 below

presents the curve of an actual PEMFC, including irreversibilities (also known as overvoltages) that decrease the voltage at varying amounts of current. There are three main overvoltages as well as an additional source of voltage loss inherent to fuel cells, and these losses will be described in the following sections. The overvoltages have varying effects, depending on the current density. The activation overvoltage dominates at low current densities, the ohmic overvoltage dominates at mid-range current densities, and the concentration overvoltage dominates at high current densities. The internal current and fuel crossover effects are not captured by the GESSDM, and are included as a modification to this model in Section 4.3.1. As can be seen from the figure, the actual open-circuit voltage is less than the theoretical maximum of 1.229 V, and it has a value ranging from 1.195 to 1.166 V for the usual operating temperatures of the PEMFC, which are between 65 and 100 °C. The voltage deviates further as the current is increased, illustrating the effects of the overvoltages.

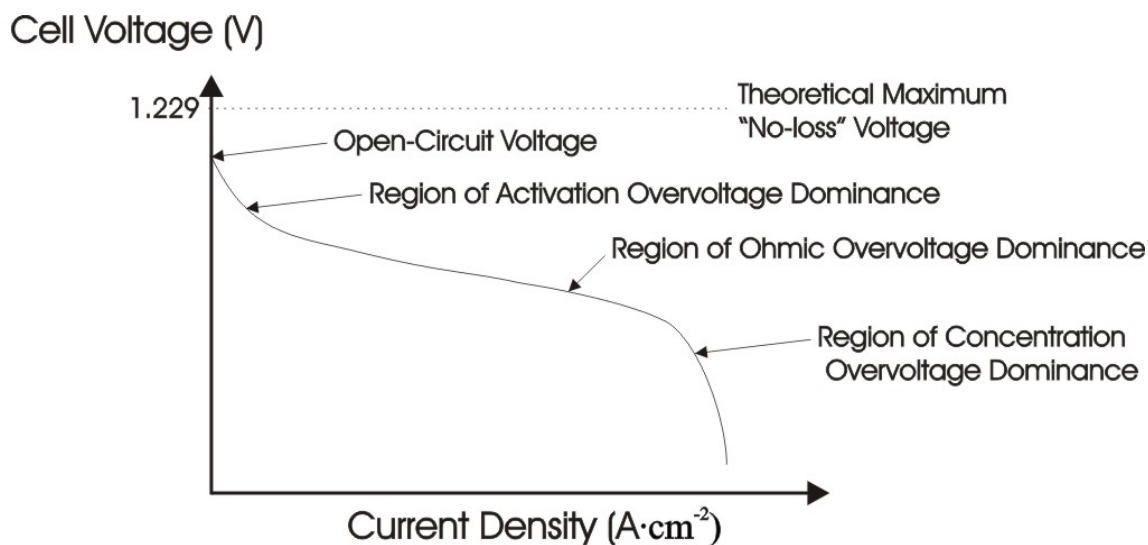


**Figure 4-2. Polarization curve of a PEMFC**

The actual voltage of the fuel cell for the practical fuel cell case is modelled in the GESSDM as [145]:

$$v_{cell} = E_{Nernst} + \psi_{act} + \psi_{ohmic} + \psi_{conc} \quad (4.23)$$

where  $\psi_{act}$  is the activation overvoltage, which is the amount of voltage lost in driving the

reaction;  $\psi_{ohmic}$  is the ohmic overvoltage, which is the amount of voltage lost to the resistance to electron flow in the electrodes and the resistance to ion flow in the electrolyte;  $\psi_{conc}$  is the concentration overvoltage, which is the voltage lost when the concentration of reactant at the electrode is diminished. The losses are discussed in the following sections. The stack voltage is simply the cell voltage multiplied by the number of cells:

$$V_{stack} = v_{cell} n_{cell} \quad (4.24)$$

The gross power output of the fuel cell stack (in W) is given by:

$$\dot{W}_{stack, gross} = I \times v_{cell} \times n_{cell} = I \times V_{stack} \quad (4.25)$$

#### 4.2.5 Activation overvoltage

Some of the voltage created by the reaction of Figure 4-1 is lost to driving the reactions at the electrodes and in driving the flow of electrons either to or from the electrode. This voltage loss is known as activation overvoltage. This loss can be decreased if steps are taken to increase the reaction rates, for example increasing the temperature or pressure in the fuel cell. Improving the catalyst materials and structure would also decrease this overvoltage. For a PEMFC, however, the activation overvoltage irreversibility is inevitably significant. The semi-empirical equation for the activation overvoltage is given by [152]:

$$\psi_{act} = \zeta_1 + \zeta_2 T_{stack} + \zeta_3 T_{stack} \ln(c_{cathode, O_2}) + \zeta_4 T_{stack} \ln(I) \quad (4.26)$$

where  $I$  is the total current and the concentration of dissolved oxygen at the gas/liquid interface is expressed as [152]:

$$c_{cathode, O_2} = \frac{\bar{p}_{cathode, O_2}}{5.08 \times 10^6 \cdot e^{\left(\frac{-498}{T_{stack}}\right)}} \quad (4.27)$$

where the expression for  $\bar{p}_{cathode, O_2}$  is given in Equation (4.17). The  $\zeta$  coefficients are empirically determined for each individual fuel cell stack. The equations for the  $\zeta$  coefficients are [145]:

$$\zeta_1 = -\frac{\Delta G_{c, anode}}{2F} - \frac{\Delta G_{c, cathode}}{\alpha_c nF} \quad (4.28)$$

$$\zeta_2 = \left( \frac{R}{nF} + \frac{R}{\alpha_c nF} \right) \ln A + \frac{R}{nF} \ln(4Fc_{H_2}^*) - \frac{R}{nF} \ln(4F) \quad (4.29)$$

$$\zeta_3 = \frac{R(1-\alpha_c)}{\alpha_c nF} \quad (4.30)$$

$$\zeta_4 = -\left( \frac{R}{2F} + \frac{R}{\alpha_c nF} \right) \quad (4.31)$$

where  $\Delta G_{c, anode}$  is the standard-state free energy of activation for chemisorption ( $\text{J}\cdot\text{mol}^{-1}$ ) at the anode and  $\Delta G_{c, cathode}$  is the same quantity at the cathode,  $\alpha_c$  is the cathodic transfer coefficient, and  $c_{H_2}^*$  is the concentration of protons in the electrolyte membrane, assumed constant. The coefficients have been determined for several stacks, as shown below in Table 4-1. The values determined for the GESSDM in reference [145] are used.

**Table 4-1. Activation overvoltage coefficients**

	$\beta_1$	$\beta_2$	$\beta_3$	$\beta_4$
Amphlett <i>et al.</i> [142], Xue and Dong [153], for Ballard Mark IV stack	-9.514	0.00312	0.0000740	-0.000187
Wang and Dong [154] for the Tri-stream, External manifold, and Radiator stack (TERS) stack	-0.944	0.00354	0.0000785	-0.000196
Fowler <i>et al.</i> [145] for Ballard Mark IV and V stacks	-0.948	†	0.000076	-0.000193

$$\dagger \beta_2 = 0.00295 + 1.97 \times 10^{-4} \cdot \ln A_{active} + 4.3 \times 10^{-5} \cdot \ln c_{H_2}^*$$

#### 4.2.6 Ohmic overvoltage

Another portion of the voltage generated by the reaction of Figure 4-1 is lost due to the resistance to electron flow in the electrodes and graphite collector plates and resistance to ion

flow in the electrolyte. Choosing MEA materials that have high conductivities can reduce the ohmic overvoltage. However, most PEMFCs use the polymeric electrolyte manufactured by Dupont known as Nafion®, and thus there is little flexibility in the electrolyte material choice to decrease the ohmic overvoltage significantly. Decreasing the thickness of the electrolyte does reduce its ohmic resistance to ion flow, but the electrolyte must maintain structural integrity and manufacturability and must prevent reactant crossover. Thus, the electrolyte cannot be made too thin. The ohmic overvoltage can be expressed in accordance with Ohm's Law as [144]:

$$\psi_{ohmic} = \psi_{ohmic}^{electronic} + \psi_{ohmic}^{ionic} + \psi_{ohmic}^{contact} = -I (R_{electronic} + R_{ionic} + R_{contact}) \quad (4.32)$$

The electronic resistance is negligible in comparison to the other two resistances. Reference [155] provides an example of a 3 mm thick moulded graphite/composite bipolar plate with a relatively high electronic resistance of  $8 \text{ m}\Omega \cdot \text{cm}^2$ ; the electronic portion would contribute only 2.4 mV (at  $1 \text{ A} \cdot \text{cm}^{-2}$ ) to the overall ohmic overvoltage. The same reference reports that the ionic and contact resistances are similar in orders of magnitude and that typical values for the total ohmic resistance is  $0.1\text{-}0.2 \text{ }\Omega \cdot \text{cm}^2$  [155]. The GESSDM considers only the ionic resistance, and the contact resistance is discussed in Section 4.3.2.

The ionic resistance term is known to be a complex function of water content and distribution in the membrane, which in turn are functions of the cell operating conditions. A general expression for the ionic resistance of the electrolyte is given by [145]:

$$R_{ionic} = \frac{r_M l}{A_a} \quad (4.33)$$

where  $r_M$  is the membrane-specific resistivity for the flow of hydrated protons (in  $\text{ohm}\cdot\text{cm}$ ),  $l$  is the thickness of membrane (in cm) and  $A_a$  is the active cell area (in  $\text{cm}^2$ ). While the other two terms in Equation (4.33) are known parameters of a specific cell, the term  $r_M$  is difficult to describe phenomenologically, and thus the following semi-empirical expression has been derived [145]:

$$r_M = \frac{181.6 \Omega \cdot \text{cm} \left[ 1 + 0.03(i) + 0.062 \left( \frac{T_{stack}}{303 \text{ K}} \right)^2 i^{2.5} \right]}{\left[ \lambda_{FC, membrane} - 0.634 - 3i \right] \cdot e^{4.18 \left( \frac{T_{stack} - 303 \text{ K}}{T_{stack}} \right)}} \quad (4.34)$$

where again  $i$  is the current density and  $\lambda_{FC, membrane}$  is an adjustable fitting parameter, influenced by the method of manufacture of the membrane and a function of the relative humidity and stoichiometric ratios at the anode and cathode and of the age and use of the membrane. The parameter is usually assigned a value between 10 and 20 [46], and is discussed further in the membrane hydration model of Section 4.3.4. It should be noted that  $\lambda_{FC, membrane}$  and both terms in square brackets are unit-less, as the relationship is empirically derived.

#### 4.2.7 Concentration overvoltage

As the fuel and oxygen are extracted from the gas streams at the anode and cathode, respectively, the initial concentration that satisfies the reaction depicted in Figure 4-1 is diminished, and there is a voltage loss as a result of the pressure drop of the reactant gases. The concentration overvoltage depends on the amount of current drawn from the cell, as well as the physical characteristics of the gas supply systems. The expression used in GESSDM for the concentration overvoltage is given by [46, 155]:

$$\psi_{conc} = \frac{RT_{stack}}{2F} \cdot \ln \left( 1 - \frac{I}{I_L} \right) \quad (4.35)$$

where  $R$  is the universal gas constant (which has a value of  $8.3145 \text{ J} \cdot (\text{mole} \cdot \text{K})^{-1}$ ),  $T_{stack}$  is the stack temperature,  $I$  is the total current in the fuel cell and  $I_L$  is the current at which the fuel is consumed at a rate that is equal to its supply rate; therefore, the current  $I$  can never be greater than  $I_L$ . Equation (4.35) has a weak mechanistic basis, and the  $\psi_{conc}$  term alters the polarization curves in a way that does not closely match experimental values for PEMFCs that use air as a reactant, which is the case for the model. Indeed, the GESSDM has not been validated in the region of high current where the concentration overvoltage dominates [145].

The empirically derived concentration overvoltage relation provided in reference [155] is

therefore suggested as a substitute. The relation is given by

$$\psi_{conc} = m \cdot e^{n \cdot i} \quad (4.36)$$

where  $m$  has been determined experimentally to be  $3 \times 10^{-5}$  V and  $n$  has been similarly determined to be  $0.125 \text{ A} \cdot \text{cm}^{-2}$ . Equation (4.36) has already been used by the fuel cell modelling community [46, 139, 156]. The development of an accurate concentration overvoltage term that is phenomenologically based is a possible area of future research.

### 4.3 Proposed Modifications to the Generalized Electrochemical Steady-State Degradation Model

The form of the model developed by the RMC researchers displays certain limitations. Refinements have been added to make the model more accurate in its application to real-world situations. The proposed refinements are: (1) internal current and fuel crossover, (2) contact resistance, (3) fuel cell transient response effects, (4) membrane hydration model, and (5) channel flow characteristics. Internal currents and fuel crossover are in all likelihood negligible, although this would have to be experimentally determined. The effect of contact resistance is such that the ohmic overvoltage term could double in magnitude. The transient response of the fuel cell to varying levels of power demand is an area of concern where rapid response to changes in throttle application is an extremely important consideration, and the cell transient response formulaic derivation by Pathapati *et al.* is used [157]. Another major concern for PEMFC system designers is ensuring that the level of membrane hydration of the cell is properly controlled and maintained. For normal cell operation, the water content of the membrane must remain within specified limits. When the water content is too great, the electrodes are “flooded”, meaning that the pores in either the catalyst layer or gas diffusion layer (GDL, also known as the porous transport layer (PTL) [158]) are blocked, and the output voltage of the cell drops precipitously. On the other hand, if the water content is too low, the proton conductivity of the membrane will drop sharply because it is directly proportional to the water content; furthermore, the thermal stress placed upon the membrane may cause it to mechanically fail, and

permanent hole damage may form [159, 160]. To address this issue, a membrane hydration model developed by Dutta *et al.* was added to the cell model [161]. The level of membrane and cell hydration levels are intimately related to the flow characteristics in the anode and cathode flow channels. The issue of water management is related to heat management in the stack as well. The heat produced by the electrochemical reaction must be transferred away from the stack in order to maintain the operating temperature within the specified range, as the operating temperature will affect the water content of the membrane. The membrane hydration model is coupled with anode and cathode flow models taken from Pukrushpan *et al.* [162]. Although these models are zero-dimensional and thus do not capture the full three-dimensional phenomena occurring in the flow channels, especially around bends in, for example, serpentine channel bipolar plates, the dynamic transport modelling does improve the model completeness. Furthermore, the humidity calculations allow for a more accurate determination of the Nernst voltage.

#### 4.3.1 Fuel crossover and internal currents

Despite the relative impermeability of the electrolyte to ion conduction, the membrane will always support the conduction of both fuel molecules and electrons as well. The diffusion of hydrogen from the anode side of the MEA to the cathode side without prior ionization is known as *fuel crossover*. The conduction of electrons through the electrolyte without passing through the external circuit, thereby having no effect on the electrical output of the cell, is known as *internal current*. The two phenomena essentially cause the same effect, since the result of a hydrogen gas molecule passing through the electrolyte without reaction and the result of two electrons passing through the electrolyte, short-circuiting the external circuit, are the same. Since there exists an equivalency between the two effects, usually only internal current with the fuel crossover effects incorporated into the overall effect is considered, although a term known as “mixed potential” is introduced in situations where the fuel crossover effect is considered separately [46]. In general, both effects are small, since hydrogen and electron permeation of the membrane rates are orders of magnitude less than hydrogen consumption rate and the electric

current generated. However, the effects are noticeable at elevated temperatures and very low current densities. For example, the OCV will decrease from 1.229 V to 0.97 V for an internal current of  $1 \text{ mA} \cdot \text{cm}^{-2}$  [46].

The result of fuel crossover and internal current is to decrease the voltage, although through different mechanisms. Fuel crossover will result in a reduction in potential of the cathode only, since the hydrogen will not participate in the electrochemical reaction at the anode. The electric current generated will not be affected. By contrast, the electrons passing through the membrane will do so after the electrochemical reactions at the electrodes, and thus both electrode potentials will be reduced [155]. To account for losses due to internal currents and hydrogen crossover, the current in the overvoltage equations (4.26), (4.32), and (4.36) can be modified to include the loss current term; thus, where before the term was  $I$ , the term would then be  $I+I_{loss}$  with the losses included. This loss term would have to be experimentally approximated by measuring the hydrogen consumption of the stack at OCV. Because this measurement has not been performed for the Palcan PC6-1200, the effect is ignored for the current work but could be incorporated into future research to improve the theoretical polarization curve accuracy.

#### 4.3.2 Contact resistance

The contact resistance depends on the clamping pressure between the bipolar plates and electrodes and also on the surface characteristics that determine the effective resistances of the contact surfaces. In order to model the contact resistance, these surface characteristics must be empirically determined. Contact resistance is inversely and non-linearly related to the clamping pressure [163]. An expression for the contact resistance is then given by [164]:

$$R_{contact} = \frac{A_{contact} K G^{D-1}}{\kappa L^D} \left[ \frac{D}{(2-D) p^*} \right]^{\frac{D}{2}} \quad (4.37)$$

where  $A_{contact}$  is the apparent contact area at the interface,  $K$  is a geometric constant,  $G$  is the surface profile topography,  $D$  is the fractal dimension of the surface profile,  $L$  is the length of the profilometric scan taken to obtain the other geometric parameters,  $p^*$  is the ratio of clamping

pressure to compressive modulus of the GDL, and  $\kappa$  is the effective conductivity of the bipolar plate and GDL in contact, given as a function of the bulk conductivities of the two materials [164]:

$$\frac{1}{\kappa} = \frac{1}{2} \left( \frac{1}{\kappa_{bipolar}} + \frac{1}{\kappa_{GDL}} \right) \quad (4.38)$$

Obtaining the parameters for Equations (4.37) and (4.38) is left for future work.

### 4.3.3 Electrochemical dynamic effects

To model the effects of the dynamic stack voltage response to a change in current demand and resultant, subsequent change in reactant flow, a capacitance  $C$  is introduced that signifies the charge double layer capacitance that occurs at the electrode-electrolyte interface of the fuel cell. Because the electrode and the electrolyte are different materials, there must be either a build-up of charge on the surfaces or a transfer of charge between the two materials. The accumulation of charge at this junction is known as the charge double layer, and such an accumulation of charge generates a voltage. In a PEMFC, the electrons will accumulate at the surface of the cathode and attract the  $H^+$  ions in the electrolyte so that the reduction of the  $O_2$  molecules can occur according to the bottom reaction of Figure 4-1. The charge double layer is thus necessary for the reaction to occur, even if it causes a reduction in the resulting voltage of the fuel cell concurrently. At higher current densities, more charge must accumulate for the reaction to occur, and this is why the activation overvoltage increases with current density, albeit at much lower rate than the large increase that occurs at very low current densities. The catalytic activity can be seen as an important cell parameter since it affects greatly the probability of the reaction [162].

The double layer charge is in effect a collection of electrical charge, and as such can be modelled using a conventional electrical capacitor. When the current through a capacitor changes, there is a lag between this change and the response-following of the capacitor to either dissipate or build up the charge, depending on whether the current is decreasing or increasing, respectively. The voltage associated with the capacitor will have the same time lag. The

charge double layer is modelled conceptually through the use of an equivalent RC circuit, as shown in Figure 4-3 below. As can be seen from the figure, the ohmic overvoltage is not affected by the charge double layer transients: a sudden change in current will cause the ohmic overvoltage to respond instantaneously.

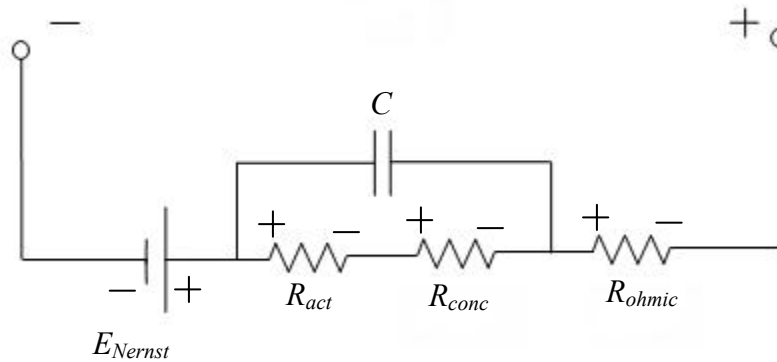


**Figure 4-3. Fuel cell equivalent RC circuit**

The capacitance of the capacitor is given by [157]:

$$C = \varepsilon \frac{A_a}{d} \quad (4.39)$$

where  $\varepsilon$  is the electrical permittivity,  $A_a$  is again the active area of the electrode, and  $d$  is the separation distance of the “plates”, or the width of the double charge layer. Theoretical predictions of  $d$  are 3-10 Å, while practical measurements have resulted in a value of approximately 45 Å [165]. The permittivity of a material is given by [166]:

$$\varepsilon = \varepsilon_0 (1 + \chi_e) \quad (4.40)$$

where  $\varepsilon_0$  is the permittivity of free space and has a value of  $8.85 \times 10^{-12} \text{ C}^2 \cdot \text{N}^{-1} \cdot \text{m}^{-2}$ , and  $\chi_e$  is the electric susceptibility of a medium that depends on its microscopic structure. A parameter known as the dielectric constant is often given in tabled form, and can be used to find the permittivity of a material using the relation [166]:

$$K = 1 + \chi_e = \frac{\varepsilon}{\varepsilon_0} \quad (4.41)$$

The capacitance is usually on the order of a few Farads, which is a fairly high capacitance

value. The activation resistance term  $R_{act}$  is then defined as [157]:

$$R_{act} = -\frac{\psi_{act}}{I} \quad (4.42)$$

The concentration activation term  $R_{conc}$  is similarly defined:

$$R_{conc} = -\frac{\psi_{conc}}{I} \quad (4.43)$$

A differential equation that allows for a model of the time lag of the voltage response of the fuel cell due to the delayed reaction of the activation and concentration overvoltage terms is then:

$$\frac{dv_{dyn}}{dt} = \frac{I}{C} - \frac{v_{dyn} - v_0}{C(R_{act} + R_{conc})} \quad (4.44)$$

where  $v_0$  is the voltage from the previous time period,  $v_{dyn}$  is the dynamic overvoltage term, and it takes the place of  $\psi_{act}$  and  $\psi_{conc}$  in Equation (4.23), giving a cell voltage of:

$$v_{cell} = E_{Nernst} - v_{dyn} + \psi_{ohmic} \quad (4.45)$$

The dynamic response of the fuel cell stack is captured by a calculation of the time required for the stack to respond to a change in current demand. The differential Equation (4.44) is solved using the known quantities for the initial current and final current input to the model and the static cell voltages at both current demands from Equation (4.23). The expression for the response time is determined to be

$$t_{response, cell} = \frac{v_{dyn} - v_0}{\frac{I_f + I_i}{2C} - \frac{v_{dyn} - v_0}{2C(R_{act} + R_{conc})}} \quad (4.46)$$

where  $\Delta v_{cell}$  is the change in the steady-state values of voltage of the two current demands, and  $I_i$  and  $I_f$  are the currents demanded of the stack at the beginning and ending of the change, respectively. The solution of Equation (4.46) to the differential Equation (4.44) is derived by assuming that  $t_{response, cell}$  is small enough that the relationship between  $v_{cell}$  at time 0 (before the change in current) and at time  $t_{response, cell}$  is linear. This allows for the integral of the equation to be calculated from the area of the two parallelograms formed on the  $v_{cell}$  versus time and  $I$  versus time graphs. All subsequent response times use the same method and assumptions. The response time is considered to be the response time for the entire stack, as all of the cells are

assumed to exhibit the same time constant.

#### 4.3.4 Membrane hydration model

The production of water is both a benefit and a hindrance to the operation of the fuel cell, as a delicate balance must be struck between having enough moisture to maintain the humidity of the membrane while also ensuring that the MEA is not flooded with excess water. Either situation will result in a reduction in performance of the fuel cell operation. The model assumes that the membrane is initially fully hydrated. The membrane hydration module calculates the mass flow of water across the membrane as well as the water content of the membrane. The model assumes uniformity in water content over the surface of the membrane, and the two outputs of the module are functions of stack current and temperature, as well as the relative humidities of the fluids flowing through the anode and cathode channels [162]. The model also ignores the effects of different pressures in the anode and cathode.

There are five sources that in combination determine the amount of water in the MEA:

- humidity of hydrogen reactant
- humidity of air reactant
- water formation at the cathode
- electro-osmotic drag
- back diffusion

The control of the humidity of the reactants is such that both are assumed to be at 100% relative humidity. The water formation at the cathode is considered in the cathode flow module of Section 4.3.6. Water transport across the Nafion® membrane is accomplished by the two last mechanisms: electro-osmotic drag and back diffusion. In electro-osmotic drag, the water molecule is transported along with the protons that migrate from the anode to the cathode to complete the electrochemical reaction. The molar rate of water transported in this manner is given by [161]

$$\dot{N}_{\text{vapour, osmotic}} = n_d \frac{i}{F} \quad (4.47)$$

where  $n_d$  is the number of water molecules that migrates with each proton (known as the electro-osmotic drag coefficient.) The electro-osmotic drag coefficient varies with the water content of the membrane, which in turn depends on the humidity of the gas flows on either side. The electro-osmotic drag coefficient is calculated from the empirical relationship [161]:

$$n_d = 0.0029\lambda_{FC, membrane}^2 + 0.05\lambda_{FC, membrane} - 3.4 \times 10^{-19} \quad (4.48)$$

where  $\lambda_{FC, membrane}$  is the water content of the membrane first described by Equation (4.34).

Back diffusion occurs when the water that forms at the cathode at the completion of the electrochemical reaction causes the water concentration to be higher than it is at the anode. This water concentration gradient forces water from the cathode to the anode. The molar rate of water that is transferred is given by [162]

$$\dot{N}_{vapour, back\ diffusion} = D_{FC, H_2O} \frac{c_{cathode, H_2O} - c_{anode, H_2O}}{t_{FC, membrane}} \quad (4.49)$$

where  $D_{FC, H_2O}$  is the diffusion coefficient of water in the membrane,  $c_{cathode, H_2O}$  and  $c_{anode, H_2O}$  are the concentrations of water at the cathode and anode, respectively, and  $t_{FC, membrane}$  is the thickness of the membrane. Equation (4.49) assumes that the concentration gradient is linear across the thickness of the membrane, a reasonable approximation [162]. The diffusion coefficient is calculated from [161]

$$D_{FC, vapour} = D_{FC, \lambda} e^{2416 \left( \frac{1}{303} - \frac{1}{T_{stack}} \right)} \quad (4.50)$$

where

$$D_{FC, \lambda} = \begin{cases} 10^{-10}, & \lambda_{FC, membrane} < 2 \\ 10^{-10} (1 + 2(\lambda_{FC, membrane} - 2)) & 2 \leq \lambda_{FC, membrane} \leq 3 \\ 10^{-10} (3 - 1.67(\lambda_{FC, membrane} - 3)) & 3 \leq \lambda_{FC, membrane} < 4.5 \\ 1.25 \times 10^{-10} & 4.5 \leq \lambda_{FC, membrane} \end{cases} \quad (4.51)$$

The concentrations are calculated from [161]

$$c_{anode, H_2O} = \frac{\rho_m}{M_m} \lambda_{anode} \quad (4.52)$$

for the anode and

$$c_{cathode, H_2O} = \frac{\rho_m}{M_m} \lambda_{cathode} \quad (4.53)$$

for the cathode, where  $\rho_m$  is the membrane dry density and  $M_m$  is the membrane dry weight, and  $\lambda_{anode}$  and  $\lambda_{cathode}$  are the water content in the anode and cathode, respectively.

The water content parameters required by both terms are calculated by [167]

$$\lambda_j = \begin{cases} 0.043 + 17.81a_j - 39.85a_j^2 + 36.0a_j^3, & 0 < a_j \leq 1 \\ 14 + 1.4(a_j - 1), & 1 < a_j \leq 3 \end{cases} \quad (4.54)$$

where the subscript  $j$  corresponds either to *anode*, *cathode*, or *membrane*, and where the water activity for steam was defined in Equation (4.10). The membrane water activity is considered to be an average of the anode and cathode activities:

$$a_{membrane} = \frac{a_{anode} + a_{cathode}}{2} \quad (4.55)$$

The value of the anode and cathode activities are determined in the anode and cathode flow models to follow in Section 4.3.5 and Section 4.3.6, where the activity is equal to the relative humidity,  $\varphi$ .

The molar flow rate of water across the membrane (where positive means that the direction is from anode to cathode) is then given by [162]

$$\dot{N}_{membrane, vapour} = n_d \frac{i}{F} - D_{FC, H_2O} \frac{(c_{cathode, H_2O} - c_{anode, H_2O})}{t_{FC, membrane}} \quad (4.56)$$

and the mass flow rate is then

$$\dot{m}_{membrane, vapour} = \dot{N}_{membrane, vapour} \cdot M_{H_2O} \quad (4.57)$$

where  $M_{H_2O}$  is the water vapour molar mass (with a value of 18.02 g·mole<sup>-1</sup>). The value of  $\lambda_{FC, membrane}$  at full humidification is 14.6 and so  $\lambda_{FC, membrane}$  will initially be assigned this value [145]. The anode and cathode flow modules use this value to determine the relative humidity at both electrodes, and the membrane hydration module uses these values to determine the water mass flow in a calculation loop for each time step of the overall model.

#### 4.3.5 Anode flow module

This module describes the flow phenomena through the anode. The anode flow model depicts the flow of hydrogen through the anode using conservation of mass and the characteristic properties of the fluids. The gases inside are assumed to be ideal. The temperature inside the anode is assumed to be the same as the temperature of the stack, and is therefore assumed constant. Also, the sum of the hydrogen and water vapour pressure at the outlet is assumed to be the same as the value of total pressure inside the anode. The same assumption is made for the temperature, humidity of the air, and the oxygen mole fraction. Finally, if the water transferred from the cathode humidifies the internal anode hydrogen stream until the relative humidity reaches 100%, any additional vapour added to the hydrogen stream condenses and accumulates in the flow channel.

The following assumptions are held for this and all subsequent fluid flow modules [168]:

- All fluid flows are fully developed laminar flow
- All gases obey the ideal gas law
- The kinetic and potential energies of the gases are considered negligible
- No external work is done on the system
- Flow specific heats are assumed to be constant throughout

The hydrogen flow module is simplified by assuming that because there is a high-pressure storage tank with a valve-controllable flow that will ensure that the desired stoichiometry is maintained. This control is assumed to be instantaneous; thus, the transient flow behaviour in the manner developed for the air flow module is unnecessary for the hydrogen flow, and no response to a change in current demand is calculated. The flow model begins with the Conservation of Mass Law, for hydrogen in the anode:

$$\frac{dm_{anode, H_2}}{dt} = \dot{m}_{anode, H_2, in} - \dot{m}_{anode, H_2, out} - \dot{m}_{anode, H_2, react} \quad (4.58)$$

The mass flow of hydrogen into the anode is given by [46]:

$$\dot{m}_{anode, H_2, in} = \frac{M_{H_2} I \lambda_{H_2} n_{cell}}{2F} \quad (4.59)$$

where  $\lambda_{H_2}$  is the stoichiometry of the hydrogen gas, and is a parameter defined for the system.

The rate of hydrogen consumption in the electrochemical reaction is given by [46]:

$$\dot{N}_{anode, H_2, react} = \frac{I \cdot n_{cell}}{2F} \quad (4.60)$$

The Conservation of Mass Law applied to the water content of the anode is

$$\frac{dm_{anode, H_2O}}{dt} = \dot{m}_{anode, vapour, in} - \dot{m}_{anode, vapour, out} - \dot{m}_{membrane, vapour} \quad (4.61)$$

where the membrane vapour term comes from the membrane hydration module. The anode can contain water in both vapour and liquid forms. It is assumed that no liquid will exit the anode: all exiting water will be in vapour form. The maximum amount of water that the hydrogen can contain is determined from [162]:

$$m_{anode, vapour, max} = \frac{P_{H_2O}^{sat} V_{anode}}{R_{vapour} T_{stack}} \quad (4.62)$$

where  $R_{vapour}$  is the vapour gas constant, with a value of  $461.5 \text{ J} \cdot \text{kg}^{-1} \cdot \text{K}^{-1}$ . If the mass of water is greater than the amount of Equation (4.85), it is assumed that it will condense instantaneously and will accumulate inside the anode. The mass of water inside the anode is calculated from one of two Equations [162]:

$$\begin{aligned} m_{anode, vapour} &= m_{anode, H_2O}; \quad m_{anode, liquid} = 0 && \text{if } m_{anode, H_2O} \leq m_{anode, vapour, max} \\ m_{anode, vapour} &= m_{anode, vapour, max}; && \text{if } m_{anode, H_2O} > m_{anode, vapour, max} \\ m_{anode, liquid} &= m_{anode, H_2O} - m_{anode, vapour} \end{aligned} \quad (4.63)$$

The partial pressure of the vapour at the inlet is determined from the relative humidity of 100% to be equal to the saturation pressure at the stack temperature. The partial pressure inside the anode is then determined from the Ideal Gas Law:

$$\bar{P}_{anode, vapour} = \frac{m_{anode, vapour} R_{vapour} T_{stack}}{V_{anode}} \quad (4.64)$$

The total pressure inside the anode is the sum of the partial pressures of hydrogen and

vapour from Equations (4.16) and (4.64)

$$P_{anode} = \bar{p}_{anode, H_2} + \bar{p}_{anode, vapour} \quad (4.65)$$

The humidity of the stream at the anode outlet is given by [162]

$$\Gamma_{anode, out} = \frac{M_{vapour}}{M_{H_2}} \frac{\bar{p}_{anode, vapour}}{\bar{p}_{anode, H_2}} \quad (4.66)$$

The outlet hydrogen flow of the anode depends on the outlet design of the stack. A PEMFC can be operated *dead-ended* wherein a purge valve periodically allows for the mixture of unused hydrogen fuel and water to be emitted. The closed valve will create a build-up of pressure in the system that is periodically released by opening the valve. For a stoichiometric ratio of  $\lambda_{H_2}$ , controlled by the hydrogen flow valve, the mass flow out of the anode is [155]:

$$\dot{m}_{anode, H_2, out} = \dot{m}_{anode, H_2, in} - \dot{m}_{anode, H_2, react} - \dot{m}_{anode, H_2, loss} \quad (4.67)$$

where  $\dot{m}_{anode, H_2, loss}$  is the mass flow of fuel lost to hydrogen crossover. The total mass flow out of the anode is then

$$\dot{m}_{anode, out} = \dot{m}_{anode, H_2, out} (1 + \Gamma_{anode, out}) \quad (4.68)$$

and the mass flow of vapour out of the anode is given by

$$\dot{m}_{anode, vapour, out} = \dot{m}_{anode, out} - \dot{m}_{anode, H_2, out} \quad (4.69)$$

However, the purge valve is normally closed, and only opens periodically to purge the outlet mixture of the anode. The mass flows determined in Equations (4.67)-(4.69) occur during the purges, where  $\tau_{purge}$  is the duration and  $f_{purge}$  is the frequency of each purge. Therefore, the periodic mass flows in these equations are multiplied by  $\tau_{purge} f_{purge}$  to obtain the resultant mass flows.

#### 4.3.6 Cathode flow module

The cathode flow module models the flow of air and reaction products through the cathode using conservation of mass and the characteristic properties of the various substances [162]. The same assumptions that were made for the anode apply to the cathode as well. The

temperature inside the cathode is assumed to be the same as the temperature of the stack, and is therefore assumed constant. Also, the sum of the air and water vapour pressure at the outlet is assumed to be the same as the value of total pressure inside the cathode. The same assumption is made for the temperature, humidity of the air, and the oxygen mole fraction. Finally, the water at the cathode is assumed to humidify the internal cathode air stream until the relative humidity reaches 100%, at which point it condenses and accumulates in the cathode flow channel.

To begin, the mass conservation laws for oxygen in the cathode is used:

$$\frac{dm_{cathode, O_2}}{dt} = \dot{m}_{cathode, O_2, in} - \dot{m}_{cathode, O_2, out} - \dot{m}_{cathode, O_2, reacted} \quad (4.70)$$

The molar flow of oxygen into the cathode is given by [46]:

$$\dot{N}_{cathode, O_2, in} = \frac{I \cdot \lambda_{air} \cdot n_{cell}}{4F} \quad (4.71)$$

The mass flow of oxygen into the cathode is then

$$\dot{m}_{cathode, O_2, in} = M_{O_2} \cdot \dot{N}_{cathode, O_2, in} \quad (4.72)$$

The rate of air consumption in the electrochemical reaction is given by [46]

$$\dot{N}_{cathode, O_2, react} = \frac{I \cdot n_{cell}}{4F} \quad (4.73)$$

The outlet molar flow of oxygen is given by the subtraction of the amount reacted from the supply:

$$\dot{N}_{cathode, O_2, out} = \dot{N}_{cathode, O_2, in} - \dot{N}_{cathode, O_2, react} \quad (4.74)$$

The mass flow of oxygen out of the cathode is then

$$\dot{m}_{cathode, O_2, out} = M_{O_2} \cdot \dot{N}_{cathode, O_2, out} \quad (4.75)$$

The mass fraction of oxygen,  $y_{cathode, O_2, in}$ , defined as the ratio of the mass of oxygen to the mass of dry air, is given by [162]

$$y_{cathode, O_2, in} = \frac{m_{O_2}}{m_{air}} = \frac{0.206M_{O_2}}{0.206M_{O_2} + 0.794M_{other\ gases}} \quad (4.76)$$

where  $M_{other\ gases}$  is easily calculated using the composition of dry air, usually taken to be  $28.97 \times 10^{-3} \text{ kg} \cdot \text{mole}^{-1}$ . The mass flow of dry air entering the cathode is then calculated by

$$\dot{m}_{cathode, air, in} = \frac{\dot{m}_{cathode, O_2, in}}{y_{cathode, O_2, in}} \quad (4.77)$$

The partial pressure of oxygen inside the cathode was given by Equation (4.17) and will be used to determine the inlet partial pressure of the dry air using:

$$\bar{p}_{cathode, air, in} = \frac{\bar{p}_{cathode, O_2, in}}{0.206} \quad (4.78)$$

Next, the Conservation of Mass Law of the other gases in dry air are considered:

$$\frac{dm_{cathode, other\ gases}}{dt} = \dot{m}_{cathode, other\ gases, in} - \dot{m}_{cathode, other\ gases, out} \quad (4.79)$$

The inlet mass flow of the other gases in dry air can use the result of Equation (4.77):

$$\dot{m}_{cathode, other\ gases, in} = (1 - y_{cathode, O_2, in}) \dot{m}_{cathode, air, in} \quad (4.80)$$

The partial pressure of the other gases is found by using the ideal gas law for gas mixtures:

$$\bar{p}_{cathode, other\ gases, in} = \bar{p}_{cathode, air, in} - \bar{p}_{cathode, O_2, in} \quad (4.81)$$

where this partial pressure will not change as the other gases pass through the cathode without reacting.

The conservation equation for water in the cathode is given by

$$\frac{dm_{cathode, H_2O}}{dt} = \dot{m}_{cathode, H_2O, in} - \dot{m}_{cathode, H_2O, out} + \dot{m}_{cathode, vapour, gen} + \dot{m}_{membrane, vapour} \quad (4.82)$$

The cathode can contain water in both vapour and liquid forms. It is assumed that no liquid will exit the cathode. All exiting water will be in vapour form. The water is produced at a rate of two moles for every four electrons released at the anode. The equation for water production is given by [46]:

$$\dot{m}_{cathode, vapour, gen} = \frac{I \cdot n_{cell} \cdot M_{H_2O}}{2F} \quad (4.83)$$

where  $M_{H_2O}$  is the molar mass of water (which has a value of  $18.018 \times 10^{-3} \text{ kg} \cdot \text{mole}^{-1}$ ). The cathode vapour generation equation can be integrated with respect to time to determine the mass at any given instant. The partial pressure of the generated vapour can then be determined from the Ideal Gas law:

$$\bar{P}_{cathode, vapour, gen} = \frac{m_{cathode, vapour, gen} R_{vapour} T_{stack}}{V_{cathode}} \quad (4.84)$$

This value is then used to calculate the generated vapour activity used for determining the Nernst voltage of Equation (4.15).

The maximum amount of water that the air can contain is determined from [162]

$$m_{cathode, vapour, max} = \frac{P_{H_2O}^{sat} V_{cathode}}{R_{vapour} T_{stack}} \quad (4.85)$$

If the mass of water is greater than the amount of Equation (4.85), it is assumed that it will condense instantaneously and will accumulate inside the cathode. The mass of water inside the cathode is then calculated from one of two equations [162]:

$$\begin{aligned} m_{cathode, vapour} &= m_{cathode, H_2O}; \quad m_{cathode, liquid} = 0 && \text{if } m_{cathode, H_2O} \leq m_{cathode, vapour, max} \\ m_{cathode, vapour} &= m_{cathode, vapour, max}; && \text{if } m_{cathode, H_2O} > m_{cathode, vapour, max} \\ m_{cathode, liquid} &= m_{cathode, H_2O} - m_{cathode, vapour} \end{aligned} \quad (4.86)$$

The partial pressure of the vapour is then determined from the Ideal Gas law:

$$\bar{P}_{cathode, vapour} = \frac{m_{cathode, vapour} R_{vapour} T_{stack}}{V_{cathode}} \quad (4.87)$$

The total pressure in the cathode can now be calculated [162]:

$$P_{cathode} = \bar{P}_{cathode, air} + \bar{P}_{cathode, vapour} \quad (4.88)$$

where

$$\bar{P}_{cathode, air} = \bar{P}_{cathode, O_2} + \bar{P}_{cathode, Other\ gases} \quad (4.89)$$

The mass flow out of the cathode is then calculated [162]:

$$\begin{aligned}
\dot{m}_{cathode, out} &= \frac{C_D A_T P_{cathode}}{\sqrt{RT_{comp, out}}} \left( \frac{P_{return}}{P_{cathode}} \right)^{\frac{1}{\gamma}} \times \\
&\quad \left\{ \frac{2\gamma}{\gamma-1} \left[ 1 - \left( \frac{P_{rm}}{P_{cathode}} \right)^{\frac{\gamma-1}{\gamma}} \right] \right\}^{\frac{1}{2}} && \text{if } \frac{P_{return}}{P_{cathode}} > \left( \frac{2}{\gamma+1} \right)^{\frac{\gamma}{\gamma-1}} \\
&= \frac{C_D A_T P_{cathode}}{\sqrt{RT_{comp, out}}} \gamma^{\frac{1}{2}} \left( \frac{2}{\gamma+1} \right)^{\frac{\gamma+1}{2(\gamma-1)}} && \text{if } \frac{P_{return}}{P_{cathode}} \leq \left( \frac{2}{\gamma+1} \right)^{\frac{\gamma}{\gamma-1}}
\end{aligned} \tag{4.90}$$

where  $P_{return}$  is the return manifold pressure, calculated in the return manifold module of Section 5.3.3, and passed to this module. The humidity at the cathode outlet is given by [162]

$$\Gamma_{cathode, out} = \frac{M_{vapour}}{M_{cathode, air}} \frac{\bar{P}_{cathode, vapour}}{\bar{P}_{cathode, air}} \tag{4.91}$$

The mass flow of air at the cathode outlet is then

$$\dot{m}_{cathode, air, out} = \frac{1}{1 + \Gamma_{cathode, out}} \dot{m}_{cathode, out} \tag{4.92}$$

while the mass flow of vapour at the outlet is

$$\dot{m}_{cathode, vapour, out} = \dot{m}_{cathode, out} - \dot{m}_{cathode, air, out} \tag{4.93}$$

The mass fraction of oxygen at the outlet is [162]:

$$y_{cathode, O_2, out} = \frac{x_{cathode, O_2, out} M_{O_2}}{x_{cathode, O_2, out} M_{O_2} + (1 - x_{cathode, O_2, out}) M_{other\ gases}} \tag{4.94}$$

where the molar fraction of oxygen is

$$x_{cathode, O_2, out} = \frac{\bar{P}_{cathode, O_2}}{\bar{P}_{cathode, air}} \tag{4.95}$$

The mass flow of oxygen out of the cathode is then

$$\dot{m}_{cathode, O_2, out} = y_{cathode, O_2, out} \dot{m}_{cathode, air, out} \tag{4.96}$$

In order to calculate the time response to a change in current, the change in pressure of the cathode is used [162]:

$$\frac{dP_{cathode}}{dt} = \frac{\gamma R_{air}}{V_{cathode}} \left( \dot{m}_{cathode, in} T_{cathode, in} + \dot{m}_{membrane, H_2O} T_{membrane} - \dot{m}_{cathode, out} T_{cathode, out} \right) \quad (4.97)$$

The time response to a change in current demand is then given by

$$t_{response, cathode} = \frac{2V_{cathode} \Delta P_{cathode}}{\gamma R_{air} \left[ \begin{array}{l} \left( \dot{m}_{cathode, in, final} T_{cathode, in, final} + \dot{m}_{cathode, in, initial} T_{cathode, in, initial} \right) + \\ \left( \dot{m}_{membrane, H_2O, final} T_{membrane, H_2O, final} + \dot{m}_{membrane, H_2O, initial} T_{membrane, H_2O, initial} \right) - \\ \left( \dot{m}_{cathode, out, final} T_{cathode, out, final} + \dot{m}_{cathode, out, initial} T_{cathode, out, initial} \right) \end{array} \right]} \quad (4.98)$$

The response time of the cathode flow to a change in current will also affect the concentration overvoltage response as well. It is unclear at present how to model this relationship.

## Chapter 5 Fuel Cell System Modelling

The stack model is incorporated into the FCS model in order to predict the performance of the entire system. The system model can be used to achieve several goals, such as sizing components and developing control strategies that help optimize the system for both cost and performance.

### 5.1 Previous Fuel Cell System Modelling

The majority of papers on the subject of FCS modelling apply the system models to FCVs (or FCHVs) and discuss the logistics of FCV automotive adoption. A smaller number of articles describe technical efforts to develop the technology. The models have concentrated on stack and balance of plant (BOP) component sizing [124, 169-171], on exploring hybridization issues [51, 172, 173], or on simulation studies [174-176]. A major limitation of these models is that the operation is steady-state for the FCS; this has obvious implications for the suitability of the models to actual vehicle situations. Other models [116, 177-181] have considered the transient response of FCSs, but all use simplified semi-empirical models similar to those of Kim *et al.*, Lee *et al.* and Squadrito *et al* [138-140].

There are several papers that approach the issue from a systems-only perspective, and do not directly address the application to which the system is to be applied. Hussein *et al.* [182] performed an interesting thermodynamic analysis that provides a formulation of the exergetic efficiency of a FCS. The accuracy is compromised, however, by the assumptions that are made. For example, it is assumed that 20% of the heat produced by the stack is transferred to the surroundings and to the cathodic air stream through natural convection and radiation while the remaining 80% is transferred to the cooling system fluid. Although this ratio may be approximately correct and largely based on experimental values, a more rigorous investigation is warranted; the model employed for the analysis is relatively simplistic. The author believes that the intent of the paper was to demonstrate the usefulness of exergy analysis in a qualitative,

not quantitative manner. Moreover, Hussein *et al.* made errors in their formulation, specifically in the exergy balance and efficiency equations. However, exergy analysis is an excellent method for determining where the largest improvements in efficiency potential exist. Eborn *et al.* [183] discuss the work conducted at the private company United Technologies, although the discussion is limited because of proprietary concerns and little information is given. The choice of modelling software, Dymola, is quite interesting for reasons that will become clear in Section 9.6.1. Turner *et al.* [184] give a rudimentary explanation of the work performed at Texas Tech University; however, the level of detail is low and very little can be gleaned from the article. Jossen *et al.* [185] use the semi-empirical model of Kim *et al.* to explore hybrid power systems of battery and fuel cell, although other BOP components are not discussed. Pukrushpan *et al.* [186] developed a FCS model to be used in a control study that includes transient effects of various flow phenomena; however, heat transfer effects (and corresponding cooling system parasitic power) and reactant pump parasitic powers were not considered. This research group has published several articles and an entire book on the subject of control strategies for FCVs. It should be noted that the results are all theoretical in nature; no experimental validation has taken place. However, the efforts are useful and information has been drawn from these sources for the current research.

## 5.2 Fuel Cell System Model

In this section, the fuel cell system is modelled. The flows of air, hydrogen and water through the system are modelled, as are the auxiliary components of the FCS and how they are integrated into the overall FCS. The flow models include the manifolds through which the reactants and products pass upstream and downstream of the stack, respectively. The BOP components include: a compressor to bring the reactant air to the required pressure, a cooling system (consisting of a water pump and radiator fan) to maintain the required operating temperature, and two humidifiers to ensure the proper level of water vapour in, and temperature of, the reactants. An attempt was made to include the time responses of these components, and

combined with the dynamic model of the voltage response, described in section 4.3.3, will allow for a time response of the system to a change in demanded current. At present, the transient component of the model has not been implemented. The system equations have been programmed in MATLAB, and the stack MATLAB functions have been coupled to the system MATLAB functions.

The schematic for a fuel cell system including flows and BOP components is shown below in Figure 5-1. Included in the figure are the hydrogen gas and air loops, the humidification system loop, and the cooling system.

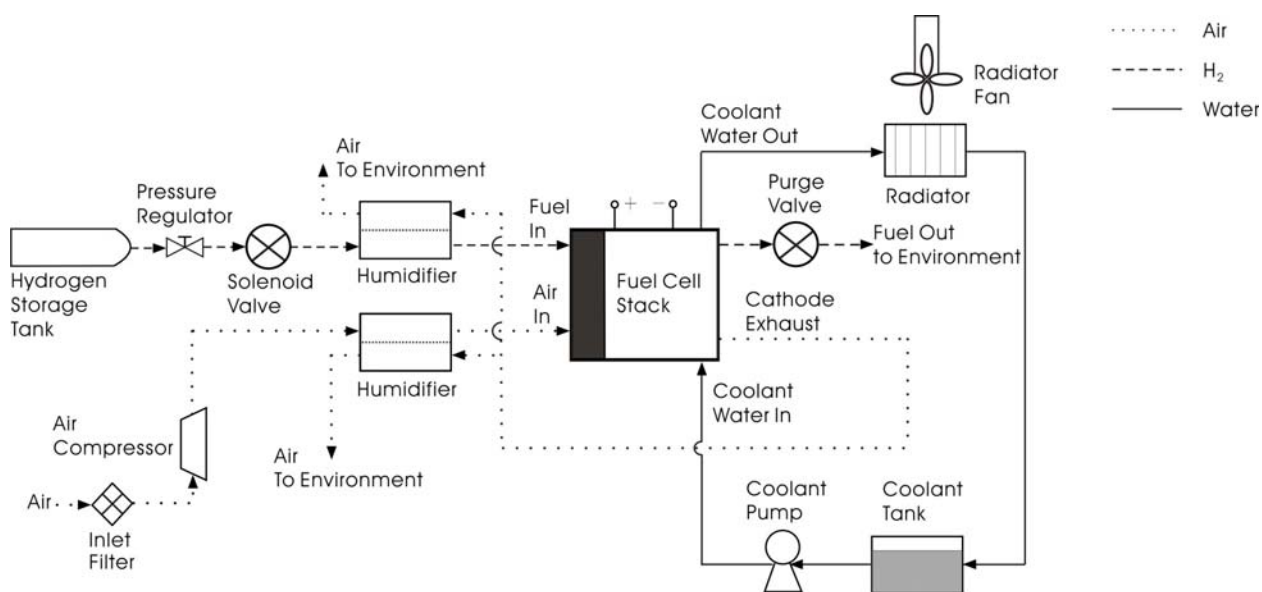


**Figure 5-1. Fuel cell system schematic**

The BOP components draw power from that produced by the fuel cell operation itself, thereby reducing the overall power output. The released hydrogen gas is at a pressure similar to that required of the stack, and thus a compressor for the anode side of the cell is often unnecessary; a pressure regulator and solenoid valve suffice in this case. There are several competing technologies for hydrogen storage, and a complex model of a chosen technology is considered unnecessary for this research. Instead, the hydrogen is simply assumed to be

available to the system. Further research could incorporate a full hydrogen storage model. In Figure 5-1, the hydrogen that does not take part in the electrochemical reaction is vented to the atmosphere. However, it is possible to allow for this wasted hydrogen gas to be combined with the pressurized hydrogen through the use of a re-circulation system. An optional re-circulation module is included in the model. Finally, the air filter is shown for completeness; it is assumed to impose negligible physical changes to the model. This assumption is potentially contradicted by research such as that presented in reference [187], where an air filter can cause a loss of up to 70% of the total power in an air handling unit. Future research could include an analysis of the losses associated with this component.

The following sections describe the various modules of which the overall FCS is comprised. The four main sections will be the air flow module, hydrogen flow module, humidification module and coolant loop module. The various BOP components were modelled and the models programmed into MATLAB. The models are based on components chosen by Pukrushpan *et al.* [152].

### **5.3 Oxidant Flow Module**

The oxidant flow module models the flow of air from the atmosphere, through the system, and then to the atmosphere at the end. The system components, whose functions are described mathematically in the air flow module, are the compressor, supply manifold, return manifold, humidifier pump and humidifier.

#### **5.3.1 Compressor module**

There are many different types of compressors, as the technology is mature and applied in many other applications, in particular diesel engines [46]. The compressor model employed in the research is derived from previous work done by Pukrushpan *et al.*, based on the Jensen and Kristensen method [162]. The structure of the model is comprised of two elements: (1) a static compressor mapping function that determines required compressor power from the rate and

temperature of the air flow through the compressor dictated by the upstream fuel cell stack, and (2) a dynamic lumped parameter model that determines the compressor speed. The speed of the latter is fed into the compressor mapping function to obtain the power [162]. The model has several simplifying assumptions: 1) the compression process is adiabatic and isentropic, 2) the change in kinetic energy of the gas as it flows through the compressor is negligible, and 3) the gas is an ideal gas, such that the specific heat at constant pressure is a constant [46].

The inputs to the compressor module are the atmospheric pressure and temperature, assumed to be STP, the voltage input to the compressor from the fuel cell stack, and the downstream pressure of the supply manifold,  $P_{supply}$ , that feeds air into the heat exchanger.

The expression for the compressor power is given as [150]:

$$\dot{W}_{comp} = c_{p,air} \dot{m}_{comp,out} \frac{T_{atm}}{\eta_{comp}} \left( \left( \frac{P_{supply}}{P_{atm}} \right)^{\frac{\gamma-1}{\gamma}} - 1 \right) \quad (5.1)$$

where  $\gamma$  is the isentropic compression ratio ( $c_p/c_v=1.4$  for air),  $T_{atm}$  and  $P_{atm}$  are the temperature and pressure of the input air, respectively (assumed STP). The mass flow rate is the mass flow of air exiting the compressor and is the mass flow in the supply manifold. It is also assumed that there is no mass build-up inside the compressor such that the mass flow into the compressor is the same as the mass flow out. The efficiency term  $\eta_{comp}$  would be obtained from a compressor efficiency map using the mass flow rate and pressure ratio across the compressor. The power consumed by the compressor is further defined as

$$\dot{W}_{comp} = \tau_{comp} \omega_{comp} \quad (5.2)$$

where  $\tau_{comp}$  (in N·m) and  $\omega_{comp}$  (in rad·s<sup>-1</sup>) are the torque required to drive the compressor and the compressor speed, respectively. The temperature change of the air as it is compressed (and is subsequently released into the supply manifold) is given by [150]:

$$T_{comp,out} = T_{comp,in} + \frac{T_{comp,in}}{\eta_{comp}} \left( \left( \frac{P_{comp,out}}{P_{atm}} \right)^{\frac{\gamma-1}{\gamma}} - 1 \right) \quad (5.3)$$

The outgoing pressure is input to the module from the supply manifold module of Section

5.3.2. The procedure for determining the inputs to the Equations (5.1)-(5.3) is as follows. Firstly, the rate of change of the compressor speed is defined as [162]:

$$J_{comp} \frac{d\omega_{comp}}{dt} = \tau_{comp, motor} - \tau_{comp} \quad (5.4)$$

where  $J_{comp}$  is the combined moment of inertia of the moving parts of the compressor and motor, and  $\tau_{comp, motor}$  is the input torque to the compressor motor, calculated from a static motor equation as [162]:

$$\tau_{comp, motor} = \eta_{comp, motor} \frac{k_{comp, t}}{R_{comp, motor}} (v_{comp, motor} - k_{comp, v} \omega_{comp}) \quad (5.5)$$

and

$$\begin{aligned} k_{comp, t} &= 0.0153 \frac{\text{V}}{\text{rad/s}} \\ k_{comp, v} &= 0.0153 \frac{\text{N} \cdot \text{m}}{\text{A}} \\ R_{comp, motor} &= 0.82 \Omega \end{aligned} \quad (5.6)$$

where the motor efficiency,  $\eta_{comp, motor}$ , would also be determined from an efficiency map for the chosen compressor. The term  $v_{motor}$  is the value of voltage generated by the fuel cell stack and sent to the compressor motor; it will be assumed to be constant. A dimensionless head parameter  $\psi_{comp}$  is then defined [162]:

$$\psi_{comp} = \frac{c_{p_{air}} T_{atm} \left( \left( \frac{P_{supply}}{P_{atm}} \right)^{\frac{\gamma-1}{\gamma}} - 1 \right)}{U_{comp}^2 / 2} \quad (5.7)$$

where  $U_{comp}$  is the compressor blade tip speed, given by

$$U_{comp} = \omega_{comp} \cdot \frac{d_{comp, blade}}{2} \quad (5.8)$$

where  $d_{comp, blade}$  is the diameter of the compressor blades. The mass flow rate is defined as [162]:

$$\begin{aligned}\dot{m}_{comp, out} &= \Phi_{comp} \rho_{air} \frac{\pi}{4} d_{comp}^2 U_{comp} \\ &= \Phi_{comp} \rho_{air} \pi d_{comp, blade}^3 \omega_{comp}\end{aligned}\quad (5.9)$$

where  $\Phi_{comp}$  is the normalized compressor flow rate and  $\rho_{air}$  is the density of air. The normalized compressor flow rate and head parameter can be shown to be related by the equation [162]:

$$\Phi_{comp} = \Phi_{comp, max} \left( 1 - e^{\left( \beta_{comp} \left( \frac{\psi_{comp}}{\psi_{comp, max}} - 1 \right) \right)} \right) \quad (5.10)$$

where  $\Phi_{comp, max}$ ,  $\beta_{comp}$ , and  $\psi_{comp, max}$  are all polynomial functions of the Mach number  $M_{comp}$  [162]:

$$\begin{aligned}\Phi_{comp, max} &= a_4 M_{comp}^4 + a_3 M_{comp}^3 + a_2 M_{comp}^2 + a_1 M_{comp} + a_0 \\ \beta_{comp} &= b_2 M_{comp}^2 + b_1 M_{comp} + b_0 \\ \psi_{comp, max} &= c_5 M_{comp}^5 + c_4 M_{comp}^4 + c_3 M_{comp}^3 + c_2 M_{comp}^2 + c_1 M_{comp} + c_0\end{aligned}\quad (5.11)$$

and the Mach number is defined as [162]

$$M_{comp} = \frac{U_{comp}}{\sqrt{\gamma R_a T_{atm}}} \quad (5.12)$$

where  $R_a$  is the air gas constant (287.05 J·kg<sup>-1</sup>·K<sup>-1</sup>). The polynomial coefficients of Equation (5.11) are regression coefficients from the pressure ratio versus flow rate graph for an Allied Signal compressor. The regression coefficient values are listed in Table 5-1 below [162].

Equations (5.10)-(5.12) and Table 5-1 are used in Equation (5.9) to express the mass flow rate as a function of compressor speed. The compressor speed is then assumed to be limited to a discrete value for each value of stack current because a continuous function of the speed would not allow for time responses between each speed value to be determined.

**Table 5-1. Compressor regression coefficients**

Source: [162], page 19.

Coefficient	Value
$a_4$	$-3.69906 \times 10^{-5}$
$a_3$	$2.70399 \times 10^{-4}$
$a_2$	$-5.36234 \times 10^{-4}$
$a_1$	$-4.63685 \times 10^{-5}$
$a_0$	$2.21195 \times 10^{-3}$
$b_2$	1.76567
$b_1$	-1.34837
$b_0$	2.44419
$c_5$	$-9.78755 \times 10^{-3}$
$c_4$	0.10581
$c_3$	-0.42937
$c_2$	0.80121
$c_1$	-0.68344
$c_0$	0.43331

The time response to a change in demand current is given by

$$t_{\text{response, comp}} = 2\Delta\omega_{\text{comp}} \left( \frac{\eta_{\text{comp, motor}} k_{\text{comp, t}} v_{\text{comp, motor}}}{J_{\text{comp}} R_{\text{motor}}} - \frac{\eta_{\text{comp, motor}} k_{\text{comp, t}} (\omega_{\text{comp, final}} + \omega_{\text{comp, initial}})}{J_{\text{comp}} R_{\text{comp, motor}}} \right)^{-1} \left( \frac{c_p T_{\text{atm}}}{\eta_{\text{comp}}} \left[ \left( \left( \frac{\dot{m}_{\text{comp, out, final}}}{\omega_{\text{comp, final}}} \right) \left( \frac{P_{\text{supply, final}}}{P_{\text{atm}}} \right)^{\frac{\gamma-1}{\gamma}} - 1 \right) + \left( \left( \frac{\dot{m}_{\text{comp, out, initial}}}{\omega_{\text{comp, initial}}} \right) \left( \frac{P_{\text{supply, initial}}}{P_{\text{atm}}} \right)^{\frac{\gamma-1}{\gamma}} - 1 \right) \right] \right) \quad (5.13)$$

Once the compressor speed is obtained, it is substituted into Equations (5.1) and (5.3) to obtain the compressor parasitic power and output temperature, respectively. The power consumed can then be divided by the motor voltage  $v_{\text{comp, motor}}$  in order to determine the current draw of the compressor.

### 5.3.2 Supply manifold module

The supply manifold module is the first module implemented by the FCS model program.

The supply manifold uses a lumped parameter model similar to the compressor. The manifold includes the volume of the pipes between the compressor and fuel cell stack. The equation for the change of mass in the control volume is given by

$$\frac{dm_{supply}}{dt} = \dot{m}_{comp, out} - \dot{m}_{supply, out} \quad (5.14)$$

Solving the differential equation provides the dynamic response to a change in current:

$$t_{response, supply} = \frac{2\Delta m_{supply}}{\left(\dot{m}_{comp, out, final} + \dot{m}_{comp, out, initial}\right) - \left(\dot{m}_{supply, out, final} + \dot{m}_{supply, out, initial}\right)} \quad (5.15)$$

Equations (5.14) and (5.15) are not necessary for steady-state calculations. The equation for the change in pressure of the air in the control volume is then given by [162]

$$\frac{dP_{supply}}{dt} = \frac{\gamma R_{air}}{V_{supply}} \left( \dot{m}_{comp, out} T_{comp, out} - \dot{m}_{supply, out} T_{supply, out} \right) \quad (5.16)$$

where the pressure of the manifold,  $P_{supply}$ , is assumed to be the same as the pressure out of the compressor,  $P_{comp, out}$ , and the temperature at the outlet of the supply manifold,  $T_{supply, out}$ , is assumed to be the inlet temperature of the cathode module. The response time for the change in pressure to respond to a change in current demand is equal to the response time for mass accumulation in the manifold of Equation (5.15), which is given by

$$t_{response, supply} = \frac{2\Delta P_{supply} V_{supply}}{\gamma R_{air} \left[ T_{comp, out} \left( \dot{m}_{comp, out, final} + \dot{m}_{comp, out, initial} \right) - T_{supply, out} \left( \dot{m}_{supply, out, final} + \dot{m}_{supply, out, initial} \right) \right]} \quad (5.17)$$

As before, Equations (5.16) and (5.17) are only used if the transient response is to be determined. If the transient response is desired, the response time can be calculated using Equation (5.17), and this value can be used to determine the mass accumulation in Equation (5.15).

The manifold acts as a nozzle, and a nozzle equation is used to calculate the flow rate of the air leaving the control volume as a function of the upstream and downstream pressures. The

upstream pressure is in this case the pressure of the supply manifold,  $P_{supply}$ ; the downstream pressure is the inlet pressure of the cathode,  $P_{cathode, in}$ . The flow rate is divided between a “choked” region and an un-choked region by a critical pressure ratio, given by [162]:

$$\left( \frac{P_{cathode, in}}{P_{supply}} \right)_{crit} = \left( \frac{2}{\gamma + 1} \right)^{\frac{\gamma}{\gamma - 1}} \quad (5.18)$$

The equation for the mass flow leaving the control volume is given by [162]:

$$\begin{aligned} \dot{m}_{supply, out} &= \frac{C_{supply, D} A_{supply, T} P_{supply}}{\sqrt{RT_{comp, out}}} \left( \frac{P_{cathode, in}}{P_{supply}} \right)^{\frac{1}{\gamma}} \times \\ &\quad \left\{ \frac{2\gamma}{\gamma - 1} \left[ 1 - \left( \frac{P_{cathode, in}}{P_{supply}} \right)^{\frac{\gamma - 1}{\gamma}} \right] \right\}^{\frac{1}{2}} \quad \text{if } \frac{P_{cathode, in}}{P_{supply}} > \left( \frac{2}{\gamma + 1} \right)^{\frac{\gamma}{\gamma - 1}} \\ &= \frac{C_{supply, D} A_{supply, T} P_{supply}}{\sqrt{RT_{comp, out}}} \gamma^{\frac{1}{2}} \left( \frac{2}{\gamma + 1} \right)^{\frac{\gamma + 1}{2(\gamma - 1)}} \quad \text{if } \frac{P_{cathode, in}}{P_{supply}} \leq \left( \frac{2}{\gamma + 1} \right)^{\frac{\gamma}{\gamma - 1}} \end{aligned} \quad (5.19)$$

where  $C_{supply, D}$  is the discharge coefficient of the nozzle and  $A_{supply, T}$  is the orifice area of the nozzle, both design parameters. The pressure of the supply manifold can then be calculated with the mass flow, which is equal to the mass flow input to the cathode module, and pressure of the cell. The latter two quantities are both known. The calculation is iterative, in that it is not initially known which form of Equation (5.19) should be used. The first equation is employed first, and if the resultant ratio does not satisfy the inequality, the second equation is then used. A check to see that the calculated supply manifold pressure and the set stack pressure satisfy the second inequality is made to ensure an error does not propagate through the model. For any change in current, the mass flow out of the supply manifold (again, equal to the inlet mass flow of the cathode) can be calculated from the inlet mass flows in the cathode flow module. This will in turn determine the supply manifold pressure.

### 5.3.3 Return manifold

The return manifold again uses the lumped parameter model similar to the supply manifold

module. The manifold includes the volume of the pipes between the fuel cell stack and atmosphere. The equations will not be repeated here for brevity.

The amount of water vapour in the exhaust stream will depend on the amount transferred to the air reactant. This amount is calculated in the humidifier module of Section 5.3.4. The amount of water exiting the return manifold is assumed to be the same as that exiting the air humidifier.

### 5.3.4 Oxidant humidifier module

The stack exhaust air is pumped into two membrane humidifiers, one each for the air and hydrogen reactant stream. The humidity is transferred to the reactants through a semi-permeable membrane so that both reactants arrive at a sufficient humidification level, assumed to be 100% relative humidity. The humidification is assumed to be controlled such that the amount of humidified exhaust air that is required for both humidifiers is met. The humidifier will also cause the inlet air to match the temperature of the stack. Whether this heat transfer results in heating or cooling will depend on the exit temperature of the compressor air and the stack temperature. A schematic of the air humidifier is shown below in Figure 5-2. Note that a counter-flow arrangement is assumed for the humidifier, and that positive fluxes of humidity and heat are in the direction from exhaust air to reactant air.

The assumptions of the humidifier model are the same as those for the rest of the system model presented in the anode flow module, with two additional assumptions [168]:

- The humidifier is thermally insulated from the surroundings, meaning that there is no heat exchange with the atmosphere
- The overall convection heat transfer coefficient is constant throughout

The amount of water necessary to fully humidify the hydrogen is [152]:

$$\dot{m}_{humid, H_2, vapour} = \frac{8.937 \cdot P_{H_2O}^{sat}}{P_{stack} - P_{H_2O}^{sat}} \dot{m}_{anode, in} \quad (5.20)$$

while the amount of water necessary to fully humidify the air stream is given by [152]:

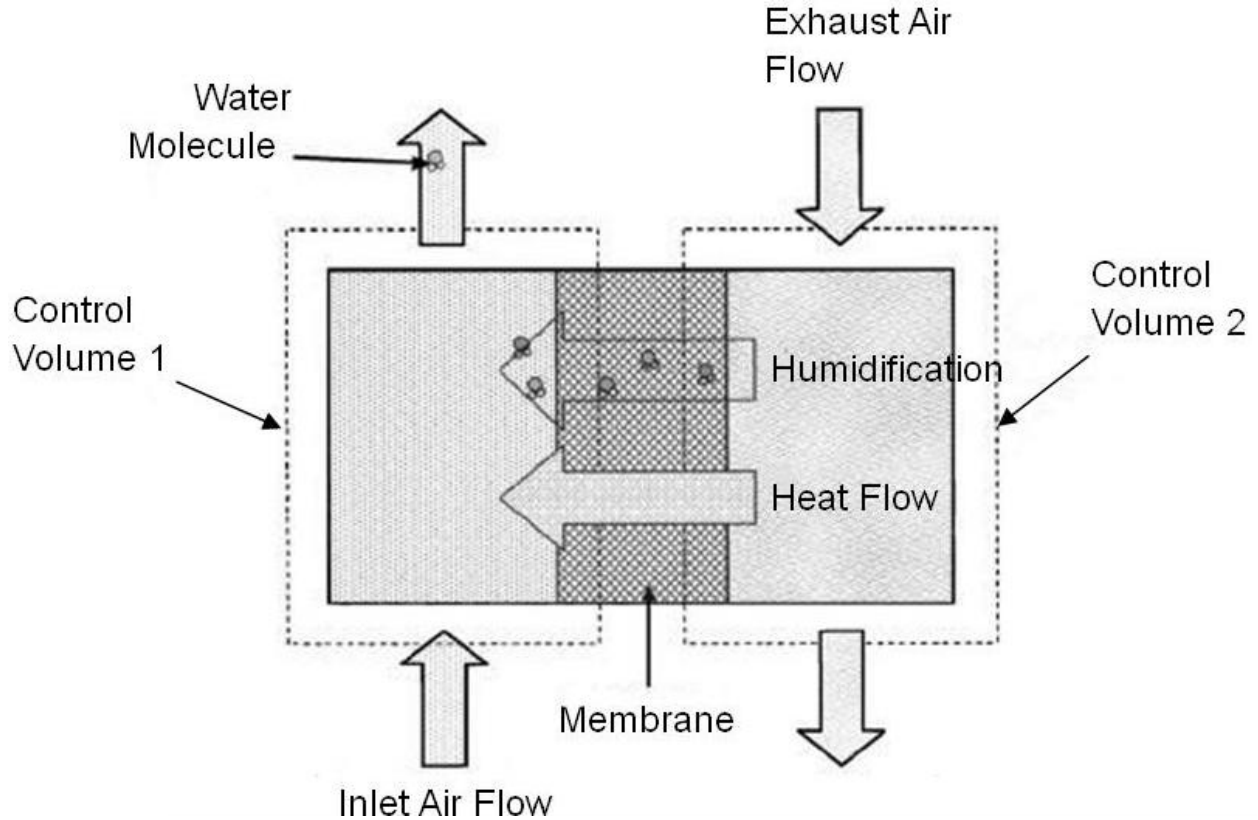


**Figure 5-2. Oxidant humidifier schematic**

Source: Adapted from [168], page 426.

$$\dot{m}_{\text{humid, air, vapour}} = \frac{0.6219 \cdot P_{\text{H}_2\text{O}}^{\text{sat}}}{P_{\text{stack}} - P_{\text{H}_2\text{O}}^{\text{sat}}} \dot{m}_{\text{cathode, in}} \quad (5.21)$$

The total mass of humidification water,  $\dot{m}_{\text{humid, total}}$ , is the sum of the vapour mass flows of Equations (5.20) and (5.21). The humidified air exhaust from the cathode outlet given in Equation (4.90) travels to the humidifiers. It is assumed that the mass of water in the cathode exhaust is greater than that required to fully humidify the reactants. The superfluous vapour in the humidification streams is exhausted to the atmosphere after exiting the humidifier.

The oxidant humidifier model begins by expressing the First Law of Thermodynamics for control volume 1 of the system [168]:

$$\dot{Q}_{\text{CV1}} + \dot{m}_{\text{comp, out}} h_{\text{comp, out}} + \dot{m}_{\text{CV2} \rightarrow \text{CV1, H}_2\text{O, transfer}} h_{\text{CV2} \rightarrow \text{CV1, H}_2\text{O, transfer}} = \dot{m}_{\text{supply, out}} h_{\text{supply, out}} + \dot{m}_{\text{CV1}} u_{\text{CV1}} + m_{\text{CV1}} \dot{u}_{\text{CV1}} \quad (5.22)$$

where  $\dot{m}_{CV1}$  is the mass accumulation,  $u_{CV1}$  is the internal energy of the mass, and  $\dot{u}_{CV1}$  is the change in internal energy of the mass in control volume 1. The First Law of Thermodynamics for control volume 2 is

$$\dot{Q}_{CV2} + \frac{\dot{m}_{cathode, out}}{2} h_{cathode, out} + \dot{m}_{CV1 \rightarrow CV2, H_2O, transfer} h_{CV1 \rightarrow CV2, H_2O, transfer} = \dot{m}_{return, out} h_{return, out} + \dot{m}_{CV2} u_{CV2} + m_{CV2} \dot{u}_{CV2} \quad (5.23)$$

where  $h_{return, out}$  is the enthalpy of the air exiting the return manifold after it has passed through the air humidifier and

$$\dot{Q}_{CV2} = -\dot{Q}_{CV1} \quad (5.24)$$

$$\dot{m}_{CV2 \rightarrow CV1, H_2O, transfer} = -\dot{m}_{CV1 \rightarrow CV2, H_2O, transfer} \quad (5.25)$$

$$h_{CV2 \rightarrow CV1, H_2O, transfer} = h_{CV1 \rightarrow CV2, H_2O, transfer} \quad (5.26)$$

The enthalpy of the water that is transferred through the membrane, Equation (5.26), is assumed to remain unchanged as it passes from one control volume to the other. The terms of Equations (5.22) and (5.23) must then be solved, and will be done so in order. The heat flux term between the control volumes is given by

$$\dot{Q}_{CV2 \rightarrow CV1} = U_{CV2 \rightarrow CV1} A_{CV2 \rightarrow CV1, membrane} \Delta T_{CV2 \rightarrow CV1} \quad (5.27)$$

where  $A_{CV2 \rightarrow CV1, membrane}$  is the membrane area, and  $U_{CV2 \rightarrow CV1}$  is the overall heat transfer coefficient given by [168]:

$$U_{CV2 \rightarrow CV1} = \frac{k_{CV2 \rightarrow CV1, membrane} N_{u, CV2 \rightarrow CV1}}{D_{h, CV2 \rightarrow CV1}} \quad (5.28)$$

where  $k_{CV2 \rightarrow CV1, membrane}$  is the thermal conductivity of the membrane,  $N_{u, CV2 \rightarrow CV1}$  is the Nusselt number, and  $D_{h, CV2 \rightarrow CV1}$  is the hydraulic diameter of the humidifier channel (assumed equal for both control volumes). The hydraulic diameter of a channel is given by [168]:

$$D_{h, CV2 \rightarrow CV1} = \frac{4W_{channel} H_{channel}}{P_{channel}}$$

(5.29)

where  $W_{channel}$ ,  $H_{channel}$ , and  $P_{channel}$  are the width, height, and perimeter of the channel, respectively. The Nusselt number is a dimensionless heat transfer coefficient that is the ratio of convection heat transfer to conduction in a fluid layer of thickness  $L$  [188]:

$$N_{u, CV2 \rightarrow CV1} = \frac{\bar{h}_{CV2 \rightarrow CV1} L_{CV2 \rightarrow CV1}}{k_{CV2 \rightarrow CV1}} \quad (5.30)$$

For the counter-flow arrangement assumed for the humidifier, the log mean temperature difference between the control volume 2 and control volume 1 is given by [188]:

$$\Delta T_{CV2-CV1} = \frac{(T_{CV2, in} - T_{CV1, out}) - (T_{CV2, out} - T_{CV1, in})}{\ln \left( \frac{(T_{CV2, in} - T_{CV1, out})}{(T_{CV2, out} - T_{CV1, in})} \right)} \quad (5.31)$$

The mass terms in the First Law of Thermodynamics equations are related using the Conservation of Mass equation:

$$\frac{dm_{CV1}}{dt} = \dot{m}_{comp, out} + \dot{m}_{CV2 \rightarrow CV1, H_2O, transfer} - \dot{m}_{supply, out} \quad (5.32)$$

and

$$\frac{dm_{CV2}}{dt} = \frac{\dot{m}_{cathode, out}}{2} + \dot{m}_{CV1 \rightarrow CV2, H_2O, transfer} - \dot{m}_{return, out} \quad (5.33)$$

The exit mass flows are calculated below.

The humidification action of the humidifier uses back diffusion in exactly the same manner as was described in the membrane hydration module. The mass flow equation is given as [168]

$$\dot{m}_{CV2-CV1, H_2O, transfer} = D_{humid, H_2O} \frac{c_{C2, H_2O} - c_{C1, H_2O}}{t_{humid, membrane}} M_{H_2O} A_{humid, membrane} \quad (5.34)$$

The water diffusion coefficient,  $D_{humid, H_2O}$ , is calculated from Equations (4.50) and (4.51). The membrane water activity is then

$$a_{membrane, 1} = \frac{a_{CV2} + a_{CV1}}{2} \quad (5.35)$$

and the water activities of the control volumes are

$$a_{CV1} = \frac{\bar{P}_{CV1, vapour}}{P_{H_2O, CV1}^{sat}} \quad (5.36)$$

and

$$a_{CV2} = \frac{\bar{P}_{CV2, vapour}}{P_{H_2O, CV2}^{sat}} \quad (5.37)$$

where the partial vapour pressures inside the control volumes are assumed to be equal to the partial vapour pressures of the outlet streams. The temperature of the membrane used to calculate the saturation pressure of the membrane is taken as the average between the two control volumes:

$$T_{membrane, 1} = \frac{T_{CV1} + T_{CV2}}{2} \quad (5.38)$$

The water contents can be calculated from Equation (4.54), with the subscript  $j$  representing control volume 1, control volume 2, and the membrane. The water concentration terms are given by [162]:

$$c_{CV2} = \frac{\rho_{membrane, dry}}{M_{membrane, dry}} \lambda_{CV2} \quad (5.39)$$

and

$$c_{CV1} = \frac{\rho_{membrane, dry}}{M_{membrane, dry}} \lambda_{CV1} \quad (5.40)$$

The humidity and relative humidity of the outlet air streams can be determined from [168]

$$\Gamma_{CV1} = \frac{M_{vapour} \bar{P}_{CV1, vapour}}{M_{air} \bar{P}_{CV1, air}} \quad (5.41)$$

$$\Gamma_{CV2} = \frac{M_{vapour} \bar{P}_{CV2, vapour}}{M_{air} \bar{P}_{CV2, air}} \quad (5.42)$$

$$\phi_{CV1} = \frac{\bar{P}_{CV1, vapour}}{P_{H_2O}^{sat}} \times 100 \quad (5.43)$$

$$\phi_{CV2} = \frac{\bar{P}_{CV2, vapour}}{P_{H_2O}^{sat}} \times 100 \quad (5.44)$$

From Equations (5.41) and (5.42), the mass flow of dry air for both reactant and exhaust air streams can be calculated [168]

$$\dot{m}_{CV1, air, out} = \frac{1}{1 + \Gamma_{CV1}} \dot{m}_{CV1, out} \quad (5.45)$$

and

$$\dot{m}_{CV2, air, out} = \frac{1}{1 + \Gamma_{CV2}} \dot{m}_{CV2, out} \quad (5.46)$$

where the mass flow of humidified reactant air leaving control volume 1 is calculated by [162]:

$$\begin{aligned} \dot{m}_{CV1, out} &= \frac{C_{humid, D} A_{humid, T} P_{CV1, out}}{\sqrt{RT_{comp, out}}} \left( \frac{P_{supply, out}}{P_{CV1, out}} \right)^{\frac{1}{\gamma}} \times \\ &\quad \left\{ \frac{2\gamma}{\gamma-1} \left[ 1 - \left( \frac{P_{supply, out}}{P_{CV1, out}} \right)^{\frac{\gamma-1}{\gamma}} \right] \right\}^{\frac{1}{2}} \quad \text{if } \frac{P_{supply, out}}{P_{CV1, out}} > \left( \frac{2}{\gamma+1} \right)^{\frac{\gamma}{\gamma-1}} \\ &= \frac{C_{humid, D} A_{humid, T} P_{CV1, out}}{\sqrt{RT_{comp, out}}} \gamma^{\frac{1}{2}} \left( \frac{2}{\gamma+1} \right)^{\frac{\gamma+1}{2(\gamma-1)}} \quad \text{if } \frac{P_{supply, out}}{P_{CV1, out}} \leq \left( \frac{2}{\gamma+1} \right)^{\frac{\gamma}{\gamma-1}} \end{aligned} \quad (5.47)$$

and the mass flow of humidified (albeit less so than upon entry) exhaust air leaving control volume 2 is determined by

$$\begin{aligned} \dot{m}_{CV2, out} &= \frac{C_{humid, D} A_{humid, D} P_{CV2, out}}{\sqrt{RT_{comp, out}}} \left( \frac{P_{atm}}{P_{CV2, out}} \right)^{\frac{1}{\gamma}} \times \\ &\quad \left\{ \frac{2\gamma}{\gamma-1} \left[ 1 - \left( \frac{P_{atm}}{P_{CV2, out}} \right)^{\frac{\gamma-1}{\gamma}} \right] \right\}^{\frac{1}{2}} \quad \text{if } \frac{P_{atm}}{P_{CV2, out}} > \left( \frac{2}{\gamma+1} \right)^{\frac{\gamma}{\gamma-1}} \\ &= \frac{C_{humid, D} A_{humid, D} P_{CV2, out}}{\sqrt{RT_{comp, out}}} \gamma^{\frac{1}{2}} \left( \frac{2}{\gamma+1} \right)^{\frac{\gamma+1}{2(\gamma-1)}} \quad \text{if } \frac{P_{atm}}{P_{CV2, out}} \leq \left( \frac{2}{\gamma+1} \right)^{\frac{\gamma}{\gamma-1}} \end{aligned} \quad (5.48)$$

The mass flows of water leaving the control volumes are given by

$$\dot{m}_{CV1, vapour, out} = \dot{m}_{CV1, out} \left( 1 - \frac{1}{1 + \Gamma_{CV1}} \right) \quad (5.49)$$

and

$$\dot{m}_{CV2, vapour, out} = \dot{m}_{CV2, out} \left( 1 - \frac{1}{1 + \Gamma_{CV2}} \right) \quad (5.50)$$

Finally, the dynamic enthalpy and internal energy equations are given by [168]

$$\frac{dh_i}{dt} = c_{p_i} \frac{dT_i}{dt} \quad (5.51)$$

and

$$\frac{du_i}{dt} = c_{v_i} \frac{dT_i}{dt} \quad (5.52)$$

In order to calculate the time response to a change in current, the change in pressure of control volume 1 is used:

$$\frac{dP_{CV1}}{dt} = \frac{\gamma R_{air}}{V_{CV1}} \left( \dot{m}_{comp, out} T_{comp, out} + \dot{m}_{CV2 \rightarrow CV1, H_2O, transfer} T_{membrane, 1} - \dot{m}_{CV1, out} T_{CV1, out} \right) \quad (5.53)$$

The time response to a change in current demand is then given by

$$t_{response, hum} = \frac{2V_{CV1} \Delta P_{CV1}}{\gamma R_{air} \left[ \begin{array}{l} \left( \dot{m}_{comp, out, final} T_{comp, out, final} + \dot{m}_{comp, out, initial} T_{comp, out, initial} \right) + \\ \left( \dot{m}_{CV2 \rightarrow CV1, H_2O, transfer, final} T_{CV2 \rightarrow CV1, H_2O, transfer, final} + \right) - \\ \left( \dot{m}_{CV2 \rightarrow CV1, H_2O, transfer, initial} T_{CV2 \rightarrow CV1, H_2O, transfer, initial} \right) \\ \left( \dot{m}_{CV1, out, final} T_{CV1, out, final} + \dot{m}_{CV1, out, initial} T_{CV1, out, initial} \right) \end{array} \right]} \quad (5.54)$$

## 5.4 Hydrogen Flow Module

As mentioned previously in the anode flow module, the hydrogen flow module is simplified by the high-pressure storage tank that allows for assumed instantaneous control to maintain stoichiometry. The transient characteristics can thus be ignored. The stack is assumed to be operated in the dead-end state, and the characteristics of the exhaust flow were described in the anode flow module of Section 4.3.5. The only module that is necessary to describe explicitly is hydrogen humidifier.

The hydrogen humidifier is modelled in the same way that the air humidifier was modelled in the previous section, and the same assumptions apply. The control volumes for the hydrogen

flow and the exhaust air in the hydrogen humidifier will be labelled 3 and 4, respectively.

The amount of water necessary to fully humidify the hydrogen was given in Equation (5.20). The model begins by expressing the First Law of Thermodynamics for control volume 3 of the hydrogen humidifier [168]:

$$\begin{aligned} \dot{Q}_{CV3} + \dot{m}_{storage, out} h_{storage, out} + \\ \dot{m}_{CV4 \rightarrow CV3, H_2O, transfer} h_{CV4 \rightarrow CV3, H_2O, transfer} = \dot{m}_{anode, in} h_{anode, in} + \dot{m}_{CV3} u_{CV3} + m_{CV3} \dot{u}_{CV3} \end{aligned} \quad (5.55)$$

where  $\dot{m}_{storage, out}$  is the mass flow of hydrogen leaving the storage tank, assumed to be at the pressure of the stack and atmospheric temperature. The First Law of Thermodynamics for control volume 4 is

$$\begin{aligned} \dot{Q}_{CV4} + \frac{\dot{m}_{humid, pump, out}}{2} h_{humid, pump, out} + \\ \dot{m}_{CV3 \rightarrow CV4, H_2O, transfer} h_{CV3 \rightarrow CV4, H_2O, transfer} = \dot{m}_{CV4, out} h_{CV4, out} + \dot{m}_{CV4} u_{CV4} + m_{CV4} \dot{u}_{CV4} \end{aligned} \quad (5.56)$$

where  $h_{CV4, out}$  is the enthalpy of the air exiting the hydrogen humidifier and expelled into the atmosphere and

$$\dot{Q}_{CV4} = -\dot{Q}_{CV3} \quad (5.57)$$

$$\dot{m}_{CV4 \rightarrow CV3, H_2O, transfer} = -\dot{m}_{CV3 \rightarrow CV4, H_2O, transfer} \quad (5.58)$$

$$h_{CV4 \rightarrow CV3, H_2O, transfer} = h_{CV3 \rightarrow CV4, H_2O, transfer} \quad (5.59)$$

The heat flux term between the control volumes is given by

$$\dot{Q}_i = U_{CV4 \rightarrow CV3} A_{CV4 \rightarrow CV3, membrane} \Delta T_{CV4 \rightarrow CV3} \quad (5.60)$$

For the counter-flow arrangement assumed for the humidifier, the log mean temperature difference between the control volume 4 and control volume 3 is given by [188]:

$$\Delta T_{CV4-CV3} = \frac{(T_{CV4, in} - T_{CV3, out}) - (T_{CV4, out} - T_{CV3, in})}{\ln \left( \frac{(T_{CV4, in} - T_{CV3, out})}{(T_{CV4, out} - T_{CV3, in})} \right)} \quad (5.61)$$

The mass terms in the First Law of Thermodynamics equations are related using the Conservation of Mass Law equation:

$$\frac{dm_{CV3}}{dt} = \dot{m}_{storage, out} + \dot{m}_{CV4 \rightarrow CV3, H_2O, transfer} - \dot{m}_{anode, in} \quad (5.62)$$

and

$$\frac{dm_{CV4}}{dt} = \frac{\dot{m}_{humid, pump, out}}{2} + \dot{m}_{CV3 \rightarrow CV4, H_2O, transfer} - \dot{m}_{CV4, out} \quad (5.63)$$

The humidification action of the humidifier uses back diffusion in exactly the same manner as was described in the membrane hydration module. The mass flow equation is given as [155]

$$\dot{m}_{CV4 \rightarrow CV1, H_2O, transfer} = D_{humid, H_2O} \frac{c_{C4, H_2O} - c_{C3, H_2O}}{t_{humid, membrane}} M_{H_2O} A_{humid, membrane} \quad (5.64)$$

The water diffusion coefficient,  $D_{humid, H_2O}$ , is calculated from Equations (4.50) and (4.51). The membrane water activity is then

$$a_{membrane, 2} = \frac{a_{CV4} + a_{CV3}}{2} \quad (5.65)$$

and the water activities of the control volumes are

$$a_{CV3} = \frac{\bar{P}_{CV3, vapour}}{P_{H_2O, CV3}^{sat}} \quad (5.66)$$

and

$$a_{CV4} = \frac{\bar{P}_{CV4, vapour}}{P_{H_2O, CV4}^{sat}} \quad (5.67)$$

where the partial vapour pressures in the control volumes are assumed to be equal to the partial vapour pressures of the outlet streams. The temperature of the membrane used to calculate the saturation pressure of the membrane is taken as the average between the two control volumes:

$$T_{membrane, 2} = \frac{T_{CV3} + T_{CV4}}{2} \quad (5.68)$$

The water contents can be calculated from Equation (4.54), with the subscript  $j$  representing control volume 1, control volume 2, and the membrane. The water concentration terms are given by [168]:

$$c_{CV3} = \frac{\rho_{membrane, dry}}{M_{membrane, dry}} \lambda_{CV3} \quad (5.69)$$

and

$$c_{CV4} = \frac{\rho_{membrane, dry}}{M_{membrane, dry}} \lambda_{CV4} \quad (5.70)$$

The humidity and relative humidity of the outlet hydrogen and air streams can be determined from [168]:

$$\Gamma_{CV3} = \frac{M_{vapour} \bar{p}_{CV3, vapour}}{M_{H_2} \bar{p}_{CV3, H_2}} \quad (5.71)$$

$$\Gamma_{CV4} = \frac{M_{vapour} \bar{p}_{CV4, vapour}}{M_{air} \bar{p}_{CV4, air}} \quad (5.72)$$

$$\phi_{CV3} = \frac{\bar{p}_{CV3, vapour}}{p_{H_2O}^{sat}} \times 100 \quad (5.73)$$

$$\phi_{CV4} = \frac{\bar{p}_{CV4, vapour}}{p_{H_2O}^{sat}} \times 100 \quad (5.74)$$

From Equations (5.41) and (5.42), the mass flow of dry air for both reactant and exhaust air streams can be calculated [168]:

$$\dot{m}_{CV3, H_2, out} = \frac{1}{1 + \Gamma_{CV3}} \dot{m}_{CV3, out} \quad (5.75)$$

and

$$\dot{m}_{CV4, air, out} = \frac{1}{1 + \Gamma_{CV4}} \dot{m}_{CV4, out} \quad (5.76)$$

where the mass flow of humidified reactant hydrogen leaving control volume 3 is calculated by [162]:

$$\begin{aligned}
\dot{m}_{CV3, out} &= \frac{C_{humid, D} A_{humid, T} P_{CV3, out}}{\sqrt{RT_{comp, out}}} \left( \frac{P_{anode, in}}{P_{CV3, out}} \right)^{\frac{1}{\gamma}} \times \\
&\quad \left\{ \frac{2\gamma}{\gamma-1} \left[ 1 - \left( \frac{P_{anode, in}}{P_{CV3, out}} \right)^{\frac{\gamma-1}{\gamma}} \right] \right\}^{\frac{1}{2}} && \text{if } \frac{P_{anode, in}}{P_{CV3, out}} > \left( \frac{2}{\gamma+1} \right)^{\frac{\gamma}{\gamma-1}} \\
&= \frac{C_{humid, D} A_{humid, T} P_{CV3, out}}{\sqrt{RT_{comp, out}}} \gamma^{\frac{1}{2}} \left( \frac{2}{\gamma+1} \right)^{\frac{\gamma+1}{2(\gamma-1)}} && \text{if } \frac{P_{anode, in}}{P_{CV3, out}} \leq \left( \frac{2}{\gamma+1} \right)^{\frac{\gamma}{\gamma-1}}
\end{aligned} \tag{5.77}$$

and the mass flow of humidified (albeit less so than upon entry) exhaust air leaving control volume 4 is determined by

$$\begin{aligned}
\dot{m}_{CV4, out} &= \frac{C_{humid, D} A_{humid, D} P_{CV4, out}}{\sqrt{RT_{comp, out}}} \left( \frac{P_{atm}}{P_{CV4, out}} \right)^{\frac{1}{\gamma}} \times \\
&\quad \left\{ \frac{2\gamma}{\gamma-1} \left[ 1 - \left( \frac{P_{atm}}{P_{CV4, out}} \right)^{\frac{\gamma-1}{\gamma}} \right] \right\}^{\frac{1}{2}} && \text{if } \frac{P_{atm}}{P_{CV4, out}} > \left( \frac{2}{\gamma+1} \right)^{\frac{\gamma}{\gamma-1}} \\
&= \frac{C_{humid, D} A_{humid, D} P_{CV4, out}}{\sqrt{RT_{comp, out}}} \gamma^{\frac{1}{2}} \left( \frac{2}{\gamma+1} \right)^{\frac{\gamma+1}{2(\gamma-1)}} && \text{if } \frac{P_{atm}}{P_{CV4, out}} \leq \left( \frac{2}{\gamma+1} \right)^{\frac{\gamma}{\gamma-1}}
\end{aligned} \tag{5.78}$$

The mass flows of the water vapour leaving the control volumes are

$$\dot{m}_{CV3, vapour, out} = \dot{m}_{CV3, out} \left( 1 - \frac{1}{1 + \Gamma_{CV3}} \right) \tag{5.79}$$

and

$$\dot{m}_{CV4, vapour, out} = \dot{m}_{CV4, out} \left( 1 - \frac{1}{1 + \Gamma_{CV4}} \right) \tag{5.80}$$

Finally, the dynamic enthalpy and internal energy equations are given by [168]:

$$\frac{dh_i}{dt} = c_{p_i} \frac{dT_i}{dt} \tag{5.81}$$

and

$$\frac{du_i}{dt} = c_{v_i} \frac{dT_i}{dt} \tag{5.82}$$

It should also be noted that a re-circulation module could be added that would increase the efficiency of the system. This module contains a passive ejector device (based on the principles of a Venturi tube [155]) to transfer the exhaust hydrogen to combine with the hydrogen flowing through the control valve of the hydrogen tank, as shown in the modified FCS schematic of Figure 5-3.

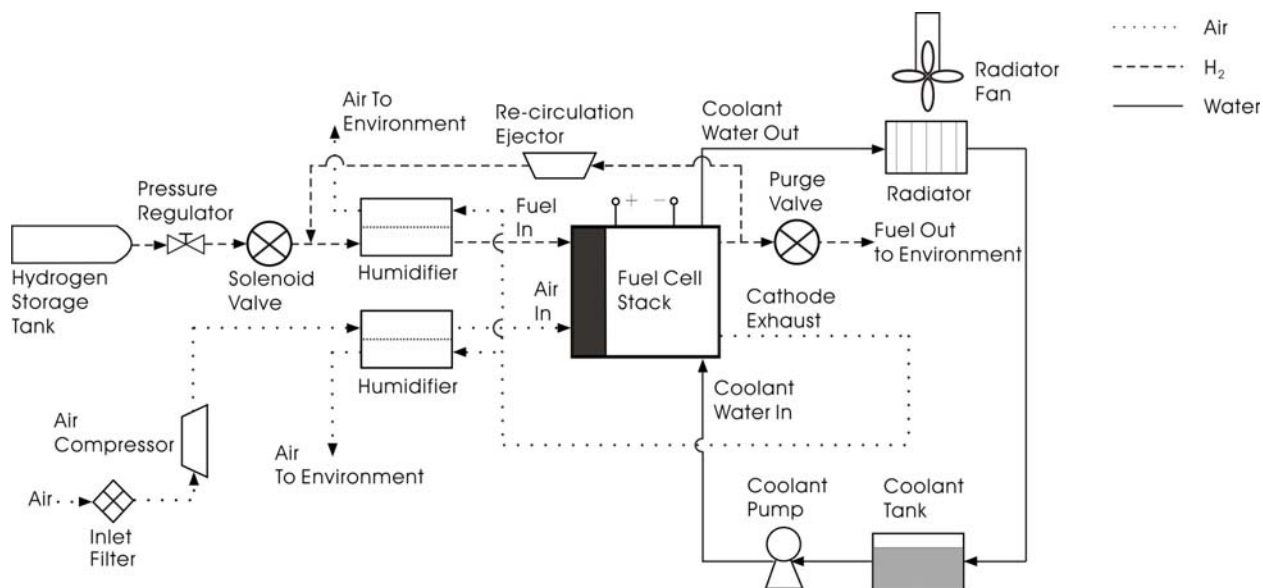


**Figure 5-3. Fuel cell system schematic with hydrogen re-circulation**

With the re-circulation system, the stoichiometry of the hydrogen can be set to be much higher, since the hydrogen that does not participate in the electrochemical reaction is not simply vented to the atmosphere. This re-circulation configuration would transfer the hydrogen at a lower pressure than that of the hydrogen entering the anode. Therefore, the pressure of the hydrogen released from the tank by the regulator would need to be increased in order to avoid a decrease in the voltage output of the stack. The passive ejector device could be replaced by a compressor to increase the pressure of the re-circulated hydrogen to equal the pressure of the stack. However, this will increase the parasitic loss. With the purge valve closed, the inlet flow of hydrogen through the ejector is the same as that exiting the anode. The pressure loss

through the re-circulation manifold would follow the same principles as the air flow through the supply and return manifolds, and the ejector operation is left for future work.

## 5.5 Thermal Management Module

Heat will be generated by the operation of the fuel cell since the enthalpy that is not converted to electrical energy will instead be converted to thermal energy. Unchecked, this will raise the temperature of the fuel cell beyond its operating temperature range, and therefore it must be addressed using a cooling system. The passage of reactant air through the cell will account for some of the heat transfer; the cooling system will account for the remaining excess heat to maintain the proper cell temperature. In order to determine the amount of heat produced by a fuel cell, an energy balance for a fuel cell stack can be provided:

$$\sum_i H_{i, in} = \sum_i H_{i, out} + \dot{W}_{stack, gross} + \dot{Q}_{total} \quad (5.83)$$

where the heat flux out of the stack will be equal to the heat produced by the stack, since all heat must be removed either through passive or active means. The enthalpies are chosen at 0 °C as the reference state. For the inlet air to the cathode, the enthalpy is given as [155]:

$$H_{cathode, air, in} = \dot{m}_{cathode, air, in} c_{p, air} T_{cathode, air, in} \quad (5.84)$$

and a similar expression can be written for the outlet enthalpy. The water vapour component of the inlet air has an enthalpy that is given by [155]:

$$H_{cathode, H_2O, in} = \dot{m}_{cathode, vapour, in} \left( c_{p, vapour} T_{cathode, vapour, in} + h_{fg}^0 \right) \quad (5.85)$$

and similar expressions can be written for the vapour at the cathode outlet, and the vapour in the anode inlet and outlet streams. The hydrogen enthalpy is given by [155]:

$$H_{anode, H_2, in} = \dot{m}_{anode, H_2, in} \left( c_{p, H_2} T_{anode, H_2, in} + h_{HHV}^0 \right) \quad (5.86)$$

where the HHV at 0 °C is a function of the value usually provided in tables at 25 °C,  $141.9 \times 10^6$  J·kg<sup>-1</sup> [155]:

$$h_{HHV}^0 = h_{HHV}^{25} - \left( c_{p, H_2} + \frac{1}{2} \frac{M_{O_2}}{M_{H_2}} c_{p, O_2} - \frac{M_{H_2O}}{M_{H_2}} c_{p, H_2O} \right) \cdot 25 \quad (5.87)$$

The heat calculated by using Equation (5.83) can be approximated by the following equation [152]:

$$\dot{Q}_{total} = (E_{max} - v_{cell}) I \cdot n_{cell} \quad (5.88)$$

where  $E_{max}$  is the maximum EMF of the fuel cell, or 1.25 V if the lower heating value (LHV) is used;  $v_{cell}$  is the voltage of the cell calculated by Equation (4.23) (or Equation (4.45) if the dynamic response is considered);  $I$  is the cell current and  $n_{cell}$  is the number of cells in the stack.  $\dot{Q}_{total}$  must be transferred away from the cell in its entirety in order to maintain the operating temperature of the fuel cell. It should be noted that by using the LHV, the implicit assumption is that all of the water produced in the cathode is in vapour form, which agrees with the assumption of the cathode flow module. This also means that the cooling effect of evaporation is implicitly included in heat production of Equation (5.88).

### 5.5.1 Passive heat loss

Heat will be lost to the surroundings and to the air stream through three heat transfer processes: radiation, convection and evaporation. The cooling system removes the heat that is not lost passively through these three processes. The amount of heat lost to the air stream and surroundings can be calculated using the following expression:

$$\dot{Q}_{passive} = \dot{Q}_{rad} + \dot{Q}_{conv, total} \quad (5.89)$$

The equation for radiation is given by [189]:

$$\dot{Q} = e\sigma A(T_{body}^4 - T_{atm}^4) \quad (5.90)$$

where  $e$  is the emissivity of the body and depends on the nature of the surface (which has an assumed value of unity for the stack),  $\sigma$  is the Stefan-Boltzmann constant (which has a value of  $5.67 \times 10^{-8} \text{ W} \cdot \text{m}^{-2} \cdot \text{K}^{-4}$ ),  $A$  is the area of the radiative body, and  $T_{body}$  is the temperature of the radiative body. The equation for heat loss due to radiation is then:

$$\dot{Q}_{rad} = e_{stack} \sigma A_{stack} (T_{stack}^4 - T_{atm}^4) \quad (5.91)$$

where  $A_{stack}$  is the surface area of the stack that is exposed to the surroundings.

The heat loss due to convection will occur differently for the various parts of the fuel cell interior. The convection lost by the vertical walls of the cell is given by [190]:

$$\dot{Q}_{conv, walls} = K_{manifold} \cdot A_{Sides} \cdot h_{air} (T_{stack} - T_{atm}) \quad (5.92)$$

where  $A_{sides}$  is the area of cathode flow channel walls,  $h_{air}$  is the heat transfer coefficient of the cell channel sides with values for parameters taken from reference [190]. The constant term  $K_{manifold}$  represents additional area due to the geometry of the manifold for the TERS fuel cell stack, and the value of 1.15 is assumed to be similar for the Palcan PC6-1200. This term should be definitely determined for the stack in future research.

The heat transfer due to convection on the top and bottom of the channel is given by [152]:

$$\dot{Q}_{conv, top+bottom} = (h_{top} + h_{bottom}) \cdot (T_{stack} - T_{atm}) \cdot A_{top, bottom} \quad (5.93)$$

where  $h_{top}$  and  $h_{bottom}$  are the heat transfer coefficients of the top and bottom of the fuel cell channel, respectively, and  $A_{top, bottom}$  is the cross-sectional area of the top and bottom of the cathode flow channel. The total heat lost to convection is then given by the sum of Equations (5.92) and (5.93):

$$\dot{Q}_{conv, total} = \dot{Q}_{conv, walls} + \dot{Q}_{conv, top+bottom} \quad (5.94)$$

The model does not calculate the amount of heat lost to evaporation due to the aforementioned usage of the LHV. This simplifies the thermal management issue, although it would be possible to ascertain the amount of heat lost due to liquid water evaporating into the air stream, if such a determination were necessary. In this case, the amount of liquid water,  $m_{cathode, liquid}$  of Equation (4.86), in the cathode is used. If the amount of liquid water is zero, the heat lost to evaporation is zero as well. If the amount of liquid water is non-zero, the amount of heat lost to evaporation will be the amount of heat required to convert a mass of liquid water to vapour water, equal to the product of the latent heat of vaporization  $l_{vap}$  and the mass of the water:

$$\dot{Q}_{evap} = l_{vap} \dot{m}_{cathode, liquid, evap} \quad (5.95)$$

This evaporation would only occur if a change in current results in a lower humidity of the air

stream below saturation, and the amount of liquid evaporated will equal the amount required to bring the relative humidity to 100%.

The remainder of the heat produced by the electrochemical reaction occurring inside the stack that is not removed passively by the processes above must be removed by the cooling system.

### 5.5.2 Active heat loss

The model uses water cooling to remove the excess heat that is not lost passively. Water-cooled designs are preferred to air-cooled designs for FCS power ratings larger than 1 kW [46]. The cooling water flows in a loop, as shown in Figure 5-1, and is circulated by a pump. When the cooling water passes through a radiator, a radiator fan removes its heat and the cooling fluid is assumed to reach the temperature of the fluid reservoir. The fluid reservoir is assumed to contain water at STP; the water flowing from the radiator is assumed to not heat the reservoir. There are thus two heat transfer processes: in the stack and in the radiator. Inside the stack, the cooling fluid is assumed to be in a cross-flow arrangement with the anode and cathode fluids, while the radiator is assumed to be a channel-filled plate that transfers heat to the surroundings by forced convection. The analysis begins with a steady-state description of the water pump.

The mass flow is assumed constant through the loop for steady-state, steady-flow (SSSF) conditions, and will be denoted by  $\dot{m}_{cool}$ . The mass flow of water required to perform the heat transfer away from the stack to the water coolant can be defined as:

$$\dot{m}_{cool} = \frac{\dot{Q}_{active}}{c_{p, H_2O} (T_{stack} - T_{cool, stack, in})} \quad (5.96)$$

where the active heat loss is the difference between the heat produced and the passive heat loss:

$$\dot{Q}_{active} = \dot{Q}_{total} - \dot{Q}_{passive} \quad (5.97)$$

and where  $c_{p, H_2O}$  is the specific heat of water at constant pressure. The First Law of Thermodynamics for the cooling system pump is

$$\dot{m}_{cool} h_{cool, pump, in} = \dot{m}_{cool} h_{cool, pump, out} + \dot{W}_{cool, pump} \quad (5.98)$$

where the enthalpy of the cooling fluid at the inlet of the pump is known. The First Law of Thermodynamics for the stack is then given by

$$\dot{Q}_{active} + \dot{m}_{cool} h_{cool, stack, in} = \dot{m}_{cool} h_{cool, stack, out} \quad (5.99)$$

The water at the inlet of the stack is assumed to be at the temperature and pressure of the outlet of the cooling system pump.

Next, the expression for the First Law of Thermodynamics for the radiator is determined to be

$$\dot{Q}_{cool, radiator} + \dot{m}_{cool} h_{cool, stack, out} = \dot{m}_{cool} h_{cool, radiator, out} \quad (5.100)$$

where the enthalpy at the outlet of the radiator is assumed to be equal to that of the reservoir. The heat removed from the cooling water, equal to the heat flux out of the radiator of Equation (5.100), is given by

$$\dot{Q}_{cool, radiator} = \dot{m}_{cool} c_{p, H_2O} (T_{reservoir} - T_{cool, stack, out}) \quad (5.101)$$

The power consumed in the radiator fan must be determined. Equations (5.100) and (5.101) describe the amount of heat that the radiator must transfer away from the cooling fluid. The radiator is a heat exchanger with forced convection caused by the radiator fan. The heat exchanged between the cooling water and the forced air can be expressed by the familiar expression for heat exchange between two control volumes

$$\dot{Q}_{cool, radiator} = U_{radiator} A_{radiator} \Delta T_{cool \rightarrow air} \quad (5.102)$$

where  $U_{radiator}$  is the overall heat transfer coefficient and is related to the thermal conductivity of the radiator material, the hydraulic diameter, and the Nusselt number of the cooling water channel, for which Equations (5.28)-(5.30) can be used for the radiator geometry. The temperature of the air after absorbing the heat flux of Equation (5.102) can then be solved, using the LMTD. The heat flux and temperature change can then be used to determine the mass flow of forced air required to effect this heat flux:

$$\dot{m}_{cool, forced air} = \frac{\dot{Q}_{cool, forced air}}{c_{p, air} (T_{cool, forced air, final} - T_{atm})} \quad (5.103)$$

where  $T_{cool, forced air, final}$  is the temperature of the forced air after absorbing the heat flux. In order to calculate the power consumed by the fan, the power equation for a wind turbine is used (in reverse.) The power output of a wind turbine is [191]

$$\dot{W}_{turbine} = \frac{1}{2} \rho_{air} A_{rotor, swept} C_p V_{air}^3 \eta_{generator} \eta_{bearing} \quad (5.104)$$

where  $A_{rotor, swept}$  is the area through which the rotors sweep,  $C_p$  is coefficient of performance (with a theoretical Betz limit maximum of 0.59 and common value of 0.35),  $\eta_{generator}$  is the generator efficiency and  $\eta_{bearings}$  is the efficiency of the bearings. The radiator fan essentially works as a wind turbine in reverse, delivering power to the air instead of receiving power from the air, and so the power consumed by the fan is given by

$$\dot{W}_{cool, fan} = \frac{\frac{1}{2} \rho_{air} A_{rotor, swept} C_p V_{cool, forced air}^3}{\eta_{motor} \eta_{bearing}} \quad (5.105)$$

where the velocity of the forced air is related to the mass flow of forced air by

$$V_{cool, forced air} = \frac{\dot{m}_{cool, forced air}}{\rho_{air} A_{rotor, swept}} \quad (5.106)$$

so that the power consumed by the cooling system fan can be simplified to

$$\dot{W}_{cool, fan} = \frac{\frac{1}{2} C_p \dot{m}_{cool, forced air}^3}{\rho_{air}^2 A_{rotor, swept}^2 \eta_{motor} \eta_{bearing}} \quad (5.107)$$

## 5.6 Fuel Cell System Net Output

The net output of the fuel cell system is the total heat removed through the active and passive processes, the water removed by the reactant streams and vented to the atmosphere, and the electrical power sent to the load. The total heat removed is assumed to equal the total amount of heat produced, given in Equation (5.83) and as an approximation in (5.88). The

amount of water removed from the system is the total water in the outlet streams of the humidifiers, given by Equations (5.50) and (5.80), and anode flow module, given by Equation (4.69).

The net electrical power sent to the load is given by

$$\dot{W}_{net, system} = \dot{W}_{gross, stack} - \dot{W}_{parasitic} \quad (5.108)$$

where the gross power was calculated in Equation (4.25), and the total parasitic power of the fuel cell system (the power consumed by control systems is assumed negligible) is given by:

$$\dot{W}_{parasitic} = \dot{W}_{comp} + \dot{W}_{cool, pump} + \dot{W}_{cool, fan} \quad (5.109)$$

Note that the parasitic power consumed by the solenoid valve is also considered negligible.

The response time to a change in current must be calculated for the system as a whole. Response times for the following components are included: (1) stack, (2) compressor, (3) supply manifold, (4) cathode flow channel, (5) return manifold, and (6) humidifier pump. It is unclear which of the six components for which response times have been modelled will respond concurrently to a change in current demand and which will respond with a time shift. It is, therefore, proposed that all are assumed to occur independently and in sequence, so that the total response time is

$$t_{response} = t_{response, cell} + t_{response, comp} + t_{response, supply} + t_{response, cathode} + t_{response, return} \quad (5.110)$$

The hydrogen flow module assumes that the change in flow of hydrogen in response to a change in current is instantaneous and the cooling loop transients have little effect on the system performance.

### 5.6.1 Efficiency analysis

Once the net system power has been determined, it is informative to calculate the system exergetic efficiency, which is based on a second law of thermodynamics analysis. The exergetic efficiency provides a true analysis of the performance of a system. The more common First Law of Thermodynamics efficiency can provide unrealistic results and thus is not utilized [192]. The exergetic efficiency is given by [193]:

$$\eta_{system, exergetic} = \frac{\dot{W}_{net, system}}{\left( \sum_{in} \dot{N}_{react, i} \cdot \xi_{react, i} - \sum_{out} \dot{N}_{prod, j} \cdot \xi_{prod, j} - \dot{Q}_{exit} \left( 1 - \frac{T_{atm}}{T_{stack}} \right) \right)} \quad (5.111)$$

where  $\xi_{react, i}$  is the exergy (also known as the availability) of a reactant flowing into the system,  $\xi_{prod, j}$  is the exergy of a product flowing out of the system, and  $\dot{Q}_{exit}$  is the heat leaving the stack. It can also be argued that the exergetic efficiency can be based on the useful output (in this case, electrical power) divided by the input exergy to the system. The contributions of the heat and products leaving the control volume are thus ignored. The only reactant containing exergy is actually the hydrogen stream. The form of exergetic efficiency used in the research is thus

$$\eta_{system, exergetic} = \frac{\dot{W}_{net, system}}{\dot{N}_{H_2, in} \cdot \xi_{H_2, in}} \quad (5.112)$$

The molar exergy of a substance (in  $kJ \cdot kmole^{-1}$ ) is given by [194]:

$$\xi_{total} = \xi_{KE} + \xi_{PE} + \xi_{TM} + \xi_{CH} \quad (5.113)$$

where  $\xi_{KE}$ ,  $\xi_{PE}$ ,  $\xi_{TM}$ , and  $\xi_{CH}$  are the exergies due to an imbalance of the substance with the reference kinetic energy, potential energy, thermo-mechanical, and chemical equilibrium point, respectively. The first two terms are assumed to be negligible, and the latter two terms are defined by [194]:

$$\begin{aligned} \xi_{TM} &= (h - h_0) - T_0(s - s_0) \\ \xi_{CH} &= \sum_j x_j (\mu_{j0} - \mu_{j00}) \end{aligned} \quad (5.114)$$

where  $h$  and  $s$  denote the specific enthalpy and entropy, respectively, at a given state. The subscript 0 in the first equation indicates that the property is associated with the reference environmental (restricted) state where pressure and temperature are at equilibrium. The double subscript in the second equation refers to the dead state where pressure, temperature and chemical potential are at equilibrium.

It should be noted that the energy and exergetic efficiencies will increase with the addition of a re-circulation system. The molar flow of hydrogen from the storage system will decrease

in step with the re-circulated hydrogen that did not react, thereby decreasing the value of the denominator of Equation (5.112). Furthermore, since the re-circulated hydrogen will be at an elevated temperature, less heat will need to be transferred in the hydrogen humidifier. This means that a smaller, cheaper humidifier could possibly be substituted.

## Chapter 6 Low-Speed Vehicle Modelling

Chapters 2 and 3 discussed the hybrid vehicles that are currently available to the consumer. In the next generation of hybrid vehicles, a growing proportion could quite possibly have fuel cell powerplants in order to achieve ZEV status. It is apparent that current design methodologies for FCHVs need to be refined in order to facilitate this transition. At present, the design of an FCHV is an immature process. The difference between the methodologies employed by ICEV and FCHV designers lies primarily in the depth of understanding of the ICE versus the FCS. However, comprehension of the physical phenomena governing FCSs is beginning to improve, and tools such as computational modelling and analysis techniques have contributed to the current, growing level of understanding. The objective is to reach a stage where the development of the FCHV can proceed in a concurrent manner, with all aspects of the design progressing at the same pace. A concurrent design methodology will allow for a superior design in a significantly shorter development time, with considerably lower costs. The methodology must allow for the design to undergo optimization that will prompt for modifications which can be inserted into the design. These benefits will mainly be realized by the reduced number of physical prototypes that will be produced, a key requirement for any vehicle in an industry where prototypes cost millions of dollars. Reduced development time is also enabled by a well-designed methodology, and this reduces costs as well. These avoided costs could encourage future investment in FCHV research and development.

The objective of this portion of the research is to model the two experimental prototype LSVs and perform simulations with the models to predict performance. The predictions made are compared with subsequent experimental results of physically testing the vehicles in the Low-Speed Vehicle Testing Facility, discussed in **Error! Reference source not found.** The results of the simulations illustrate the strengths and weaknesses of the current design, and the analysis leads to suggestions for design modifications.

## 6.1 Previous Fuel Cell Hybrid Scooter Modelling

Work directed at the development of FCHS technology originating in research programs at academic facilities is conspicuously absent from the available literature. Very few papers have been published that discuss FCHS technology: Tso *et al.* [195], Wang *et al.* [196], Colella [197], Lin [7, 73], and Laven [198] essentially represent the entire set of papers published in the scientific literature. The first four papers include discussion on current market trends and predicted future prospects in terms of “big picture” performance characteristics measures. This discussion accounts for the entire content of the papers by Tso *et al.* and Wang *et al.*; these papers are largely non-technical feasibility studies. Colella describes the construction of a prototype “low-power” scooter (a FCS that serves as a power assist to a bicycle) and compares the performance results with a similarly powered battery bicycle. The prototype was not optimized, and the performance of both the fuel cell bicycle and the commercial battery bicycle were disappointing, although the explanation for the dismal performance of the latter is not thoroughly examined. The paper by Lin is a summary of his Master’s thesis, reference [7]. The thesis includes a feasibility and market analysis for FCHS growth in his native Taiwan. The technical aspects of fuel cells and modelling of the FCHS are also presented. Lin’s model, however, does not extend past the schematic design stage, and as a result cannot be validated by actual test data. No prototype was built, and thus the result of the research is essentially a feasibility study, albeit comprehensive and technical. Finally, the Master’s thesis of Laven is devoid of any FCS or FCV model, and is basically a “how to” publication of assembling a fuel cell scooter from assorted components. Meanwhile, the private companies working on the development of FCHSs do not publish any studies or results, presumably as a result of proprietary concerns.

Overall, the research into contemporary, related work reveals that the field of FCHS is in its infancy; it is the author’s judgement that this situation is unlikely to change until FCs are firmly established in other automotive applications, if ever.

## 6.2 Low-Speed Vehicle Models

To prepare for the current research, in 2003 IESVic acquired two identical QQEM50-Z battery-powered scooters from Qing Qi, a Chinese supplier. One of the scooters was subsequently modified substantially by Palcan Fuel Cells Ltd. into a FCHS that was used to measure the performance of the installed FCS; the unaltered electric scooter is the metric against which the FCHS is compared. The FCHS was designed to allow for simple FCS testing and instrumentation rather than as a road vehicle. The lone difference between the two scooters is the type of powertrain, as the auxiliary components and traction motor components of the powertrain have also remained unchanged. Thus, the differences in performance can be attributed exclusively to the power plant differences of those powertrains. Both scooters have been modelled in ADVISOR 2004 and, as discussed in Section 6.3, the models have undergone the same simulations to contrast the performance achievements.

### 6.2.1 Vehicle body

The BS was originally designed to compete with the current state-of-the-art 50 cc ICE scooters. This LSV is intended for urban commuting where speeds larger than  $50 \text{ km}\cdot\text{hr}^{-1}$  are not required. The vehicle is thus designed to be very light so that a small electric motor can be used to minimize costs. The distribution for the BS is 36.4 kg for the front wheel and 53.6 kg for the rear wheel for a total of 90 kg. The transformation of the BS into the FCHS has resulted in a weight distribution of 45.4 kg for the front wheel and 68.0 kg for the rear wheel for a total of 113.4 kg. This means that the difference in powertrain masses of the LSVs is 23.4 kg. To each scooter mass was added a hypothetical rider mass; the rider is assumed to be in the 50<sup>th</sup> percentile of body mass index for a male aged 20-29, with a mass of 75.7 kg [199]. This mass coincides exactly with that of the author; this match precludes the need for modifications to test procedures for both the dynamometer and road testing. The simulations and subsequent experimental validation tests of the LSVs therefore assume a mass of 165.7 kg for the BS and 189.1 kg for the FCHS. The ADVISOR method for calculating the overall mass does not arrive

at this value; however, the program allows for a mass override, and this function is exploited throughout the simulations.

The wheelbase is measured to be 1.18 m, and the coefficients for the power at the wheels, the product of the torque at the wheels of Equation (3.40) and the wheel angular velocity, are assumed to be  $C_{rr}=0.014$ ,  $C_D=0.9$ , and  $A_F=0.6 \text{ m}^2$ . These values are taken from reference [7], although more exact values for the prototype LSVs would no doubt increase the accuracy of the simulation results.

Modelling continues with the wheel and axle. The wheel radius is measured to be 0.2 m. The MOIs of the wheel and motor assembly of both scooters are difficult to determine. The usual method would be to employ the suspended weight test, wherein a known weight is attached to the wheel and suspended at a pre-determined angle away from directly below the center of rotation of the wheel. The weight is then released and the number of so-called *strong* pendulum swings, in which the weight clearly passes through vertical, is counted in addition to the time taken for the weight to come to rest. However, the motor in the scooter design does not have freewheel capability, and thus the motor is always engaged. This makes a MOI determination from this method impossible, and the MOI of the wheel and motor assembly must be determined with a different method.

The tire and rim dimensions are shown below in Figure 6-1. The radius from the wheel center, C on the diagram, to the outer edge of the tire is 20 cm. The tire cross-section is assumed to be comprised of a semi-circle with diameter 7.9 cm with two tapering sides, with a thickness of 0.5 cm. The rim is more difficult to estimate. The thickest point of the rim is 5.31 cm, but the thickness varies from the tire to the wheel center. It is assumed that the cross-section of the equivalent rim mass is a rectangle that is  $5.31 \text{ cm} \times 2.43 \text{ cm}$ .

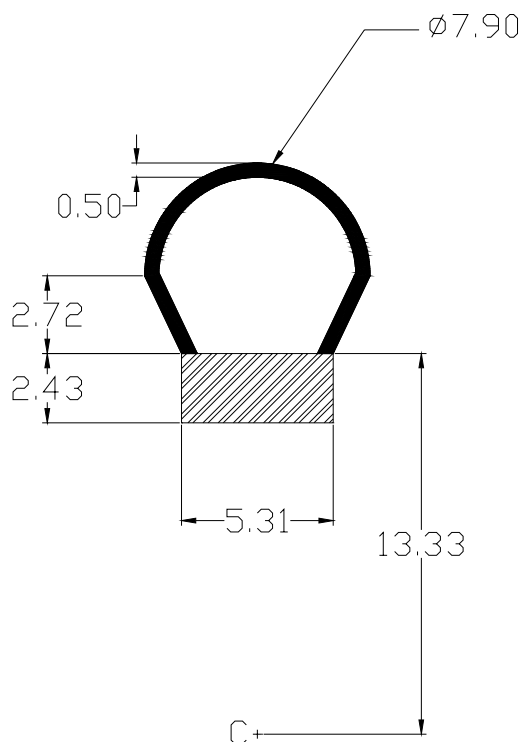


**Figure 6-1. Scooter tire and rim dimensions**

The MOI of each of the four components is determined separately. The volume of each component is determined using the 2<sup>nd</sup> Theorem of Pappus, which states [200]

$$V = Ad_{centroid} \quad (5.115)$$

where  $A$  is the cross-sectional area and  $d_{centroid}$  is the distance the centroid must travel in the revolution of the volume. The centroid can also be used to calculate the moment of inertia

$$I = \frac{1}{2} m_{component} r_{centroid}^2 \quad (5.116)$$

where the mass of each component is calculated assuming densities of  $\rho_{rubber}=2000 \text{ kg}\cdot\text{m}^{-3}$  and  $\rho_{aluminum}=2643 \text{ kg}\cdot\text{m}^{-3}$ , and  $r_{centroid}$  is the distance from the centroid to the axis of the wheel. The MOI of the wheel is thus estimated to be  $0.037 \text{ kg}\cdot\text{m}^2$ .

The rotor inertia values for the hub motors could not be obtained from the motor manufacturer. Inertia values were available for motors manufactured by industry-leading Heinzmann GmbH and Co., and these are used for an extrapolation. The Heinzmann Series

RN-EC brushless DC hub motors at 130 W and 150 W and the RN brushed DC hub motor at 400 W are used [201]. The rotor inertias for these power outputs are  $0.014 \text{ kg}\cdot\text{m}^2$ ,  $0.016 \text{ kg}\cdot\text{m}^2$ , and  $0.039 \text{ kg}\cdot\text{m}^2$  respectively. Extrapolating this to the 600 W output power of the scooter motor gives an approximate MOI for the motor of  $0.057 \text{ kg}\cdot\text{m}^2$ . The total MOI of the rear wheel and motor assembly is thus estimated to be  $0.094 \text{ kg}\cdot\text{m}^2$ .

## 6.2.2 Electric machine

The propulsion system for both LSVs uses a 48 V DC brushed permanent magnet hub motor, the characteristics of which were supplied by the Chinese motor manufacturer to be [202]:

- $P_{\text{rated}} = 600$
- $T_{\text{peak}} = 60 \text{ N}\cdot\text{m}$
- $N_{\text{max}} = 520 \text{ rpm}$
- $\eta_{\text{max}} = 83\%$

The current in a DC motor is the difference between the supply voltage and back EMF generated by the motion of the rotor, divided by the armature resistance. The equation for the total current is given by [42]:

$$I_{\text{motor}} = \frac{E_s}{R_a} - \frac{K_m \phi}{R_a} \omega_{\text{rotor}} \quad (5.117)$$

where  $E_s$  is the supply voltage,  $R_a$  is the armature resistance,  $K_m$  is the motor constant,  $\phi$  is the magnetic flux passing through the armature coil (in Wb), and  $\omega$  is the rotor rotation speed (in  $\text{rad}\cdot\text{s}^{-1}$ ). The equation of the motor torque as a function of current is then [42]:

$$T_{\text{motor}} = K_m \phi I_{\text{motor}} \quad (5.118)$$

As can be seen from Equations (5.117) and (5.118), the current and torque are maximized at zero rotor rotation, where there is no back EMF. The equation for the torque is given by [42]:

$$T_{\text{motor}} = \frac{K_m \phi}{R_a} E_s - \frac{(K_m \phi)^2}{R_a} \omega_{\text{rotor}} \quad (5.119)$$

where it can be seen from Equation (5.119) that the slope of the torque-angular velocity curve is

equal to

$$m = \frac{K_m \phi}{R_a} \quad (5.120)$$

For the values provided for the peak torque and maximum speed, the slope can be determined to have a value of  $-1.1018 \text{ N}\cdot\text{m}\cdot(\text{rad}\cdot\text{s}^{-1})^{-1}$ . The y-intercept is equal to the peak torque,  $60 \text{ N}\cdot\text{m}$ . There are now two equations with two unknowns:  $K_m \phi$  and  $R_a$ . These two parameters are solved to obtain values of  $0.881 \text{ V}\cdot(\text{rad}\cdot\text{s}^{-1})^{-1}$  for  $K_m \phi$  and  $0.705 \Omega$  for  $R_a$ .

Using the values for the rated power and motor voltage, the current at the rated power can be determined from the equation:

$$\begin{aligned} \dot{W}_{motor} &= \eta_{motor} \dot{W}_{in} \\ &= \eta_{motor} I_{motor} V_{motor} \end{aligned} \quad (5.121)$$

where the efficiency is unknown but can be determined through an iterative process. A value of 83% is the initial estimate, but the resultant torque and angular velocities do not match the output of 600 W. The efficiency at the rated power is found to be 76%. The current at the rated power is 16.4, the torque is  $14.5 \text{ N}\cdot\text{m}$  and the angular velocity is  $41.3 \text{ rad}\cdot\text{s}^{-1}$ .

The losses in a motor are given by [42]

$$P_{loss} = k_c T^2 + k_i \omega + T_{friction} \omega + k_w \omega^3 + C \quad (5.122)$$

where  $k_c$  is a constant that depends on the electrical resistance in the brushes and coil and also on the magnetic flux,  $k_i$  is a constant (approximately) that depends on the magnetic field strength,  $T_{friction}$  is friction torque in the bearings (and brushes, if present),  $k_w$  is a constant that depends on the size and shape of the motor and cooling mechanism of the motor, and  $C$  is a constant value that depends on the amount of power that must be supplied to the motor regardless of speed and torque. The five terms represent the copper losses, the iron losses, the friction losses, the windage losses, and the constant power loss, respectively, in the motor. This power loss must be added to the product of the motor voltage and generated current to determine the requisite input power. The efficiency of the motor is then given by [42]

$$\eta_{motor} = \frac{\dot{W}_{out}}{\dot{W}_{in}} = \frac{T_{motor} \omega_{motor}}{T_{motor} \omega_{motor} + k_c T_{motor}^2 + k_i \omega_{motor} + T_{friction} \omega + k_w \omega_{motor}^3 + C} \times 100\% \quad (5.123)$$

The values of the constants for the prototype LSV motors are assumed to be  $k_c = 0.9$ ,  $k_i = 0.1$ ,  $k_w = 0.00001$ , and  $C = 0$ . The friction term is assumed to be negligible in comparison to the other losses and the constant losses are assumed to be zero since the EM is a brushed PM [42]. The maximum efficiency of the motor, as provided by the motor manufacturer, is 83%. The efficiency map from the 15.88 kW PM motor in ADVISOR was used to estimate the LSV motor efficiency map. The estimate motor efficiency map can be plotted as a function of speed and torque, and the 3-D plot and 2-D contour plots are shown in Figure 6-2 and Figure 6-3 below. The 2-D contour plot has the rated torque-speed curve estimate for the LSV motors superimposed.

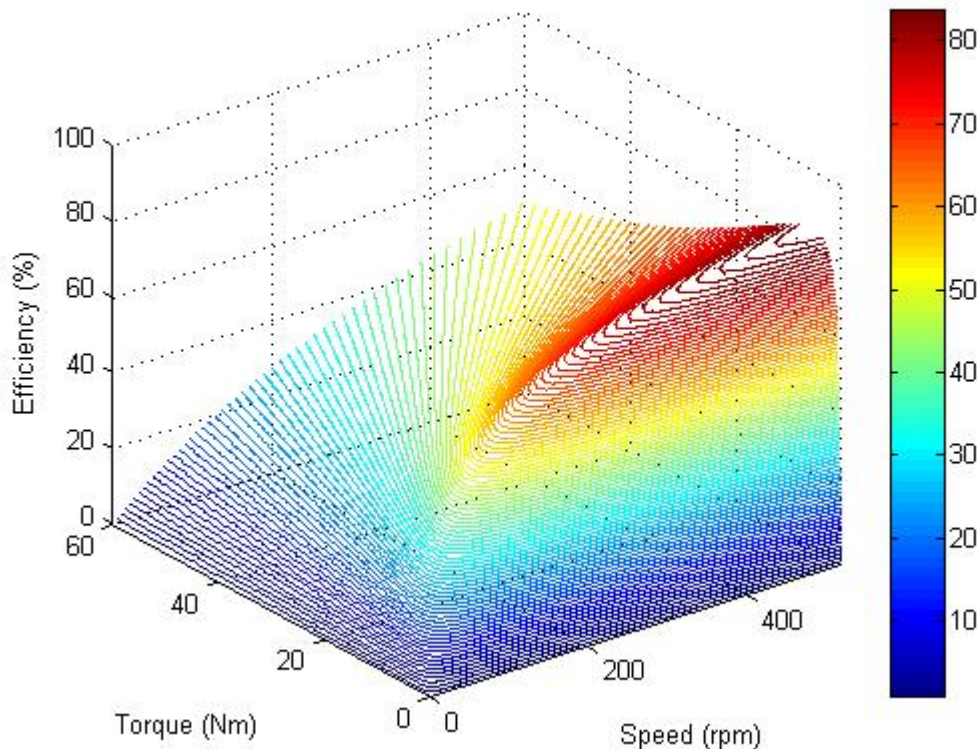
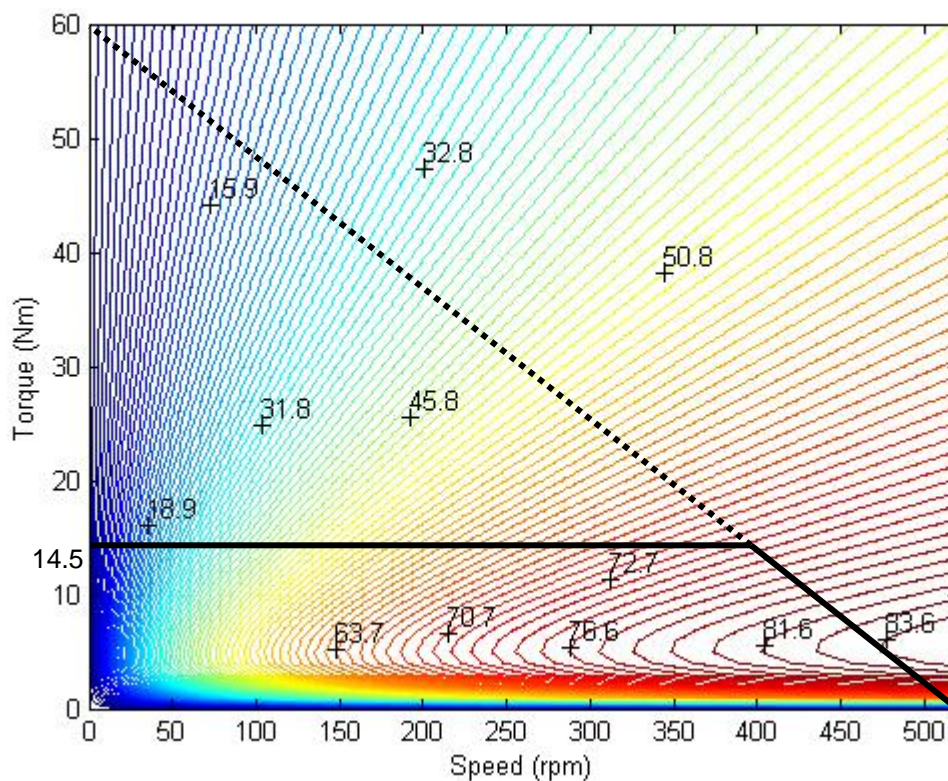


Figure 6-2. Three-dimensional motor efficiency map estimate



**Figure 6-3. Contour plot of the motor efficiency map estimate**

### 6.2.3 Fuel cell hybrid scooter powertrain model

The model for the FCHS powertrain uses many of the same components as the BS; the fuel converter model is added, and the ESS and power management strategy model differ as well. The schematic of the powertrain is shown below in Figure 6-4; note that the depiction is an extension of the FCS schematic shown in Figure 5-1. The prototype FCHS uses metal hydride tanks for hydrogen storage; a radiator (not shown) below the stack transfers the heat to the metal hydride tanks. As mentioned previously, the hydrogen storage is not modelled, and the flow and pressure of hydrogen is assumed to be adequate. The output of the DC/DC converter is 48 V. The cooling system water pump and solenoid valve are at 12 V, not the 48 V of the power circuit; in this case, the pump and valve are connected in parallel to only one of the batteries that

make up the ESS, not all four. The schematic also does not show the 12 V auxiliaries, which consist of a headlight, turn signals, relays (for the motor and fuel cell stack), temperature thermocouple and fuel cell current sensor, which could be connected to a different battery in the ESS.

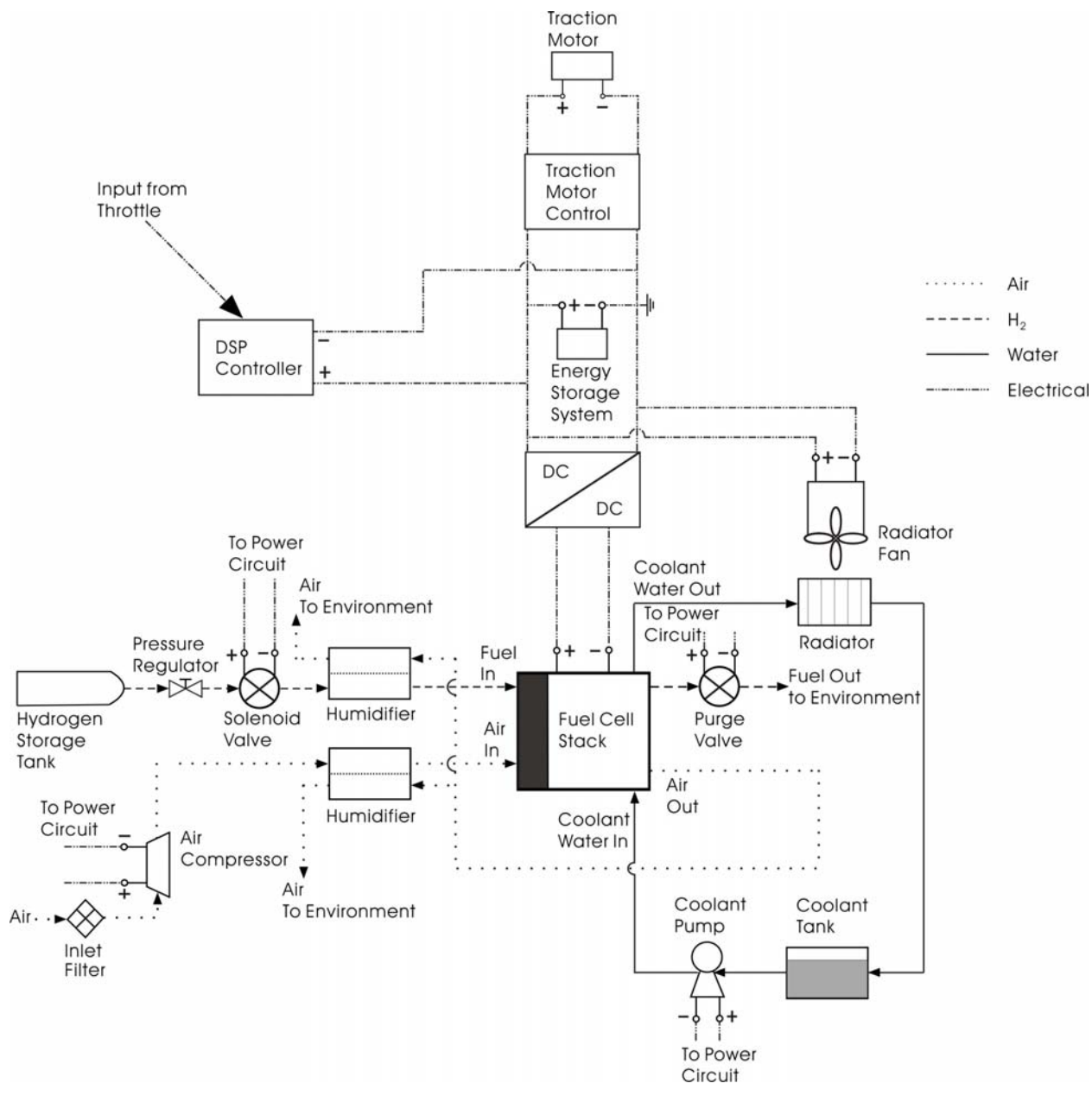


Figure 6-4. Schematic of the prototype fuel cell hybrid scooter powertrain

The fuel cell stack model from Chapter 4 and the system model from Chapter 5 are

incorporated into an ADVISOR module. The number of cells is specified to be 39 to match the actual number in the vehicle. The optimization of the operating parameters of this system will be shown to be 1.369 kW in Section 8.3. The module calculates the gross power, net power, heat generated and parasitic power. The input to the module occurs when the power management strategy sends the value of the current demand based on the drive cycle acceleration and resultant motor demand, as well as the ESS SOC.

#### 6.2.4 Battery models

The FCHS has four B.B. Battery BP5-12 12 V 5 A·hr (20 hr rate) L-A batteries installed. The BS has four Discover D12180 12 V 18 A·hr (20 hr rate) L-A batteries installed. The L-A module in ADVISOR is modified to reflect the characteristics of these particular batteries that are available from the product specification sheets [203, 204]. The module that is modified in ADVISOR is the internal resistor module, the simplest model provided by the program. This simple model was selected because the specification sheets provide very little data that could be used to determine the parameters that are required for the more complex ADVISOR models. The internal resistor model is shown below in Figure 6-5.

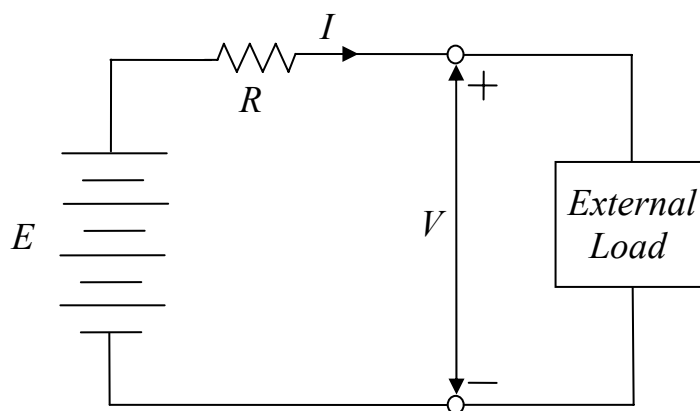


**Figure 6-5. Internal resistor battery model**

The figure shows the four batteries connected in series to achieve the required 48 V voltage. In a real battery, the instantaneous voltage of the battery changes if the battery is being charged

or discharged. The internal resistor model represents this by assuming a constant OCV,  $E$  in the figure, from the batteries but a changing voltage at the external load terminals. Thus, for charging or discharging of the battery, voltage at the terminals is

$$V_{terminal} = E \pm IR \quad (5.124)$$

One of the main limitations of this model is that Equation (5.124) does not capture the dynamic effects of a change in the external load. To model this response, capacitors can be introduced into the equivalent circuit. The OCV and resistance of a battery are also not static values of the battery; these parameters will vary, for example, since both are sensitive to temperature in a complex manner. Battery models are not known for high accuracy in predicting battery performance in practice because of the aforementioned model limitations but also because of difficult-to-quantify factors such as previous usage profiles and variation between cells of a battery module.

The model is semi-empirical, and it was assumed that both the FCHS and BS batteries would have similar properties. Bench-testing of the batteries or a request for information from the battery manufacturer could elucidate the veracity of this assumption. The ADVISOR module has data for the battery cells for an SOC from 0 to 1 and for temperatures ranging from 273 to 213 K. The amp-hour efficiency, which is a measure of the round-trip efficiency of the battery, is assigned a value of 0.9 for all temperatures. The discharge resistance varies from 0.1 to 0.028  $\Omega$ , while the charge resistance varies from 0.055 to 0.15  $\Omega$  at SOC of 1 and 0, respectively. The OCV varies from 11.419 to 13.159 V at the same limits of the SOC. Limits to the minimum and maximum voltage are set at 9.5 and 13.2 V, respectively. The battery model also allows for thermal effects to be taken into consideration, although the parameters for the FCHS battery were unknown and the decision was not to make use of this capability. If parameters such as the heat capacity of the module, area exposed to air, and thickness of the module case material can be determined, this thermal model could prove useful.

### 6.2.5 Control strategy models

The power management strategy used for the FCHS is the generic one in ADVISOR for FCHVs; it is unknown how the actual scooter power management strategy differs from the generic ADVISOR strategy and as a result, how this will affect the comparison between theoretical predictions and experimental outcomes. Furthermore, it is expected that much work could be done to improve the fuel consumption with a power management strategy that uses DP to balance performance with fuel consumption optimization, and this is left for future work. Two HV power management strategy options are available within the strategy module: charge-depleting and charge-sustaining. Charge-depleting strategies allow the ESS SOC to fall below 60%, while charge-sustaining strategies maintain the SOC between 60 and 80% by using the fuel converter to charge the ESS at opportune moments in the drive cycle [40]. The latter strategy type is usually chosen so that the ESS will not be damaged by deep discharge cycles. The SOC of the ESS and the power required by the power bus are the inputs to the power management strategy module. Based on these values, the fuel cell system power requirement is determined. The power management strategy keeps the fuel cell system off until a threshold power is reached, although there is an option to keep the fuel cell on at all times. This threshold power varies, and is dependent upon the power demand and ESS SOC. If the fuel cell is turned off, it must remain off for 90 s, unless the SOC falls below its limit.

There is no power management strategy for the BS except for a regulator to prevent further power to the motor when the ESS SOC reaches the lower threshold. The lower threshold is in this case zero, as a charge-sustaining strategy is not possible. All else being equal, the batteries of a BV will therefore have a shorter lifetime than batteries in a hybrid vehicle.

## 6.3 LSV Simulations

The LSV models both undergo the same ADVISOR simulations. Five simulations were chosen:

1. Acceleration test

2. Gradeability test
3. NYCC drive cycle test
4. Step input to  $16 \text{ km} \cdot \text{hr}^{-1}$  test
5. Range test

The following five sections discuss the results of the simulations, with particular attention to the comparison between the performances of the two LSVs. An assumption is made that the auxiliary components for both LSVs draw 300 W for all simulations.

### 6.3.1 Acceleration simulation

The acceleration test is a simple program in ADVISOR that simply provides the overall vehicle performance; the test does not reveal the performance of individual vehicle components in the manner that the full drive cycle tests do. To run the test, three pairs of speeds, between which the acceleration is to be determined, are entered. Options for the test include the ability to disable the ESS, set the ESS to a certain initial SOC, and to determine the top speed, the distance in a user-defined amount of time or, conversely, the time required to travel a user-defined distance. The output of the test is simply the calculated vehicle performance values. The acceleration tests are used to calibrate the models. Outdoor tests of the BS were conducted and the acceleration test simulations were made to approximate the outdoor test results. This replication is achieved by modifying some of the parameters in the component models discussed previously to the reported values.

A comparison of the results of the road acceleration tests and acceleration simulations for the BS is shown below in Table 6-1. All reported results are averages from the multiple trials. For the first road test, a distance of 26.2 m was measured on an approximately flat, paved roadway. The BS throttle was set to WOT and the vehicle was made to accelerate from stationary and the time elapsed to cover the distance was recorded. The second road test involved a determination of the top speed of the vehicle. The third test involved a measurement of the time required to accelerate from one speed to another; the maximum acceleration capability of the vehicle is determined from these results. All three tests suffer from the

relatively large experimental uncertainty of hand-timing; the latter two tests have the added experimental uncertainty of the reliance on the BS speedometer to provide the vehicle velocity.

**Table 6-1. Acceleration simulation results for the battery scooter model**

<b>Test</b>	<b>Road Test Result</b>	<b>Simulation Test Result</b>	<b>% Difference</b>
Time required for travel of 26.2 m	7.8 s	9.0 s	14.3%
Top speed test	28.1 km·hr <sup>-1</sup>	32.5 km·hr <sup>-1</sup>	14.5%
Time required for acceleration from 0 to 10 km·hr <sup>-1</sup>	-	4.0 s	-
Time required for acceleration from 0 to 20 km·hr <sup>-1</sup>	10.2 s	10.2 s	0.0%
Time required for acceleration from 20 to 30 km·hr <sup>-1</sup>	13.6 s	16.7 s	20.2%
Maximum acceleration achieved	0.54 m·s <sup>-2</sup>	0.8 m·s <sup>-2</sup>	38.8%

As can be seen from the table, the variation between the experimental and simulated results ranges from an exact match for the acceleration time to 20 km·hr<sup>-1</sup> to a substantial percent difference of 38.8% for the maximum acceleration achieved. Several attempts to decrease the differences between the tests were made, but improvement could not be achieved.

The FCHS simulation results could not be verified by experimental results because of malfunctioning of the FCHS. This disappointing occurrence is discussed in more detail in Section 9.3. The FCHS acceleration simulation results are presented in Table 6-2 along with a percent difference test with the BS acceleration simulation results.

The acceleration simulation results show that the FCHS model acceleration capability is greater than that of the BS model. The time required to travel the 26.2 m is 7% less and the top speed and maximum acceleration achieved are 7.1% and 22.2% greater, respectively. These increased performance results are due to the greater amount of current that the combination of FCS and ESS are able to provide to the motor. However, this increased capacity is mitigated to some degree by the greater mass of the FCHS model.

**Table 6-2. Acceleration simulation results for the fuel cell hybrid scooter model**

<b>Test</b>	<b>Simulation Test Result</b>	<b>% Difference with Battery Scooter results</b>
Time required for travel of 26.2 m	8.4 s	7.0%
Top speed test	34.9 km·hr <sup>-1</sup>	7.1%
Time required for acceleration from 0 to 10 km·hr <sup>-1</sup>	3.3 s	19.2%
Time required for acceleration from 0 to 20 km·hr <sup>-1</sup>	10.0 s	2.0%
Time required for acceleration from 20 to 30 km·hr <sup>-1</sup>	14.9 s	5.7%
Maximum acceleration achieved	1.0 m·s <sup>-2</sup>	22.2%

### 6.3.2 Gradeability simulation

The gradeability simulation in ADVISOR is similar to the acceleration simulation in that the output is simply the vehicle performance result. Either the desired grade or velocity of the vehicle is specified, and the program will determine the other value. The velocities that were achievable by the two LSV models were determined for various grades. A maximum of 4% is presented due to the dynamometer testing results, discussed in Section 7.3.1. It was found that the dynamometer eddy current brake is incapable of providing sufficient power for grades of 5% or higher. The results for both LSVs are presented below in Table 6-3. The 0% grade value is taken from the top speed determined in the acceleration simulations.

Analysis of the gradeability test results reveals that the powerplant of the FCHS is generally much more powerful, as the velocities the FCHS achieves are higher. It is interesting to note, however, that the BS achieves a higher velocity at the 1% grade. No explanation for this anomalous result has been determined.

**Table 6-3. Gradeability simulation results for the LSV models**

<b>Grade (%)</b>	<b>Battery Scooter Velocity Result (km·hr<sup>-1</sup>)</b>	<b>Fuel Cell Hybrid Scooter Velocity Result (km·hr<sup>-1</sup>)</b>	<b>% Difference</b>
0	32.5	34.9	7.1
1	23.5	23.3	0.9
2	18.5	19.3	4.2
3	13.2	15.1	13.4
4	7.6	10.9	35.7

### 6.3.3 New York City Cycle simulation

The first drive cycle selected for simulation is the New York City Cycle (NYCC). This drive cycle represents typical usage for a scooter. The cycle is a short commute in a congested traffic network, and it depicts a series of accelerations and decelerations with very little constant velocity. The cycle peak velocity is 44 km·hr<sup>-1</sup> and the average speed is 11 km·hr<sup>-1</sup> over a 598 s time interval. The distance travelled is 1.90 km. The entire cycle velocity versus time graph is shown in Figure 6-6 below.

Both LSV models were subjected to the NYCC simulation cycle, and the results are presented below in Table 6-4. The power management strategy of the FCHS was modified to charge-depleting in order to provide an equivalent test with the BS that must obviously have such a power management strategy. The fuel cell is turned off at the beginning of the cycle, and the power management strategy determines when the fuel cell must be turned on according to the demands of the drive cycle and the SOC of the ESS.

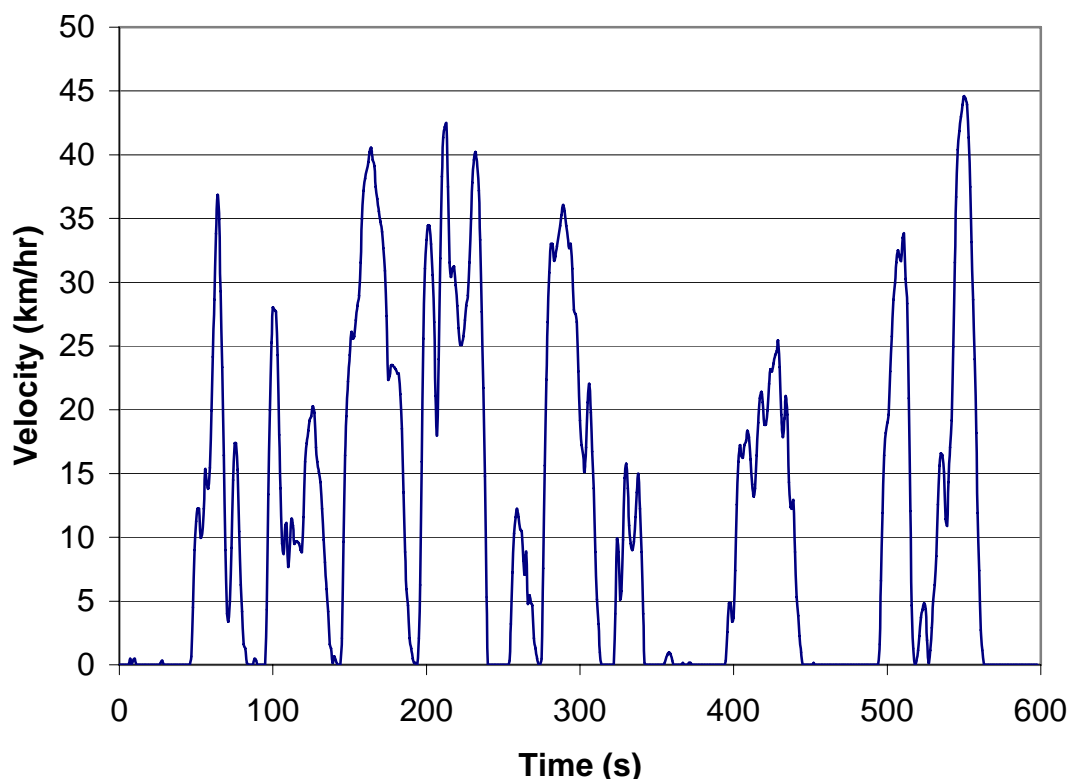


**Figure 6-6. New York City Cycle drive cycle**

Source: Adapted from [118].

**Table 6-4. New York City Cycle simulation results for the LSV models**

<b>Result</b>	<b>Fuel Cell Hybrid Scooter</b>	<b>Battery Scooter</b>
Average Velocity ( $\text{km} \cdot \text{hr}^{-1}$ )	10.1	9.9
Peak Velocity ( $\text{km} \cdot \text{hr}^{-1}$ )	30.4	30.0
Distance Travelled (km)	1.68	1.65
Average % Error from NYCC Velocity Request	8.2%	8.6%
Maximum % Error from NYCC Velocity Request	51.3%	54.7%
Total Energy Consumption (kJ)	624	484
Fuel consumption $\text{L} \cdot (100 \text{ km})^{-1}$ **	1.2	0.92
Rolling Resistance Energy Consumption (kJ)	44	38
Aerodynamic Resistance Energy Consumption (kJ)	15	15

\*\*Fuel consumption is in terms of gasoline equivalency

As can be seen from the table, the FCHS achieves a higher performance than does the BS, albeit at the cost of some fuel efficiency. The average percent error of the FCHS velocity with

respect to the NYCC drive cycle is -8.2%, while that of the BS is -8.6%. The FCCHS also travelled slightly further. Both LSV powertrains must provide 15 kJ of energy to account for the aerodynamic resistance, but the FCCHS powertrain must provide 44 kJ to the rolling resistance versus only 38 kJ for the BS. This is due to the increased mass of the FCCHS.

The percent difference of the fuel consumption of the FCCHS to the BS is 17%. To calculate the fuel consumption, the total energy for each LSV is used and converted into the equivalent energy contained in gasoline. It is assumed that the LHV of gasoline is  $42,900 \text{ kJ}\cdot\text{mole}^{-1}$  and that the density is  $0.74616 \text{ kg}\cdot\text{L}^{-1}$  (at 293 K) [205]. The mass of hydrogen fuel used by the FCCHS during the course of the NYCC is 5.2 g.

#### 6.3.4 Step input drive cycle simulation

The final simulation that is conducted is a step-input from stationary to a velocity of  $17 \text{ km}\cdot\text{hr}^{-1}$  that approximates the step-input dynamometer test discussed in Section \*\*\*. The step input occurs six seconds into the drive cycle and is held for 44 seconds. The FCCHS power management strategy has to be modified for this drive cycle since the fuel cell was not turned on during the drive cycle during the first trial. A setting allowing the fuel cell to be on at the start of the cycle is activated. The results of the step-input tests are presented below in Table 6-5.

**Table 6-5. Step input simulation results for the LSV models**

<b>Result</b>	<b>Fuel Cell Hybrid Scooter</b>	<b>Battery Scooter</b>
Average Velocity ( $\text{km}\cdot\text{hr}^{-1}$ )	3.76	3.73
Peak Velocity ( $\text{km}\cdot\text{hr}^{-1}$ )	17.0	17.0
Distance Travelled (m)	181.3	179.9
Average % Error from Step Input Velocity Request	1.1%	1.2%
Maximum % Error from Step Input Velocity Request	38.1%	38.1%
Total Energy Consumption (kJ)	68	38
Fuel consumption $\text{L}\cdot(100 \text{ km})^{-1}$	1.1	0.66
Rolling Resistance Energy Consumption (kJ)	5	4
Aerodynamic Resistance Energy Consumption (kJ)	1	1

As can be seen from the table, the FCCHS again achieves a higher performance than does the BS, and the fuel consumption is again higher. The average percent error of the FCCHS velocity with respect to the NYCC drive cycle is -1.1%, while that of the BS is -1.2%. The FCCHS also again travels slightly further. Energy consumption due to aerodynamic resistance is 1 kJ for both scooters, and the energy consumption due to rolling resistance is 5 kJ for the FCCHS and 4 kJ for the BS. The percent difference of the fuel consumption of the FCCHS to the BS is 50%. It is assumed that forcing the fuel cell to be on when not necessary causes the fuel consumption to rise dramatically.

### 6.3.5 Range simulation

The last simulation to which the LSV models were subjected is a range test. The range test is a modification of the step-input test, in that the velocity abruptly changes to 24 km/hr at six seconds into the drive cycle. This speed is maintained for the duration of the cycle, set to last 45 minutes. Both ESS SOC's are set to 90% at the beginning of the test. The results of the range test are presented below in Table 6-6.

**Table 6-6. Range simulation results for the LSV models**

<b>Result</b>	<b>Fuel Cell Hybrid Scooter</b>	<b>Battery Scooter</b>
Average Velocity ( $\text{km}\cdot\text{hr}^{-1}$ )	6.64	6.64
Peak Velocity ( $\text{km}\cdot\text{hr}^{-1}$ )	6.67	6.67
Distance Travelled (km)	17.9	17.9
Average % Error from Range Velocity Request	0.05%	0.06%
Maximum % Error from Range Velocity Request	38.1%	58.5%
Total Energy Consumption (kJ)	3373	2205
Fuel consumption $\text{L}\cdot(100 \text{ km})^{-1}$	0.59	0.38
Rolling Resistance Energy Consumption (kJ)	466	409
Aerodynamic Resistance Energy Consumption (kJ)	178	178
Final SOC (%)	45%	8.4%

Both LSV models follow the cycle quite closely. The FCCHS consumes more energy, but its ESS SOC at the conclusion of the test is much higher than that of the BS. The BS ESS has such

a low final SOC that it is not clear if in practice the battery could still be providing sufficient power, although the simulation results give no indication of this. At the very least, this type of driving cycle would cause damage to the ESS if it is a battery, although not if a UC is employed. This test illustrates that while the BS may achieve higher fuel efficiency than the FCHS, the difference masks the consequences of deep discharge cycles for BVs.

The distance travelled in this range test is approximately the actual range of the BS model. The range of 17.9 can be confirmed from the specification sheet of the BS battery. At the range test speed and 48 V, the current from the batteries is 5.14 A. According to the specification sheet, at this current, the battery capacity is 15.42 A·hr [204]. In terms of kJ, the battery capacity is 661 kJ at the nominal battery voltage of 12 V. Each battery contains this energy, for a total of 2644 kJ. The batteries began the test at 90% of full capacity, for a total energy at the start of the test of 2380 kJ. At the conclusion of the test, the batteries would have 174.6 kJ, or 6.6% of full capacity. The percent difference between this value and the SOC determined by the simulation is 24%.

The amount of hydrogen and therefore the number of MH tanks that would be required on-board the FCHS can also be determined. For the energy consumed during the range test, 28.1 g of hydrogen is required. Each Palcan MH tank holds 300 L of hydrogen [206]. By mass, each tank contains 27.0 g. The range test thus requires 1.04 tanks. This also means that the FCHS should be able to travel 51.9 km, assuming that all of the hydrogen in the MH tanks could be released and that the vehicle is travelling at the constant velocity of 24 km·hr<sup>-1</sup>.

## Chapter 7 Low-Speed Vehicle Testing

For any model that is constructed, the key to the acceptance of its suitability to real-world applications is experimental validation. It is therefore up to the model developer to validate the predictive abilities of the model before it achieves a level of credibility that allows its use as a practical tool.

The IESVic LSVTF enables empirical testing of the LSVs for model validation. The experimental tool in this facility is a custom-built dynamometer system designed by Sezer Teczan as his Master's project. The dynamometer system transfers the rolling output of the motorized scooter rear wheel through a belt and pulley system in one direction; the system also imposes the torque produced by an eddy current brake to the rollers in the opposite direction [207]. The roller system simulates a portion of the inertia of the vehicle and its payloads. The eddy current brake supplies the remainder of the vehicle torque and also the driving loads of the vehicle, which include rolling resistance, aerodynamic drag, and hill climbing. The output torque of a load sensor which is connected to the stator of the eddy current brake and also to the pulley and roller system is measured. Two RPM sensors, one at the vehicle wheel and one at the roller pulley, measure the speed of the vehicle wheel and roller, respectively. The torque and speeds are sent to the dynamometer control computer via a computer data acquisition harness. The eddy current brake is manually controlled by a controller unit that is used to vary the current and hence the torque output of the brake; this allows for adjustments in the loading of the vehicle to be made during testing. The lab computer uses the DYNO-MAX® commercial software to set up the testing process and to process and store all experimental data [208].

Finally, the vehicle throttle is controlled by an 8-bit microcontroller designed and programmed by former M.Sc. student Richard Stackhouse. The scooter throttles are modified so that both can accept a pulse-width modulation (PWM) signal from the microcontroller. It is determined that a PWM signal of 225 corresponds to the wide-open throttle (WOT) setting of the scooters. Since the microcontroller is 8-bit, it sends a PWM signal from 0 up to 255; the latter value could cause damage to the motor. The decision was made to never exceed a PWM value

of 225. The microcontroller has two control functions: calibration and drive cycle. In the former, the PWM value can be manually controlled through manipulation of the microcontroller dial. The second control function uses a pre-programmed drive cycle that is converted into a simple computer program and loaded into the microcontroller BASIC Stamp circuit to control the scooter throttle. More information on the microcontroller can be found in reference [209].

This experimental set-up allows for useful data accumulation. A computer-aided design (CAD) rendering of the dynamometer components is shown below in Figure 7-1. The numbered parts in the figure are:

- |                |                          |                             |
|----------------|--------------------------|-----------------------------|
| 1. Roller Unit | 2. Eddy-Current Absorber | 3. Belt                     |
| 4. Pulleys     | 5. Bushing Flanges       | 6. Alignment Plate          |
| 7. I-Beams     | 8. L-Angles              | 9. Bearings                 |
| 10. Torque Bar | 11. Load Cell            | 12. Load Cell Support Plate |

Not shown are the two rpm sensors. One is a magnetic sensor that measures the rotational speed of the rollers, and the other an optical sensor used to measure the rotational speed of the wheel. The two rpm sensors are used to determine if there is slip at the wheel.

The two prototype LSVs along with the FCS of the FCHS are shown below in Figure 7-2. The LSVs are resting on the dynamometer platform, and the FCHS is in the foreground.

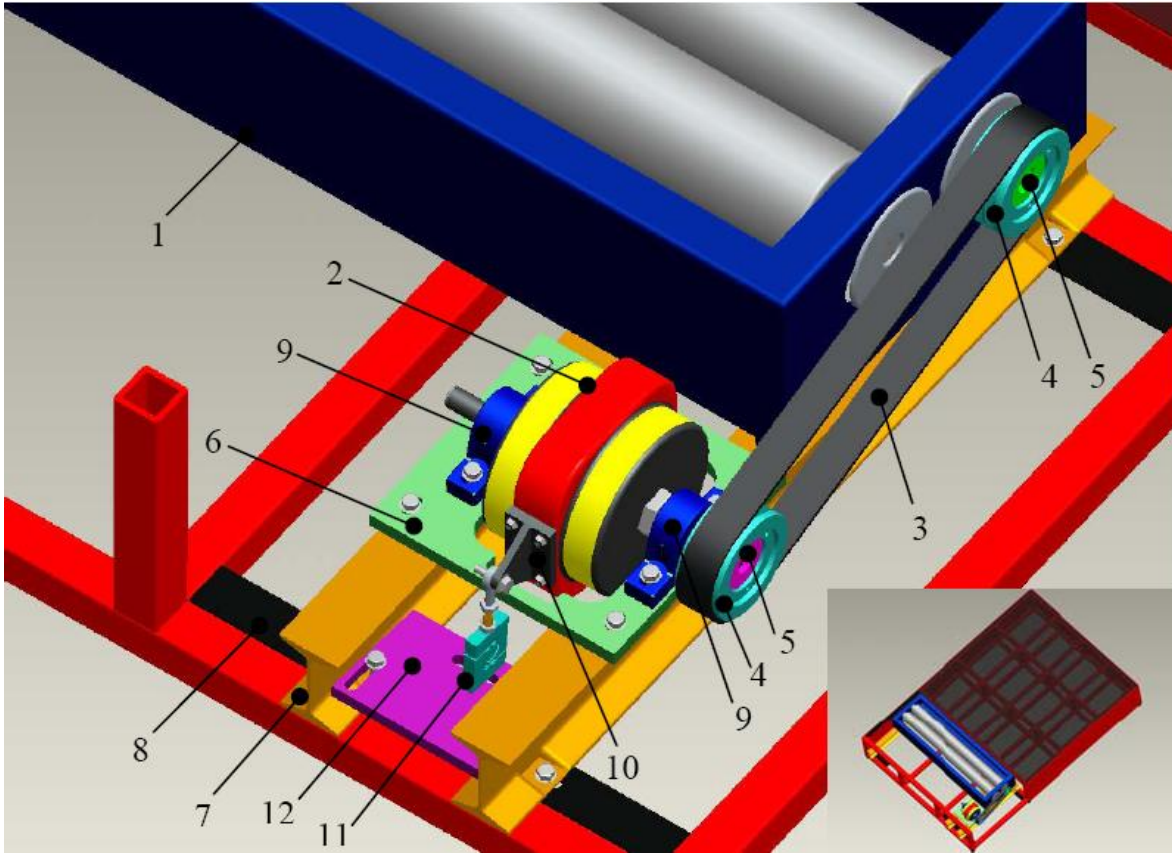


**Figure 7-1. Dynamometer components**

Source: [207], page 56.



**Figure 7-2. Prototype low-speed vehicles and the fuel cell system of the fuel cell hybrid scooter**

Source: [210], page 12.

The computer software screens for the dynamometer are shown below in Figure 7-3. There are three pertinent experimental metrics: the torque (labeled “M-Torque” and “Torque”), “Roller rpm”, and “Wheel rpm”. The panel display labeled “Speedome” is an estimate from the average of the roller and wheel velocities calculated from the rpm values. The Wheel rpm value is actually larger than the actual value by a factor of four; the rpm gauge would not read low-speed values with only one light reflection strip on the wheel, and so four strips are placed evenly around the circumference of the wheel.



Figure 7-3. Test screen of the dynamometer computer software

## 7.1 Dynamometer Relationships

To test an LSV, the back tire is positioned on the rollers such that an equal amount of the back tire weight rests on each roller. A block is placed ahead of the front wheel to prevent forward motion of the vehicle. The vehicle is then restrained either by hand or by straps to prevent rolling about the axis of the bike. Care must be taken to position the vehicle in the same location for each test.

The software tracks the rpm sensors on the roller and on the back wheel as well as the torque output measured by the load cell. The rpm values of the two sensors are related by the equation:

$$\frac{\omega_{roller}}{\omega_{wheel}} = \frac{r_{wheel}}{r_{roller}} \quad (5.125)$$

for the no-slip condition. If the rpm values do not satisfy Equation (5.125), then slip is occurring between the wheel and rollers. Some slip is inevitable, but care was taken to ensure that the slip remained under 5%.

The equation of rotational motion about the center of the rollers (taken as a single roller) is given by

$$T_{brake} + T_{dyno, friction} - F_{wheel \rightarrow roller} r_{roller} = J_{roller+pulleys+rotor} \alpha_{roller} \quad (5.126)$$

where  $T_{dyno, friction}$  is dynamometer friction torque. This friction torque term is due to the friction in the roller bearings, pulley, and rotor section of the dynamometer. The MOI of the roller, pulleys, and rotor is derived from experimental tests as discussed below.  $F_{wheel \rightarrow roller}$  is the force from the wheel acting on the rollers, and is the sum acting on both rollers.  $T_{brake}$  is the torque imposed by the eddy current brake; the total torque is assumed to be equally distributed between the rollers. The angular acceleration of the roller is extrapolated from the measured rotational roller speeds taken by the magnetic rpm sensor. The torque output is a measure of the system response to the applied torque on the rollers; this corresponds to the sum of the dynamometer friction torque and the eddy current brake torque.

The equation of rotational motion about the center of the wheel is given by

$$T_{motor} - T_{wheel, friction} - F_{rollers \rightarrow wheel} r_{wheel} = J_{motor+wheel} \alpha_{wheel} \quad (5.127)$$

From Equations (5.126) and (5.127), the torque of the motor can be determined

$$T_{motor} = \left( T_{brake} + T_{dyno, friction} - J_{roller+pulleys+rotor} \alpha_{roller} \right) \frac{r_{wheel}}{r_{roller}} + T_{wheel, friction} + J_{motor+wheel} \alpha_{wheel} \quad (5.128)$$

where the angular acceleration values of the roller and wheel are extrapolated from the measured rotational speeds taken by the magnetic and optical rpm pick-up sensors, respectively. The MOIs are calculated as described in the following section, as are the resistance torques in the wheel and dynamometer system.

With the motor torque and speed of the wheel known, the power output of the motor can be calculated. The total motor torque can be separated into static and dynamic components. In the equations and calculations that follow, the friction torque terms are assumed to be functions of velocity only, and not functions of acceleration. The same assumption is made for the brake torque. Therefore, there is no dynamic component for either the friction torque or the brake torque. The static component of Equation (5.128) is

$$T_{motor, static} = \left( T_{brake} + T_{dyno, friction} \right) \frac{r_{wheel}}{r_{roller}} + T_{wheel, friction} \quad (5.129)$$

The static dynamometer friction torque is measured directly during experimentation. The static wheel friction torque is more difficult to measure, as discussed in Section 7.2. The dynamic component of Equation (5.128) is

$$T_{motor, dynamic} = J_{roller+pulleys+rotor} \alpha_{roller} \frac{r_{wheel}}{r_{roller}} + J_{motor+wheel} \alpha_{wheel} \quad (5.130)$$

where the dynamic components are obviously zero when the vehicle is neither accelerating nor decelerating. As mentioned previously, the torque reading output by the system is the sum of the dynamometer friction and brake torques:

$$T_{output} = T_{brake} + T_{dyno, friction} \quad (5.131)$$

The torque of the eddy current brake simulates the load from the road in the real-world scenario. Ideally, the torque from the eddy current brake would vary with speed such that the

power at the wheels equation is satisfied:

$$P_{wheels} = \omega_{wheel} r_{wheel} \left[ m_{vehicle} \alpha_{wheel} r_{wheel} + m_{vehicle} g \sin \phi + m_{vehicle} g C_{rr} \cos \phi + \frac{1}{2} \rho_{air} C_D A_F \bar{v}_{aero}^2 \right] \quad (5.132)$$

The power at the wheels can also be separated into static and dynamic components:

$$P_{wheel, static} = m_{vehicle} g \omega_{wheel} r_{wheel} \sin \theta + m_{vehicle} g \omega_{wheel} r_{wheel} C_{rr} \cos \theta + \frac{1}{2} \rho A_f C_D \omega_{wheel} r_{wheel} \bar{v}_{aero}^2 \quad (5.133)$$

and

$$P_{wheels, dynamic} = m_{vehicle} \alpha_{wheel} \omega_{wheel} r_{wheel}^2 \quad (5.134)$$

The static torque of the motor is then

$$T_{motor, static} - T_{wheel, friction} = m_{vehicle} g r_{wheel} \sin \theta + m_{vehicle} g r_{wheel} C_{rr} \cos \theta + \frac{1}{2} \rho A_f C_D r_{wheel} \bar{v}_{aero}^2 \quad (5.135)$$

where the motor torque has been assumed to be the same at the wheels, with no loss in efficiency, because of the nature of the direct connection of a hub motor. The dynamic component is then

$$T_{motor, dynamic} = m_{vehicle} \alpha_{wheel} r_{wheel}^2 \quad (5.136)$$

Ideally, the software would allow for an input of a drive cycle and simultaneously control the eddy brake torque and throttle of the vehicle accordingly. However, in the current experimental set-up, the throttle control is an open-loop system, meaning that there is no feedback loop connecting the load torque and throttle. This ability is essential for a fully functional drive cycle test. Furthermore, the eddy brake torque cannot be controlled by the software, and must be manually controlled by varying the current. This deficiency in the current set-up means that during the tests, for each velocity of the drive cycle, the experimenter must manually select the appropriate current; this will undoubtedly decrease the accuracy of the system, especially the transient response. The full dynamic road load cannot therefore be imposed on the vehicle. It is recommended that the optional Electronic Servo Load Control package be purchased to allow for the dynamometer software to control the eddy brake torque for future research.

## 7.2 Dynamometer Calibration

Before the vehicle testing can begin, the dynamometer set-up must be calibrated. The first calibrations are determinations of the static dynamometer friction torque and the system MOI. To determine the dynamometer friction torque, the eddy brake current is set to zero for a range of roller speeds, and the friction torque measured by the load cell is recorded. The results of this test are presented below in Figure 7-4.

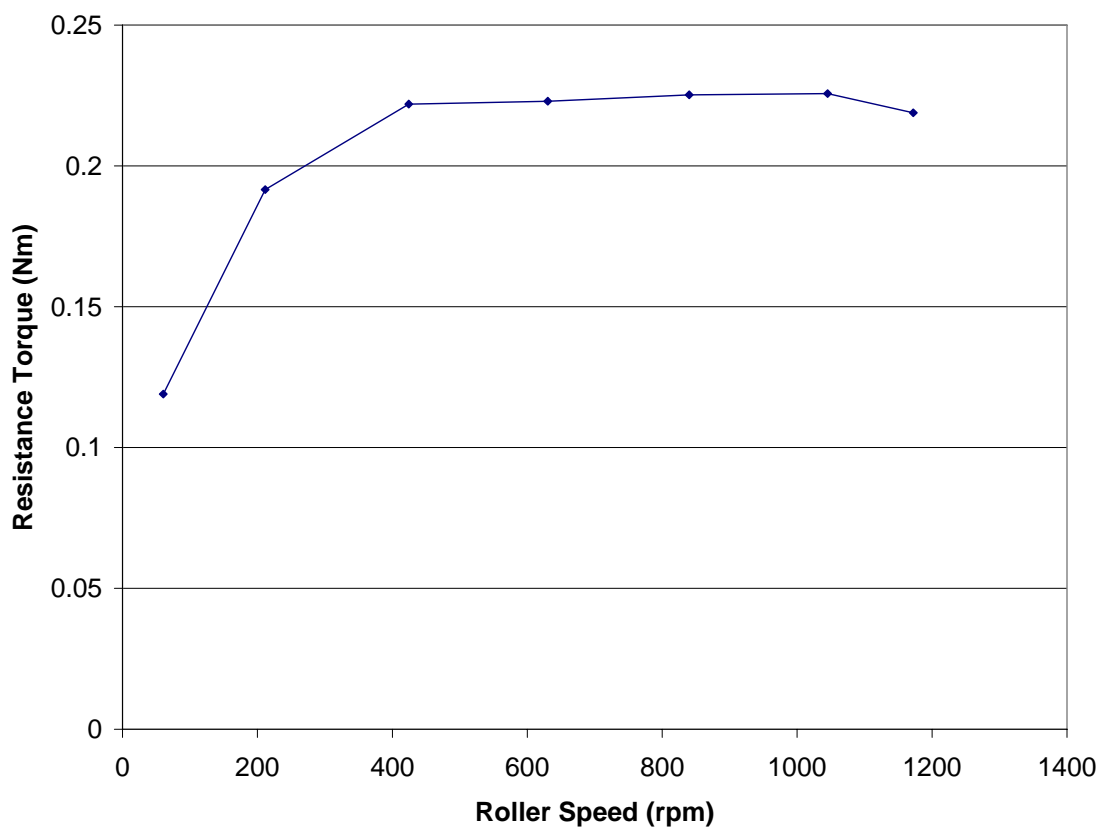


**Figure 7-4. Measured dynamometer friction torque versus roller speed**

The static dynamometer system friction torque can therefore be approximated for a given roller speed. By inserting the dynamometer system friction torque into Equation (5.129), the difference between the motor torque,  $T_{motor, static}$ , and the wheel friction torque,  $T_{wheel, friction}$ , can be determined.

The next step in the calibration is to determine the MOI of the roller, pulley and rotor

system. An attempt was made to accomplish this by removing the scooter wheel from contact with the rollers and using the measured torque (with no eddy current braking) and time required for the deceleration to calculate the angular acceleration and thus the MOI for a range of beginning and ending speeds. The results of these tests were not reasonable. The reason is determined to be the inability of the rpm gauges to provide accurate measurements at very low speeds: a visual inspection of the gauge readings as the rollers slowed showed that a significant lag exists between the time the rollers stopped rotating and the time at which the gauge readings reflect this halt.

The dynamometer system MOI was therefore estimated directly from the component contributions. The two rollers have a combined MOI of  $0.361 \text{ kg}\cdot\text{m}^2$ , while the eddy current brake has a MOI of  $0.011 \text{ kg}\cdot\text{m}^2$ , as provided by Land and Sea Inc, the component supplier [208]. This results in a total MOI of  $0.372 \text{ kg}\cdot\text{m}^2$ . Estimations of the MOIs of the flanges and pulley have allowed for the conclusion that these components contribute negligibly to the overall MOI of the dynamometer system.

The MOI of the wheel and motor assembly was estimated in Section 6.2.1 to be  $0.094 \text{ kg}\cdot\text{m}^2$ . The wheel friction torque can be determined for each scooter by having the scooter wheel rotating at a set of speeds and for each speed setting the throttle to zero and allowing the wheel to come to rest. According to Equation (5.127), the only torque on the wheels is the wheel friction torque. The elapsed times for the wheels to become stationary are used to calculate the angular accelerations of the wheels. Similar to the problems encountered with the system MOI tests, the rpm gauge on the wheel does not operate accurately for low speeds, and it was necessary to measure the elapsed times by hand. The angular acceleration multiplied by the previously determined MOI is equal to the friction torque of the wheel, and this can be repeated for the range of speeds. The calculated wheel friction torques versus roller angular velocity are shown below in Figure 7-5 for both LSVs. The accuracy of the wheel friction torques is somewhat compromised by hand-timing and visual determination of the point at which the wheel stops rotating. It is also possible that a remnant magnetic field in the motor exists

after turning off the motor which, according to Lenz' Law, may slow down the wheel more than otherwise. This will skew the results of the calibration, but no method for determining the magnitude of the skew has been devised, and it is thus neglected.

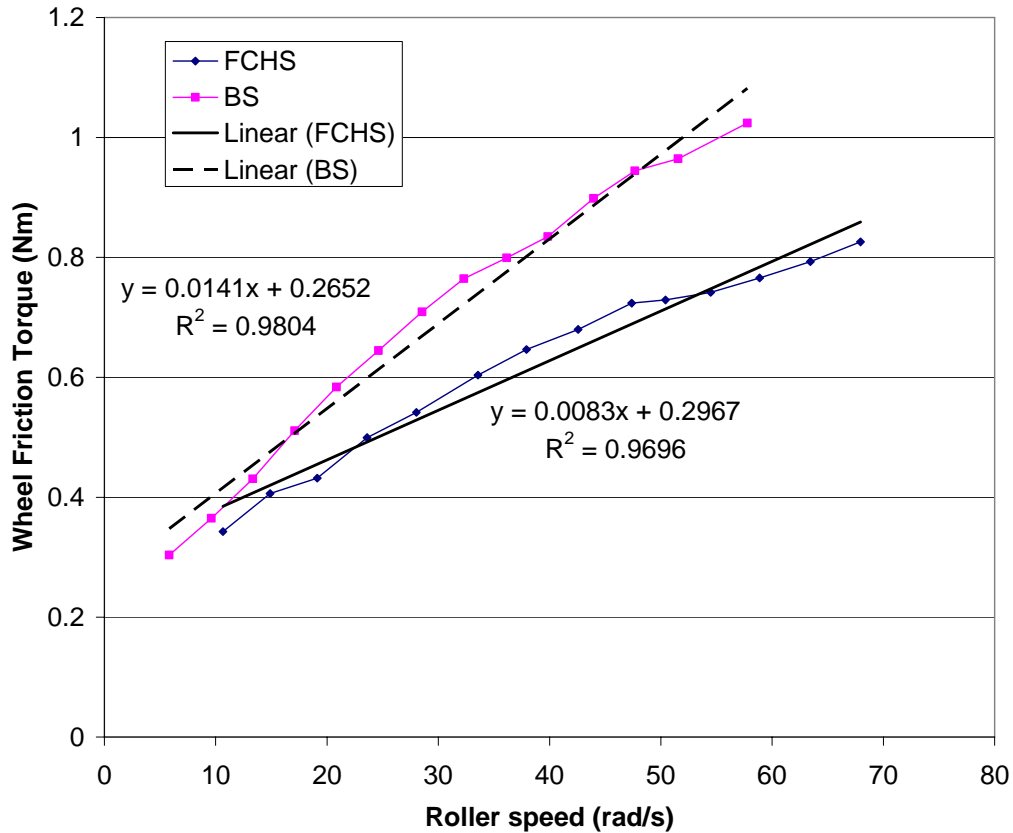


**Figure 7-5. Scooter wheel friction torques versus roller speed**

The relationship between the friction torque and roller angular velocity is approximately linear for both scooters, and is shown on the figure to be

$$T_{wheel,friction} = 0.0141\omega_{roller} + 0.2652 \quad (5.137)$$

for the BS and

$$T_{wheel,friction} = 0.0083\omega_{roller} + 0.2967 \quad (5.138)$$

for the FCHS. It can be seen from the figure that the BS has more wheel friction than the FCHS for all roller speeds. This is likely due at least in part to the increased usage of the BS

that has created friction in its wheel axle and rotor bearings.

The torque measured by the control software is, as mentioned, the total of the eddy current brake torque and the dynamometer friction torque. This total of the static case can be calculated for the BS and FCHS for any given speed, inclination, and wind speed. Assuming no inclination and zero wind, the equation of the required measured torque for the BS as a function of vehicle velocity (in  $\text{m}\cdot\text{s}^{-1}$ ) is given as

$$\begin{aligned} T_{dyno, static, BS} &= T_{brake} + T_{dyno, friction} \\ &= (22.764 + 0.3198v_{vehicle}^2) r_{roller} \end{aligned} \quad (5.139)$$

and for the FCHS, the measured torque as a function of vehicle velocity is

$$T_{dyno, static, FCHS} = (25.978 + 0.3198v_{vehicle}^2) r_{roller} \quad (5.140)$$

The final calibration is to determine the current in the eddy current brake that corresponds to each braking torque over the velocity range. The torques are calculated from Equations (5.139) and (5.140). The current required to achieve this torque at the each vehicle velocity was measured. These current and torque values as a function of vehicle velocity (in  $\text{km}\cdot\text{hr}^{-1}$ ) are shown below in Figure 7-6 for both LSVs.

It can be seen from the figure that the required current falls sharply as the vehicle velocity approaches  $6 \text{ km}\cdot\text{hr}^{-1}$ . Beyond this velocity, the current remains relatively constant. This is true for the static case only; if accelerations are introduced, the current will fluctuate significantly. It should be noted that Equations (5.139) and (5.140) can be easily modified to include the inclination term for the gradeability tests and wind terms to simulate real-world conditions.

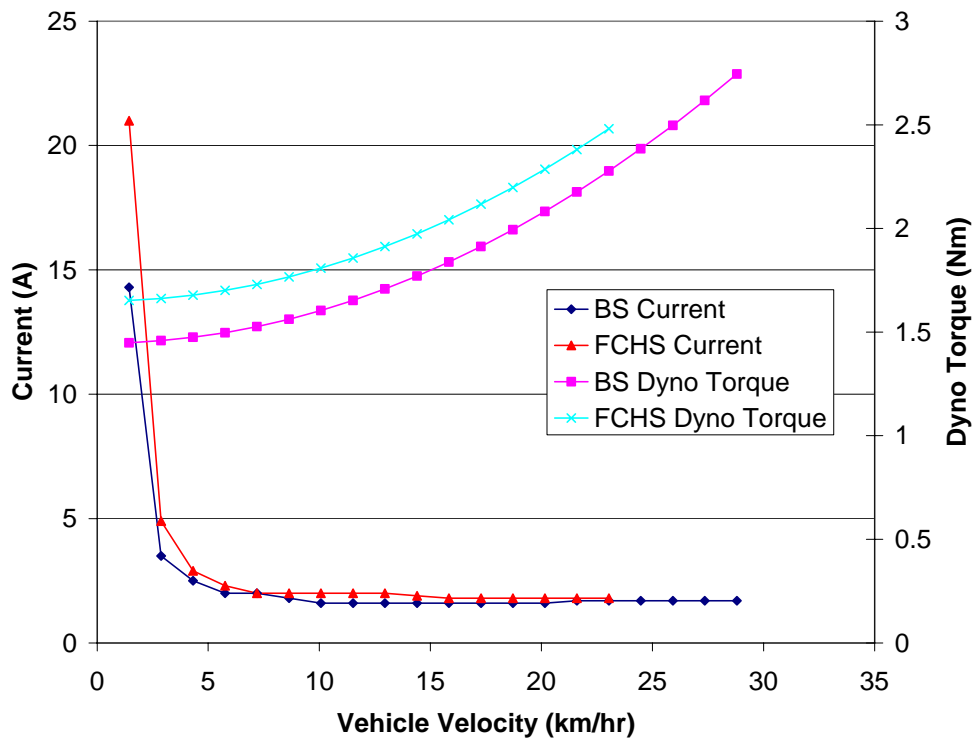


Figure 7-6. Required current and calculated torque versus vehicle velocity

### 7.3 Experimental Results

The LSVs were subjected to two separate tests: a gradeability test and a step-input test. The BS also underwent a range test. The FCHS performance was disappointing in that at high loads, power from the FCS was lost. It has been surmised that the cause is flooding in the membrane due to the inability of the stack to purge sufficient quantities of water. This will be discussed in more detail in Section 9.5. The FCHS was incapable of completing the gradeability test and the majority of the step-input test.

#### 7.3.1 Dynamometer gradeability test

The gradeability tests consisted of setting the throttle to WOT (i.e. PWM=225), and varying the current of the eddy current brake. The brake torque was manipulated to simulate the static road load at each speed. The maximum speed achieved by the BS for each grade was measured.

The dynamometer system could not provide torques high enough to test grades 5% or higher. The gradeability test results for the battery scooter with the ADVISOR gradeability simulation results from Section 6.3.2 are shown below in Table 7-1.

**Table 7-1. Results of the dynamometer and simulation gradeability tests**

<b>Grade (%)</b>	<b>Battery Scooter Velocity Result (km·hr<sup>-1</sup>)</b>	<b>ADVISOR Simulation result (km·hr<sup>-1</sup>)</b>	<b>% Difference</b>
0	27.0	32.5	18.5%
1	24.8	23.5	5.4%
2	19.8	18.5	6.8%
3	16.2	13.2	20.4%
4	12.4	7.6	48.0%

For a 0% grade, the scooter can travel up to 27.0 km·hr<sup>-1</sup>, while for a grade of 4%, the scooter can travel up to 12.4 km·hr<sup>-1</sup>. The former velocity is thus determined to be the scooter top velocity. At the 0% grade, the maximum velocity for the dynamometer test is 18.5% less than the simulated result; at the 4% grade the dynamometer result was 48% greater than the simulated result. It is clear that the correlation between the two values is low.

The torque and power output of the motor for each grade can be calculated for each grade by using Equation (5.129). The torque read by the dynamometer software and the values previously found for the dynamometer friction torque from Figure 7-4 are used to determine the eddy current brake torque. The wheel friction torque is obtained from Equation (5.137). The torque values are summarized below in Table 7-2.

A partial torque-speed curve can be plotted using the results of the gradeability test. The motor torques from Table 7-2 and roller speeds are then extrapolated to the axes to get the full curve. The rated torque is also determined from the maximum power achieved by the BS during the gradeability test. The calculated torque-speed curve is presented in Figure 7-7 below.

The linear fit to the data points is shown in the figure. The extrapolation of this line of

Table 7-2. Motor torque values for the dynamometer gradeability test

Grade (%)	Dynamometer Friction Torque (Nm)	Eddy Current Brake Torque (Nm)	Wheel Friction Torque (Nm)	Motor Torque (Nm)
0	0.221	2.4	1.93	10.1
1	0.226	3.2	1.79	12.6
2	0.225	3.9	1.49	14.5
3	0.223	4.7	1.26	16.8
4	0.222	5.6	1.03	19.3

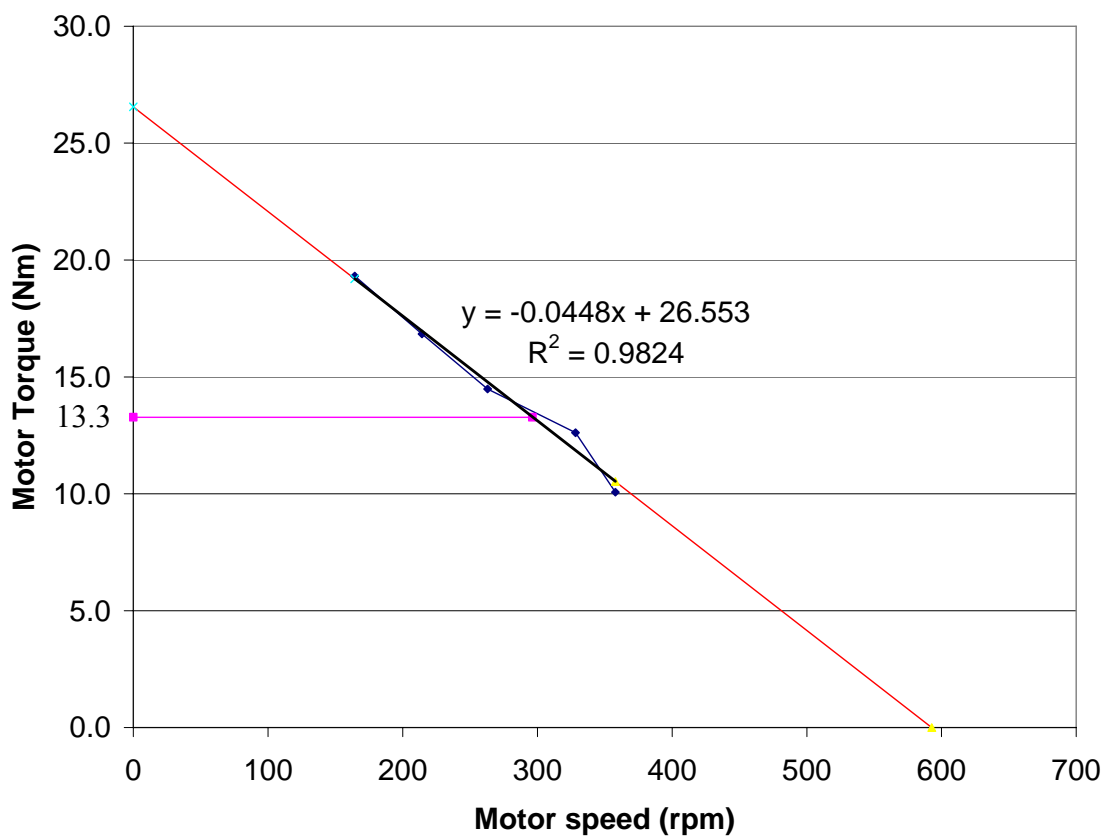


Figure 7-7. Torque-speed curve from dynamometer gradeability results

best-fit is in red. This extrapolation intersects the axes at 26.553 N·m and 590.7 rpm. The rated torque is determined to be 13.3 N·m, which occurs at a motor speed of 296.4 rpm. This results in a maximum power output of 412 W. To find  $K_m\phi$  and  $R_a$ , the best fit curve is used, although it is modified to angular velocity. Solving the two equations reveals that  $K_m\phi$  is

$0.77335 \text{ N}\cdot\text{m}\cdot\text{A}^{-1}$  and  $R_a$  is  $1.39799 \text{ } \Omega$ . These values have a percent difference with the modelled values of 13% and 66%, respectively. It is not clear at this point which method determined the correct values. The WOT setting of the scooter may be limiting the output of the motor in some unknown fashion; however, no matter what the capacity of the motor is, the operation allowed by the LSV control system must be assumed. The values determined in this section will be used in the subsequent drive cycle. The power of the motor and a comparison with the value at the wheels is presented below in Table 7-3.

**Table 7-3. Comparison of the power at the wheels and output by the motor**

<b>Grade (%)</b>	<b>Power at wheels (W)</b>	<b>Motor Power (W)</b>	<b>% Difference</b>
0	305.1	377.4	21.2%
1	372.2	433.8	15.3%
2	357.9	398.9	10.8%
3	349.5	377.8	7.8%
4	314.6	332.3	5.5%

The percent difference between the modelled power required at the wheels for propulsion and the output power of the motor varies from 21.2% to 5.5%. This shows that the chosen parameter values for the vehicle are resulting in an underestimation either of the power required at the wheels or the loss in power transfer from the motor to the wheel.

### 7.3.2 Dynamometer step-input test

The step-input drive cycle is pre-programmed into the microcontroller. The drive cycle consists of four consecutive accelerations separated by varying stationary periods. The settings are: (1) PWM=90, (2) PWM=100, (3) PWM=130, and (4) PWM=150. The accelerations are held for 20 s, 30 s, 40 s, and 40 s, respectively. The throttle settings were adjusted from higher initial values so that the FCHS could complete a full cycle, although the operational problems exist here as well. For the BS, four trials at increasing currents for the eddy current brake were conducted: 0 A, 2 A, 4 A, and 6A. For the FCHS, only the 0 A trial could be conducted; at

higher currents, the FCS operation problems forced a cancellation of these tests. The peak roller speeds achieved by the LSVs for the various trials are presented in Figure 7-8.

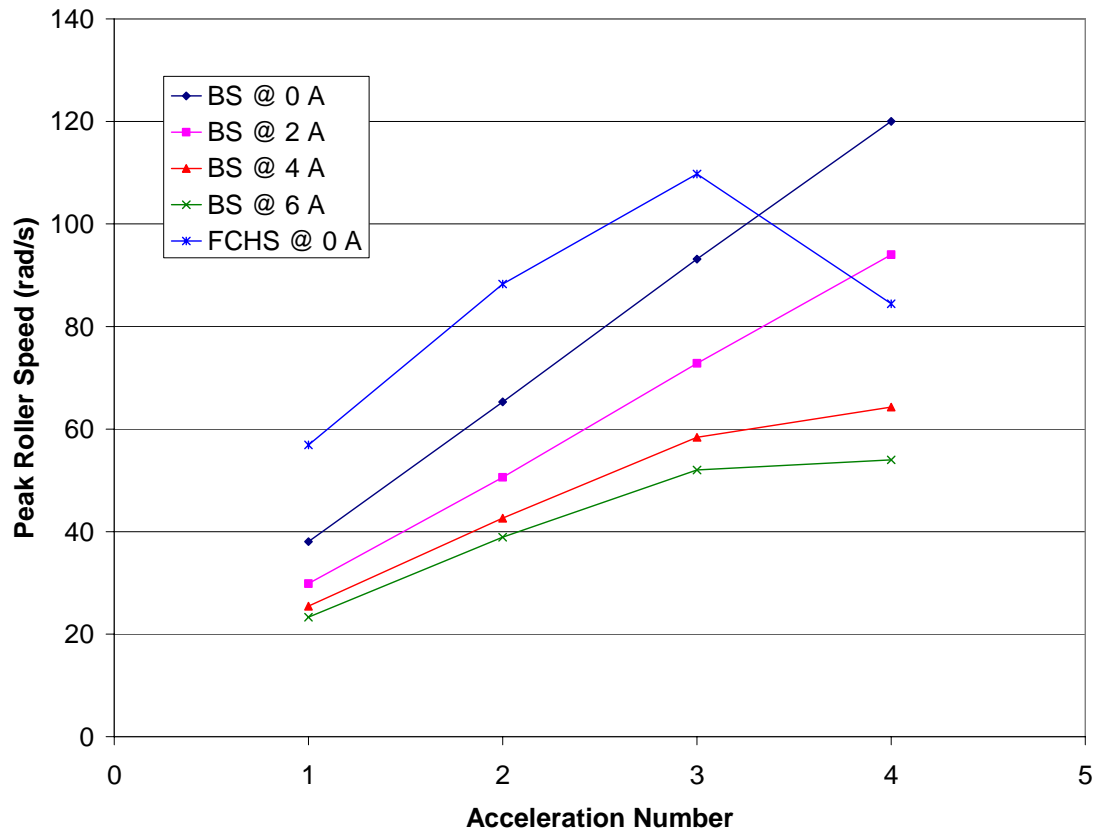


**Figure 7-8. Peak roller speeds achieved by the LSVs during the step-input dynamometer tests**

As expected, the roller speeds achieved by the BS decrease as the eddy current torque is increased. The average of the four acceleration peaks varies from  $79.1 \text{ rad}\cdot\text{s}^{-1}$  for 0 A to  $42.1 \text{ rad}\cdot\text{s}^{-1}$  at 6 A. The FCHS at 0 A achieves an average peak roller speed of  $84.8 \text{ rad}\cdot\text{s}^{-1}$ ; the power demanded during the fourth acceleration causes the aforementioned operation problems and the average is thus decreased from what it likely would have reached without this mitigating factor. Even with this discrepancy, the percent difference in average peak roller speed over the step-input drive cycle at 0 A that the FCHS and BS are able to achieve is 7.0%. This confirms the modelling result that the powertrain of the FCHS is more powerful than that of the BS.

The torque outputs of the motor can be determined as well. Firstly, the motor torque at the

peak speed is found, by the same process as in the gradeability test. A static analysis is sufficient because at the peak speed, there is no acceleration. The motor torque values for each trial are presented in Figure 7-9.

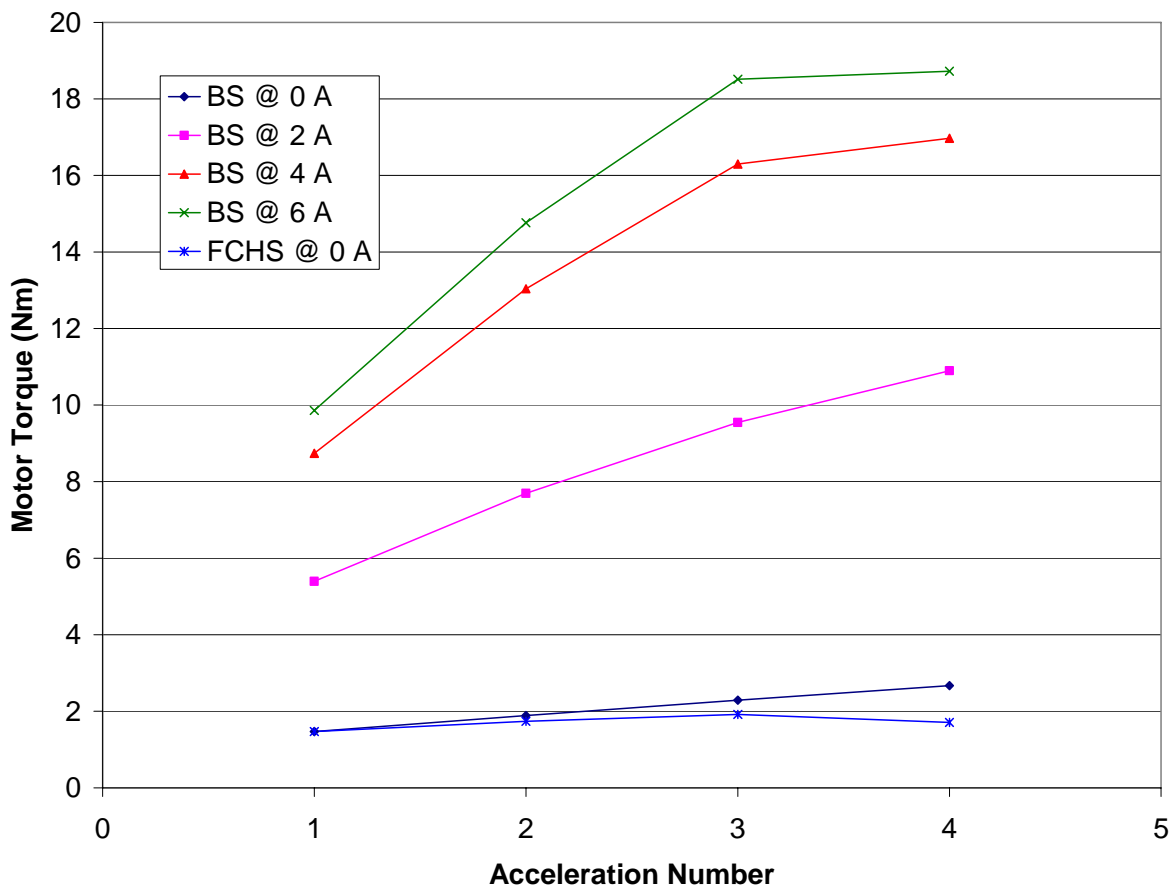


**Figure 7-9. LSV motor torque values at peak speed for the step-input tests**

The results conform to expectations for the BS. The peak motor torque output of the BS is 18.7 N·m. The average of the torques at 0 A is 2.1 N·m while the average at 6 A is 15.5 A. The average of the torques for the FCHS is 1.71 N·m. The percent difference between the averages for the BS and FCHS motor torques at 0 A is 20.5%, but it is interesting to note that the FCHS torque is less than that of the BS despite a higher acceleration achieved. This is likely due to the lower wheel friction of the FCHS. The calculated powers at the peak speeds are presented in Figure 7-10.

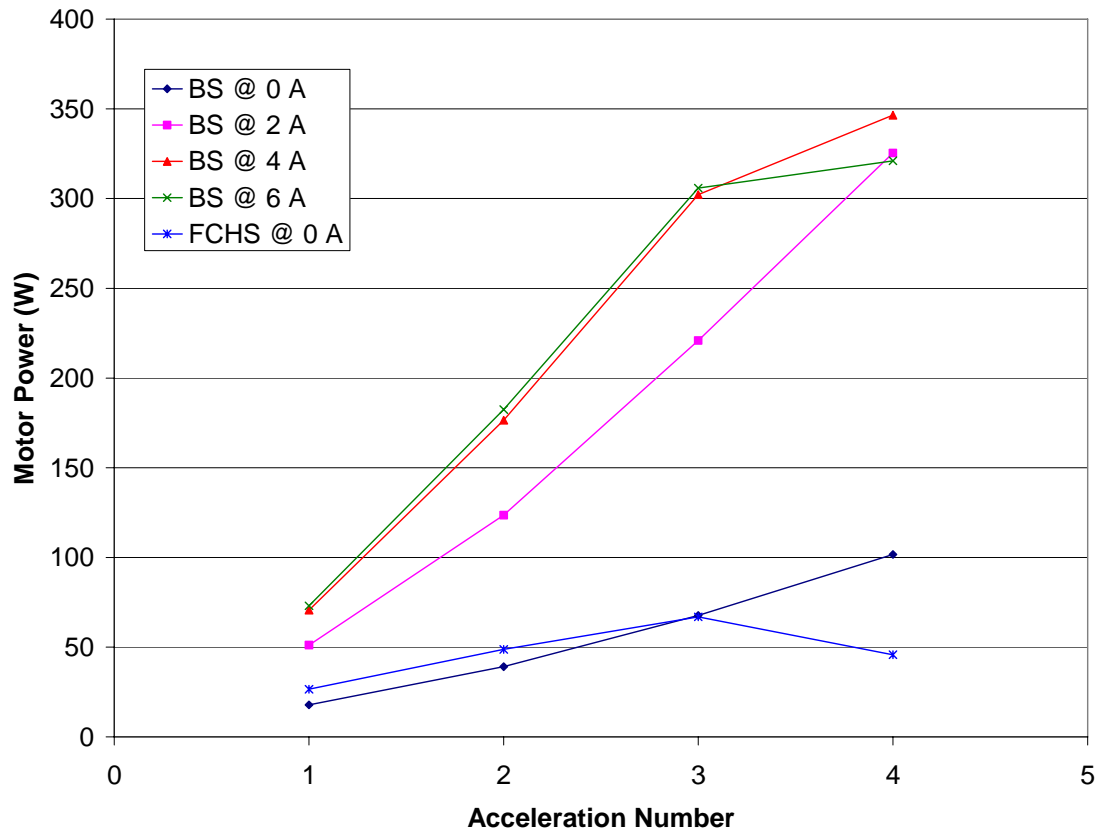


**Figure 7-10. LSV motor power values at peak speed for the step-input tests**

The peak motor power output by the BS is 346.5 W. The average of the motor powers at 0 A is 56.6 W while the average at 6 A is 220.6 A. The average of the power for the FCHS is 47.0. The percent difference between the averages for the BS and FCHS motor torques at 0 A is 18.6%.

The maximum torques and powers for the motor will be output when the vehicle is accelerating. In this case, the dynamic portion of the motor torque, Equation (5.130), must be calculated as well. The MOIs determined for the dynamometer system and LSV wheel are used. The motor torques for the LSVs during the step-input test at the maximum acceleration are shown below in Figure 7-11.

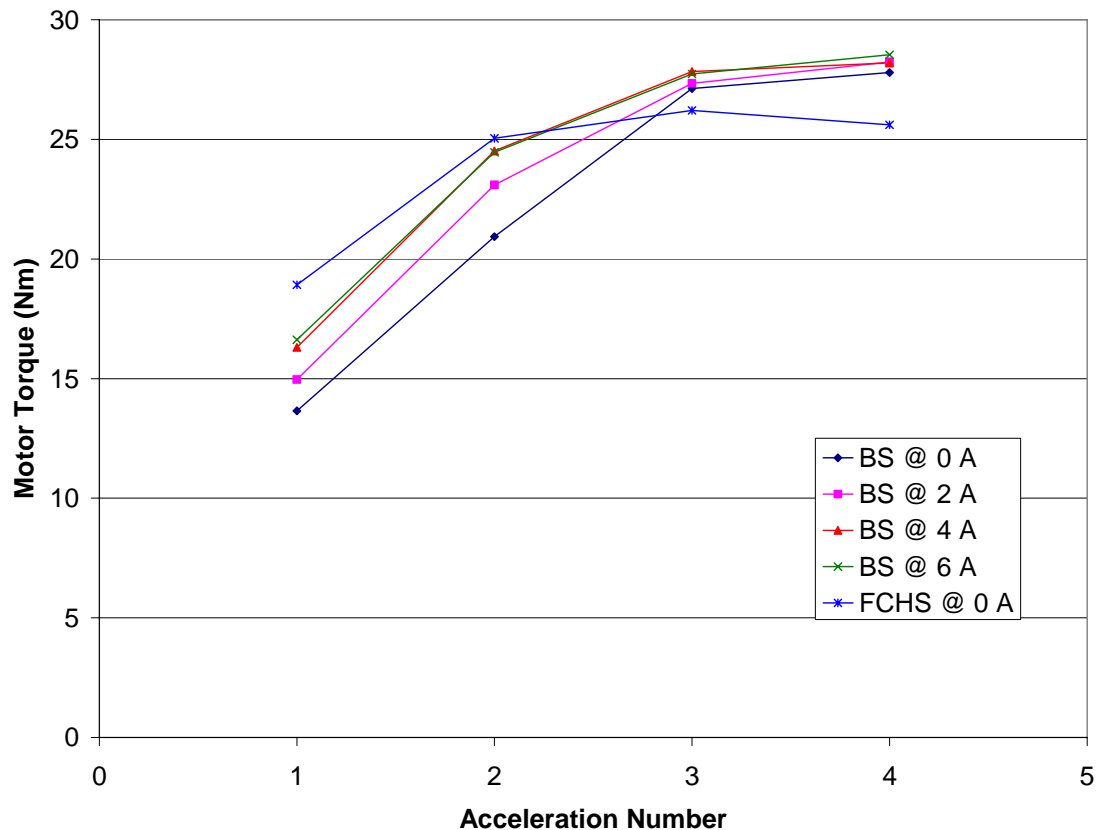


**Figure 7-11. LSV motor torque values at peak acceleration for the step-input tests**

The peak torque output by the BS is 28.5 N·m, while the maximum for the FCHS is 26.2 N·m. It should again be noted that the FCHS torque would be significantly higher if the operation at high powers was not compromised by the faulty operation. The average of the BS motor powers at 0 A is 56.6 W while the average at 6 A is 220.6 W. The average of the power for the FCHS is 47.0 W. The percent difference between the averages for the BS and FCHS motor torques at 0 A is 18.6%. The motor powers for the LSVs during the step-input test at the maximum acceleration are shown below in Figure 7-12.

The motor power at peak acceleration shown in the figure has some interesting features. Most notably, the power of the BS motor at its maximum value for 0 A, 348.9 W, and its maximum value for 6 A, 174.9 W, have a percent difference of 66.4%. The power at 0 A is nearly a factor of two greater than the power at 6 A. The power of the FCHS motor output is

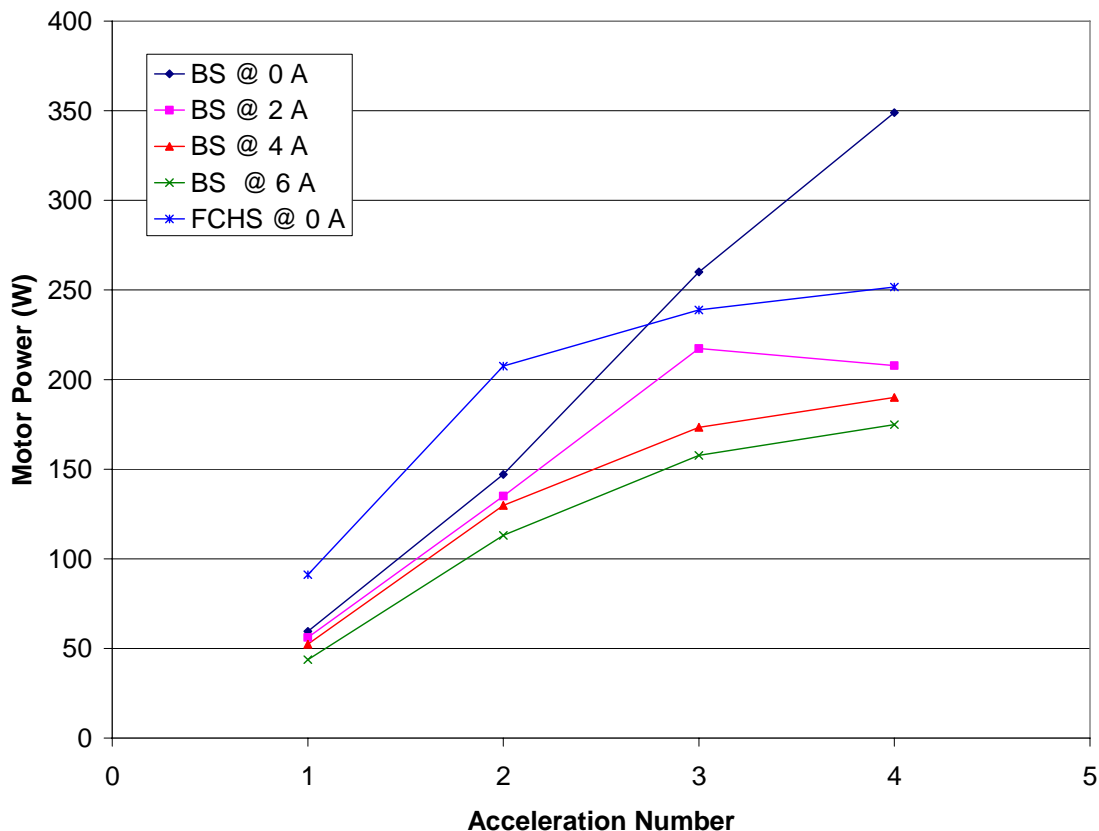


**Figure 7-12. LSV motor power values at peak acceleration for the step-input tests**

207.5 W and the power of the BS motor is 147.1 W, respectively, for the second acceleration. The motor power percent difference at this point in the drive cycle is 34.1%. This result shows that the FCS and battery hybrid powertrain is significantly more powerful than that of the BS, as expected.

### 7.3.3 Dynamometer range test

The range test was conducted to measure the distance the BS is capable of travelling at a constant velocity. The velocity chosen was  $24.4 \text{ km}\cdot\text{hr}^{-1}$ , or 1003 rpm for the rollers. As the test progressed and the system lost power, the PWM value was changed when the scooter stopped maintaining a speed that was within 1% of the designated roller speed, i.e. below 993 rpm. The test began with the PWM level at 197 and finished at a PWM value of 216, at 41 minutes and 31 seconds. The end time was determined when the scooter could no longer maintain a speed

within 1% of the designated roller speed, even at WOT. At the test end, increasing the throttle beyond the 216 value did not provide enough power to continue the test. The time range of the PWM values used during the test are shown below in Table 7-4. As can be seen in the table, the time at each PWM value decreases steadily from nearly seven minutes to well under a minute at the end. The test had an interesting conclusion in that the BS motor shut down just as the experiment was to be shut down. It is speculated that the voltage from the batteries fell below the minimum level required by the motor since the batteries were essentially depleted.

The results of the BS range test were that the vehicle was able to travel at  $24.0 \text{ km}\cdot\text{hr}^{-1}$  for 16.6 km. From Section 6.3.5, the predicted range of the BS is 17.9 km, for a percent difference of 7.6%. Again, the model appears to underestimate the energy requirements for vehicle motion.

**Table 7-4. Battery scooter range test pulse-width modulation changes**

<b>PWM Value</b>	<b>Time range</b>
197	Start-6:50
198	6:51-9:16
199	9:17-13:17
200	13:18-17:43
201	17:44-21:15
202	21:16-25:12
203	25:13-27:02
204	27:03-29:57
205	29:58-30:55
206	30:56-33:25
207	33:26-35:01
208	35:02-36:29
209	36:29-37:28
210	37:29-38:24
211	38:25-39:08
212	39:09-39:47
213	39:48-40:25
214	40:26-40:41
215	40:42-40:55
216	40:56-41:31 (End)

## **Chapter 8 Fuel Cell System Optimization**

Concurrent engineering design is an extremely valuable tool for reducing costs and design lead time. An important step in this process is to use optimization techniques to determine the optimal design without the need to construct expensive and time-consuming physical prototypes. The possible solutions to hasten fuel cell commercialization in vehicles discussed in Section 1.6.3 are implemented much more powerfully if coupled with optimization. For example, if the optimal hybridization for a particular vehicle is determined, the costs and performance of the vehicle will improve.

To explore the capabilities of optimization, two design studies are carried out. The first study uses the unmodified GESSDM and steady-state system modules to provide a platform to carry out the optimization process. Two applications for a FCS are examined: (1) the power demand is expected to vary, as in a vehicle, and (2) the power demand is constant, as in a stationary power plant. Subsequently, a second study that builds on the work of the first and examines how to optimize the operation parameters of the fuel cell system of the FCHS is presented. This optimization is one step in an iterative design process that would allow for a reduced FCS size; a smaller FCS would in turn reduce costs, weight and volume. Other potential strategies for improving the design will be discussed in the Conclusions section.

### **8.1 Previous Fuel Cell-Related Optimization**

Optimization is widely used in many different design areas, but has only been recently introduced in the fuel cell design literature. In the case of fuel cell system design, the mechanisms governing the operation of a fuel cell are of such a complex nature that the objective function might have a plethora of local minimums, and therefore, optimization of such systems can be quite challenging. A search of the scientific literature reveals that attempts at rigorous optimization of FCSs and applications are relatively rare. Given the dubious credibility of the current fuel cell models, fuel cell system optimization is rightfully still in its infancy; as more

confidence in the models is achieved more attempts will undoubtedly occur. Nevertheless, fuel cell research using optimization techniques has been conducted by several research groups. The following sections outline the optimizations that have been done at the fuel cell, stack and system levels.

### 8.1.1 Fuel cell optimization

Grujicic *et al.* [211] used a two-dimensional computational fuel cell dynamics model in order to optimize the electric current per fuel-cell width at a cell voltage of 0.7 V. The optimization algorithm was the sequential quadratic programming (SQP) method and the design parameters to obtain the maximum electric current were operational parameters (air inlet pressures) and geometrical parameters (cathode thickness, cathode length per one shoulder segment of the flow channel and the fraction of cathode length associated with the flow channel).

Mawardi *et al.* [212] employed a one-dimensional mechanistic fuel cell model to optimize the power density with respect to the constraints of several operating parameters. The optimization allowed for quantitative discussion of the effects of membrane and electrode thicknesses and CO concentration on the values of the optimum operating conditions. Most recently, Wu *et al.* [213] performed an optimization on the operating conditions of a PEMFC using metamodeling and a full three-dimensional CFC model. The operating parameters analyzed were the cathode humidification level, the cathode pressure, the cathode stoichiometry and the cell temperature.

### 8.1.2 Fuel cell stack optimization

Wang and Dong [214] used a semi-empirical model based on data from the Ballard Mark IV stack and a novel optimization scheme they named the Adaptive Response Surface Method (ARSM) to find an optimal configuration of a patented fuel cell stack design. The particular stack, known as the Tri-stream External-manifolding Radiator Stack (TERS), was shown to have improved performance and the optimization also minimized the cost of the stack. The semi-empirical model does not include the phenomena that are required for an accurate,

comprehensive fuel cell stack model. The optimization maximized power for five design variables: air stoichiometry, stack width, stack height, convection fin width, and number of cells in the stack. The objective function was constrained to solutions with a total volume of  $0.5 \text{ m} \times 1 \text{ m}^2$ .

### 8.1.3 Fuel cell system optimization

Xue and Dong [153] used a semi-empirical model of the Ballard Mark IV fuel cell along with several models for the auxiliary systems based on performance curves in order to create a model of the FCS. The optimal active stack intersection area and air stoichiometric ratio to maximize net power output were obtained and the production costs were minimized.

Godat and Marechal [215] used a very simple fuel cell stack model as part of a system that includes a steam methane reformer (SMR), water gas shift (WGS) and preferential oxidation (PROX) reactor for complete fuel processing. The optimization objective was to determine the optimal values for the steam to carbon ratio, SMR temperature, stack temperature and fuel utilization level.

Frangopoulos and Nakos [216] conducted a combined performance and cost optimization of a PEMFC for a marine application. Interestingly, the FC stack model used was the GESSDM. The optimization of performance used only the temperature and current density as the design variables, ignoring the large effects that pressure and air stoichiometry have on the system performance, as outlined in the following section.

A previous fuel cell system optimization at IESVic was performed by Guenther and Dong [217], who implemented a cost-based optimization of a FCS using an empirical model of the fuel cell stack and the DIviding RECTangles (DIRECT) optimization algorithm. The goal was to minimize cost for a given required performance. This was done by assigning costs per unit of power for the fuel cell system, motor and ESS and using the New York City Cycle (NYCC) drive cycle. The results showed a 60% improvement in cost for the three components over the initial design.

## 8.2 Study optimization of a fuel cell system

In order to be able to use an optimization technique, a problem that contains several conflicting objectives must be identified. For single cell optimization, where the output power is to be maximized, the conflicting goals are mainly due to heat and water management issues. For example, if the air stoichiometry is small, the air will not be able to eliminate all the water produced in the cathode of the cell and flooding will occur at the GDL (or PTL), which will result in a large reduction of the generated power. On the other hand, if the stoichiometry is too large, the membrane will dry out, reducing the proton conductivity and therefore reducing the output power. There exists an optimum value of the air stoichiometry for which there is enough water for the membrane to be humidified without flooding occurring in the gas diffusion layer; it is at this value where the maximum output power occurs. The model used in the optimizations assumes that the membrane is fully hydrated; therefore, the aforementioned conflict of objectives does not occur. Due to the lack of conflicting objectives, optimization of the output power of a single cell or a fuel cell stack yields unrealistic results, as the design variables have mutually exclusive effects on the overall performance. Increasingly complex models are necessary to perform stack and single fuel cell optimization.

In this study, to handle conflicting objectives the fuel cell system is optimized as a whole. In this case, the power consumed by the auxiliary systems creates several conflicts of interest when the net output power is to be maximized. The operation of the fuel cell is improved significantly at a high temperature and pressure; however, these increases would result in higher power losses due to the auxiliary systems, in particular due to the cooling system and the air compressor, respectively. It is because of these conflicting interests that the design of a fuel cell system is a good candidate for optimization.

The GESSDM without degradation is used because the transient effects added with the modifications could not be used in subsequent work. This study was a preparation for optimization of a low-speed FCHS in ADVISOR, which does not have transient simulation capabilities.

Since it is unknown whether the objective function will be unimodal, multiple optimization algorithms are considered. Many different algorithms have been developed by researchers in the field of optimization. Three popular and successful techniques have been chosen for this work:

- (1) simulated annealing (SA)
- (2) genetic algorithm (GA)
- (3) sequential quadratic programming (SQP)

The first two are global optimization algorithms, while the third is a local optimization algorithm. The reader is directed to SA references [218, 219], GA references [220, 221] and SQP references [222, 223] for more information on the details of the optimization algorithms; these algorithms are also summarized in Appendix C. The local optimization algorithm is chosen so that the shape and nature of the objective function can be examined. If the SQP algorithm does not produce results similar to those of the global optimization methods, then it will be clear that the objective function is not unimodal and smooth, but in fact contains local minima which “trapped” the local optimization algorithm.

To solve the optimization problem the fuel cell system model described in the previous section is coupled to the optimization algorithms described above as shown in Figure 8-1. The coupling between the optimization algorithm and the model is achieved through the design variables and the objective function and constraints. First, either the optimization algorithm or the user selects the initial value for the design variables. In the case of global methods, the initial value for the design variables is selected randomly. In the case of a local method, the user gives the initial value for the design variables. The value of the design variables is then given to the fuel cell system model. The fuel cell system model then computes the performance of the system; from those results, the program computes the value of the objective function subject to the design constraints. With this information, the optimization algorithm chooses a new set of design variables that can potentially increase the system performance. This process is repeated until a convergence criterion is satisfied or the maximum number of iterations is

achieved, depending on the optimization algorithm used. For example, if a local optimization algorithm is used, the new set of design variables is determined from the gradient of the objective function. The optimization algorithm automatically calls the fuel cell system model with a small perturbation in each one of the design variables and computes the numerical gradient using adaptive forward differences. The program will then choose the next set of design variables that will result in a value of the objective function that follows the gradient towards the optimal value.

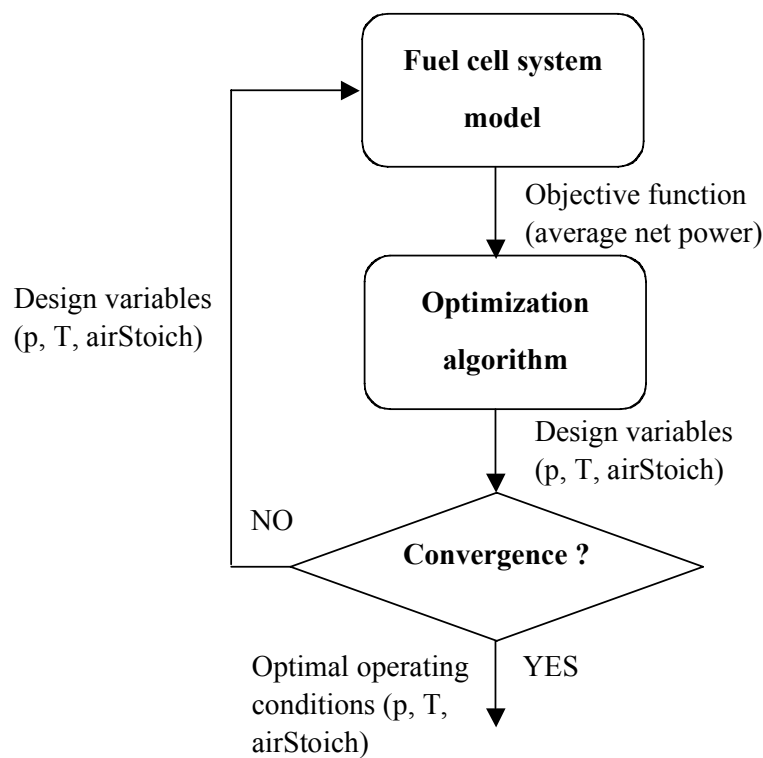


**Figure 8-1. Flow diagram of optimization methodology**

### 8.2.1 Multi-objective optimization

In this portion of the study, the optimization of a fuel cell system that must operate over a wide range of power requirements is performed. An example of such an application is in a FCHS. In a FCHS, the power demands on the fuel cell system change with varying levels of acceleration and velocity. Therefore, it is desired to obtain the fuel cell system operating

conditions that yield the maximum average net power or average exergetic efficiency over varying power demands to maximize acceleration and velocity or vehicle range performance, respectively. The fuel cell system design optimization problem is then formulated as a multi-objective optimization problem:

$$\begin{aligned} \text{Maximize: } f(\mathbf{x}, i) &= \sum_{j=1}^N w_j \dot{W}_j(\mathbf{x}, i_j) \\ \text{w.r.t. } \mathbf{x} & \\ \text{subject to: } \mathbf{x}_{\max} &\geq \mathbf{x} \geq \mathbf{x}_{\min} \end{aligned} \quad (8.1)$$

or

$$\begin{aligned} \text{Maximize: } f(\mathbf{x}, i) &= \sum_{j=1}^N w_j \eta_j(\mathbf{x}, i_j) \\ \text{w.r.t. } \mathbf{x} & \\ \text{subject to: } \mathbf{x}_{\max} &\geq \mathbf{x} \geq \mathbf{x}_{\min} \end{aligned} \quad (8.2)$$

where  $\dot{W}_j(\mathbf{x}, i_j)$  is the net power and  $\eta_j(\mathbf{x}, i_j)$  is the system exergetic efficiency obtained from the fuel cell system at a current density  $i_j$  for objective  $j$ ,  $w_j$  is the weighting of objective  $j$ , and  $\mathbf{x}$  is the vector of design variables. The net power output and exergetic efficiency of the fuel cell system are obtained using the computational model described above. The design variables include the *operating temperature*, the *air stoichiometry*, and the *operating pressure* of the fuel cell stack. The upper and lower limits of these design variables are  $\mathbf{x}_{\max} = [373, 5, 15]$  and  $\mathbf{x}_{\min} = [338, 1.5, 1]$ , respectively. If only two objectives were present, it would be possible to create a Pareto curve to see the trade-off between objectives; in this case, however, the objectives are the maximization of the average net power and average exergetic efficiency for every value of current density from 0.1 to 1.3 A·cm<sup>-2</sup>. The multi-objective optimization problem with different weights will yield different optimal operating conditions. In this study, the objective is to optimize over the entire range of current densities with all values assigned equal importance. The weighting coefficients are then uniformly assigned a value of 1, meaning that the optimization is essentially non-weighted.

The maximization of the net power is solved using the three optimization algorithms described above. The results are provided in Table 8-1. The solutions of the three methods

are almost identical. The solution achieved using the GA has a small error. Increasing the number of generations in the algorithm will reduce this error. The SA algorithm stopped when a convergence criterion of three successive iterations with a difference in the objective function smaller than  $1 \times 10^{-6}$  was satisfied. The GA algorithm stopped after running 200 generations; the convergence criterion was not specified. Finally, the SQP algorithm stopped when the gradient of the objective function reached a value less than  $1 \times 10^{-8}$ . In principle, the solution of the SQP is dependent on the given initial point. Therefore, multiple initial points were implemented in the SQP optimization. All converged on the same value.

**Table 8-1. Solution to the non-weighted multi-objective problem: average net power**

<b>Optimization Algorithm</b>	<b>Objective Function: Avg. Net Power (W)</b>	<b>Solution: [ T (K), AirStoich (-), P (bar) ]</b>	<b>Number of Function Evaluations</b>	<b>CPU Time (s)</b>
Simulated Annealing	664	[ 367, 1.5, 2.04 ]	3001	55.1
Genetic Algorithms	664	[ 366, 1.5, 2.01 ]	4000	615.8
SQP	664	[ 367, 1.5, 2.04 ]	100	3.0

Due to the different nature of the methods and the different convergence criteria it is difficult to do a thorough comparison of the computational expense of these methods. Looking at the number of function evaluations and the required computational time in Table 8-1 for the three methods, we can observe that the local method (SQP) converges to the solution very quickly. Similar results were obtained when the initial starting point was varied. From this assessment, it can be observed that the shape of the objective function is likely to be smooth and convex (unimodal) since the local method converges to the same solution regardless of the choice for the initial point.

In order to be able to show the improvements given by the new operating conditions, the performance of the fuel cell system is compared to the performance of the same fuel cell at nominal operating conditions. The fuel cell system running at the nominal operating condition is

known as the base case in the rest of the paper. The base operating conditions include a temperature of 355 K, air stoichiometry ratio of 2.5, and a pressure of 3 bar. The hydrogen stoichiometry is constant at 1.1. Performances of the fuel cell system operating at the calculated optimal operating conditions and at base operating conditions are compared. The differences between the base and optimized operating conditions were: 3.2% (temperature); -40% (air stoichiometry); and -31.9% (pressure).

Figure 8-2 depicts the net output power of the fuel cell system at the optimal and base operating conditions. A large increase in both the average and peak net output powers can be observed under optimal operating conditions. With the optimal peak at 933 W and the base peak at 728 W, the optimal conditions present a significant increase in the net power of 21.9%. This increase in net power is due to a decrease in the necessary power of the auxiliary devices since the gross output power between the base and optimized operating conditions is similar, as shown in Figure 8-3. The optimization has also moved the point at which maximum net power is achieved to a higher current density, from  $0.89 \text{ A}\cdot\text{cm}^{-2}$  to  $1.01 \text{ A}\cdot\text{cm}^{-2}$ , a change of 11.6%.

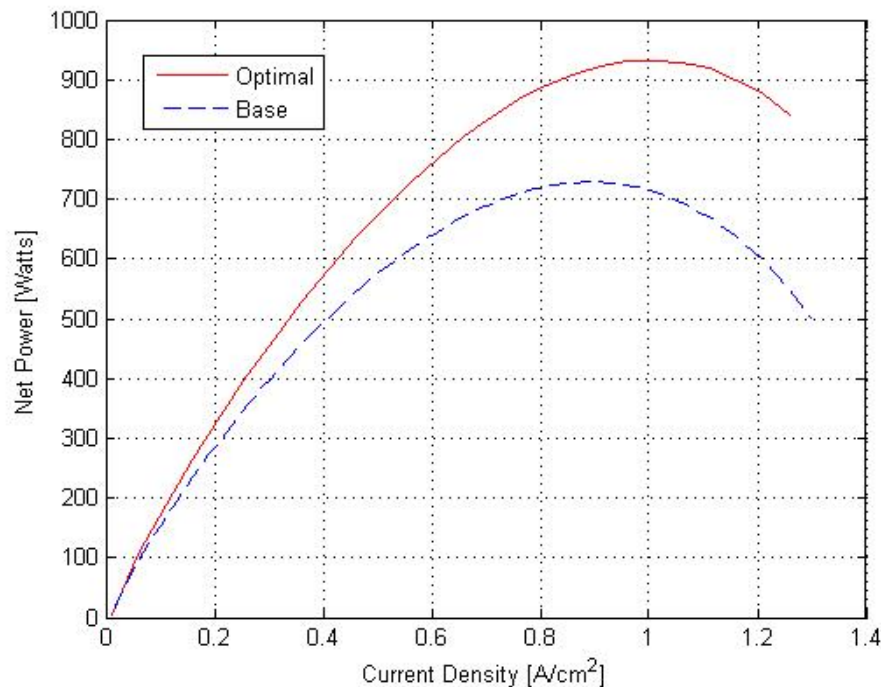


**Figure 8-2. Net Power curve for the non-weighted, multi-objective problem: average net power**

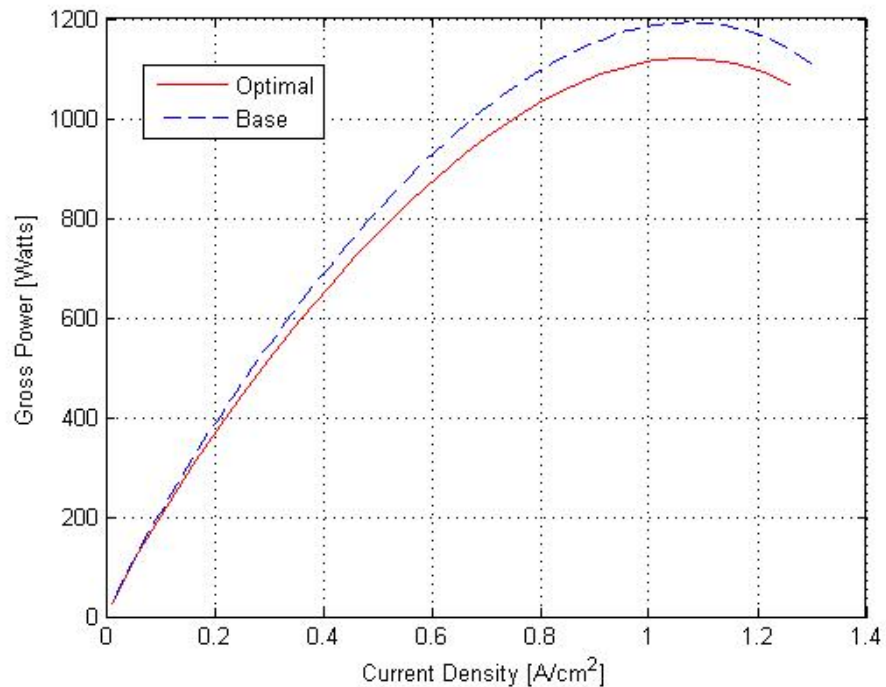


**Figure 8-3. Gross power curve for the non-weighted, multi-objective problem: average net power**

At the base operating conditions and at an arbitrary current density of  $0.76 \text{ A}\cdot\text{cm}^{-2}$ , the consumed powers in the cooling pump, humidifier pump and air compressor are 5.0 W, 5.0 W (minimum allowed power) and 350 W, respectively. At the optimal operating conditions and identical current density, the cooling pump, humidifier pump and air compressor consume powers of 5.0 W, 5.0 W and 130 W, respectively. This represents decreases of 0%, 0%, and 62.8% in the power consumption of each parasitic device. The parasitic powers of the cooling and humidifier pumps are unchanged since 5.0 W is defined as the minimum power draw of the devices, and both the base case and optimal solution show that this is more than sufficient power to fulfill the cooling and humidification requirements. The large increase in net power is mainly due to the massive reduction in the power consumed by the air compressor, caused by a large reduction in the air stoichiometric ratio and operating pressure. The compressor power is reduced dramatically at all current densities, as shown in Figure 8-4.

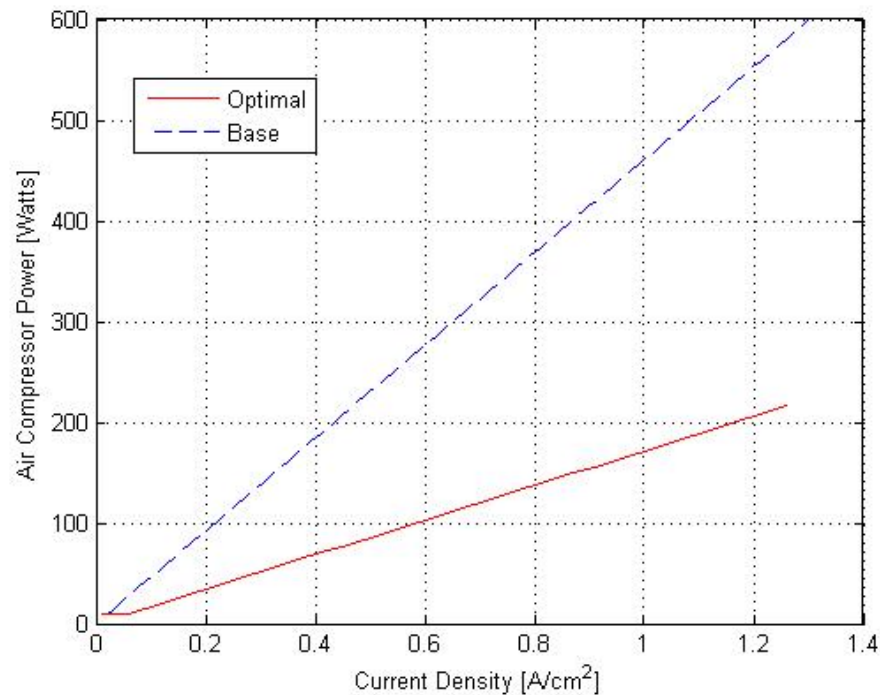


**Figure 8-4. Air compressor power curve for the non-weighted, multi-objective problem: average net power**

The efficiency of the fuel cell system is also dramatically improved by the optimization. Figure 8-5 illustrates the exergetic efficiency as a function of current density for both the optimal and base cases. The peak exergetic efficiency is 0.70 (at 0.06 A·cm<sup>-2</sup>) for the optimized operating conditions, while the peak exergetic efficiency is 0.65 (at 0.06 A·cm<sup>-2</sup>) for the base case, for a percent improvement of 7.4%.

It is also possible, and interesting, to see the difference in performance when the design objective is to maximize the average system exergetic efficiency. The optimization results when the objective function is the average exergetic efficiency are included in Table 8-2 below.

In this design optimization problem, the maximum average net system exergetic efficiency obtained was 0.52. The peak value of 0.70 (at 0.11 A·cm<sup>-2</sup>) is slightly higher than in the previous average net power optimization by 0.3%; more importantly, however, the current density at which the peak exergetic efficiency is achieved is at a higher, more useful level. The exergetic efficiency as a function of current density is shown below in Figure 8-6. The

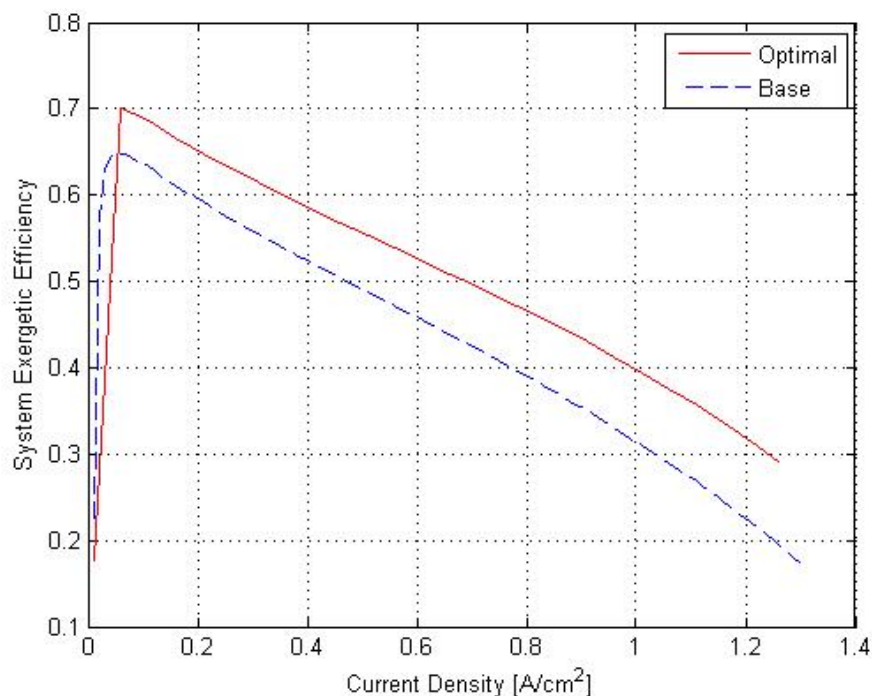


**Figure 8-5. System exergetic efficiency curve for the non-weighted, multi-objective problem:  
average net power**

**Table 8-2. Solution of the non-weighted multi-objective problem: average exergetic efficiency**

<b>Optimization Algorithm</b>	<b>Objective Function: Avg. Exergetic Efficiency</b>	<b>Solution: [ T (K), AirStoich (-), P (bar) ]</b>	<b>Number of Function Evaluations</b>	<b>CPU Time (s)</b>
Simulated Annealing	0.52	[ 361, 5.0, 1.04 ]	3301	23.4
Genetic Algorithms	0.52	[ 361, 5.0, 1.04 ]	4000	306.9
SQP	0.52	[ 361, 5.0, 1.04 ]	189	3.7

peak net system power is 920 W (at 1.01 A·cm<sup>-2</sup>), which is 1.3% lower than in the case of average net system power optimization. An optimization of the exergetic efficiency of a system is useful because it can directly contribute to lower initial investment and operating costs. The shortage of maximum average power can be addressed by using a hybrid power system with a battery or ultracapacitor to boost the system power when required.

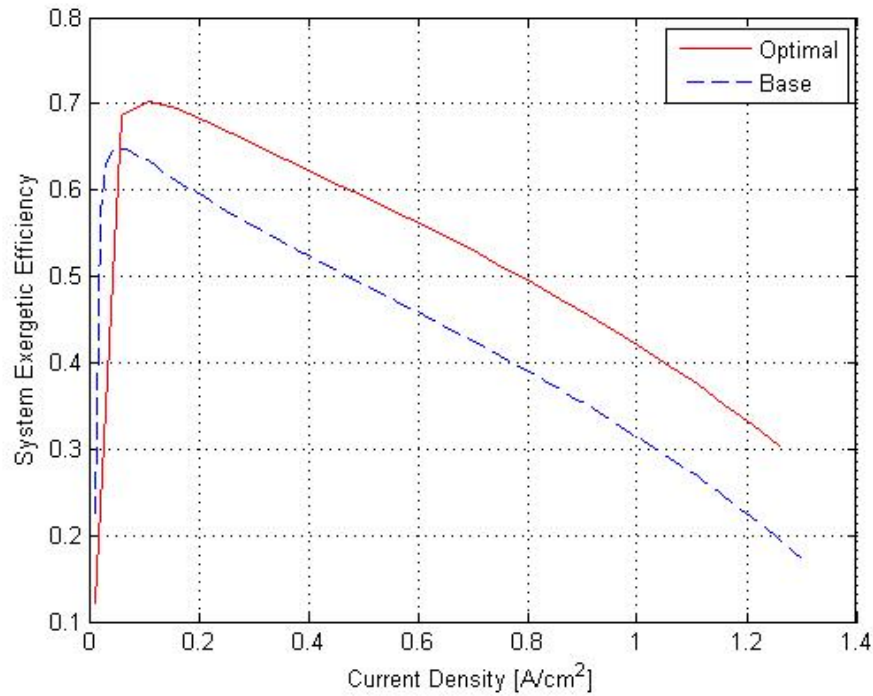


**Figure 8-6. System exergetic efficiency curve for the non-weighted, multi-objective problem:  
average system exergetic efficiency**

### 8.2.2 Single-objective optimization problem

Another important application of PEM fuel cell system is to serve as the power plant for a mobile or stationary power unit to provide a stable power supply. In this portion of the study, the fuel cell system is to be operated at either the maximum net power or point of maximum exergetic efficiency. For the simple power generation application, it is possible to maintain the fuel cell system at a single operating point. Therefore, the fuel cell operating conditions and the current density that yields the maximum net power, or maximum exergetic efficiency, are to be obtained. The optimization problem can be formulated as

$$\begin{aligned}
 &\text{Maximize: } f(\mathbf{x}) = \dot{W}(\mathbf{x}) \\
 &\quad \text{w.r.t. } \mathbf{x} \\
 &\text{subject to: } \mathbf{x}_{\max} \geq \mathbf{x} \geq \mathbf{x}_{\min}
 \end{aligned} \tag{8.3}$$

or

$$\begin{aligned} & \underset{\text{w.r.t. } \mathbf{x}}{\text{Maximize:}} f(\mathbf{x}) = \eta(\mathbf{x}) \\ & \text{subject to: } \mathbf{x}_{\max} \geq \mathbf{x} \geq \mathbf{x}_{\min} \end{aligned} \quad (8.4)$$

The upper and lower limits of the design variables are defined as  $\mathbf{x}_{\min} = [338, 1.5, 1, 0.1]$  and  $\mathbf{x}_{\max} = [373, 5, 15, 1.3]$ .

This problem is also solved using the three optimization algorithms described and the solutions are presented in Table 8-3. Furthermore, two initial design points were used to solve the problem using the local method. For SQP-1,  $\mathbf{x}_0 = [353, 2.5, 3, 0.75]$  and for SQP-2,  $\mathbf{x}_0 = [353, 2.5, 1, 0.75]$ .

**Table 8-3. Solution to the single-objective problem: peak net power**

<b>Optimization Algorithm</b>	<b>Objective Function: Peak Net Power (W)</b>	<b>Solution: [ T (K), AirStoich (-), P (bar), i (A·cm<sup>-2</sup>) ]</b>	<b>Number of Function Evaluations</b>	<b>CPU Time (s)</b>
Simulated Annealing	935	[ 353, 5.0, 1.03, 0.98 ]	4401	7.8
Genetic Algorithms	935	[ 353, 4.57, 1.03, 0.98 ]	4000	92.6
SQP-1	934	[ 368, 1.5, 1.95, 1.01 ]	140	0.2
SQP-2	935	[ 353, 5.0, 1.03, 0.98 ]	244	0.3

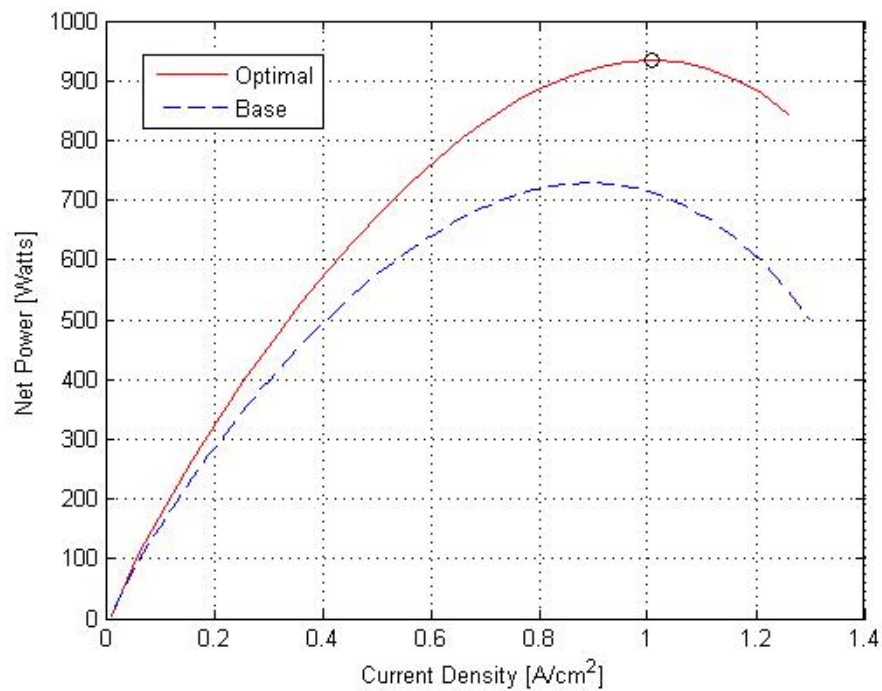
In this case, there are two different solutions with widely varying operating conditions found by the global and local algorithms. There is again a small discrepancy observed between the solution obtained using the GA and SA optimization methods, even though, in effect, both algorithms found the same solution. As in the previous case, an increase in the number of generations or the population in GA would likely result in a better result at the expense of a longer computation time. The existence of two distinct solutions suggests that the objective function is non-unimodal. One solution, located by the local SQP-1 algorithm, is at a very high temperature and high pressure with low air stoichiometry (the minimum value is reached); the

other solution, found by both global algorithms and the SQP algorithm with a different initial starting point, is at a much lower temperature and pressure, but with a high air stoichiometry (the maximum value is reached).

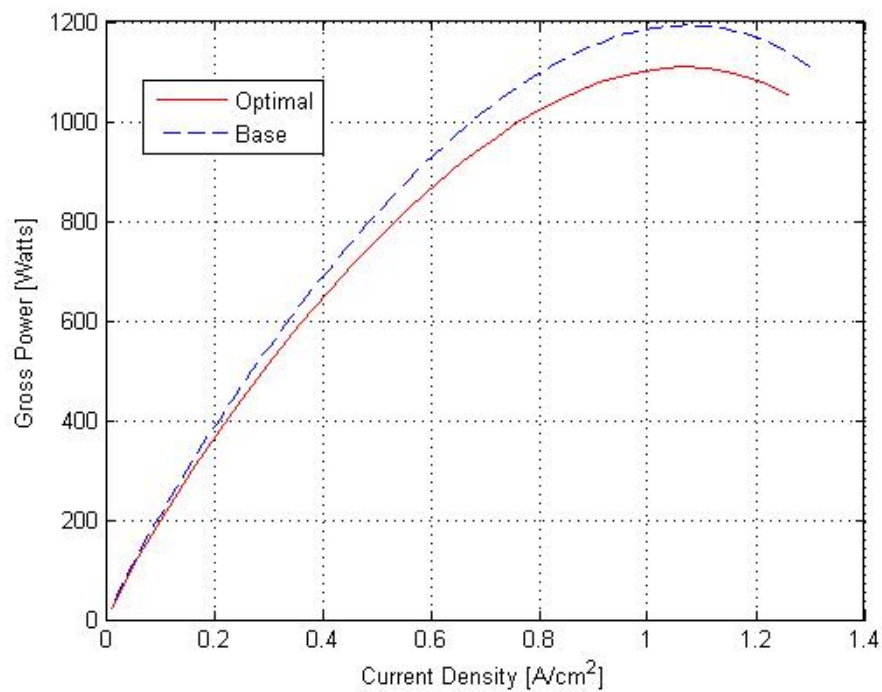
The operating conditions for the solution located by the SQP algorithm (SQP-1) are similar to the solution of the multi-objective function problem, although a distinction between the two results is obvious. The optimal temperature is greater for the stationary application than for the vehicular application, while the optimal operating pressure is less. The optimal air stoichiometry is the same for both applications, at the lower bound of the design variable limits. The difference between the maximized net power curves shows that a slight compromise was required between the performances at high and low current densities for the multi-objective optimization problem: the peak net system power for the multi-objective problem is 0.08% less than the peak net system power determined for the single objective problem.

Figure 8-7 shows a curve of the maximum net output power with respect to the current density at the base and optimal operating conditions for the solution found by the SQP-1 algorithm. The peak of the optimized net system power curve is denoted by the small (black) circle at the maximum value. It is interesting to note that the maximum net power is achieved at the same current density,  $1.01 \text{ A}\cdot\text{cm}^{-2}$ , for which the maximum average net power was determined in the multi-objective problem. The gross power curves are shown in Figure 8-8.

Figure 8-9 and Figure 8-10 depict the net and gross system power for the global algorithms' solution, respectively. The net power curve is essentially the same as that for the SQP-1 algorithm, with slight differences in peak net power values and current density at which the peak net power is achieved. However, the gross power curve is quite different, showing that the gross power of the fuel cell stack has been reduced significantly. The decrease is due to the large reduction on the operating pressure and temperature. Even though the gross power is reduced, the increase in net power can be explained by looking at Figure 8-11 which shows the compressor power for the global algorithms' solution. When contrasted with the compressor power curve of Figure 8-4, a dramatic reduction in power can be easily observed. This



**Figure 8-7. Net power curve for the single-objective problem: peak net power (SQP-1 algorithm)**



**Figure 8-8. Gross power curve for the single-objective problem: peak net power (SQP-1 algorithm)**

reduction in compressor power is mainly due to the decrease of the pressure ratio in Equation

(5.1). As the pressure ratio tends to one the compressor power goes to zero. This shows that there is a large penalty for increasing the cathode pressure of the fuel cell stack.

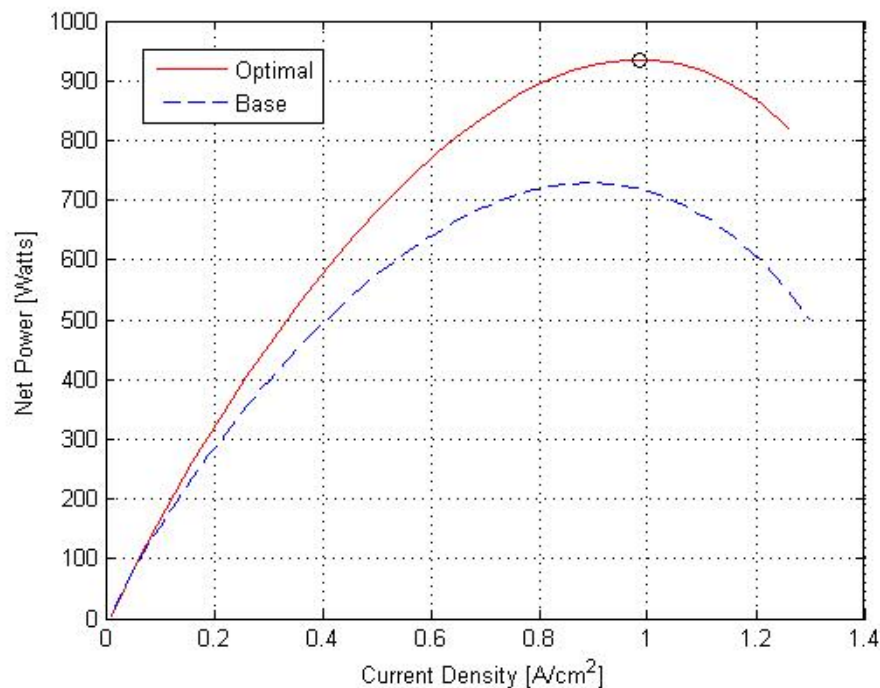


**Figure 8-9. Net power curve for the single-objective problem: peak net power (global optimization and SQP-2 algorithms)**

As in the previous multi-objective optimization problem, the system exergetic efficiency is optimized. The results of the optimization process are depicted below in Table 8-4.

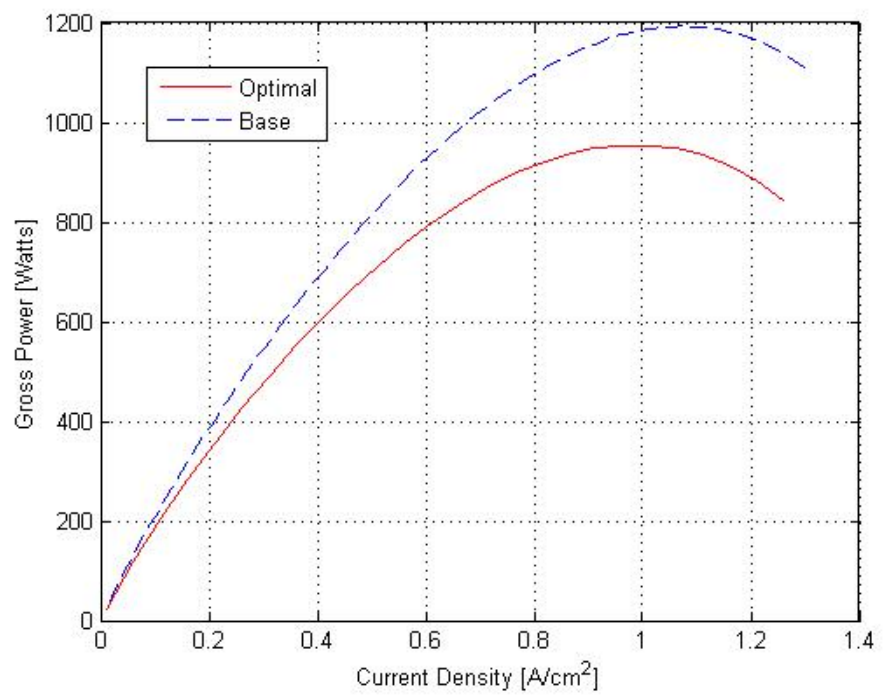


Figure 8-10. Gross power curve for the single-objective problem: peak net power (global optimization and SQP-2 algorithms)

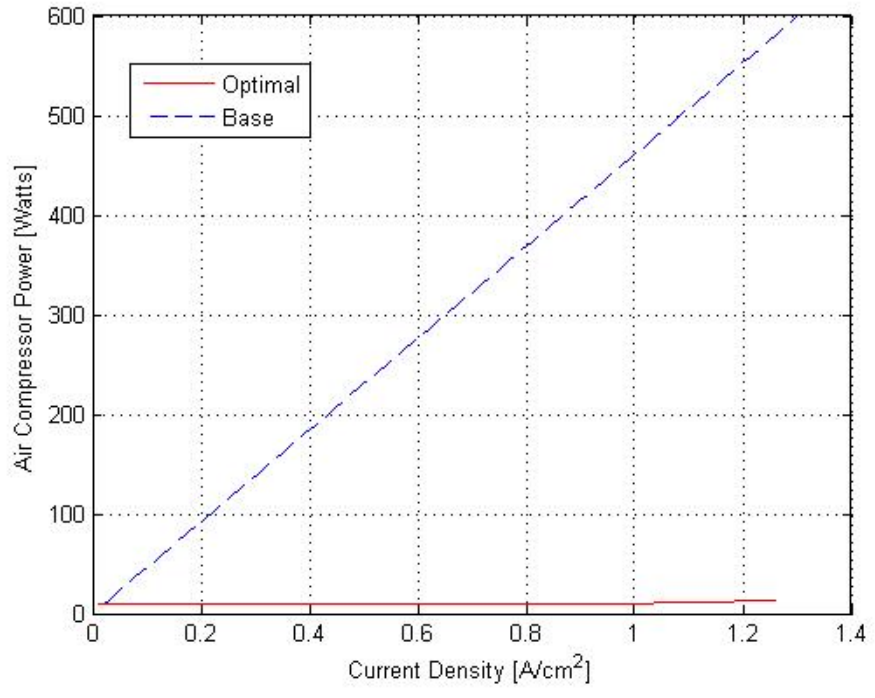
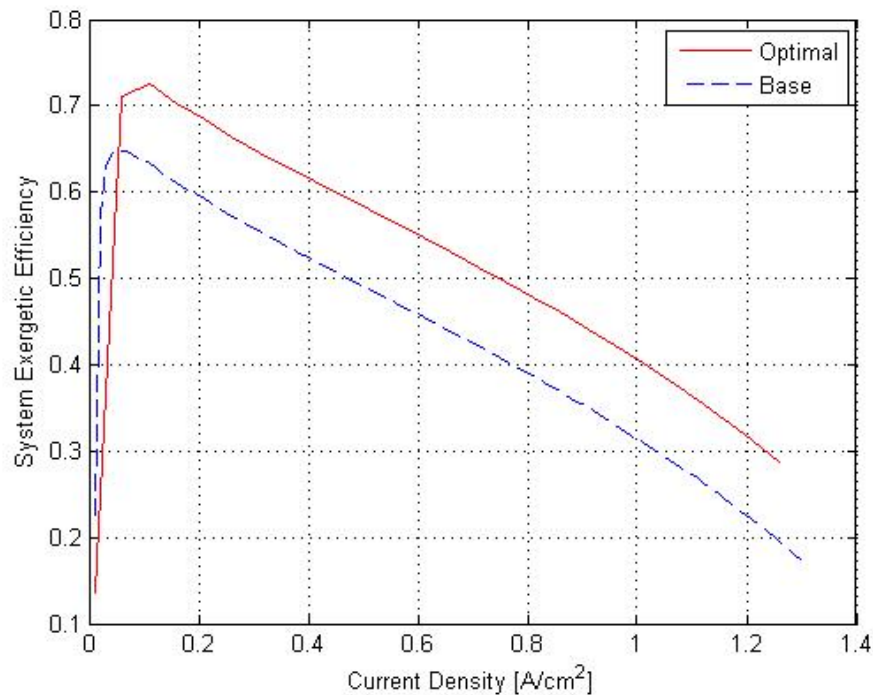


Figure 8-11. Air compressor power curve for the single-objective problem: peak net power (global optimization and SQP-2 algorithms)

**Table 8-4. Solution to the single-objective problem: peak system exergetic efficiency**

<b>Optimization Algorithm</b>	<b>Objective Function: Peak Exergetic Efficiency</b>	<b>Solution: [ T (K), AirStoich (-), P (bar), i (A·cm<sup>-2</sup>) ]</b>	<b>Number of Function Evaluations</b>	<b>CPU Time (s)</b>
Simulated Annealing	0.73	[ 363, 5.0, 1.16, 0.10 ]	4401	5.3
Genetic Algorithms	0.73	[ 363, 5.0, 1.16, 0.10 ]	4000	64.8
SQP	0.73	[ 363, 5.0, 1.18, 0.10 ]	506	0.8

The maximum peak exergetic efficiency was 0.73, which is an increase from the previous single-objective of 4.0% and 4.3% for the low and high stoichiometry solutions, respectively. The peak of the net system power fell below that of the previously optimized average to 868 W (at 0.96 A·cm<sup>-2</sup>), although it remained higher than that of the base operating case. The exergetic efficiency curve as a function of the current density is shown in Figure 14 below. As stated previously, the maximization of the system exergetic efficiency rather than the net system power can reduce the overall costs of the system. The shortfall in power can be mitigated through the introduction of a battery or ultracapacitor in a hybridization scheme.



**Figure 8-12. System exergetic efficiency curve for the single-objective problem: peak system exergetic efficiency**

### 8.3 Study Optimization of a Fuel Cell Hybrid Scooter Powertrain

The techniques of the previous section are then applied in a second study with the intent to improve the performance and cost of the prototype FCHS. In the first study, a non-weighted optimization is conducted. This concept is enhanced in the second study by determining the power requirements of the application and adding these as weights to the objective functions of the multi-objective optimization problem. The result is to optimize the operating conditions of the FCS of a FCHS undergoing a given drive cycle. A decision was made to employ only the Simulated Annealing algorithm since it is a GO, so it will find the global optimum, and it converges more quickly than the Genetic Algorithm method.

The extent of the optimization of FCVs and FCHVs in the literature is relatively scarce; most of the research has been conducted by the National Renewable Energy Laboratory (NREL) in Golden, Colorado. A collaboration between the NREL and Virginia Polytechnic Institute and State University optimized the DOH for FCHV performance. The conclusions were that the

power management strategy and component choice together have a complex effect on the vehicular performance [224]. A follow-up study by Wipke *et al.* examined how optimizing the level of DOH and power management strategy simultaneously for a FCHV can affect its performance [225]. Markel *et al.* used optimization to derive optimal designs and fuel economy of FCHVs and FCVs for a given vehicle range and for fuel cell transient response times that varied from 0 to 40 seconds to transition from 10% to 90% of maximum power [226]. From this review of the literature, it is clear that there have been no previous attempts at optimization of a vehicle at the scale of a LSV.

The drive cycle chosen for the study is again the NYCC, the same cycle used in the simulation tests of Section 6.3.3, as this drive cycle represents typical usage for a scooter. Initial ADVISOR simulations are run with the same base operating conditions as before (temperature of 355 K, air stoichiometry ratio of 2.5, and a pressure of 3 bar) to ensure that the vehicle powertrain model provides adequate power to follow the load cycle of the NYCC. These simulations also allow for a determination of the power requirements demanded by the power management strategy of the FCS. The number of cells in the stack that will just satisfy the load with base conditions was determined to be 38. At this number, the power request (PR) was met for all points of the cycle. Since the prototype FCHS has 39 cells, the vehicle should theoretically be capable of meeting the requirements of the drive cycle. The power request data was then analyzed in order to determine the weight factors for the optimization. The power request distribution is subdivided into categories according to the magnitude of power, as shown in Table 8-5.

The percentage of the cycle at each power request distribution category is depicted in Figure 8-13 below. As shown in the figure, the power requested of the FCS never exceeds 1100 W during the cycle; the peak power demand is in fact 1083 W. The current densities that correspond to all portions of the un-weighted optimized net power curve that have values greater than 1100 W are given a weighting of zero. The weight factors were determined through a combination of the power request distribution and the net power curve versus current density plot

Table 8-5. Power request categories

Power Request Distribution Category	Power Request Magnitude (W)
P1	PR<300
P2	300<PR<400
P3	400<PR<500
P4	500<PR<600
P5	600<PR<700
P6	700<PR<800
P7	800<PR<900
P8	900<PR<1000
P9	1000<PR<1100

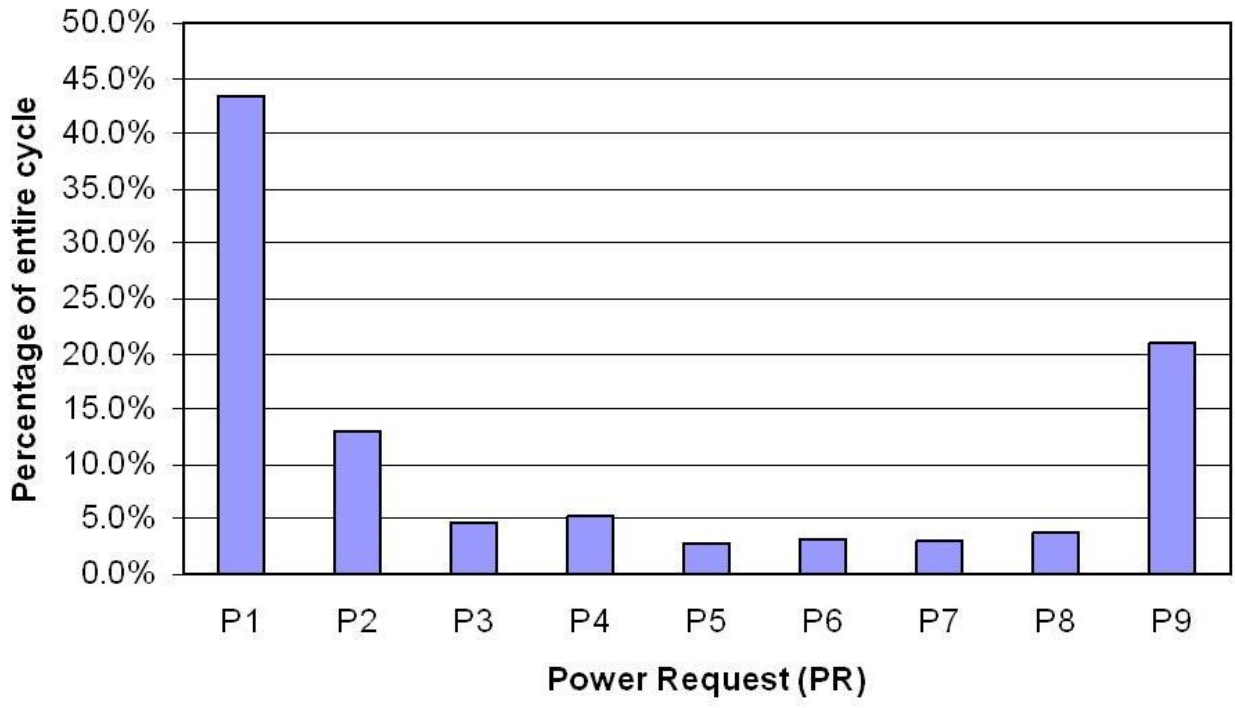


Figure 8-13. New York City Cycle fuel cell system power request distribution

derived from the solution of an additional optimization problem in which the average net power is maximized for all current densities where the weight factors were all set to equal 1. With the weights assigned to the objective functions, the multi-objective strategy from the first study is duplicated; however, the optimization problems are slightly modified. The maximization of the

average net power will include a determination of the minimum number of cells in the stack for which the powertrain will be able to meet the demands of the NYCC. The optimization of the exergetic efficiency, that also varies the number of cells in the stack, will allow for a determination of the most efficient operation over the NYCC, and hence the lowest amount of hydrogen consumption. It should be noted that the FCS is being designed to meet the static demands; in the event that its transient response is slower than is required by the road and driver demand, the ESS is used to compensate.

The optimization of the system with the current design of 39 cells is performed first. The results of the optimizations are presented in Table 8-6. The optimizations of the average net power and of the average net exergetic efficiency are included.

**Table 8-6. Optimization solutions for weighted, multi-objective problems, 39 cells**

<b>Objective function</b>	<b>Solution</b>	<b>Solution: [ T (K), AirStoich (-), P (bar) ]</b>
Average Net Power	992 W	[373, 1.5, 3.09]
Average Exergetic Efficiency	35%	[370, 1.5, 2.77]

The maximum power for the first optimization is 1369 W, while the maximum net power for the second is 1367 W. These values are quite close, with a percent difference of only 0.2%, so the superior choice would be to use the parameters that would maximize the efficiency and thus reduce the hydrogen consumption.

To reduce the hydrogen consumption still further while still satisfying the power requirements, the number of cells in the stack is inserted into the optimization by becoming a design variable. The exergetic efficiency is the objective function. The air stoichiometry, meanwhile, is removed since the solutions invariable occur at the lower limit of 1.5. The value is thus set to 1.5. The optimization results when the objective function is the average exergetic efficiency are included in Table 8-7 below. The solution for a range of cells is included to elucidate the sensitivity of the other two design variable, temperature and pressure, to the

solution.

**Table 8-7. Solutions of the weighted, multi-objective problem: average exergetic efficiency**

<b>Solution:</b> <b>Average Exergetic Efficiency</b>	<b>Number of cells in stack</b>	<b>Temperature (K)</b>	<b>Pressure (bar)</b>
0.348	31	373	3.22
0.348	32	373	3.18
0.349	33	373	3.15
0.349	34	373	3.12
0.35	35	373	3.06
0.35	36	372	2.98
0.35	37	371	2.90
0.35	38	371	2.83
0.351	39	370	2.77
0.351	40	369	2.71
0.351	41	368	2.65
0.351	42	368	2.6
0.352	47	365	2.38

It can be observed from the objective function and design variables from Table 8-7 that the solution is relatively insensitive to the number of cells in the stack. The percent difference between the solution at 47 cells and 31 cells is only 1.1%. The temperature and pressure at the solution also show clear downward trends, with percent differences from 31 to 47 cells of 2.2% and 30.0%, respectively. The decision to reduce the number of cells will depend on the costs of the cells in comparison to the costs savings that can be gained by using smaller heat exchangers and/or a smaller compressor for the lower temperatures and pressures at larger cell numbers. The power demand cycle will also have an effect since it is preferable to operate the cells at a lower current density. Operating at lower current densities is only possible if the required power can be met at these current density levels. It is likely that fewer cells will be the superior design decision and thus the minimum number of cells for which the cycle power demand is met will be used. Using a 31 cell design and the exergetic efficiency as the objective function, the maximum power is determined to be 1091 W. This maximum power is higher than the

maximum demanded by the NYCC, but only 0.8% higher, which would not allow for a factor of safety. The decision is thus made to use 32 cells in the stack design. This change in cell number ensures that all power levels are satisfied.

The fuel consumption of the vehicle undergoing the NYCC can then be compared for the current design of 39 cells and base case operating conditions and the results for the optimization of exergetic efficiency. From Section 6.3.3, the current design of the FCHS model achieves a fuel consumption of  $1.2 \text{ L}\cdot(100 \text{ km})^{-1}$ . After optimization for exergetic efficiency and where the stack is reduced to 32 cells, the fuel consumption becomes 560 kJ, which corresponds to a fuel economy in terms of gasoline equivalent of  $0.93 \text{ L}\cdot(100 \text{ km})^{-1}$ . The percent difference between the base case value and the optimized value is 25.7%. From the amount of hydrogen contained in the three MH tanks, it is observed that the prototype FCHS with its current design could complete 5.15 NYCCs, or 9.7 km. The design with fewer fuel cells would theoretically be able to complete 5.74 NYCCs, or 10.8 km. The optimization has thus shown that a significant improvement over the base case is possible by using this technique to determine the optimal operating conditions and number of cells in the stack.

## **Chapter 9 Conclusions and Outlook**

The hybrid vehicle has the potential to revolutionize the automotive industry. Traditionally, the large automotive companies have segregated parts of the vehicle system and these parts have been developed in near-isolation. The new-found emphasis on emissions and efficiency improvements that have provided the conditions for the HV to become increasingly popular may also cause a radical change in the way that automotive companies develop products. Integration and optimization of systems concurrently throughout the vehicle are now key strategies to remaining competitive. Real-time energy flow management is required to optimize the vehicle operation [227]. This is especially true now that the system complexity is so much greater with the powertrains of HVs. The degrees of freedom available to the designer have risen dramatically. The need for computer modelling, simulation and design optimization throughout the development process is thus expected to continue to increase. The objective of this dissertation was to use these techniques to construct virtual prototypes of several HV powertrains in order to evaluate the designs. The following sections outline the main conclusions and contributions resulting from the various aspects of the research. The suggestions for future work are also included in each section.

### **9.1 Internal combustion engine hybrid vehicle powertrains**

A comprehensive review of the current state of the art of commercialized hybrid vehicle powertrains has been presented, which are at this time entirely ICE-based. The multi-regime architecture nomenclature was introduced, and leading designs have been identified and examined. The review of multi-regime designs is the first of its kind in the scientific literature, and is useful for gauging the trends of hybrid vehicle powertrain development.

Since the multi-regime architecture has only recently been introduced in the literature, much work needs to be done in developing comprehensive models of the architectural design and components. One multi-regime architecture was selected for modelling and simulation. A

study was conducted in which a selected multi-regime powertrain architecture is compared with the THS design, a parallel hybrid, and a conventional architecture. The study vehicle was a commercial delivery truck, and two cases for a full and an empty payload were considered. The modelled vehicles were compared with respect to fuel consumption over four drive cycles that are typical operating conditions for this type of vehicle. The comparison revealed that the multi-regime architecture had a lower fuel consumption than the THS and conventional architectures for all simulations. The average fuel consumption for the multi-regime architecture was higher than that of the parallel hybrid, but the multi-regime architecture had a lower fuel consumption for the simulations with high average speeds. The THS had the highest fuel consumption by a wide margin, leading to the speculation that the design is inappropriate for this type of application. Previous studies on multi-regime architectures provided only normalized results and none compared the performance against any other type of powertrain design. This study is thus a significant contribution of the research.

The study and review of the state of the art illustrated that the potential of the multi-regime architecture to gain significant market share in vehicular powertrains is large. Like all hybrids, the ESS allows for regenerative braking, an AER, and the capacity to shut the engine off when it is not required. These features reduce brake wear and harmful emissions and increase the fuel economy. The multi-regime designs are also capable of improving the costs and performance in comparison to other hybrid architectures. The multi-regime architecture does not require as large an EM as does a series hybrid, and the efficiency at high loads is improved. Conversely to a parallel design, the multi-regime architecture allows for the engine to be de-coupled from the driveline, allowing for smaller engines and more efficient operation, especially at low speeds. Finally, the multiple power-split modes of the multi-regime architecture studied allow for efficient operation over a wider range of loads than the single-mode power-split design of the THS.

The main aspect missing from the developed multi-regime architecture is a well-designed power management strategy. The supervisory power management strategy of the ECU of a HV

coordinates the operation of vehicle sub-systems to achieve performance targets such as maximizing fuel economy and reducing exhaust emissions. This high-level control challenge is known as the power management problem. The current model employs a modified version of the strategy developed in ADVISOR for the single-mode power-split design. It was concluded that the power management strategy could be improved substantially.

There have been many papers published in the literature discussing various methodologies of power management strategy development. One of the most common methods is to employ heuristic control techniques such as control rules, fuzzy logic, or neural networks [228, 229]. However, these methods will not provide the optimal strategy and may not provide efficient operation for drive cycles that have not been considered in the algorithm programming stage. In order to obtain the optimal power management strategy, one of two optimization methods is commonly used. The first class of optimization methodologies deals with instantaneous optimization algorithms, such as DP, designed for real-time application [230-232]. The second class are based on GO algorithms to which the drive cycle is provided *a priori*, and the optimal strategy for the given drive cycle is determined. The latter strategy outperform instantaneous optimization results, but require a sizeable amount of computational time and power and cannot be done in real-time [233, 234]. As a result, GO methods have been largely confined to simulation studies. However, GO methods can provide optimal results that can be used as a benchmark for evaluating the real-time power management strategy performance of the instantaneous algorithms. The instantaneous optimization algorithm that achieves a performance that most closely matches that of the GO methods will be the optimal real-time power management strategy.

While the power management strategy is vitally important, the sizing optimization of the powertrain components is crucial to the overall optimization of the design as well. The sizes of the ICE, ESS, and EMs directly affect the amount of the fuel consumed by the vehicle for any given drive cycle in addition to the performance characteristics such as acceleration and top speed. The efficiency of the ICE is particularly sensitive to the operating cycle of the vehicle,

while the ESS must be appropriately sized to be able to handle large transients and long periods of high loads on the vehicle. With the power management strategy in place, the sizes of the powertrain components can be optimized while considering practical constraints such as size availability and cost, as well as volume constraints.

For a given multi-regime architecture, it is proposed that an iterative process be used for improving performance and cost through the combined optimization of the power management strategy and component sizing. First, an initial guess for the powertrain components will be made, and the optimal power management strategy for these components will be determined. The power management strategy is then fixed and the component sizing optimization is conducted. This process will continue until the improvements with each iteration become marginal. This strategy forms a new method for identifying the global optimal design of both optimal power management strategy and optimal component selection. Combining the two optimization problems will allow for a truly optimal design. Work on this methodology has begun within the author's research group in collaboration with an industry partner, Azure Dynamics. The objective is to repeat the previous comparison study of multiple powertrain designs with the developed power management strategy for the multi-regime architecture. Eventually, the optimal architecture, power management strategy, and component selection for a variety of vehicle types could be catalogued.

## **9.2 Fuel cell system model**

FCS models are becoming increasingly accurate, but progress must continue to account for all of the complex phenomena and interactions within the stack and BOP components. Fully mechanistic models are not yet developed that can provide the high degree of accuracy required. Empirical models are only useful in assessing the performance of a given design; an assessment of the effects of any changes to the design is impossible. Semi-empirical models will therefore continue to be useful tools to researchers since this type exhibits the necessary accuracy and has the capacity to model design changes.

In this dissertation, a semi-empirical FC stack model based on previous work by other researchers was programmed in MATLAB. The stack model was coupled to a BOP models that were also coded in MATLAB. The resultant FCS model is more comprehensive than other FCS models presented in the literature. In addition, several proposed modifications to the model are presented to increase the comprehensiveness of the modelled FCS phenomena, including modules that model the effects of:

- fuel crossover and internal currents
- contact resistance
- electrochemical dynamic effects
- membrane hydration
- reactant flow
- dynamic response of BOP components

The derivation of the required equations has been performed, and once the parameters are determined for the FCS of the prototype FCHS, the modules can be added to the MATLAB code. With these additions, both the stack and system models would be significant contributions to the field.

The current model was used in a study in which optimization of several system operating parameters, namely temperature, pressure and air stoichiometry, to maximize performance was conducted. Three optimizations were carried out:

1. Non-weighted, multi-objective (no application operating data known *a priori*)
2. Single-objective (for a system to be used at a single operating point)
3. Weighted, multi-objective (when application operating data is known *a priori*)

The optimizations successfully showed the usefulness of a determination of the optimal operating conditions for a FCS. The weighted, multi-objective optimization was especially significant, since FCS operating parameter optimization had not been previously applied to an actual application such as the FCHS in the scientific literature. The optimization techniques demonstrated that either average net power or system exergetic efficiency can be maximized,

according to the desired system performance. The simulated range of the FCHS was increased substantially, while the FCS cost was reduced by determining the minimum number of cells in the stack required to meet the power demand.

The optimizations showed how proper operating parameter control could increase the performance of a FCS significantly. Furthermore, the results indicate that adding more design variables to the optimization could provide even further improvements in performance. A sensitivity analysis of the possible candidates for design variables could be conducted to gauge which parameters would have the most effect.

### **9.3 LSV models**

The prototype LSVs were modelled in ADVISOR and MATLAB/Simulink. This is the first instance in the scientific literature in which this vehicle type has been modelled. ADVISOR has numerous included vehicle models, and different modules were chosen and modified to fit the requirements of the two LSVs. The FCS model was coupled to the selected ADVISOR modules to create the overall model of the FCHS.

The LSV models then underwent simulations to predict the performance of the vehicle models in five tests: acceleration, gradeability, NYCC drive cycle, step-input cycle and range test. The FCHS outperformed the BS in all speed, acceleration, and range metrics. The BS achieved lower fuel consumption values, due to its higher efficiency and lower vehicle weight. The differences in predicted performance reflect the increased capacity to deliver current to the motor by the FCHS powertrain.

There are several aspects of the vehicle models that could be improved. For example, the hydrogen storage is not modelled, and the flow and pressure of hydrogen is assumed to be adequate for the FCHS for all current densities. Metal hydride tanks require heat to release the hydrogen molecules from the material in an endothermic reaction. The flow of hydrogen and heat transfer mechanism must thus be modelled to provide a more realistic representation of the actual hydrogen supply system. It was found that it was difficult to determine how much

hydrogen is in the metal hydride tanks at any point because the tank is not pressurized with hydrogen. The adsorption of the hydrogen has little effect on the tank pressure. When re-charging the tanks, the tanks became warm (because of the endothermic reaction of hydrogen adsorption), and when discharging, the tanks became cold. Thus, when the temperature reached an equilibrium point with the surroundings, the tank was nearly full or nearly empty. A more accurate method to ascertain the amount of hydrogen remaining in the tank is an important area of improvement in the vehicle design. Research into the methods for determining hydrogen levels in a metal hydride tank should be conducted.

Very little information could be obtained for several of the LSV components, most notably the hub motors, ESSs and the power management strategy for the FCHS. The efficiency map for the motor as a function of torque and speed was extrapolated from a larger motor of the same type; confidence in the accuracy of such an approach is not high. If information cannot be obtained from the motor manufacturer, bench testing of the motor should occur. This information can be transferred either into an empirical model or the parameters of a theoretical model can be adjusted until the performances match. The same procedure should be followed for the LSV ESSs. The discharging and charging efficiencies were assumed to be equal to batteries from other manufacturers with different capacities, and the validity of this assumption is questionable. The battery models can also become more complex with the addition of dynamic and thermal responses which should make the model much more accurate. The design of the power electronics and ECU of the FCHS is currently not well-understood, and the power-sharing strategy of the FCS and ESS is not known. It is suggested that the powertrain equipment is bench-tested to confirm its operation so that the modelled power management strategy accurately reflects reality.

Several of the other vehicle parameters were best estimates from the literature and do not necessarily reflect the actual characteristics of the prototype LSVs. For example, the coefficients of the road load equation,  $C_{rr}$ ,  $C_D$  and  $A_F$ , could be determined more exactly. Once the enhancements to the vehicles models are in place, more experimental validation with the

dynamometer and on-road testing can be conducted in an iterative process until confidence in the model parameters has been achieved.

#### **9.4 Dynamometer testing**

The dynamometer in the LSVTF was used successfully to test the performance of the prototype LSVs. The facility was proven to be a valuable tool for validating theoretical results. To prepare for the testing, calibration of the system was performed. The friction torque of the system was measured over the range of roller speeds. The MOIs of the dynamometer system and wheel and motor assembly were estimated. The friction torque of the wheels for both the BS and FCHS were measured. The LSVs were subjected to gradeability, top speed, step-input, and range tests, although the FCHS malfunctioned during testing and only the step-input test was partially successful. A discussion on the possible causes of the degraded performance of the FCHS is discussed below in Section 9.5.

The results allowed for a determination of the output torque and power of the motor during the test. For the step-input test at zero eddy current brake torque, the powertrain of the FCHS exhibited superior power to that of the BS, although at the higher powers, the powertrain of the former malfunctioned. For the remainder of the testing, the BS was the sole test vehicle since the FCHS could not perform properly at its maximum output. The BS model underestimated the top speed, but overestimated the speeds achievable at all grades. This result indicates that the torque at high speeds may have been underestimated in the model while the torque available at other speeds may have been overestimated. Another possibility is that the friction in the wheels has been underestimated or that the calculated MOIs are inaccurate. The source of the discrepancy can be determined by bench-testing the individual components and obtaining parameters directly from the manufacturer.

The LSVTF could be improved by modifying the current configuration to a closed-loop design. To accomplish this, the Electronic Servo Load Control optional package should be purchased from Land and Sea. This would allow for control of the eddy current brake torque

and vehicle throttles using the DYNO-MAX software. Without this enhancement of the dynamometer, no dynamic tests can be performed. More calibration would be useful once the dynamic testing capabilities have been added. Specifically, knowing the second order of friction torque coefficients for the dynamometer system and wheels would help increase the accuracy of the results.

## **9.5 Fuel cell hybrid scooter design**

The results of the dynamometer testing of the FCHS indicate that this particular Palcan PC6-1200 unit has severe performance issues at high current densities. It is not clear whether these problems are design flaws or whether the problems are confined to this unit. It would be interesting to be able to test other PC6-1200 units to answer this question. The performance degradation is likely due to either water management or hydrogen flow problems.

The potential water management issue is that the MEA is flooded because insufficient water is being removed by the air stream. During prior testing of the stack, observations were made that confirm the suspicion that there is indeed flooding of the MEA [235], and there are several possible reasons for this occurrence. Firstly, there could be a large pressure drop from the inlet of the oxidant flow piping to the exit. This would prevent the humidified air stream from having enough pressure to remove sufficient quantities of the water forming at the cathode. If this large pressure drop is present, its source should be identified and corrected. It is possible that a build-up of water in the bipolar plate flow channels is causing the drop in potential, and a re-design of the plate might be necessary. Another possible source of the pressure drop is the return manifold. The exhaust piping from the stack is extensive and the pressure drop may be too great in order to allow the water to be ejected. Shortening this piping could reduce the voltage reduction and perhaps eliminate the malfunctioning at high current densities. It is also possible that, if the build-up occurs in the manifold, orienting the stack vertically so that the exhaust is gravity-assisted might mitigate the flooding issues.

Secondly, it is feasible that the operating temperature and/or pressure of the stack are too low,

which could have two deleterious effects. It might allow liquid water to form at the cathode instead of water vapour, and liquid water must evaporate in order to be removed. The air stream would also become saturated at the lower temperature with a lower amount of water vapour and thus not be able to remove the required mass of water. The cooling system could be over-compensating for the heat produced in the stack. It is not clear how the cooling system is controlled currently, but if the method of control is determined, an increase in the operating temperature and pressure could reduce and perhaps alleviate the problem.

Finally, the MEA may be flooding due to significant hydrophilia of the porous layers of the MEA components. If the MEA materials do not release the water molecules, these molecules will block the catalyst sites and prevent the electrochemical reaction from occurring. Research on optimizing the materials and design of MEAs and of PTLs could help reduce this contribution towards the flooding issues at the cathode.

It was also noticed during testing that the pressure gauges of the FCHS MH tanks indicated very low flow levels of hydrogen. This observation must be confirmed, perhaps by measuring the time required to consume the entire amount of hydrogen in the tank compared to the expected consumption level. If it is determined that the flow of hydrogen is insufficient, it is imperative that measures be taken to correct this problem. The configuration of the MH tanks and the fan that transfers heat from the stack could also be modified to improve performance. Currently, some of the heat from the stack is transferred to the tanks positioned underneath by the fan. However, since it is well-known that heat rises, an improved design would be to place the tanks above the stack rather than below. Furthermore, the tanks are currently exposed to a significant amount of forced convection by air passing through a grate below the seat when the vehicle is in motion (although this is obviously less of a concern for the dynamometer testing). Transferring more heat to the tanks and allowing less cooling would result in a higher flow of hydrogen. It is possible that the malfunctioning at high current densities arises because of insufficient hydrogen flow. It would also be extremely useful to substitute a pressurized hydrogen tank for the metal hydride tanks to determine if lack of hydrogen in the stack is the cause of the decreased

performance.

It could also be highly beneficial to test the system independently to the FCHS body and motor. Removing the FCS from the vehicle and bench-testing the system in its entirety and could assist in model development, but also determine which parts of the current design could be improved. The number of papers in the literature with an extensive description of the system, including component model numbers, is low. This research could be a significant contribution.

## 9.6 Design tools

### 9.6.1 Simulation software

As mentioned in Section 3.2.4, the simulation software package, ADVISOR that was used throughout the dissertation is *backward-looking* instead of *forward-looking*. The flow of a backward-looking model was discussed in this section. A forward-looking structure is a more accurate representation of an actual vehicle. The inputs to the forward-looking model come from the driver, namely the accelerator and brake pedal that transfer acceleration and braking requests, respectively, and the outputs are the system states of the vehicle, such as the vehicle velocity, battery SOC, and fuel consumed. Thus the driver is the “controller” of the model, mimicking the real-world situation. However, multiple iterations may be required of the program as it attempts to match the velocity demanded by the drive cycle: the driving command of the driver will usually require multiple passes in order to obtain the proper velocity. It is also difficult to optimize the components during the selection process because of the way the model is structured.

The advantages of using a forward-looking structure type of vehicle simulation software packages include the ability to create power management strategies that can be directly transferred to hardware, a convenience that backward-looking types do not provide. The forward-looking model represents more realistically the actual conditions of a real-world vehicle, and the vehicle simulation software industry is moving towards forward-looking consolidation [236]. It is therefore obvious that the structure type of the simulation package is of great

consequence and should be considered carefully. ADVISOR, while popular with researchers and employed through extensive use in previous work by the author's research group, is backward-looking and it was posited during the course of the degree that a transition to a forwards simulation package was warranted.

In 2004, ADVISOR was sold to a private company and ceased to be open-source. By this point, the forward-looking Powertrain Systems Analysis Toolkit (PSAT) developed by Argonne National Laboratory (ANL) had largely overtaken ADVISOR in popularity with North American researchers. A move to PSAT was considered, but the decision to shift to the open-source software known as Modelica was made instead. This was done in part because similar to ADVISOR, PSAT is empirically based and thus cannot be used unless extensive empirical data for a specific component exists. Modelling software that is more mechanistically based is required in order to provide flexibility in model development.

Modelica is an object-oriented modelling language developed by an international group known as the Modelica Association; Modelica 1.0 was released in 1997. Modelica is the industry standard for physical modelling and simulation in Europe and is quickly becoming the standard in Asia. A forward-looking commercial package from Dynasim AB known as Dymola was purchased. The Dymola software contains the open-source libraries as well as two additional packages: the Smart Electric Drives Library and the PowerTrain Library. Both contain physical models of the various components that are required to build a physical vehicle model that can be EV, ICEV, or many types of HV.

Work has begun on transferring the models developed in ADVISOR to the Dymola software, and the power management strategy for the multi-regime architecture is currently being developed in this environment as well. It can be concluded that the use of ADVISOR should be discontinued.

### 9.6.2 Computer-aided design model

Another aspect to the virtual prototyping process is to create a CAD model using a computer-aided design/computer-aided manufacturing/computer-aided engineering

(CAD/CAM/CAE) software package. This could be useful in design improvement to ensure that volume constraints are taken into consideration and also for structural and vibration analysis. The likely platforms would be Pro-Engineer or SolidWorks, two industry-leading tools for computer-based engineering and design. The various vehicle components as well as the vehicle platform itself would be produced in the CAD environment to create the virtual prototype through which the “packaging” or locating of each component will be accomplished, in order to determine the feasibility of the component selection. A library of component virtual prototypes could be assembled so that different configurations of packaging could be attempted. Eventually, the packaging process could employ optimization techniques to achieve the optimal component arrangement.

The two software packages have built-in FEA modules which can be used to measure structural integrity, heat transfer characteristics and vibrational stability capabilities of the system. The “packaged” vehicle model assembly could be subjected to a variety of tests to determine the robustness of the design. Another useful enhancement would be to develop a manufacturing planning module to estimate the expected production costs and ease of manufacture of the system. The latter exercise, known as Virtual Manufacturing (VM) [237], could have a significant impact on the potential for commercialization of FCHVs. Without significant advances in manufacturing techniques, the introduction of FCHVs into the market may continue to be unduly delayed.

### 9.6.3 Mathematical optimization

During the research, global and local optimization algorithms were compared for several of the optimization problems. Where similar results were obtained from both methods, it can be concluded that the optimization problems investigated are mostly convex and unimodal. In these cases, the use of a local optimization technique is preferred since its application results in the same solution as the global methods using less computation time. However, the addition of design variables and constraints will likely affect the nature of the objective function, and local methods must be used carefully. The complex systems of FCHVs beget convoluted,

multiple-objective functions with multifaceted relationships between the objective function and design variables and design constraints [154]. It is recommended to use a combination of global and local optimization algorithms in the future in order to study the nature of the problems and understand more clearly the characteristics of the objective functions.

To build a more comprehensive objective function which includes, for example, geometric values as design variables, a sensitivity analysis of the possible variables should take place. The purpose of a sensitivity analysis is to examine the relative contributions to performance of each design variable while also measuring the effect of each design variable on the others. A design variable can be weighted lower or set to a fixed value to determine if there is a weak correlation between the variable and the response, or objective function, or if there is a weak correlation between the variable and the other design variables. The sensitivity analysis is conducted using a pre-determined performance measure such as range or acceleration. The overall vehicle performance is directly related to the performance of the individual components that make up the powertrain. The sensitivity analyses will be performed to determine which powertrain components have the largest impact on vehicle performance with respect to its operating efficiency map. It is worth noting that the sensitivity analyses can be performed on a continuous variable such as the width of an individual fuel cell, or on a discrete variable such as material choice [154]. This allows for a valuable flexibility in determining the optimal vehicle design.

## **9.7 Hybrid vehicle outlook**

It must be acknowledged that while ICEHVs have enormous potential for reducing emissions and increasing efficiency, the likelihood of an ICE-based vehicle achieving ZEV status is remote. EVs may be able to exploit this need to gain market acceptance, although the probability of BVs or UCVs becoming dominant is low. Unless a revolutionary ESS is developed that can deliver both range and re-charging times comparable to ICEHVs, the FCHV is likely the technology that is positioned most favourably. In the medium- to long-term

timeline, there is a strong possibility that FCHVs will be commercialized and may eventually supplant the ICE as the main automotive propulsion technology. In order to achieve this environmentally beneficial situation, the design methodology for FCHVs must continue its development so that optimal designs with reduced costs can be obtained in an efficient manner.

The ICEV has been undergoing constant improvement for well over 100 years and ICEHV designs have now benefitted from nearly two decades of intensive research and development efforts. Many vehicle designs and technological modifications have failed to proceed past the prototype stage, and many others have failed even to reach the prototype level. The entire process to reach the level of performance currently provided by contemporary ICEV models has been time-consuming and extremely expensive. A point has been reached, however, where designers of ICEVs have sufficient knowledge of current and past states-of-the-art and experience with virtually all the variations possible that they are able to design the body and frame of the automobile first and then choose the size and configuration of engine that corresponds with the geometric and performance specifications. Indeed, the designer can use “off the shelf” components for which there are substantial operating data, and so confidence in the predicted performance of the integrated system is easily achieved. This development is possible because there is a profound understanding of the physical phenomena associated with the ICE. In addition, most design tools developed for the automobile industry have been targeted towards ICEVs, and the technology has benefitted greatly because of this bias. The ICEHV does not benefit from these same advantages to the extent of the ICEV, but many of the components remain the same, and this facilitates the design process.

Conversely, the designers of FCHEVs do not have the many years of experience that ICE and ICEHV have with the powertrain components. In many cases, an existing vehicle platform is used for an FCHV, instead of using a platform specifically designed to house a FCS and ESS powertrain. Furthermore, ICE and FCHV designers possess vastly different depths of understanding of the ICE versus the FCS and ESS system. Comprehension of the physical phenomena governing FCSs is beginning to improve, however, and this is resulting in

increasingly accurate FCS models. More accurate models will allow for optimization and superior FCS designs. Simulation tools are beginning to support FCHV components as well, assisting the design process for these vehicles. These design tools allow for the possibility of a superior design in a significantly shorter development time, with considerably lower costs. These benefits will mostly be realized by the reduced number of physical prototypes that will be produced, a key requirement for FCHV applications, since past prototypes have cost millions of dollars and these inordinate costs will surely discourage future investment in FCHV research and development.

In the opinion of the author, the most likely powertrain design that will achieve all of the cost and performance goals will be a plug-in design with a FCS as the range extender and a combination of battery and UC as the ESS. The vehicle will operate for the most part in the AER, with the battery providing the bulk energy storage and the UC acting as a buffer to minimize the transients experienced by the battery. The AER will be the most efficient operating regime of the design, since the round-trip efficiency of the ESS is high. The FCS will only be used when the SOC of the ESS reaches a minimum state, which should occur rarely for most urban users. The hybridization will reduce costs since the FCS, the most expensive component, could be relatively low-power. Most importantly, the vehicle will be a ZEV, and the harmful emissions that are associated with the vehicles of today can be essentially eliminated.

## References

- [1] Micklethwait, J. e. (2006). "Roads to Somewhere." *The Economist*, June 24th-30th, pp. 36-37.
- [2] Micklethwait, J. e. (2006). "More of everything." *The Economist*, September 16th-22nd, pp. 18-19.
- [3] Deffeyes, K. (2005). *Beyond Oil: The View from Hubbert's Peak*, Wang and Hill, New York.
- [4] Cacciola, R., Sarva, M., and Polosa, R. (2002). "Adverse respiratory effects and allergic susceptibility in relation of particulate air pollution: flirting with disaster." *Allergy*, **57**, pp. 281-286.
- [5] Rodgers, A., Vaughan, P., Prentice, T., Edejer, T., Evans, D., and Lowe, J. (2002). "The World Health Report 2002: Reducing Risks, Promoting Healthy Life." *Public Report*, World Health Organization.
- [6] Environment Canada.  
Webpage:<http://www.ec.gc.ca/cleanair-airpur/CAOL/transport/publications/trucks/truck3.htm>, *Environment Canada*. Accessed on August 20, 2006.
- [7] Lin, B. (1999). "Conceptual design and modeling of a fuel cell scooter for urban Asia," *Master's Thesis*, Princeton, New Jersey.
- [8] Cyranoski, D. (2005). "Satellite view alerts China to soaring pollution." *Nature*, **437**(12), pp. 12.
- [9] Public Health Toronto. Webpage:[http://www.toronto.ca/health/smog/smog\\_new.htm](http://www.toronto.ca/health/smog/smog_new.htm), *Public Health Toronto*. Accessed on August 24, 2006.
- [10] Intergovernmental Panel on Climate Change, (2007). "Climate Change 2007: Synthesis Report, Summary for Policymakers," *Fourth Assessment Report*, 24 pages.
- [11] Brohan, P., Kennedy, J., Harris, I., Tett, S., and Jones, P. (2006). "Uncertainty estimates in regional and global observed temperature changes: a new data set from 1850." *Journal of Geophysical Research: Atmospheres*, **111**(D12106), pp. 1-21.
- [12] Stainforth, D. A., Aina, T., Christensen, C., Collins, M., Faull, N., Frame, D. J., Kettleborough, J. A., Knight, S., Martin, A., Murphy, J. M., Piani, C., Sexton, D., Smith, L. A., Spicer, R. A., Thorpe, A. J., and Allen, M. R. (2005). "Uncertainty in predictions of the climate response to rising levels of greenhouse gases." *Nature*, **433**(7024), pp. 403-406.
- [13] Stern, N. (2006). "Stern Review: Economics of Climate Change." *Commissioned report*, HM Treasury.
- [14] Zogby International Survey.  
Webpage:[www.zogby.com/wildlife/NWFfinalreport8-17-06.htm](http://www.zogby.com/wildlife/NWFfinalreport8-17-06.htm), *Zogby International Survey*. Accessed on August 28, 2006.
- [15] Environment Canada. Webpage:[http://www.ec.gc.ca/press/2001/010711\\_xsl\\_e.htm](http://www.ec.gc.ca/press/2001/010711_xsl_e.htm), *Environment Canada*. Accessed on October 23, 2005.

- [16] Mouawad, J. (2007). "Record Price of Oil Raises New Fears." *New York Times*, October 17, pp. 7.
- [17] Lovins, A. (2005). "Energy End-Use Efficiency." Rocky Mountain Institute.
- [18] fueleconomy.gov. Webpage:[www.fueleconomy.gov/feg/hybrid\\_sbs\\_cars.shtml](http://www.fueleconomy.gov/feg/hybrid_sbs_cars.shtml), fueleconomy.gov. Accessed on August 27, 2006.
- [19] Toronto Star. Webpage:<http://www.thestar.com/Business/article/287046>, Accessed on December 20, 2007.
- [20] CBC News.  
Webpage:<http://www.cbc.ca/technology/story/2008/01/17/transport-cannon.html>, *CBC News*, "Ottawa to introduce 'made-in-Canada fuel economy standards'". Accessed on January 17, 2008.
- [21] Quong, S. (2007). "The UCS Vanguard: A vehicle to reduce global warming emissions using today's technologies and fuels." *Industry Report*, Union of Concerned Scientists.
- [22] MSNBC.com. Webpage:<http://www.msnbc.msn.com/id/18286221/>, "Toyota overtakes GM in global vehicle sales",. Accessed on June 20, 2007.
- [23] driveclean.gov. Webpage:[www.driveclean.ca.gov/en/gv/home/index.asp](http://www.driveclean.ca.gov/en/gv/home/index.asp), driveclean.gov. Accessed on September 15, 2006.
- [24] Stein, R. (1967). *The Automobile Book*, Paul Hamlyn Ltd., London, UK.
- [25] Moreira, J., and Goldemberg, J. (1999). "The alcohol program." *Energy Policy* **27**, pp. 229-245.
- [26] Roig-Franzia, M. (2007). "A culinary and cultural staple in crisis." *Washington Post*, January 27, pp. A01.
- [27] Niven, R. (2005). "Ethanol in gasoline: environmental impacts and sustainability review article." *Renewable & Sustainable Energy Reviews*, **9**, pp. 535-555.
- [28] MacLean, H., and Lave, L. (2003). "Evaluating automobile fuel/propulsion system technologies." *Progress in Energy and Combustion Science*, **29**(1), pp. 1-69.
- [29] Heffel, J. W. (2003). "NOx emission and performance data for a hydrogen fueled internal combustion engine at 1500 rpm using exhaust gas recirculation." *International Journal of Hydrogen Energy*, **28**(8), pp. 901-908.
- [30] Mercedes-Benz.  
Webpage:[http://www.mercedes-benz.com/content/mbcom/international/international\\_website/en/com/Brandworld\\_Home.html](http://www.mercedes-benz.com/content/mbcom/international/international_website/en/com/Brandworld_Home.html), Accessed on October 24, 2007.
- [31] Daimler AG.  
Webpage:<http://www.daimler.com/dccom/0-5-7165-1-728464-1-0-0-0-0-0-12080-7165-0-0-0-0-0-0.html>, Accessed on November 7, 2007.
- [32] SMMT Communications, (2007). "The evolution of the car, Industry report.
- [33] Heavenrich, R. (2007). "Light-Duty Automotive Technology and Fuel Economy Trends: 1975 through 2007." *Report Number 420-R-07-008*, U.S. Environmental Protection Agency.
- [34] Husain, I. (2003). *Electric and Hybrid Vehicles: Design Fundamentals*, CRC Press, Boca Raton, FL.

- [35] Lipman, T., and Hwang, R. (2003). "Hybrid electric and fuel cell vehicle technological innovation: hybrid and zero-emission vehicle technology links." *Proceedings of the 2003 20th International Electric Vehicle Symposium and Exposition*, Long Beach, CA.
- [36] Paine, C. (2006). "Who Killed the Electric Car?" Sony Pictures Classics.
- [37] Khateeb, S., Farid, M., Selman, J., and Al-Hallaj, S. (2004). "Design and simulation of a lithium-ion battery with a phase change material thermal management system for an electric scooter." *Journal of Power Sources*, **128**, pp. 292-307.
- [38] Tesla Motors. Webpage:[www.teslamotors.com/index/php?js\\_enabled=1](http://www.teslamotors.com/index/php?js_enabled=1), *Tesla Motors*. Accessed on August 25, 2006.
- [39] Becker, H., and Ferry, V. (1957). "Low voltage electrolytic capacitor." U.S. Patent Office, Assigned to: General Electric Company, Patent No.: 2,800,616.
- [40] Miller, J. (2004). *Propulsion Systems for Hybrid Vehicles*, Institution of Electrical Engineers, London, United Kingdom.
- [41] Dong, Z., (2007). *Personal Communication*.
- [42] Larminie, J., Lowry, J. (2003). *Electric Vehicle Technology Explained*, John Wiley & Sons, New York.
- [43] Burke, A. (2005). "Hybrid vehicles: design approaches, component options, and potential fuel economy improvements." Institute of Transportation Studies, University of California at Davis.
- [44] United States Advanced Battery Consortium, (2007). "USABC Goals for Advanced Batteries for EVs," *Industry report*, 1 page.
- [45] "Hydrogen Fuel Cells: Innovation for the 21st Century". Webpage:<http://inventors.about.com/library/weekly/aa090299.htm>, Accessed on December 5, 2004.
- [46] Larminie, J., and Dicks, A. (2003). *Fuel Cell Systems Explained*, 2nd Ed., John Wiley & Sons, New York.
- [47] Shen, J. (2004). "Emerging Enabling Technologies in Vehicular Power Electronics." *Proceedings of the 2004 3rd Annual Summer Workshop of the NDIA Intelligent Vehicles Symposium*.
- [48] Costamagna, P., and Srinivasan, S. (2001). "Quantum jumps in the PEMFC science and technology from the 1960s to the year 2000: Part I. Fundamental scientific aspects." *Journal of Power Sources*, **102**, pp. 242-252.
- [49] Ballard Power Systems, Inc. Webpage:[http://www.ballard.com/be\\_informed/fuel\\_cell\\_technology/roadmap](http://www.ballard.com/be_informed/fuel_cell_technology/roadmap), *Ballard Power Systems, Inc.* Accessed on March 24, 2006.
- [50] Ahluwalia, R., Wang, X., Lasher, S., Sinha, J., Yang, Y., and Sriramulu, S. (2007). "Performance of automotive fuel cell systems with nanostructured thin film catalysts." *Proceedings of the 2007 Fuel Cell Seminar and Exposition*, San Antonio, TX.
- [51] Atwood, P., Gurski, S., Nelson, D. (2001). "Degree of hybridization modeling of a fuel cell hybrid electric sport utility vehicle." *SAE Paper 2001-01-0236*.
- [52] Wouk, V. (2000). "The hybrids are coming!" *Proceedings of the 2000 17th International*

- Electric Vehicle Symposium*, Montreal, QC.
- [53] Motavalli, J. "The Quest for a Plugged-In Prius." *New York Times*, April 2, 2006, pp.
- [54] AFS Trinity Power Corporation. Webpage:[www.afstrinity.com](http://www.afstrinity.com), *AFS Trinity Power Corporation*. Accessed on September 20, 2006.
- [55] Electric Drive Transportation Association, (2007). "*23rd Electric Vehicle Symposium Conference Proceedings*, Anaheim, CA.
- [56] hybrid-vehicle.org. Webpage:<http://www.hybrid-vehicle.org/hybrid-vehicle-history.html>, *hybrid-vehicle.org*. Accessed on September 20, 2006.
- [57] Associates, J. P. a. (2007). "2007 U.S. Hybrid Vehicle Forecast Second Quarter Update." JD Power and Associates.
- [58] Miller, J. (2006). "Hybrid Electric Vehicle Propulsion System Architectures of the e-CVT Type." *IEEE Transactions on Power Electronics*, **21**(3), pp. 756-767.
- [59] HybridCarBlog.com.  
Webpage:<http://www.hybridcarblog.com/2008/01/new-gm-hybrid-every-3-months.html>, *Industry blog*. Accessed on January 5, 2008.
- [60] Gaedt, L., Kok, D., Goodfellow, C., Tonkin, D., Picod, C., and Neu, M. (2004). "HyTrans - A micro-hybrid transit from Ford." In: *International Conference on Automotive Technology*, Istanbul, Turkey.
- [61] Service, R. F. (2004). "The hydrogen backlash." *Science*, **305**(5686), Aug 13, pp. 958-961.
- [62] Romm, J. J. (2004). *The Hype About Hydrogen: Fact and Fiction in the Race to Save the Climate*, Island Press, Washington, D.C.
- [63] St-Pierre, J., Wilkinson, D. P., Knights, S., and Bos, M. L. (2000). "Relationships between water management, contamination and lifetime degradation in PEFC." *Journal of New Materials for Electrochemical Systems*, **3**(2), pp. 99-106.
- [64] Gao, W. (2005). "Performance comparison of a fuel cell-battery hybrid powertrain and a fuel cell-ultracapacitor hybrid powertrain." *IEEE Transactions on Vehicular Technology*, **54**(3), pp. 846-855.
- [65] Honda Motor Co. Webpage:<http://www.hondanews.com/categories/1097/releases/4326>, Accessed on October 29, 2007.
- [66] Chevrolet Motor Co. Webpage:<http://www.chevrolet.com/fuelcell/>, Accessed on January 7, 2008.
- [67] Jamerson, F. (2004). *Electric Bikes Worldwide Reports*, Electric Bicycle Battery Company, Naples, FL.
- [68] Honda Motor Co.  
Webpage:<http://powersports.honda.com/scooters/model.asp?ModelName=Metropolitan&ModelYear=2006&ModelId=CHF506>, *Honda Motor Co., Inc.* Accessed on November 22, 2005.
- [69] Electric Vehicle Technologies, Inc.  
Webpage:[http://www.evtworld.com/scooters\\_168.asp#](http://www.evtworld.com/scooters_168.asp#), *Electric Vehicle Technologies, Inc.* Accessed on November 20, 2005.

- [70] eGo Vehicles, Inc.  
Webpage:[http://www.egovehicles.com/Products/index.cfm?doc\\_id=122](http://www.egovehicles.com/Products/index.cfm?doc_id=122), *eGo Vehicles, Inc.* Accessed on November 20, 2005.
- [71] Vectrix Corp., Inc.  
Webpage:<http://www.vectrix.com/ContentResources/1/69575286/32/BROCHUREVECTRIXELECTRIC.pdf>, Accessed on January 7, 2008.
- [72] Powerzinc Electric (Shanghai), I. (2001). "Test Report of th Performance of Electric Vehicles Powered by Zinc-Air Fuel Cells." *Company Release*.
- [73] Lin, B. (2000). "Conceptual design and modeling of a fuel cell scooter for urban Asia." *Journal of Power Sources*, **86**(1-2), Mar, pp. 202-213.
- [74] Honda Motor Co. Webpage:[http://world.honda.com/news/2004/204824\\_03.html](http://world.honda.com/news/2004/204824_03.html), *Honda Motor Co., Inc.* Accessed on November 21, 2005.
- [75] Vectrix Corp, Inc. Webpage:<http://www.vectrixusa.com/brochures/FuelCell.pdf>, *Vectrix Corp, Inc.* Accessed on November 22, 2005.
- [76] Asia Pacific Fel Cell Technology, Inc. Webpage:[http://www.apfct.com/lastest\\_pro.html](http://www.apfct.com/lastest_pro.html), Accessed on November 1, 2005.
- [77] Intelligent Energy, Inc.  
Webpage:[http://www.intelligent-energy.com/images/uploads/env\\_brochure.pdf](http://www.intelligent-energy.com/images/uploads/env_brochure.pdf), *Intelligent Energy, Inc.* Accessed on November 10, 2005.
- [78] Rowell, L., Korte, J. (2003). "Launch vehicle design and optimization methods and priority for the advanced engineering environment." *NASA Technical Report NASA/TM-2003-212654*.
- [79] Gates Corporation.  
Webpage:[http://www.gates.com/europe/news/index.cfm?id=1437&show=newsitem&location\\_id=254&go=HyTrans](http://www.gates.com/europe/news/index.cfm?id=1437&show=newsitem&location_id=254&go=HyTrans), *Gates Corporation*. Accessed on November 15, 2006.
- [80] Zhang, Y., Lin, H., Zhang, B., and Mi, C. (2006). "Performance Modeling and Optimization of a Novel Multi-mode Hybrid Powertrain." *Journal of Mechanical Design*, **128**, pp. 79-89.
- [81] Westbrook, M. (2001). *The Electric Car: Development and future of battery, hybrid and fuel-cell cars*, Institution of Electrical Engineers, London, United Kingdom.
- [82] ISE Corporation Ltd.  
Webpage:[http://www.isecorp.com/ise\\_products\\_services/gasoline\\_hybrid\\_drive\\_system/](http://www.isecorp.com/ise_products_services/gasoline_hybrid_drive_system/), *ISE Corporation Ltd.* Accessed on December 8, 2006.
- [83] Schmidt, M. R. (1996). "Four-mode, Input-split, Parallel, Hybrid Transmission." U.S. Patent Office, Assigned to: General Motors Corporation, Patent No.: 5,571,058.
- [84] (2006). "Commercial Hybrid Vehicles: Market Analysis for Series, Parallel, Hydraulic, and Electric Drive Systems." ABI Research.
- [85] Miller, J., and Everett, M. (2005). "An assessment of ultra-capacitors as the power cache in Toyota THS-II, GM-Allison AHS-2 and Ford FHS hybrid propulsion systems." In: *20th Annual IEEE Applied Power Electronics Conference and Exposition*, Austin, TX.
- [86] Ai, X., Mohr, T., and Anderson, S. (2004). "An electro-mechanical infinitely variable

- speed transmission." *Proceedings of the 2004 SAE World Congress*, Paper No. 2004-01-0354, 27-40.
- [87] Villeneuve, A. (2004). "Dual Mode Electric Infinitely Variable Transmission." In: *International CVT and Hybrid Transmission Congress*, Davis, CA.
- [88] Lave, L., and MacLean, H. (2002). "An environmental-economic evaluation of hybrid electric vehicles: Toyota's Prius vs. its conventional internal combustion engine Corolla." *Transportation Research Part D: Transport and Environment*, **7**(2), pp. 155-162.
- [89] Liu, J., Peng, H., and Filipi, Z. (2005). "Modeling and analysis of the Toyota Hybrid System." In: *IEEE/ASME International Conference on Advanced Intelligent Mechatronics*, Monterey, CA, Paper MB1-04.
- [90] Kamiya, M. (2006). "Development of traction drive motors for the Toyota Hybrid System." *IEEE Transactions on Industry Applications*, **126**(4), pp. 473-479.
- [91] Oyobe, H., Nakamura, M., Ishikawa, T., Sasaki, S., Minezawa, Y., Watanabe, Y., and Asano, K. (2005). "Development of ultra low-cost, high-capacity power generation system using drive motor and inverter for hybrid vehicles." In: *Fortieth Industry Applications Conference*, Hong Kong, China.
- [92] Liu, J., and Peng, H. (2006). "Control Optimization for a Power-Split Hybrid Vehicle." *Proceedings of the 2006 American Control Conference*, Minneapolis, MN.
- [93] The Hybrid Experience Report.  
Webpage:[http://www.hybridexperience.ca/Toyota\\_Prius\\_Fuel\\_Performance.htm](http://www.hybridexperience.ca/Toyota_Prius_Fuel_Performance.htm),  
*hybridexperience.ca*. Accessed on April 2, 2007.
- [94] Schmidt, M. R. (1996). "Two-mode, Input-split, Parallel, Hybrid Transmission." United States Patent Office, Assigned to: General Motors Corporation, Patent No.: 5,558,588.
- [95] Zhang, D., Chen, J., Hsieh, T., Rancourt, J., and Schmidt, M. R. (2001). "Dynamic modelling and simulation of two-mode electric variable transmission." *Institution of Mechanical Engineers -- Part D -- Journal of Automobile Engineering*, **215**(11), pp. 1217-1223.
- [96] Grewe, T., Conlon, B., and Holmes, A. (2007). "Defining the General Motors 2-Mode Hybrid Transmission." *Proceedings of the 2007 SAE World Congress*, Detroit, MI.
- [97] Schmidt, M. R. (1999). "Two-mode, Compound-split Electromechanical Vehicular Transmission." U.S. Patent Office, Assigned to: General Motors Corporation, Patent No.: 5,931,757.
- [98] Schmidt, M. R., Klemen, D., Nitz, L., and Holmes, A. (2005). "Two-mode, Compound-split, Hybrid Electro-mechanical Transmission Having Four Fixed Ratios." U.S. Patent Office, Assigned to: General Motors Corporation, Patent No.: 6,953,409 B2.
- [99] Chevrolet Motor Co.  
Webpage:[http://www.chevrolet.com/pop/hybrid/2007/highlights\\_en.jsp](http://www.chevrolet.com/pop/hybrid/2007/highlights_en.jsp), Accessed on October 15, 2007.
- [100] Dyck, G., Dries, P., Bagherpour, M., and Czepak, J. (2006). "Electro-mechanical Continuously Variable Transmission." Assigned to: Silvatech Global Systems, Ltd., Patent No.: 7,008,342 B2.

- [101] Miller, J. (2005). "Comparative Assessment of Hybrid Vehicle Power Split Transmissions." In: *Fourth Vectronics Institute Winter Workshop Series*, Warren, MI.
- [102] Miller, J. (2005). "Hybrid Propulsion Systems: The Gasoline-Electric Strong Hybrid." In: *NDIA Workshop*, Traverse City, MI.
- [103] Ahn, K., Cho, S., Cha, S., and Lee, J. (2006). "Engine operation for the planetary gear hybrid powertrain." *Proceedings of the Institution of Mechanical Engineers -- Part D -- Journal of Automobile Engineering*, **220**, pp. 1727-1735.
- [104] Meisel, J. (2006). "An analytic foundation for the Toyota Prius THS-II powertrain with a comparison to a strong parallel hybrid-electric powertrain." *Proceedings of the 2006 SAE 2006 World Congress*, Detroit, MI, Document No. 2006-2001-0666.
- [105] Zhang, D., Chen, J., Schmidt, M. R., and Hsieh, T. (2004). "Dynamic modelling and simulation of one- and three-mode electric variable transmissions." *International Journal of Vehicle Design*, **35**(3), pp. 241-259.
- [106] Schmidt, M. R. (1996). "Two-mode, Compound-split, Electro-mechanical Vehicular Transmission." U.S. Patent Office, Assigned to: General Motors Corporation, Patent No.: 5,558,589.
- [107] Schmidt, M. R. (1996). "Two-mode, Split Power, Electro-mechanical Transmission." U.S. Patent Office, Assigned to: General Motors Corporation, Patent No.: 5,577,973.
- [108] Schmidt, M. R. (2007). "Powertrain with an Electrically Variable Transmission." U.S. Patent Office, Assigned to: General Motors Corporation, Patent No.: 7,166,050 B2.
- [109] Schmidt, M. R., Klemen, D., and Holmes, A. (2007). "Powertrain with Electrically Variable Transmission." U.S. Patent Office, Assigned to: General Motors Corporation, Patent No.: 7,169,073 B2.
- [110] Holmes, A., Schmidt, M. R., Klemen, D., Hendrickson, J., and Sowul, H. (2007). "Electrically Variable Transmission with Selective Fixed Gear Ratio Operation." U.S. Patent Office, Assigned to: General Motors Corporation, Patent No.: 7,220,203 B2.
- [111] Ai, X., and Mohr, T. (2003). "Continuous variable transmission." United States Patent Office, Assigned to: The Timken Company, Patent No.: 6,595,884.
- [112] Ai, X., and Mohr, T. (2005). "Output-split and Compound-split Infinitely Variable Transmission." United States Patent Office, Assigned to: The Timken Company, Patent No.: 6,964,627 B2.
- [113] Schmidt, M. R., and Klemen, D. (1996). "One-mode, Input-split, Parallel Hybrid Transmission." U.S. Patent Office, Assigned to: General Motors Corporation, Patent No.: 5,558,595.
- [114] Schmidt, M. R. (1998). "Three-mode, Input-split Hybrid Transmission." U.S. Patent Office, Assigned to: General Motors Corporation, Patent No.: 5,730,676.
- [115] Holmes, A., and Schmidt, M. R. (2002). "Hybrid Electric Powertrain Including a Two-Mode Electrically Variable Transmission." Assigned to: General Motors Corporation, Patent No.: 6,478,705.
- [116] Wipke, K., Cuddy, M., Bharathan, D., Burch, S., Johnson, V., Markel, A., Sprik, S. (1999). "ADVISOR 2.0: A second-generation advanced vehicle simulator for systems

- analysis." *Technical Report NREL/TP-54025928*, National Renewable Energy Laboratory.
- [117] (2001). "Comparing the Benefits and Impacts of Hybrid Electric Vehicle Options." *Report Number 1000349*, Electric Power Research Institute (EPRI), Palo Alto, CA.
- [118] ADVISOR 2002 Documentation Notes, (2002). "*National Renewable Energy Laboratory*,
- [119] Transportation Techniques LLC. Webpage:[www.transteq.com/press\\_release.asp](http://www.transteq.com/press_release.asp), *Transportation Techniques LLC*. Accessed on December 4, 2006.
- [120] Yamaguchi, J. (2006). "Hybrids for Commerce." *Automotive Engineering International*, November 2006, pp. 66-68.
- [121] ISE Corporation Ltd.  
Webpage:[http://www.isecorp.com/ise\\_products\\_services/diesel\\_hybrid\\_drive\\_system/](http://www.isecorp.com/ise_products_services/diesel_hybrid_drive_system/), *ISE Corporation Ltd*. Accessed on December 8, 2006.
- [122] Haraldsson, K., and Wipke, K. (2004). "Evaluating PEM fuel cell system models." *Journal of Power Sources*, **126**(1-2), Feb 16, pp. 88-97.
- [123] Cheddie, D., and Munroe, N. (2005). "Review and comparison of approaches to proton exchange membrane fuel cell modeling." *Journal of Power Sources*, **147**(1-2), Sep 9, pp. 72-84.
- [124] Boettner, D. D., Paganelli, G., Guezennec, Y. G., Rizzoni, G., and Moran, M. J. (2002). "Proton exchange membrane fuel cell system model for automotive vehicle simulation and control." *Journal of Energy Resources Technology, Transactions of the ASME*, **124**(1), pp. 20-27.
- [125] Maggio, G., Recupero, V., and Pino, L. (2001). "Modeling polymer electrolyte fuel cells: an innovative approach." *Journal of Power Sources*, **101**(2), Oct 15, pp. 275-286.
- [126] Eaton, B., von Spakovsky, M., Ellis, M., Nelson, D., Olsommer, B. (2001). "A mathematical model of the membrane layer of a proton exchange membrane fuel cell." *Proceedings of the 2001 ASME: International Mechanical Engineering Congress Exposition*, New York.
- [127] Dannenberg, K., Ekdunge, P., and Lindbergh, G. (2000). "Mathematical model of the PEMFC." *Journal of Applied Electrochemistry*, **30**(12), Dec, pp. 1377-1387.
- [128] You, L. X., and Liu, H. T. (2002). "A two-phase flow and transport model for the cathode of PEM fuel cells." *International Journal of Heat and Mass Transfer*, **45**(11), May, pp. 2277-2287.
- [129] Secanell, M., Carnes, B., Suleman, A., and Djilali, N. (2007). "Numerical optimization of proton exchange membrane fuel cell cathodes." *Electrochimica Acta*, **52**(7), pp. 2668-2682.
- [130] Kulikovskiy, A. A. (2003). "Quasi-3D modeling of water transport in polymer electrolyte fuel cells." *Journal of the Electrochemical Society*, **150**(11), Nov, pp. A1432-a1439.
- [131] Berning, T., Lu, D. M., and Djilali, N. (2002). "Three-dimensional computational analysis of transport phenomena in a PEM fuel cell." *Journal of Power Sources*, **106**(1-2), Apr 1, pp. 284-294.
- [132] Nguyen, P., Berning, T., and Djilali, N. (2004). "Computational model of a PEM fuel cell

- with serpentine gas flow channels." *Journal of Power Sources*, **130**, pp. 149-157.
- [133] Comsol, I. (2005). *FEMLAB Chemical Module Model Library User's Manual*.
- [134] Noponen, M., Birgersson, E., Ihonen, J., Vynnycky, M., Lundblad, A., and Lindbergh, G. (2004). "Two-phase non-isothermal PEFC model: Theory and Validation." *Fuel Cells*, **4**(8), pp. 365-377.
- [135] Ziegler, C., Yu, H. M., and Schumacher, J. O. (2005). "Two-phase dynamic modeling of PEMFCs and simulation of cyclo-voltammograms." *Journal of the Electrochemical Society*, **152**(8), pp. 1555-1567.
- [136] Li, S., and Becker, U. (2004). "A three-dimensional CFD model for PEMFC." *Proceedings of the 2004 Fuel Cell Science, Engineering and Technology Conference*, American Society of Mechanical Engineers, New York, United States, Rochester, NY, 157-164.
- [137] Sivertsen, B. R., and Djilali, N. (2005). "CFD-based modelling of proton exchange membrane fuel cells." *Journal of Power Sources*, **141**(1), Feb 16, pp. 65-78.
- [138] Lee, J. H., and Lalk, T. R. (1998). "Modeling fuel cell stack systems." *Journal of Power Sources*, **73**(2), Jun 15, pp. 229-241.
- [139] Kim, J., Lee, S. M., Srinivasan, S., and Chamberlin, C. E. (1995). "Modeling of proton-exchange membrane fuel cell performance with an empirical equation." *Journal of the Electrochemical Society*, **142**(8), Aug, pp. 2670-2674.
- [140] Squadrito, G., Maggio, G., Passalacqua, E., Lufrano, F., and Patti, A. (1999). "An empirical equation for polymer electrolyte fuel cell (PEFC) behaviour." *Journal of Applied Electrochemistry*, **29**(12), Dec, pp. 1449-1455.
- [141] Pisani, L., Murgia, G., Valentini, M., and D'Aguzzo, B. (2002). "A new semi-empirical approach to performance curves of polymer electrolyte fuel cells." *Journal of Power Sources*, **108**(1-2), Jun 1, pp. 192-203.
- [142] Amphlett, J. C., Baumert, R. M., Mann, R. F., Peppley, B. A., Roberge, P. R., and Harris, T. J. (1995). "Performance Modeling of the Ballard-Mark-Iv Solid Polymer Electrolyte Fuel-Cell .1. Mechanistic Model Development." *Journal of the Electrochemical Society*, **142**(1), Jan, pp. 1-8.
- [143] Amphlett, J. C., Mann, R. F., Peppley, B. A., Roberge, P. R., and Rodrigues, A. (1996). "A model predicting transient responses of proton exchange membrane fuel cells." *Journal of Power Sources*, **61**(1-2), Jul-Aug, pp. 183-188.
- [144] Mann, R. F., Amphlett, J. C., Hooper, M. A. I., Jensen, H. M., Peppley, B. A., and Roberge, P. R. (2000). "Development and application of a generalised steady-state electrochemical model for a PEM fuel cell." *Journal of Power Sources*, **86**(1-2), Mar, pp. 173-180.
- [145] Fowler, M. W., Mann, R. F., Amphlett, J. C., Peppley, B. A., and Roberge, P. R. (2002). "Incorporation of voltage degradation into a generalised steady state electrochemical model for a PEM fuel cell." *Journal of Power Sources*, **106**(1-2), Apr 1, pp. 274-283.
- [146] Dong, Z., (2005). *Personal Communication*.
- [147] Cownden, R., Nahon, M., and Rosen, M. A. (2001). "Modelling and analysis of a solid

- polymer fuel cell system for transportation applications." *International Journal of Hydrogen Energy*, **26**(6), Jun, pp. 615-623.
- [148] Biyikoglu, A. (2005). "Review of proton exchange membrane fuel cell models." *International Journal of Hydrogen Energy*, **30**(11), Sep, pp. 1181-1212.
- [149] Scott, D. S. (2004). "Inside fuelcells." *International Journal of Hydrogen Energy*, **29**(12), Sep, pp. 1203-1211.
- [150] Van Wylen, G., Sonntag, R., and Borgnakke, C. (1994). *Fundamentals of Classical Thermodynamics*, 4th Ed., John Wiley & Sons, Inc., Toronto, Canada.
- [151] Shapiro, N., and Moran, M. (2004). *Fundamentals of Engineering Thermodynamics*, 5th Edition Ed., Wiley, New York, United States.
- [152] Dong, Z. (2004). "Fuel Cell System Modeling Notes." *IESVic Document*.
- [153] Xue, D., and Dong, Z. (1998). "Optimal fuel cell system design considering functional performance and production costs." *Journal of Power Sources*, **76**(1), Nov 1, pp. 69-80.
- [154] Wang, G., and Dong, Z. (2000). "Design optimization of a complex mechanical system using adaptive response surface method." *Transactions of the Canadian Society for Mechanical Engineering*, **24**(1B), pp. 295-306.
- [155] Barbir, F. (2005). *PEM Fuel Cells: Theory and Practice*, Elsevier Academic Press, San Diego, USA.
- [156] Laurencelle, F., Chahine, R., Hamelin, J., Fournier, M., Bose, T. K., and Laperriere, A. (2001). "Characterization of a Ballard MK5-E proton exchange membrane stack." *Fuel Cells*, **1**(1), pp. 66-71.
- [157] Pathapati, P. R., Xue, X., and Tang, J. (2004). "A new dynamic model for predicting transient phenomena in a PEM fuel cell system." *Renewable Energy*, **30**(1), Jan, pp. 1-22.
- [158] Peppley, B. A., (2005). *Personal Communication*.
- [159] Badrinarayanan, P. (2001). "A Methodology to Understand Water and Thermal Management in an Automotive Fuel Cell System," *Master's Thesis*, University of California at Davis, Davis, CA.
- [160] Eggert, A. (2001). "Water and Thermal Management of Fuel Cell Systems: Impact of Variable System Characteristic on WTM Parasitic Loads," *Master's Thesis*, University of California at Davis Davis, CA.
- [161] Dutta, S., Shimpalee, S., and Van Zee, J. W. (2001). "Numerical prediction of mass-exchange between cathode and anode channels in a PEM fuel cell." *International Journal of Heat and Mass Transfer*, **44**(11), pp. 2029-2042.
- [162] Pukrushpan, J. T., Stefanopoulou, A. G., and Peng, H. (2004). *Control of Fuel Cell Power Systems : Principles, Modeling, Analysis, and Feedback Design*, Springer, New York.
- [163] Zhou, P., Wu, C., and Ma, G. (2006). "Contact resistance prediction and structure optimization of bipolar plates." *Journal of Power Sources*, **159**, pp. 1115-1122.
- [164] Mishra, V., Yang, F., and Pitchumani, R. (2004). "Electrical contact resistance between gas diffusion layers and bi-polar plates in a PEM fuel cell." *Proceedings of the 2004 2nd International Conference on Fuel Cell Science*, Rochester, NY.

- [165] Harrington, D., (2006). "Electrochemistry 645," *Class notes*, page 29.
- [166] Griffiths, D. (1989). *Introduction to Electrodynamics*, 2nd Ed., Prentice Hall, New Jersey.
- [167] Pukrushpan, J. T., Peng, H., and Stefanopoulou, A. G. (2004). "Control-Oriented Modeling and Analysis for Automotive Fuel Cell Systems." *Journal of Dynamic Systems, Measurement, and Control*, **126**(1), pp. 14-25.
- [168] Chen, D., and Peng, H. (2005). "A thermodynamic model of membrane humidifiers for PEM fuel cell humidification control." *Journal of Dynamic Systems, Measurement, and Control*, **127**(3), pp. 424-432.
- [169] Barbir, F., Balasubramanian, B., and Neutzler, J. (1999). "Trade-off design analysis of operating pressure and temperature in PEM fuel cell systems." *American Society of Mechanical Engineers, Advanced Energy Systems Division (Publication) AES*, **39**, pp. 305-315.
- [170] Boettner, D. D., Paganelli, G., Guezennec, Y. G., Rizzoni, G., and Moran, M. J. (2002). "Component power sizing and limits of operation for Proton Exchange Membrane (PEM) fuel cell/battery hybrid automotive applications." *Proceedings of the 2002 ASME Advanced Energy Systems Division*, American Society of Mechanical Engineers, New York, NY, New York, NY, pp. 189-197.
- [171] Hamelin, J., Agbossou, K., Laperriere, A., Laurencelle, F., and Bose, T. K. (2001). "Dynamic behavior of a PEM fuel cell stack for stationary applications." *International Journal of Hydrogen Energy*, **26**(6), Jun, pp. 625-629.
- [172] Akella, S., Sivashankar, N., and Gopalswamy, S. (2001). "Model-based systems analysis of a hybrid fuel cell vehicle configuration." *Proceedings of the 2001 American Control Conference, Jun 25-27 2001*, Institute of Electrical and Electronics Engineers Inc, Arlington, VA, 1777-1782.
- [173] Friedman, D., Eggert, A. Badrinarayanan, P., Cunningham, J. (2001). "Balancing stack, air supply and water/thermal management demands for an indirect methanol PEM fuel cell system." *SAE Paper 2001-01-0535*.
- [174] Guzzella, L., and Amstutz, A. (1999). "CAE tools for quasi-static modeling and optimization of hybrid powertrains." *IEEE Transactions on Vehicular Technology*, **48**(6), Nov, pp. 1762-1769.
- [175] Ogden, J. M., Steinbugler, M. M., and Kreutz, T. G. (1999). "A comparison of hydrogen, methanol and gasoline as fuels for fuel cell vehicles: implications for vehicle design and infrastructure development." *Journal of Power Sources*, **79**(2), Jun, pp. 143-168.
- [176] Rubin, Z., Munns, S., Moskwa, J. (1997). "The development of vehicular power train system modeling methodologies: philosophy and implementation." *Proceedings of the 1997 International SAE Congress and Exhibition*, Detroit.
- [177] Geyer, H., Ahluwalia, R., and Kumar, R. (1996). "Dynamic response of steam-reformed, methanol-fueled, polymer electrolyte fuel cell systems." *Proceedings of the 1996 Intersociety Energy Conversion Engineering Conference*, Vol. 2, pp. 1101-1106.
- [178] Guzzella, L. (1999). "Control-oriented modelling of fuel cell-based vehicles."

*Proceedings of the 1999 NSF Workshop on the Integration of Modeling and Control for Automotive Systems.*

- [179] Hauer, K. H., Friedman, D., Moore, R., Ramaswamy, S., Eggert, A., Badrinarayana, P. (2000). "Dynamic response of an indirect methanol fuel cell vehicle." *SAE Paper 2000-01-0370*.
- [180] Padulles, J., Ault, G. W., Smith, C. A., and McDonald, J. R. (1999). "Fuel cell plant dynamic modelling for power systems simulation." *Proceedings of the 1999 34th Universities Power Engineering Conference*, Univ. Leicester, Leicester, UK, pp. 21-25.
- [181] Pischinger, S., Schonfelder, C., Bornscheuer, W. (2001). "Integrated air supply and humidification concepts for fuel cell systems." *SAE Paper 2001-01-0233*.
- [182] Hussein, M., Baschuk, J., Li, X., and Dincer, I. (2005). "Thermodynamic analysis of a PEM fuel cell power system." *International Journal of Thermal Sciences*, **44**, pp. 904-911.
- [183] Eborn, J., Pedersen, L., Haugstetter, C., and Ghosh, S. (2003). "System level dynamic modeling of fuel cell power plants." *Proceedings of the 2003 American Control Conference*, Denver, CO, Vol. 3, pp. 2024-2029.
- [184] Turner, W., Parten, M., Vines, D., Jones, J., and Maxwell, T. (1999). "Modeling a PEM fuel cell for use in a hybrid electric vehicle." *Proceedings of the 1999 49th IEEE Vehicular Technology Conference*, Vol. 2, pp. 1385-1388.
- [185] Jossen, A., Garche, J., Doering, H., Goetz, M., Knaupp, W., and Joerissen, L. (2005). "Hybrid systems with lead-acid battery and proton-exchange membrane fuel cell." *Journal of Power Sources*, **144**(2), Jun 15, pp. 395-401.
- [186] Pukrushpan, J., Peng, H., and Stefanopoulou, A. (2002). "Simulation and analysis of transient fuel cell system performance based on a dynamic reactant flow model." *Proceedings of the 2002 ASME: Dynamic Systems and Control Division Conference*, American Society of Mechanical Engineers, New York, NY 10016-5990, United States, New Orleans, LA, Volume 71, pp. 637-648.
- [187] Liu, M., Claridge, D., and Deng, S. (2003). "An air filter pressure loss model for fan energy calculation in air handling units." *International Journal of Energy Research*, **27**, pp. 589-600.
- [188] Kreith, F., and Bohn, M. (1993). *Principles of Heat Transfer*, 5th Ed., West Publishing Company, St. Paul, MN.
- [189] Benson, H. (1991). *University Physics*, John Wiley & Sons, New York.
- [190] Pastula, M. (1997). "Radiator Stack PEM Fuel Cell Architecture, System Modeling and Flow Field Design," *Master's Thesis*, University of Victoria.
- [191] American Wind Energy Association.  
Webpage: <http://www.awea.org/faq/windpower.html>, Accessed on January 4, 2008.
- [192] Scott, D. S. (2007). *Smelling Land: The Hydrogen Defense Against Climate Catastrophe*, Canadian Hydrogen Association, Toronto, Canada.
- [193] Wright, S. E. (2004). "Comparison of the theoretical performance potential of fuel cells and heat engines." *Renewable Energy*, **29**(2), Feb, pp. 179-195.

- [194] Adrian, B. (2002). "Fundamentals of exergy analysis, entropy generation minimization, and the generation of flow architecture." *International Journal of Energy Research*, **26**(7), pp. 0-43.
- [195] Tso, C., and Chang, S. Y. (2003). "A viable niche market - fuel cell scooters in Taiwan." *International Journal of Hydrogen Energy*, **28**(7), Jul, pp. 757-762.
- [196] Wang, J. H., Chiang, W. L., and Shu, J. P. H. (2000). "The prospects - fuel cell motorcycle in Taiwan." *Journal of Power Sources*, **86**(1-2), Mar, pp. 151-157.
- [197] Colella, W. G. (2000). "Market prospects, design features, anal performance of a fuel cell-powered scooter." *Journal of Power Sources*, **86**(1-2), Mar, pp. 255-260.
- [198] Laven, A. (1999). "Development of a prototype fuel cell-powered motor scooter," *Master's Thesis*, University of Nevada at Reno, Reno, NV.
- [199] National Center for Health Statistics, (1996). "National Health and Nutrition Examination Survey: Anthropometric Reference Data, United States, 1988-1994," *Public Health Service*, Table 5.
- [200] Wolfram MathWorld. Webpage:<http://mathworld.wolfram.com/Torus.html>, *Torus characteristics*. Accessed on February 12, 2008.
- [201] Heinzmann.  
Webpage:[http://www.heinzmann.com/index.php?option=com\\_content&task=view&id=31&Itemid=129&lang=en](http://www.heinzmann.com/index.php?option=com_content&task=view&id=31&Itemid=129&lang=en), *RN DC motor specifications*. Accessed on January 10, 2008.
- [202] Qingyn, L., Technician, Wuxi Anchi Electrical Machinery Co., Ltd. (2008). *Personal Communication*.
- [203] B.B. Battery Co., (2008). "BP5-12 VRLA Rechargeable Battery," *Specification Sheet*, 2 pages.
- [204] Discover Energy, (2008). "D12180 12 V 18Ah (20 hr) VRLA battery," *Product specification sheet*, 2 pages.
- [205] Royal Dutch Shell, (2007). "Shell Eco-Marathon Rules," *Competition rules*, page 20.
- [206] Palcan Power Systems, Inc. Webpage:[www.palcan.com/s/Products/asp](http://www.palcan.com/s/Products/asp), *Palcan Power Systems, Inc*. Accessed on October 23, 2005.
- [207] Tezcan, S. (2005). "Development of a Fuel Cell Hybrid Low-Speed Electric Vehicle Testing Facility," *Master's Thesis*, University of Victoria, Victoria, BC.
- [208] Land and Sea, Inc., DYNO-MAX 2000 Pro Version 2009.2038 SP #2002.
- [209] Stackhouse, R. (1999). "Modeling, Design, and Testing of Electric Bicycles," *Master's Thesis*, University of Victoria, Victoria, BC.
- [210] Dong, Z. (2004). "Palcan-UVic Fuel Cell-Battery Hybrid Electric Scooter: Technical Specifications." *Technical report*, IESVic.
- [211] Grujicic, M., and Chittajallu, K. M. (2004). "Design and optimization of polymer electrolyte membrane (PEM) fuel cells." *Applied Surface Science*, **227**(1-4), Apr 15, pp. 56-72.
- [212] Mawardi, A., Yang, F., and Pitchumani, R. (2005). "Optimization of the Operating Parameters of a Proton Exchange Membrane Fuel Cell for Maximum Power Density." *Journal of Fuel Cell Science and Technology*, **2**(2), pp. 121-135.

- [213] Wu, J., Liu, Q., and Fang, H. (2006). "Toward the optimization of operating conditions for hydrogen polymer electrolyte fuel cells." *Journal of Power Sources*, **156**(2), pp. 388-399.
- [214] Wang, G., Dong, Z., Aitchison, P. (2001). "Adaptive Response Surface Method - A Global Optimization Method Scheme for Approximation-based Design Problems." *Journal of Engineering Optimization*, **33**(6), pp. 707-734.
- [215] Godat, J., and Marechal, F. (2003). "Optimization of a fuel cell system using process integration techniques." *Journal of Power Sources*, **118**(1-2), pp. 411-423.
- [216] Frangopoulos, C., and Nakos, L. (2006). "Development of a model for thermoeconomic design and operation optimization of a PEM fuel cell system." *Energy*, **31**, pp. 1501-1519.
- [217] Guenther, M., Dong, Z. (2005). "Modeling and Design Optimization of Low-Speed Fuel Cell-Battery Hybrid Electric Vehicles." *Proceedings of the 2005 International Green Energy Conference*.
- [218] Johnson, D., Aragon, C., McGeoch, L., Schevon, C. (1989). "Optimization by Simulated Annealing: An Experimental Evaluation: Part I, Graph Partitioning." *Operations Research*, **37**(6), Nov.-Dec. 1989, pp. pp. 865-892.
- [219] Aarts, E., Korst, J. (1989). *Simulated Annealing and Boltzmann Machines: A Stochastic Approach to Combinatorial Optimization and Neural Computing*, John Wiley & Sons, New York, NY.
- [220] Mitchell, M. (1996). *An Introduction to Genetic Algorithms*, MIT Press, Cambridge, MA.
- [221] Mohamed, I., and Jenkins, N. (2004). "Proton exchange membrane (PEM) fuel cell stack configuration using genetic algorithms." *Journal of Power Sources*, **131**(1-2), pp. 142-146.
- [222] Boggs, P. (1995). "Sequential Quadratic Programming." *Acta Numerica*, **4**, pp. 1-51.
- [223] Lawrence, C., and Tits, A. (2001). "A Computationally Efficient Feasible Sequential Quadratic Programming Algorithm." *Society for Industrial and Applied Mathematics*, **11**(4), pp. pp. 1092-1118.
- [224] Wipke, K., Markel, T., Nelson, D. (2001). "Optimizing Energy Management Strategy and Degree of Hybridization for a Hydrogen Fuel Cell SUV." *Proceedings of the 2001 18th Electrical Vehicle Symposium*, Berlin, Germany.
- [225] Wipke, K., Chintawar, P., Weller, R., and Willis, G. (2003). "An engineering system for automated design and optimization of fuel cell powered vehicles." *Proceedings of the 2003 ASME: Fuel Cell Science, Engineering and Technology Conference*, American Society of Mechanical Engineers, New York, NY 10016-5990, United States, Rochester, NY, pp. 449-454.
- [226] Markel, T., and Wipke, K. (2001). "Optimization techniques for hybrid electric vehicle analysis using advisor." *Proceedings of the 2001 2001 ASME International Mechanical Engineering Congress and Exposition, Nov 11-16 2001*, American Society of Mechanical Engineers, New York, NY 10016-5990, United States, New York, NY, United States, 147-155.

- [227] Chien, A. (2008). "Revolution in the making." *Ricardo Quarterly Review*, **Q1**, pp. 26-29.
- [228] Baumann, B., Washington, G., Glenn, B., and Rizzoni, G. (2000). "Mechatronic design and control of hybrid electric vehicles." *IEEE/ASME Transactions on Mechatronics*, **5**(1), pp. 58-72.
- [229] Schouten, N., Salman, M., and Kheir, N. (2002). "Fuzzy logic control for parallel hybrid vehicles." *IEEE Transactions on Control Systems Technology*, **10**, pp. 460-468.
- [230] Sciaretta, A., Back, M., and Guzzella, L. (2004). "Optimal control of parallel hybrid electric vehicles." *IEEE Transactions on Control Systems Technology*, **12**(3), pp. 352-363.
- [231] Seiler, J., and Schroder, D. (1998). "Hybrid vehicle operating strategies." *Proceedings of the 1998 15th International Electric Vehicle Symposium*, Brussels, Belgium.
- [232] Paganelli, G. (1999). "Design and control of a parallel hybrid car with electric and thermal powertrain," *M.Sc.*, University of Valenciennes, Valenciennes, France.
- [233] Delprat, S., Paganelli, G., Guerra, T., Santin, J., Delhom, M., and Combes, E. (1999). "Algorithmic optimization tool for evaluation of HEV control strategies." *Proceedings of the 1999 16th International Electric Vehicle Symposium*, Beijing, China.
- [234] Rimeaux, S. (1999). "Hybrid vehicle powertrain: modelling and control." *Proceedings of the 1999 16th International Electric Vehicle Symposium*, Beijing, China.
- [235] Guenther, M. (2005). "Modeling and design optimization of low-speed fuel cell hybrid electric vehicles," *Master's Thesis*, University of Victoria, Victoria, BC.
- [236] Hauer, K., Moore, R. (2003). "Fuel Cell Vehicle Simulation - Part 1: Benchmarking Available Fuel Cell Vehicle Simulation Tools." *Fuel Cells*, **3**(3), pp. 84-94.
- [237] Wang, L. Q., Shan, S. Q., and Wang, G. G. (2004). "Mode-pursuing sampling method for global optimization on expensive black-box functions." *Engineering Optimization*, **36**(4), Aug, pp. 419-438.
- [238] Kulikovskiy, A. A., Scharmann, H., and Wippermann, K. (2004). "Dynamics of fuel cell performance degradation." *Electrochemistry Communications*, **6**(1), Jan, pp. 75-82.
- [239] Knights, S. D., Colbow, K. M., St-Pierre, J., and Wilkinson, D. P. (2004). "Aging mechanisms and lifetime of PEFC and DMFC." *Journal of Power Sources*, **127**(1-2), Mar 10, pp. 127-134.
- [240] Hards, G., Ralph, T., Wilkinson, D. P., and Campbell, S. (1996). "Low cost electrode development and performance in Ballard stack hardware." *Proceedings of the 1996 Fuel Cell Seminar*, Orlando, FL, 544-547.
- [241] Nakayama, T. (2000). "Current status of the fuel cell research and development plan at NEDO." *Proceedings of the 2000 Fuel Cell Seminar*, Portland, OR, 391-394.
- [242] Isono, T., Suzuki, S., Kaneko, M., Akiyama, Y., Miyake, Y., and Yonezu, I. (2000). "Development of a high performance PEFC module operated by reformat gas." *Journal of Power Sources*, **86**, pp. 269-274.
- [243] Meada, H., Yoshimura, A., and Fukumoto, H. (2000). "Development of a 10 kW class PEFC module." *Proceedings of the 2000 Fuel Cell Seminar*, Portland, OR, 379-400.
- [244] Mitsuda, K., Gonio, Y., Meada, H., and Fukumoto, H. (1998). "Development of PEFC

- technology of Mitsubishi Electric." *Proceedings of the 1998 Fuel Cell Seminar*, Palm Springs, FL, 541-544.
- [245] Sishtla, C., Koncar, G., Platon, R., Gamburzev, S., Appleby, A., and Velev, O. (1998). "Performance and endurance of a PEMFC operated with synthetic reformat fuel feed." *Journal of Power Sources*, **71**, pp. 249-255.
- [246] Wilson, M., Zawodzinski, C., and Daugherty, M. (2001). "Small Battery-Fuel Cell Alternative Technology Development." *Proceedings of the 2001 DOE Hydrogen Program Review*.
- [247] Metropolis, N., Rosenbluth, A., Rosenbluth, M., Teller, A., and Teller, E. (1953). "Equations of State Calculations by Fast Computing Machines." *Journal of Chemical Physics*, **21**(6), pp. 1087-1092.
- [248] Dong, Z. (2004). "Algorithm of Simulated Annealing." IESVic Document, University of Victoria.
- [249] Cruz, D. (2003). "Optimization of an Electrostrictive Inchworm Actuator using Genetic Algorithms." University of Victoria.
- [250] Antoniou, A., and Lu, W. (2004). *Optimization: Theory and Practice*, Kluwer Ed.

## Appendix A: Vehicle Classifications

The previous sections have introduced the nomenclature used in this dissertation for all vehicle types. The classifications and acronyms for these vehicles are summarized below in Table A-1. The

**Table A-1. Classification and acronym summary**

Vehicle Type	Classification	PZEV or ZEV?
Spark-ignition internal combustion engine	ICE	No/PZEV <sup>†</sup>
Compression-ignition internal combustion engine	ICE	No
Battery vehicle	EV	ZEV
Fuel cell vehicle	EV	ZEV
Ultracapacitor vehicle	EV	ZEV
Battery-ultracapacitor hybrid vehicle	HV	ZEV
Internal combustion engine-battery hybrid vehicle	HV	No/PZEV <sup>†*</sup>
Internal combustion engine-ultracapacitor hybrid vehicle	HV	No/PZEV <sup>†*</sup>
Internal combustion engine-fuel cell hybrid vehicle	HV	No/PZEV <sup>†*</sup>
Internal combustion engine-battery-ultracapacitor	HV	No/PZEV <sup>†*</sup>

hybrid vehicle		
Fuel cell-battery hybrid vehicle	HV	ZEV
Fuel cell-ultracapacitor hybrid vehicle	HV	ZEV
Fuel cell-battery-ultracapacitor hybrid vehicle	HV	ZEV

†If hydrogen is the fuel to be combusted, a PZEV classification can be assigned.

\*The classification will depend on the DOH and power management strategy of the vehicle.

## Appendix B: Stack Degradation

As the cumulative time of operation of a fuel cell increases, the output voltage will gradually decrease. In addition to the work on the GESSDM done by Fowler *et al.* [145], research in this area has also been conducted by Kulikovsky *et al.* and Knights *et al.* [238, 239]. Fuel cell degradation is a relatively under-researched phenomenon [158], but will have a critical impact on the design of any FCHV since its expected lifetime must be comparable with that of the ICEV in order to be commercially competitive. The potential causes of the decrease are numerous and difficult to describe with a direct formulaic model. However, causes with like effects can be grouped together in three broad categories:

- loss of catalytic activity
- loss of conductivity
- loss of reactant mass transfer

The main cause of permanent voltage degradation is contamination of the reactants. Contaminant compounds includes primarily CO, but also sulphur and other organic compounds [145]. Flooding of the cell will cause temporary voltage degradation, but it can also cause long-term voltage degradation because of the corrosive effect of water contact with the MEA materials [63]. Several studies have been conducted to determine the rate of voltage degradation [240-245]. For pure hydrogen fuels, the degradation rate was found to be approximately  $4 \mu\text{V}\cdot\text{hr}^{-1}$ . Reformate fuels were also tested, and the degradation rate ranged from  $4.3 \mu\text{V}\cdot\text{hr}^{-1}$  to  $40 \mu\text{V}\cdot\text{hr}^{-1}$ , depending on the concentration of hydrogen.

An interesting study [246] was conducted on a fuel cell designed at the Los Alamos National Laboratory; the cell was of a “dry” design, meaning that no external humidification or severe water management issues exist. Because less water is present in the cell, the cell was found to have less degradation due to corrosion and catalyst particle ripening (or growth), and after 2000 hr of operation, no degradation was measured. The Palcan PC6-1200 will in all likelihood experience degradation but its effect is not considered in this research.

A change in catalytic activity will affect the reaction rate at the electrode at which the

activity has decreased. The activation overvoltage term will thus increase in importance over the lifetime of the fuel cell. The causes of this loss of catalytic activity in the fuel cell include [145]:

- loss of catalyst surface area due to sintering
- loss of catalyst material through erosion effects
- loss of active sites in the electrode due to contact with the membrane
- loss of active sites due to contaminants binding onto the electrodes
- loss of surface area of the carbon support due to corrosion

The term  $\zeta_2$  of Equation (4.29) can be modified to include a degradation term proposed from a linear degradation model that attempts to account for a decrease in catalytic activity over the operating life of the fuel cell. The equation now becomes [145]:

$$\zeta_2 = k_{cell} + \left( \frac{R}{nF} + \frac{R}{\alpha_c nF} \right) \ln A + \frac{R}{nF} \ln(4FC_{H_2}^*) - \frac{R}{nF} \ln(4F) \quad (C.1)$$

The  $k_{cell}$  term is defined by [145]:

$$k_{cell} = k_{cell}^0 + k_{cell}^{DR} \cdot \frac{\kappa}{T_{stack}} \quad (C.2)$$

where  $k_{cell}^0$  is the original reaction rate parameter when the age of the fuel cell,  $\kappa$  (in hours), equals zero and where  $k_{cell}^{DR}$  is the degradation rate. The term  $k_{cell}^0$  from Equation (C-2) is a parameter that includes rate constants for both the anode and cathode reactions in addition to cell-specific properties such as the effective catalyst surface area and the relative concentrations of water and protons at the electrode-electrolyte interface [145]. The term can be thought of as a value of the apparent catalytic activity.

The degradation terms were determined empirically through measurement taken at intervals during the operation of a cell lasting 6000h [145]. As a result, the degradation terms  $k_{cell}^0$  and  $k_{cell}^{DR}$  are assigned values of 0.00295  $\mu\text{V}$  and 0.055  $\mu\text{V}\cdot\text{K}\cdot\text{hr}^{-1}$ , respectively. Figure C-0-1 is a plot of the degradation in catalytic activity term  $k_{cell}$  as a function of age in hours.

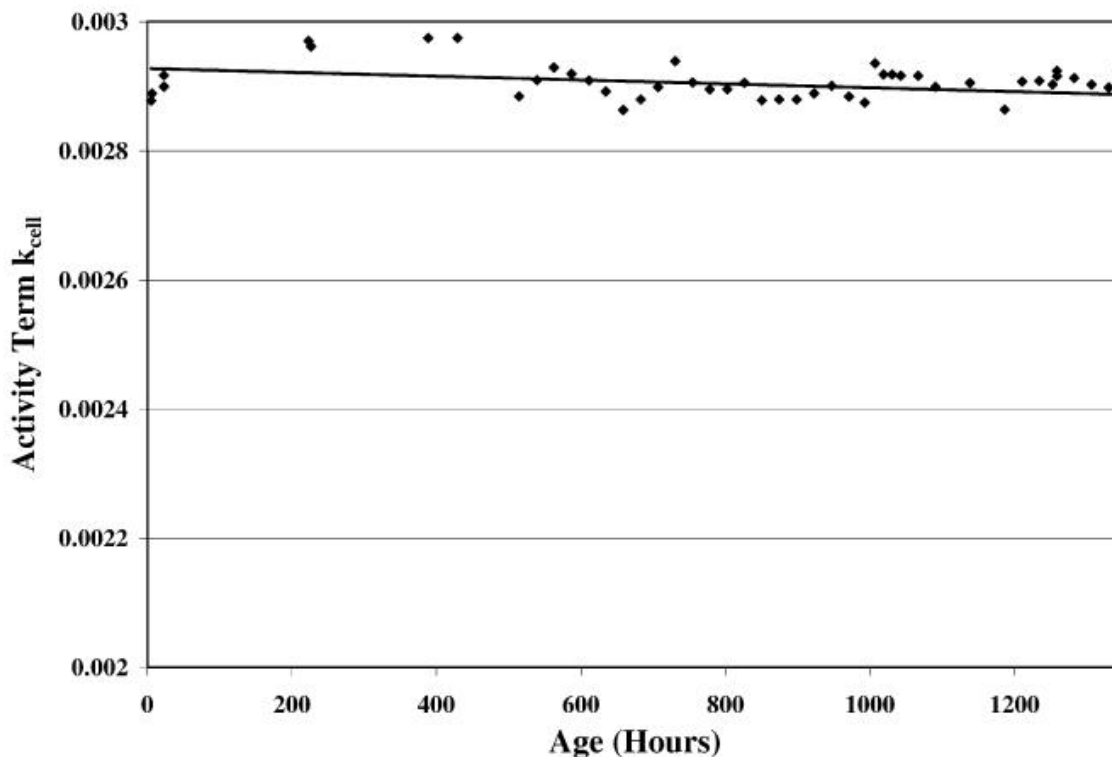


**Figure C-0-1. Catalytic activity term versus age**

Source: [145], page 281.

A loss in conductivity is a result of an increase in ionic resistance in the membrane only, as the electrical resistance is considered negligible; however, if significant corrosion of the bipolar plates, catalyst support or electrodes occurs, the electrical resistance may become significant relative to the ionic resistance. The increased ionic resistance effects are the result of causes that include [145]:

- membrane contaminants
- polymer degradation
- reduction in membrane water content
- delamination of the membrane and catalyst due to thermal and hydration cycles causing mechanical stress cycling, also known as fatigue

The decrease in proton conductivity of the membrane can be modelled by incorporating a decrease in  $\lambda_{FC, membrane}$  in Equation (4.34) such that [145]:

$$\lambda_{FC, membrane} = \lambda_{FC, membrane}^0 + \lambda_{FC, membrane}^{DR} \kappa \quad (C.3)$$

where  $\lambda_{FC, membrane}^0$  is the original curve-fitting parameter when age again equals zero hours,  $\lambda_{FC, membrane}^{DR}$  is the membrane conductivity degradation rate, and  $\kappa$  is again the age of the membrane given in terms of hours of use.

The ohmic degradation terms were also experimentally determined in [145]. The terms  $\lambda_{FC, membrane}^0$  and  $\lambda_{FC, membrane}^{DR}$  are assigned values of 14.6 and  $-0.0007\text{hr}^{-1}$ , respectively. Figure C-0-2 is a plot of the increase in internal resistance and decrease in the adjustable fitting parameter  $\lambda_{FC, membrane}$ .

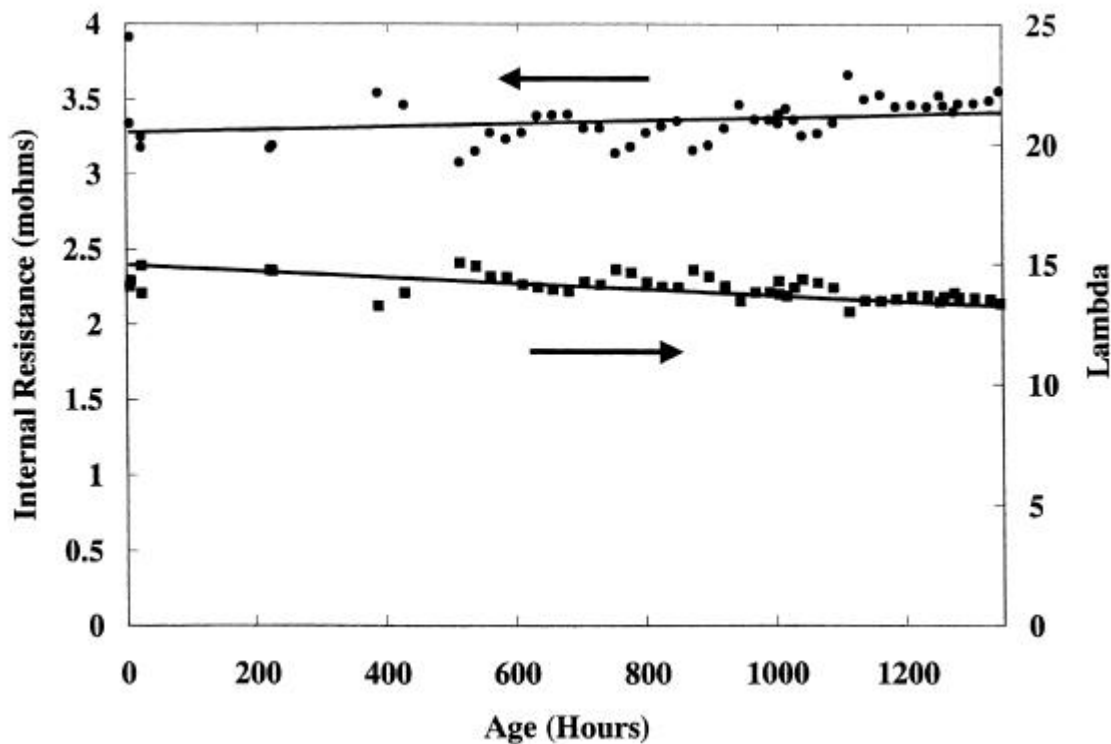


Figure C-0-2. Internal resistance and semi-empirical membrane parameter versus age

Source: [145], page 280.

A decrease in the rate of mass transfer of the reactants is another cause of voltage degradation. As the electrodes age, the mass transfer rate of the catalyst agglomerate decreases, caused in part by a decrease in the porosity factor for diffusion in the catalytic region. The

causes of this rate decrease include [145]:

- increased tortuosity in the reactant pathway due to catalyst particle ripening
- changing water removal characteristics in the polymer active catalyst layer due to material degradation
- compression of the gas diffusion layer due to mechanical stress
- changing water removal characteristics in the gas diffusion layer and carbon catalyst support due to surface chemistry changes

Modelling the mass transfer rate component of voltage degradation has not resulted in phenomenological formulae at present, and so the long-term effects of voltage degradation at high current densities is currently unknown.

The total degradation model predictions and comparison with experimental results are shown below in Figure C-0-3. The test unit is a single cell that is operated for 1350 h continuously at 80 °C and 0.4 A·cm<sup>-2</sup>, 2.1 barg, and stoichiometric ratio of H<sub>2</sub> to air of 1.2:2. The operation was purposefully made to “stress” the cell by

- operating with 75% H<sub>2</sub> and 25% CO<sub>2</sub> for 60 h of the operation
- operating partially dehydrated and flooded for short periods (under 30 min)
- load-cycled numerous times
- thermal cycling between 50-80 °C during the first 500 h

The cell was hand-assembled, which may have contributed to degradation because of unknown irregularities being introduced in the MEA. The cell was also tightened significantly to reduce leakage, and the seals of the cell were degraded during the over 2000 h of operation. These factors may have contributed in a manner that is difficult to quantify [145].

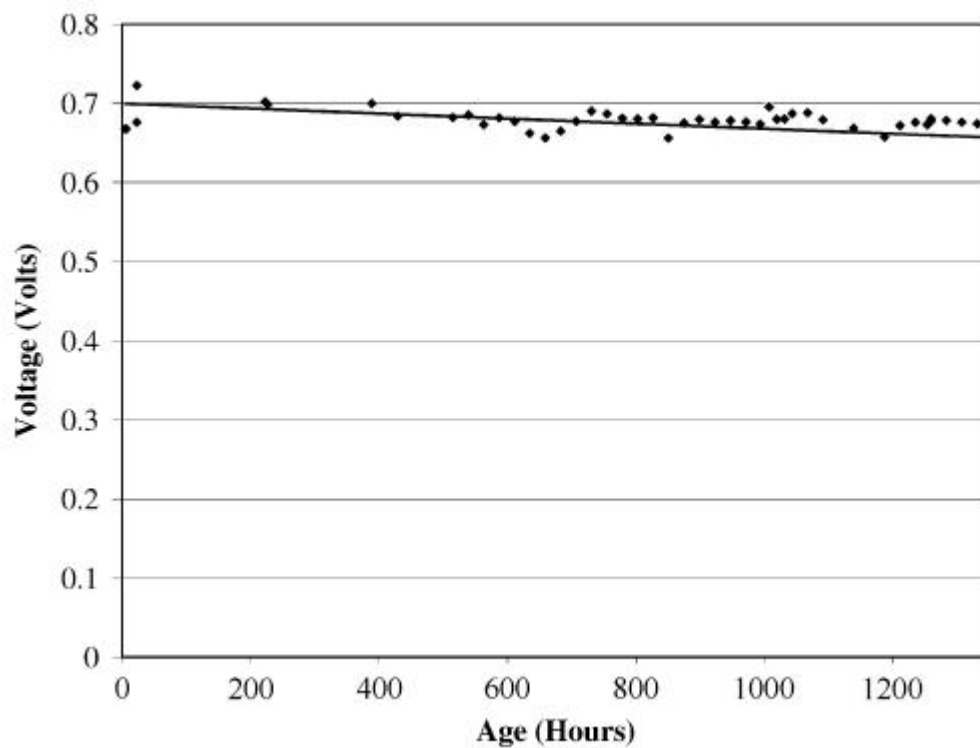


**Figure C-0-3. Voltage degradation model versus experimental results**

Source: [145], page 280.

## Appendix C: Optimization Algorithms

### Simulated Annealing (SA)

SA is a Global Optimization (GO) algorithm that uses the analogy of the physical annealing process of a solid material. SA is a generalized version of a Monte Carlo method for describing the equations of state of a system [247]. The analogy uses the behaviour of a material as it recrystallizes during annealing. In annealing, a material is heated and its form is disordered. The melt is then allowed to cool in a step-wise temperature gradient slowly, so that thermal equilibrium is reached at each step in temperature. Because thermal equilibrium is reached at each temperature step, the atoms of the material are allowed to settle down to the state of absolute minimum energy, even if local minima of energy exist in the material. Thus, the system becomes more ordered, and approaches the zero kinetic energy state of  $T=0$  adiabatically. For SA, the minimum energy level of the solid is analogous to the minimum of the objective function. Continuing the analogy, local minima correspond to metastable states of the material, which occur if the cooling is done too quickly (where quenching occurs) or if the initial temperature is too low. The algorithm uses a perturbation of the initial state vector in seeking an improvement in the current state, and thus a decrease in the objective function value, or “cost”. The algorithm accepts or rejects the new cost value based on a probabilistic relationship with the current “temperature”. The probability of accepting a higher cost decreases with increasing temperature, and analogously to the physical annealing process, and the global minimum cost is eventually located.

The simulated annealing method is capable of solving non-linear programming (NLP) problems of the form:

$$\begin{aligned} &\text{minimize: } f(x) \\ &\text{subject to: } g_i(x) = 0, \text{ for } i = 1, \dots, m, \text{ where } m \geq 0 \\ &\quad h_j(x) \geq 0, \text{ for } j = m + 1, \dots, n \text{ where } n \geq m. \end{aligned}$$

In the case of the project model, the application of the optimization algorithm is described in

detail in Section 4. At present, it is sufficient to note that the optimization problem of the model is an unconstrained problem with boundary limits on the design variables. The following is a summary of the steps in the simulated algorithm method [248]:

- Step 1. Choose the starting point at which the objective function will be evaluated,  $x_0$ . Choose an initial step vector,  $v_0$ . Choose the starting temperature  $T_0$ , where  $T_k$  is the control parameter. The control parameter is reduced according to the value chosen for the reduction coefficient,  $r_T$ . Choose the termination criteria, which for the project is when the change in  $f(x_i)$  is less than  $1 \times 10^6$  on three successive iterations.
- Step 2. Set the starting point  $x_0 = x_{opt}$ , where  $x_{opt}$  is the location of the objective function minimum. Set the index corresponding to successive points,  $i=0$ . Set the index corresponding to successive cycles,  $j=0$ . Set the index corresponding to successive temperature reductions,  $k=0$ . Set the index corresponding to successive step adjustment,  $m=0$ . Set the index corresponding to the direction along which the trial point is generated with respect to the last accepted point,  $h=1$ .
- Step 3. Compute  $f_0 = f(x_0)$ . Set  $f_{opt} = f_0$ .
- Step 4. From the current starting point,  $x_i$ , generate a random point  $x'$  along the direction  $h$ :

$$x' = x_i + r v_{m_h} \vec{e}_h,$$

where  $r$  is a random number generated in the range  $[-1, 1]$  from a so-called pseudorandom number generator, which is a code that is capable of producing unpredictable, unbiased, and usually independent bits. The term  $v_{m_h}$  is the component of the step vector  $v$  that is along the same direction  $h$ , and the term  $\vec{e}_h$  is the vector of the coordinate direction corresponding to the current  $h$ .

- Step 5. If the coordinate corresponding to the current  $h$  of  $x'$ ,  $x'_h$ , is outside the domain

defined for the objective function, then return to Step 4.

Step 6. Compute  $f'=f(x')$ .

Step 7. If  $f' \leq f_i$ , then the new point is accepted, go to Step 10. Otherwise proceed to Step 8.

Step 8. Calculate the acceptance probability,  $p$ :

$$p = e^{\left(\frac{f_i - f'}{T_k}\right)}$$

Step 9. Generate a pseudorandom number  $p'$  in the range  $[0, 1]$ . If  $p' < p$ , the new point is accepted, proceed to step 10. Otherwise, go to Step 4.

Step 10. Set  $x_{i+1} = x'$ . Set  $f_{i+1} = f'$ . If  $f' < f_{opt}$ , then set  $x_{opt} = x'$ , and  $f_{opt} = f'$ .

Step 11. Check  $f_{opt}$  against the termination criteria. If the termination criteria are satisfied, then STOP. Otherwise, go to Step 4.

## Genetic Algorithms (GA)

Genetic Algorithms (GA) is a GO technique that uses the analogy of species evolution to solve non-linear optimization problems. In the evolution analogy, the most advantageous qualities are passed down from one generation to the next by the rules of heredity, resulting in a gradual, yet constant, improvement of the 'fitness' of the overall species. The reason for the improvement or tendency of the superior genes to propagate is that individuals with these genes are more likely to survive than individuals that do not possess them. The superior genes thus have a better chance of surviving after the collective death of a generation and continue in the subsequent generation. GA methods generate a large set or population of potential solutions to a problem. The algorithm then evaluates the 'fitness level' of each solution and decides which solutions are the closest to the optimal solution. The solutions then 'breed' new solutions, with the nearest solutions to the optimum possessing a higher likelihood of breeding than do the less optimal solutions.

There are essentially eight components that make up a GA program [221]: (1) population, (2) initialization, (3) objective and fitness functions, (4) selection rules, (5) crossover (or

recombination) rules, (6) mutation rules, (7) reinsertion rules, and (8) termination rules. A flowchart of the process is illustrated below in Figure D-1.

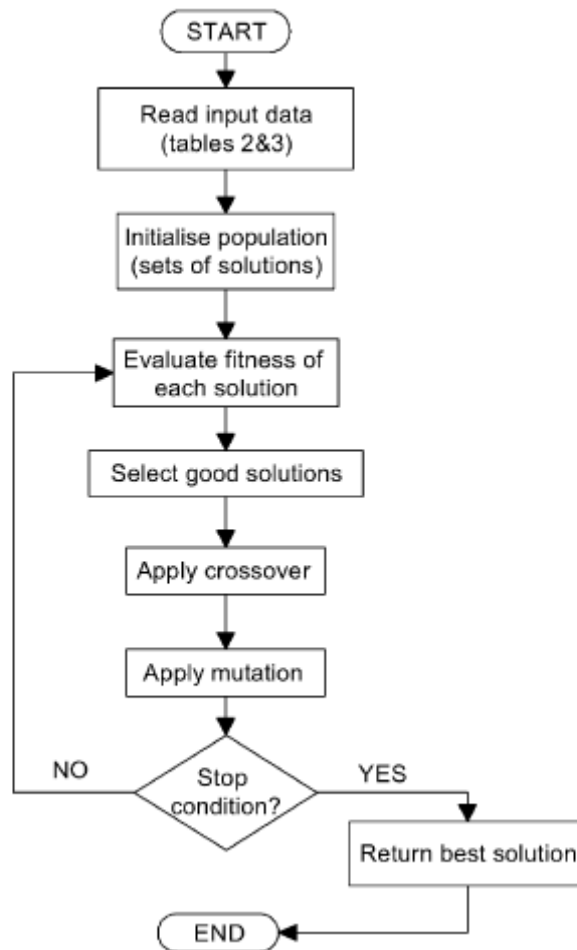


**Figure D-0-1. Flowchart for the GA process**

Source: [221], page 144.

The population of a GA, or set of solutions, is represented by a series of strings corresponding to the sets of genes that make up individuals. The algorithm is iterative and proceeds to create and delete individuals among the population according to the selection rules while determining the overall size of the population in accordance with the reinsertion rules. At each iteration, after the fitness of the solutions is evaluated, a new generation of solutions is created. The population size is important to the performance of the GA, since a larger population will be more “diverse”, and contain a larger search area. The GA of this report uses

20 individuals in each population. The population must be initialized at the beginning of the search, and there are many different methods for performing this initialization. The most common method, and the method used for the project, is to produce a completely random population when specific knowledge of the search area is not known *a priori*.

For a minimization problem, the fitness of an individual can be measured by the relative value of the objective function; a low fitness would indicate a high numerical value and vice versa. The objective function  $f$  and fitness  $F$  are related to each other by a transformation function  $g$  by:

$$F(x) = g(f(x)). \quad (5)$$

The transformation function can have many forms, from a linear scaling transformation to an exponential scaling transformation. Because the project optimization problem is unconstrained, it is sufficient to allow the relative fitness measure be equal to the value of the objective function. The selection rules set for the algorithm determine whether the individual will be ‘allowed’ to reproduce and pass on its genes. Similar to the transformation function, the selection rules can come from one of many approaches. The approach used for the project algorithm is known as stochastic sampling with replacement (SSR). In this approach, the sum of the individual fitness values is calculated, and the individuals are mapped one-to-one into contiguous intervals in the range from 0 to the sum. The interval size depends on the fitness value of the individual. A random number is generated in the same range, and the individual whose interval contains the randomly generated number is selected for crossover. For the project algorithm, this process is repeated to obtain two individuals chosen for the crossover step.

Crossover, also known as recombination, is the process whereby the characteristics of the parents’ genes are passed to the offspring of the reproduction process. The selections of which genes are passed onto the next generation are determined by the crossover rules of the genetic process. The result may be offspring that have a higher or lower (or equal) level of fitness to the parent individuals, although the probability of producing more fit offspring is greater than the probability of producing less fit offspring. The simplest crossover rule procedure is the

single-point method, in which a random crossover point that is less than the string length (but greater than 1) is chosen, and then the offspring will consist of one individual with the first parent's genes up to the crossover point and then the second parent's genes from the crossover point until the end of the string, while the second individual will be a complement to the first. The process of crossover is depicted below in Figure D-2.

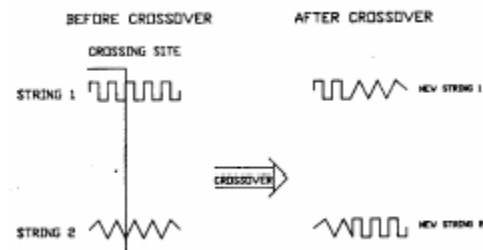


**Figure D-0-2. Illustration of the crossover process**

Source: [249], page 3

Mutation is a natural process that has been an essential component to evolution, and certainly one of the reasons for the extraordinary development of *homo sapiens*. Mutation occurs when one gene of (or bit of the entire string) is randomly altered after the crossover process so that the offspring are not perfect replicas of their parents. The reason for its inclusion is to allow for genes resulting in high levels of fitness that have been selected out of the gene pool to be brought back in by the mutations of the remaining genes.

The reinsertion rules determine which individuals are replaced after the reproductive processes of crossover and mutation. The size of the population may vary, although it is apparent that if the population is allowed to increase in size, this will result in potentially excessive CPU time, while a population that is allowed to decrease in size will eventually become 'extinct'. The most common reinsertion strategy, and the one used for the project algorithm replaces the least fit members of the population after each new generation is completed, known as an elitist strategy.

The termination rules determine the stopping point of the algorithm. The implementation

of a GA optimization does not always result in a global minimum of the objective function, because the GA method stopping criteria is most commonly set by the user at the number of generations to be ‘bred’. If the number of iterations is not large enough, a global minimum may not be found: evolution is an unpredictable and complex process with an uncertain outcome. However, the search algorithm is not random, and an improvement towards the optimal solution is expected with each iteration. The project algorithm allowed for the creation of 200 generations before issuing a solution.

### **Sequential Quadratic Programming (SQP)**

Sequential quadratic programming (SQP), also known as recursive sequential programming, is a local optimization technique based on the linearization of the optimality conditions of the original non-linear constrained problem. The linearization of the optimality conditions yields a quadratic programming problem as an approximation to the original problem [222, 250].

The MATLAB function `fmincon` uses the SQP algorithm to solve constrained optimization problem. Since the `fmincon` algorithm is used for optimization of the fuel cell system in this report, in this section, an overview of the general sequential quadratic programming optimization algorithm is given.

There are several different approaches to the implementation of the SQP algorithm. Boggs gives a good overview of the different possible methodologies in [222]. In this report, the steps for solving a non-linear constrained problem in the form:

$$\begin{aligned} &\text{minimize: } f(x) \\ &\text{subject to: } h(x) = 0 \end{aligned}$$

are described. Any optimization problem can be reformulated into the aforementioned optimization problem form; therefore, the described methodology can be used to solve any constrained optimization problem.

There are several implementations of the sequential quadratic programming algorithm. Here, one possible implementation is presented. The following steps summarize the sequential

quadratic programming algorithm:

- Step 1. Set  $k = 0$ ,  $\mathbf{x}_k = \mathbf{x}_0$ ,  $r_k = 1$  and  $\mathbf{J}_k = \mathbf{I}$  where  $\mathbf{I}$  is the identity matrix.
- Step 2. Evaluate  $f(\mathbf{x}_k)$  and  $\mathbf{h}(\mathbf{x}_k)$ .
- Step 3. Evaluate gradient of objective function and constraints.
- Step 4. Compute the search direction,  $\mathbf{d}$ , and the new Lagrange multipliers  $\mathbf{l}_{k+1}$  by solving the QP problem:

$$\begin{aligned} \text{minimize: } & \frac{1}{2} \mathbf{d}^T \mathbf{J}_k \mathbf{d} + \mathbf{d}^T \mathbf{p}_k \\ \text{subject to: } & \mathbf{h}_k + \mathbf{d}^T \mathbf{H}_k - \frac{1}{2} r_k \mathbf{l}_k = 0, \end{aligned}$$

where  $\mathbf{J}_k$  is the BFGS approximation of the Hessian of the Lagrangian of the original problem at iteration  $k$ ,  $\mathbf{p}_k$  is the gradient of the original objective function at iteration  $k$ ,  $\mathbf{H}_k$  contains the gradient of the active constraints at iteration  $k$ ,  $\mathbf{l}_k$  are the Lagrange multipliers at iteration  $k$ ,  $r_k$  is a penalty factor and  $\mathbf{h}_k$  contains the value of the active constraints at iteration  $k$

- Step 5. Compute  $\alpha^*$  by performing a line search in  $\alpha$  to minimize

$$f(\mathbf{x}_k + \alpha \mathbf{d}) + \frac{1}{r_{k+1}} \mathbf{h}(\mathbf{x}_k + \alpha \mathbf{d})^T \mathbf{h}(\mathbf{x}_k + \alpha \mathbf{d})$$

where

$$r_{k+1} = 2\xi \left[ \frac{\mathbf{h}(\mathbf{x}_k)^T \mathbf{h}(\mathbf{x}_k)}{\mathbf{l}_{k+1}^T \mathbf{l}_{k+1}} \right]^{1/2} \text{ and } 0 < \xi < 1$$

- Step 6. Update design variables using  $\mathbf{x}_{k+1} = \mathbf{x}_k + \alpha^* \mathbf{d}$
- Step 7. Update the Hessian matrix approximation,  $\mathbf{B}_{k+1}$ , using the BFGS update
- Step 8. Check for convergence. If  $\frac{f(\mathbf{x}_{k+1}) - f(\mathbf{x}_k)}{f(\mathbf{x}_k)} \leq \varepsilon$  in two consecutive iterations, or if  $\mathbf{d}_i \leq \varepsilon$  for all  $i=1, \dots, n$  convergence is achieved, STOP. Otherwise, Update the

iterations counter,  $k = k + 1$ . Go to STEP 2. Notice that  $f(\mathbf{x}_{k+1})$  will need to be evaluated and  $\varepsilon$  represents a specified tolerance, in this case  $1e-8$ .